Tribological Performance Inspired by Nature: Plant Oils, Fungi and Algae

by

Vasily Rublev

A thesis submitted to Imperial College London for the degree of Doctor of Philosophy and Diploma of Imperial College

September 2025

Tribology Group

Department of Mechanical Engineering

Imperial College London

Statement of Originality.

I hereby declare that the work presented in this thesis is my own unless stated otherwise. No part has been submitted for a degree at this or any other university. To the best of my knowledge the work is original, and all the work of others is clearly cited and appropriately referenced.

Signed: Vasily Rublev

Date: 1st October 2025

Copyright Statement.

The copyright of this thesis rests with the author. Unless otherwise indicated, its contents are licensed under a Creative Commons Attribution-Non-Commercial 4.0 International Licence (CC BY-NC).

Under this licence, you may copy and redistribute the material in any medium or format. You may also create and distribute modified versions of the work. This is on the condition that: you credit the author and do not use it, or any derivative works, for a commercial purpose.

When reusing or sharing this work, ensure you make the licence terms clear to others by naming the licence and linking to the licence text. Where a work has been adapted, you should indicate that the work has been changed and describe those changes.

Please seek permission from the copyright holder for uses of this work that are not included in this licence or permitted under UK Copyright Law.

Acknowledgments

I would like to thank Dr Marc Masen for his consistent guidance and support throughout this research and Prof. Philippa Cann for her helpful discussions and contributions.

I am also thankful to Dr Gustavo Luengo from L'Oreal Research & Innovation for his collaboration and expert input on part of this research.

Finally, I would like to express my appreciation to all members of the Tribology Group at Imperial College London for their support, technical help and an enjoyable environment.

Table of Contents

Statement of Originality....2
Copyright Statement. 3
Acknowledgments....4
Abstract....10
List of Symbols 11
List of Figures 13
List of Tables 18
1. Introduction 19
1.1. General Motivation 19
1.2. Research Objectives 21
1.3. Thesis Outline....22
2. Literature Review....24
2.1. Purpose of Lubrication....24
2.2. Lubrication Regimes....24
2.2.1. Hydrodynamic Regime 25
2.2.2. Mixed Regime 26
2.2.3. Boundary Regime....26
2.3. Tribological Mechanisms in Boundary Regime....26
2.3.1. Adsorbed Layers 27
2.3.2. Particle Lubrication....27
2.3.3. Surface Texturing 28
2.3.4. Hydration Lubrication 28
2.4. Wear Mechanisms in Boundary Lubrication 28
2.4.1. Abrasive Wear....28
2.4.2. Adhesive Wear....29
2.4.3. Surface Fatigue Wear 30

2.4.4. Tribochemical Wear 30
2.5. Bio-Lubrication 30
2.6. Oil-based Bio-Lubrication 32
2.6.1. Plant Oils 32
2.6.2. Algal Oils 34
2.6.3. Animal Fats 35
2.6.4. Synthetic Esters 35
2.7. Water-based Bio-Lubrication 35
2.7.1. Polysaccharides 35
2.7.2. Proteins and Peptides 37
2.7.3. Phospholipids and Liposomes 38
2.8. Intended Applications and Operating Conditions 38
2.9. Summary 39
3. Methods 41
3.1. Tribological Assessment 41
3.1.1. High Frequency Reciprocating Rig (HFRR) 41
3.1.2. Biotribology Machine (BTM) 46
3.2. Rheological Assessment 47
3.2.1. Viscosity Evaluation 47
3.2.2. Hydrogel Assessment 47
3.3. Indentation Testing 49
3.3.1. Hydrogel Indentation 49
3.3.2. Indentation Model Validation 51
3.4. Dynamic Light Scattering (DLS) 51
3.5. Summary 52
4. Plant Oils as Direct-Use Bio-Lubricants 53
4.1. Introduction 53

4.2. Historical Perspective of Direct-use 54
4.3. Modern Eco-Friendly Lubricants 55
4.4. Testing Direct Use of Plant Oils 57
4.5. Optimisation 68
4.6. Critical Overview 69
4.7. Conclusions 70
5. Biomimetic Approach in Water-Based Lubrication 71
5.1. Introduction 71
5.2. Biomimetic Approach to Water-Based Lubrication 72
5.2.1. Step 1. The Problem 73
5.2.2. Step 2. Limitations 73
5.2.3. Step 3. Natural Solutions 74
5.2.4. Step 4. Exploration 75
5.2.5. Summary of Biomimetic Phase 77
5.2.6. Step 5. Evaluation of Principle 77
5.3. Conclusions 82
6. Water-Based Lubricants from Mushrooms 83
6.1. Introduction 83
6.2. Lubricant Preparation and Characterisation 84
6.2.1. Materials 85
6.2.2. Fungal Solutions Preparation 85
6.2.3. Lubricant Characterisation 86
6.3. Results 88
6.3.1. Tribological Performance 88
6.3.2. Effect of Lentinan Concentration 94
6.4. Discussion 95
6.5. Conclusions 100

7. Hydrogels from Natural Polysaccharides 101
7.1. Introduction 101
7.2. Non-Ionic Hydrogels 110
7.2.1. Materials 111
7.2.2. Non-Ionic Hydrogel Preparation 111
7.2.3. Results 113
7.2.4. Summary 117
7.3. Ionic Hydrogels 118
7.3.1. Materials 118
7.3.2. Ionic Hydrogel Preparation 118
7.3.3. Results 119
7.3.4. Summary 123
7.4. Discussion 124
7.4.1. Effect of Gelation Mechanisms on Hydrogel Properties 124
7.4.2. Mesh Size 127
7.4.3. Components of Friction Force 130
7.4.4. Guidelines for Tailoring Hydrogels 132
7.5. Conclusions 133
8. A New Model for Contact of Soft Solids 134
8.1. Introduction 134
8.2. Limit Radius Model Definition 135
8.3. Experimental Validation 138
8.3.1. Materials and Methods 138
8.3.2. Indentation Curves 138
8.3.3. Elastic Modulus Evaluation 141
8.4. Static Scenario 142
8.4.1. Case A: Polynomial 144

8.4.2. Case B: Boussinesq-type 147
8.5. Application of the Model 150
8.6. Conclusions 152
9. Conclusions and Future Work 154
9.1. Summary of Findings 154
9.2. Limitations 155
9.3. Recommendations for Future Work 156
Bibliography 158
Appendix A – Static Scenario 186
Definitions 186
Derivation 186
Appendix B – Case A Deformation 189
Appendix C – Case B Deformation 194

Abstract

Mineral oil-based lubricants pose significant environmental risks due to poor biodegradability and toxicity, particularly when released into ecosystems. Sustainable lubrication therefore demands functional alternatives. This thesis investigates bio-based strategies inspired by natural systems, focusing on materials from plants, fungi and algae.

First plant oils were evaluated as renewable biolubricants used without chemical modification. Tribological testing demonstrated reductions in both friction and wear. Mixtures of oils combined the advantages of individual components, providing a practical route for improving performance. A biomimetic approach was then applied to water-based lubrication using fungal polysaccharides. Extracts from mushrooms and aqueous β-glucan solutions reduced friction and wear, linked to polysaccharide concentration and particle size distribution. These findings establish fungal polysaccharides as promising candidates for bio-lubrication.

Polysaccharides from plants and algae were subsequently explored as hydrogels. Both non-ionic and ionic gelation mechanisms were investigated. Different metallic ions were added to assess their impact on hydrogel properties. Hydrogels exhibited tuneable viscoelastic properties and frictional behaviour, governed by the balance between network density, water mobility, and polymer-ion interactions. An existing model was applied to separate friction into deformational and interfacial components, allowing analysis of tribological behaviour through other material parameters.

To address the limitations of Hertz-based contact models for soft solids, a novel theoretical framework was developed. The limit radius model introduces a finite limit radius, beyond which deformations vanish, providing improved predictions of contact mechanics. Validation against experimental data confirmed the suitability of a polynomial-type deformation profile.

Together, these findings demonstrate that natural and nature-inspired materials offer functional pathways to sustainable lubrication and theoretical advances provide accurate interpretation of their tribological behaviour. Plant oils, fungal polysaccharides and polysaccharide hydrogels each present distinct advantages and limitations, advancing the development of environmentally compatible lubricants.

List of Symbols

Symbol	Description	Unit
a	Contact radius	m
a_{Hertz}	Hertz contact radius	m
$A_{contact}$	Hertz contact area	m^2
A_{disk}	Disk wear scar cross sectional area	m^2
d	Ball wear scar diameter	m
D	Ball specimen diameter	m
E	Elastic modulus	Pa
E^*	Reduced elastic modulus	Pa
E'	Reduced Young's modulus	Pa
F	Friction force	N
F_{def}	Deformational component of Friction force	N
F_{int}	Interfacial component of Friction force	N
F_r	Radial force	N
F_z	Indentation force	N
G	Dimensionless materials parameter	$-$
G'	Storage modulus	Pa
G''	Loss modulus	Pa
h_m	Minimum film thickness	m
H	Brinell hardness	$-$
k_B	Boltzmann constant	J/K
k_{ball}	Ball wear coefficient	$\frac{mm^3}{Nm}$
k_{disc}	Disc wear coefficient	$\frac{mm^3}{Nm}$
K	Ratio of Limit radius to Contact radius	$-$
L	Sliding distance	m
L_0	Limit radius	m
P	Applied load	N
r	Radius from the central axis	m
R	Radius of the spherical indenter	m
R'	Reduced radius	m

s	Stroke	m
t	Thickness of the sample	m
T	Temperature	K
u_m	Mean entrainment velocity	m/s
u_r	Deformation in the radial direction	m
u_z	Deformation in the vertical direction	m
U	Dimensionless speed parameter	$-$
v	Poisson's ratio	$-$
V_{ball}	Ball wear scar volume	m^3
W	Dimensionless load parameter	$-$
α	Viscosity pressure coefficient	Pa^{-1}
β	Viscoelastic hysteresis loss fraction	$-$
δ	Indentation depth	m
δ_a	Indentation depth at the contact radius	m
ε_r	Strain in radial direction	$-$
ε_z	Strain in vertical direction	$-$
ε_θ	Strain in circumferential direction	$-$
η	Viscosity at ambient pressure	$Pa\ s$
ξ	Mesh size	m
σ_r	Stress in radial direction	Pa
σ_z	Stress in vertical direction	Pa
σ_θ	Stress in circumferential direction	Pa
τ	Interfacial shear strength	Pa
χ	Parameter from Dimitriadis correction	$-$
$\frac{d\delta_a}{dr}$	Gradient at contact radius	$-$
$\tan\delta$	Loss ratio	$-$

List of Figures

Figure 1. Stribeck curve with indications of lubrication regimes. 25
Figure 2. Solid lubrication mechanisms: a) rolling, b) mending and c) polishing. 27
Figure 3. Example of textured surface, entrapping debris. 28
Figure 4. Abrasive wear types: a) 2-body and b) 3-body type 29
Figure 5. Adhesive wear during asperity contact. 29
Figure 6. Classification of Bio-Lubrication systems. 30
Figure 7. Bioinspired (nature) inspiration influencing various tribological conditions: (a) drag reduction in shark skin; (b) adhesion switch in gecko foot; (c) club of mantis shrimp; (d) flexibility of pangolin scales; (e) scorpion back; (f) drag reduction in penguin skin; (g) turtle shell; (h) fibered hierarchical layer of bamboo; (i) dung beetle back; (j) adhesion shift in sea horse tail; (k) friction anisotropy in snakeskin; (l) layered structure of Venus flower basket; (m) antibacterial cicada wings; (n) seashell; (o) hydrophobicity of lotus leaf; (p) trabecular bone network; (q) honeycomb cells; (r) adhesion manipulation in tree frog paw; (s) self-sharpening of maize leaf; and (t) hierarchical structure of softwood. (45). 31
Figure 8. Triglyceride with fatty acids of different chain lengths and saturations: palmitic acid, oleic acid and α-linolenic acids, from top to bottom respectively (54). 33
Figure 9. Oxidative stability vs fluidity of plant oils (7). 34
Figure 10. Main types of monosaccharides composed in polysaccharides (74). 36
Figure 11. Typical molecular size and structures of proteins and peptides (86). 37
Figure 12. Diagram of a liposome including the amphiphilic phospholipid component that forms its concentric lipid bilayers (89). 38
Figure 13. Schematic of the used setup. 42
Figure 14. The coefficient of friction values from the test measurements. Error bars indicate minimum and maximum obtained values. 45
Figure 15. The example of obtained disk wear scar cross-section from WLI. 45
Figure 16. BTM operational setup before applying the load. 46
Figure 17. The measured frictional force for 10 cycles for alginate Ca hydrogel. 46
Figure 18. Rheology test setup on DHR-1 with loaded hydrogel sample. 48
Figure 19. Storage and Loss moduli distributions with frequency for carrageenan hydrogels. 48
Figure 20. Biomomentum Mach-1 setup for evaluating mechanical properties of hydrogels. 49

Figure 21. Raw (left) and filtered (right) force-displacement data for carrageenan Zn hydrogel for Hertz model.....50
Figure 22. Static scenario: force-indentation graphs of hard and soft silicones under dry conditions.....51
Figure 23. The particle size distribution of Lentinan solutions.....52
Figure 24. Obtained dynamic viscosities for tested plant oils.....60
Figure 25. Calculated film thicknesses of tested plant oils with lubrication regimes. 60
Figure 26. Average coefficients of friction for tested plant oils. Error bars indicate minimum and maximum obtained values. 61
Figure 27. Disk wear scar profiles for a) Avocado, b) Broccoli, c) Jojoba, d) Lemon Kernel, e) Macadamia and f,g) Castor oils. Note height scale for g) is different for clarity. 63
Figure 28. Average disk wear scar cross-sectional values for tested plant oils. Error bars indicate minimum and maximum obtained values. 64
Figure 29. Images of ball wear scars of a) Broccoli, b) Jojoba and c) Castor oils.....65
Figure 30. Average ball wear scar volumes for tested plant oils. Error bars indicate minimum and maximum obtained values.....65
Figure 31. Obtained performance of mixing castor and macadamia oils in a) COFs, b) Disk wear scar cross-sectional areas and c) Ball wear scar volumes.....69
Figure 32. Slimy Spike (Gomphidius Glutinosus) (152). 73
Figure 33. Schematic representation of the basic molecular structure of glucan molecule. N and N* represent the number of specific repetitions of each structure (173).....75
Figure 34. Obtained coefficients of friction during the friction tests.....80
Figure 35.Obtained coefficients of friction for deionised water and tested mushroom solutions. Error bars indicate minimum and maximum obtained values.....81
Figure 36. Structure of Lentinan (195). 86
Figure 37.Dynamic viscosities of tested fungal-based water lubricants. 86
Figure 38. Obtained DLS intensity graphs of tested water-based lubricants.....87
Figure 39. The time-dependant coefficients of friction from HFRR. 89
Figure 40. Coefficients of friction of fungal-based water solutions. Average of 3 repeats, error bars indicate minimum and maximum obtained values. 90
Figure 41. Disk wear scar cross-sectional areas of fungal-based water solutions. Average of 3 repeats, error bars indicate minimum and maximum obtained values. 91
Figure 42. Disk wear scar images of a) deionised water, b) Shiitake 1% powder, c) Poria 1% powder and d) Enoki 1% powder. Note, scales are different for clarity.....92

Figure 43. Cross-sectional profiles of a) Hexadecane, b) Bovine serum, c) Deionised water and d) Shiitake 1% powder. Note, height scales for samples are made different for clarity. 92
Figure 44. Ball wear scar volumes of fungal-based water solutions. Average of 3 repeats, error bars indicate minimum and maximum obtained values. 93
Figure 45. Tribological performance of Lentinan solutions: a) Average coefficients of friction, b) Disk wear scar cross-sectional areas and c) Ball wear scar volumes. 94
Figure 46. Disk wear scar cross-sections of a) deionised water, b) 0.1% Lentinan, c) 1% Lentinan and d) 5% Lentinan. 95
Figure 47. SEM image of particles in 0.1% Lentinan solution on stainless steel disk after Cr-coating. 96
Figure 48. Obtained DLS intensity graphs of a) Lentinan 0.1% and b) filtered Lentinan 0.1% solutions. 97
Figure 49. Comparison of tribological performance of deionised water and 0.1% Lentinan solutions: a) Coefficients of friction, b) Disk wear scar cross-sectional areas, c) Ball wear scar volumes.....98
Figure 50. Wear scar cross-sections of a) Lentinan 0.1% and b) Filtered Lentinan 0.1% solutions.....99
Figure 51. Chemical structures of carrageenans (218). 103
Figure 52. Scheme of carrageenan gel formation (218).....103
Figure 53. Chemical structure of agar (221). 104
Figure 54. Scheme of agar hydrogel formation (222). 104
Figure 55. Structures of high (HA) and low acyl (LA) gellan gum (75). 105
Figure 56. Structures of alginates: (A) - monomers, (B) – chain conformation, (C) – block distribution (226). 106
Figure 57. "Egg-box" model of alginate gelation with Ca2+ ions (227). 106
Figure 58. Structure of repeating segment of pectin (228).....107
Figure 59. Gelation mechanisms of a) high-methoxyl and b) low-methoxyl pectin (14). ..107
Figure 60 Acrylic gel forms for hydrogel preparation: Petri dish (left), Ø20 mm and Ø25 mm acrylic forms (right). 112
Figure 61. Obtained storage and loss moduli distributions for non-ionic hydrogels. 115
Figure 62. Obtained reduced elastic moduli for non-ionic hydrogels. 116
Figure 63. Obtained coefficients of friction for non-ionic hydrogels. Agar Fe (star) was not assessed due to lack of structural integrity. 116

Figure 64. Interfacial shear strength of non-ionic hydrogels. Agar Fe (star) was not assessed due to lack of structural integrity. 116
Figure 65. Obtained storage and loss moduli distributions for ionic hydrogels. 121
Figure 66. Obtained reduced elastic moduli for ionic hydrogels. 122
Figure 67. Obtained coefficients of friction for ionic hydrogels. Pectin Ca (star) was not assessed due to lack of structural integrity. 122
Figure 68. Interfacial shear strength for ionic hydrogels. Pectin Ca (star) was not assessed due to lack of structural integrity. 122
Figure 69. Evaluated mesh sizes for non-ionic hydrogels. 128
Figure 70. Evaluated mesh sizes for ionic hydrogels. 129
Figure 71. Correlation of interfacial shear strengths and mesh sizes. 129
Figure 72. Friction force, separated into deformation and interfacial components, for non-ionic hydrogels. Data labels correspond to the deformational component's percentage of total friction force. 131
Figure 73. Friction force, separated into deformation and interfacial components, for ionic hydrogels. Data labels correspond to the deformational component's percentage of total friction force. 131
Figure 74. Indentation of a rigid sphere into a soft elastic layer of known thickness. 136
Figure 75. Comparison of force-indentation graphs of indentation speeds for hard and soft silicones with dry and lubricated conditions. 139
Figure 76. Comparison of force-indentation graphs of dry (solid lines) and lubricated (dashed lines) surface conditions for hard silicone. 140
Figure 77. Comparison of force-indentation graphs of dry (solid lines) and lubricated (dashed lines) surface conditions for soft silicone. 140
Figure 78. Obtained elastic moduli of hard and soft silicones, using Hertz model and Dimitriadis-corrected Hertz model. 142
Figure 79. The variation of n-independent term with different multiples of Hertz contact radius at a range of indentation depths. 143
Figure 80. Case A limit radius variation with indentation depth at several n values. 145
Figure 81. Example Case A displacements at indentation depths of 0.5 and 1.0 mm at different n-values. 145
Figure 82. Values of n and contact radii, fulfilling the definition of K and geometry condition, for indentation depths of 0.5 and 1.0 mm, evaluated using Case A. 146

Figure 83. Comparison of Hertz contact radii with acceptable contact radii from limit radius model. 146
Figure 84. Values of n, fulfilling all conditions, using Hertz contact radius. 147
Figure 85. Case B limit radius variation with indentation depth at several n-values. 148
Figure 86. Example Case B displacements at indentation depths of 0.5 and 1.0 mm at different n-values. 148
Figure 87. Values of n and contact radii, fulfilling the definition of K and geometry condition, for indentation depths of 0.5 and 1.0 mm, evaluated using Case B. 149
Figure 88. Comparison of Hertz contact radii with obtained contact radii from Case B limit radius model. 150
Figure 89. The comparison of force-indentation profile from experiments, corrected Hertz model and limit radius model with n=2.5 for a) hard and b) soft silicones. 151
Figure 90. Distributions of n values with respect to indentation depth for a) hard and b) soft silicones. 151
Figure 91. The comparison of force-indentation profiles from experiments, corrected Hertz model and limit radius model with variable n for a) hard and b) soft silicones. 152

List of Tables

Table 1. Test conditions for HFRR Tribological assessment. 44
Table 2. Rheological test conditions for the respective chapters. 47
Table 3. Role of fatty acid types on plant oil tribological performance. 58
Table 4. Features of chosen plant oils. 59
Table 5. Wear coefficients of tested plant oils for disk wear. 64
Table 6. Wear coefficients of tested plant oils for ball wear. 66
Table 7. Cladogram of identified mushroom genera. 76
Table 8. Summary of measured hydrogel properties. 109
Table 9 Amounts of polymer and deionised water for base non-ionic hydrogel preparation. 112
Table 10. Loss ratio of tested non-ionic hydrogels.....114
Table 11 Weights of natural polymers, deionised water and ion chlorides for ionic hydrogel preparation.....118
Table 12. The volumes of hydrogel and ion solutions used for filling the respective acrylic forms.....119
Table 13. Loss ratios of tested ionic hydrogels. 120

1. Introduction

This chapter introduces the research presented in this thesis. First the motivation for developing environmentally friendly lubrication strategies is outlined by emphasising the environmental impact of conventional mineral oil-based lubricants. The need for alternative lubrication approaches is then highlighted. The chapter sets out the research objectives, defining the overall aim and specific directions of the work. Finally, the structure of the thesis is presented to guide the reader through the studies undertaken.

1.1. General Motivation

Lubricants are the backbone of a wide range of industries and are crucial for modern economies. The primary role of lubricants is to reduce friction and wear between contact surfaces, thus extending component lifetimes, improving energy efficiency and ensuring the reliability of mechanical systems. Without lubricants, global manufacturing, automotive transport and energy generation would face severe performance and sustainability issues.

The global lubricant market shows the scale of this dependence. In 2021, the global lubricant market was valued at $157.6 billion, and the projected valuation reaches $182.6 billion by 2025 (1). The worldwide demand in 2019 was evaluated as 36.8 million metric tonnes and the projected growth is at 2.1% annually (2). This scale highlights both their economic importance and their significant environmental footprint.

At present, the majority of lubricants is petroleum derived. These products are cheap and versatile, but their environmental effect is enormous. An estimated 50% of lubricants used worldwide are lost to the environment through spills, evaporation, combustion and leakage, while the rest becomes waste lubricant oil (WLO) (1,3). For example, in the European Union market alone, out of approximately 4.3 million tonnes of lubricants sold only 38% were collected as waste (1). Globally, around 12 million tonnes of lubricants are released into the environment annually (4). Over 95% of these lubricants are derived from petroleum (3). Such losses produce serious ecological risks, as mineral oil-based lubricants form films on water surfaces that suffocate aquatic organisms and devastate ecosystems both in water and soil (5). These environmental impacts are particularly serious in loss lubrication applications, where lubricants are unavoidably released into the environment, such as in railways, forestry and marine stern tubes (6–9).

The need to reduce these environmental impacts promoted interest in biolubricants, which are produced from renewable and biodegradable sources. Biolubricants are non-toxic to organisms and have significantly reduced environmental impact (10,11). The biodegradation rates of biolubricants can typically reach 75-95% within 28 days, compared to only 10-40% for mineral oils (9). Following the accepted eco-label criteria from Organisation of Economic Co-operation and Development (OECD), biodegradability of lubricant must be at least 60% within 28 days when measured by OECD test guidelines 301B, 301C and 301F (3). Thus, biolubricants easily satisfy biodegradation criteria. However, the adoption of biolubricants remains limited. Even in European market, the most developed market with the most restrictions in using hazardous materials, biolubricants represent only 3-3.5% of total consumption (10). Although this sector is expanding with an estimated compound annual growth of 5.4% from 2016 to 2024, progress is slow due to performance and economic barriers (10).

The need for transition to biolubricants aligns with global sustainability targets. Developing renewable, biodegradable and low-toxicity lubricants contributes to several United Nations Sustainable Development Goals (SDGs) adopted in 2015 (12):

- SDG 6: Clean Water and Sanitation by reducing aquatic contamination
- SDG 7: Affordable and Clean Energy by improving energy efficiency through friction reduction
- SDG 12: Responsible Consumption and Production by reducing waste pollution and using renewable resources
- SDG 13: Climate Action by lowering dependence on fossils and reducing greenhouse gas emissions
- SDG 14: Life below Water by reducing marine pollution
- SDG 15: Life on Land by reducing degradation of natural habitats from pollution

Moreover, government policies regulate lubricant use in sensitive environments. The EU ecolabel scheme requires lubricants to contain a high percentage of renewable raw materials (3). In the United States, the Environmental Protection Agency mandates the use of environmentally acceptable lubricants in marine applications under the Vessel General Permit (VGP) (13).

Bio-lubricants from plants, algae, fungi and other biological sources are a promising alternative. They are naturally biodegradable, renewable and water-compatible, offering a

reduction in environmental impact and toxicity associated with mineral oil-based lubricants (3). At the same time, biological systems themselves can inspire advanced lubrication strategies, such as highly efficient friction reduction from mucins, polysaccharides and phospholipids in nature. However, the tribological mechanisms of bio-based systems remain underexplored. Technological and economic challenges restrict their large-scale application. Addressing these challenges requires a systematic investigation of how natural and nature-based systems operate and how their tribological performance can be implemented as alternatives to mineral oil-based lubricants.

To summarise, the modern lubricant industry faces a double challenge: reliance on mineral oils must be reduced and high-performance sustainable alternatives must be developed. Bio-lubricants are a promising solution but remain underdeveloped. Scientific and engineering progress requires fulfilling the following two steps:

1. Understand the natural and nature-inspired systems' mechanisms of friction and wear reduction
2. Translate these mechanisms into functional solutions for real-world applications

This thesis directly addresses these challenges by investigating several approaches to sustainable tribology with a range of bio-lubricants from plants, fungi and algae.

1.2. Research Objectives

The overall objective of this thesis is to enhance our understanding of how natural and nature-inspired systems can contribute to sustainable lubrication. Currently industry relies predominantly on the use of conventional mineral oil-based lubricants and synthetic additives, which impose significant environment damage. In contrast, natural materials can provide renewable, biodegradable and environmentally compatible alternatives. To realise this potential, such systems must be systematically explored, and their operating principles must be understood, in order to translate them into practical applications. To address this broad aim three objectives are proposed:

- To investigate bio-based oils as potential lubricants, considering their advantages and limitations
- To explore water-based lubrication strategies inspired by natural systems, with emphasis on their friction and wear performance

- To link experimental observations with broader conceptual framework for understanding soft matter tribology

These objectives are set to identify the potential of natural materials from plants, algae and fungi for tribological applications and to provide a foundation for their further study and development.

1.3. Thesis Outline

This thesis is structured in nine chapters. Each chapter provides the necessary background to the described investigation and introduces the featured work. Results, discussion and conclusions are also introduced in each chapter to conclude and review the investigated work. Materials used are described in each chapter and all employed experimental methods and data processing steps are provided in detail in Chapter 3.

Chapter 2 provides the theoretical and contextual background for this thesis. First, the fundamentals of tribology are introduced, including lubricating regimes and wear mechanisms. A focus on the boundary lubrication regime is made, as the most difficult regime to address. The second part of the chapter reviews current research on bio-lubrication. Oil-based systems, such as plant oils, algal oils, animal fats and synthetic esters, and water-based systems, such as polysaccharides, proteins, peptides and phospholipids, are outlined. The review identifies key gaps in knowledge, which motivated the experimental studies presented in latter chapters.

Chapter 4 examines the direct-use approach to bio-lubrication, where natural substances such as plant oils are used in their unmodified form. This approach has deep historical roots, as oils, fats and water, have long been used as simple ready-available lubricants. In this thesis, direct-use approach is defined as straightforward application of pure natural oils without chemical modification or synthetic additives. Six plant oils were systematically tested to access their friction and wear performance. The results show that the plant oils can reduce friction and wear, however their inherent structure imposes constraints on lubricant stability. These findings highlight both the advantages and limitations of a direct-use approach, supporting the need for a more sophisticated methodology.

An alternative biomimetic approach is introduced in Chapter 5. This approach, with its main steps, is explained and applied for identifying new sources of additives for water-based lubrication. Polysaccharides from fungi and algae were identified as valuable sources. An initial exploration of fungal extracts is provided and highlights the potential of using fungal

polysaccharides in lubrication. The performance of these polysaccharides was evaluated in detail and will be presented in the latter chapters.

Chapter 6 focusses on the use of fungal polysaccharides, specifically β-glucans. Three popular fungal species were used to produce water-based fungal solutions, using mushroom powders and pure β-glucan. Their tribological performance was evaluated and the corresponding mechanism is proposed with emphasis on the effects of particle size and concentration.

Chapter 7 investigates hydrogels from plant and algal polysaccharides. Even at concentrations below 1% these polysaccharides form crosslinked hydrogel networks (14). The effect of adding divalent ions to hydrogels with different crosslinking mechanisms is examined. The resulting changes in material properties and tribological performance are evaluated.

Chapter 8 introduces a limit radius model, a new theoretical framework for modelling indentation in soft solids. Unlike a classical Hertz contact model, the limit radius model accounts for the entire deformation profile, including the region outside of the contact area. This transition region is defined by a finite limit radius. Both static and dynamic scenarios are derived, and deformation profiles are evaluated against experimental observations.

Chapter 9 concludes the research work, outlining the main outcomes of each of the accomplished studies. The use of new natural sources for water-based lubrication is outlined. The corresponding mechanisms of their operation are described. Finally, future work and new areas of development for water-based lubrication are addressed.

2. Literature Review

This chapter provides background knowledge on the principles and mechanisms of lubrication, with a particular focus on Boundary lubrication. The chapter aims to establish a clear understanding of how lubricants operate under different regimes and to highlight the challenges of Boundary lubrication. The chapter first introduces the role of lubricants in mechanical systems and then explains the classical lubrication regimes. The mechanisms of improving tribological performance in Boundary regime are then examined, and dominant wear mechanisms are outlined. The chapter concludes with a review of Bio-Lubrication, going through oil-based and water-based systems and identifying research gaps that are addressed in the later chapters.

2.1. Purpose of Lubrication

In any mechanical system a direct contact between surfaces leads to the onset of friction and material removal. Friction can be necessary to perform a mechanical function, like in braking systems and clutches. However, in most cases friction is undesirable, as it leads to energy losses and excessive wear. If left unmitigated, this wear can result in the failure of the system components (7). To mitigate these negative effects a lubricant is introduced into the contact to reduce friction and wear by separating the moving surfaces (7,15). In a process of lubrication, the lubricant supports partially or fully the applied load and physically separates the contacting surfaces by forming a continuous layer or film. Lubricants can exist in liquid, solid or gaseous forms. Their primary function is the reduction of friction and wear. A range of other critical functions is associated with the use of lubricants. They dissipate heat at the contact interface, prevent corrosion by forming protective layers, provide electrical insulation and remove debris from the contact zone (7,15,16). Understanding the principles of lubrication and the behaviour of lubricants under different operating conditions is essential for designing reliable and efficient mechanical systems.

2.2. Lubrication Regimes

Operating conditions in the contact determine the effectiveness of lubrication. Factors such as load, speed, temperature, surface roughness and lubricant properties determine the formation of the lubricating film. The combination of these conditions leads to different lubrication regimes, characterised by the amount of separation between the contact surfaces.

Graphically, lubrication regimes could be illustrated by the Stribeck curve, shown in Figure 1. In a Stribeck curve coefficient of friction (COF) is linked to a dimensionless parameter – Hersey number. This number combines the lubricant viscosity, sliding speed and applied load. As this number increases by increasing speed, lowering the load or using a more viscous lubricant the mechanism of lubrication transitions between three main regimes: Boundary lubrication, Mixed lubrication and Hydrodynamic lubrication (7,15,17). In the Boundary regime a continuous film cannot be maintained, and the surfaces are predominantly in direct contact. In the Mixed lubrication the load is partially supported by a lubricant film and partially by direct asperity contacts. In the Hydrodynamic regime the lubricant film is fully developed, achieving complete separation of the contact surfaces.

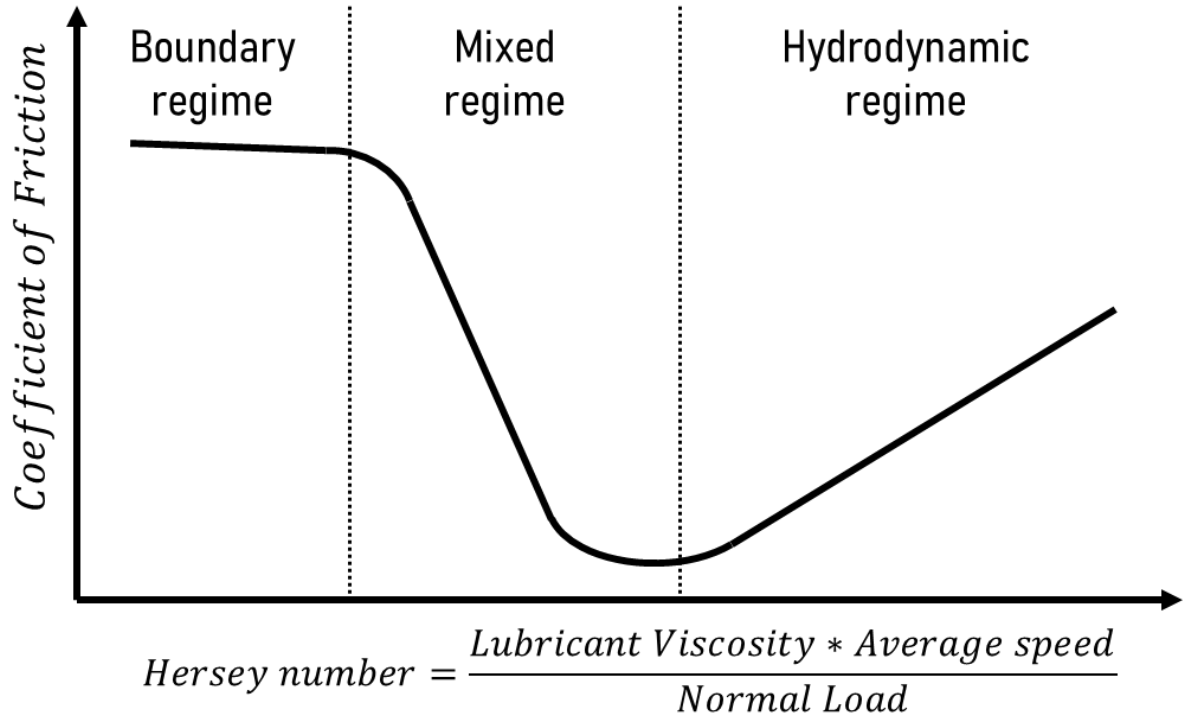


Figure 1. Stribeck curve with indications of lubrication regimes.

2.2.1. Hydrodynamic Regime

In the Hydrodynamic lubrication regime, the contact surfaces are fully separated by a formed lubricant film (17). As there is no direct contact between the surfaces the load is fully supported by the lubricant film. This regime usually occurs at high sliding speeds under low or moderate applied load and with lubricants of high viscosity to sustain thick stable films. Due to the absence of direct asperity contact wear in hydrodynamic regime is minimal, compared to other regimes. Friction forces arise only from viscous shearing of the lubricant film (16). Therefore, the magnitude of friction is directly related to the lubricant viscosity.

2.2.2. Mixed Regime

The intermediate regime between hydrodynamic and boundary lubrication is the Mixed lubrication. In this regime the contact surfaces are not fully separated by lubricant film, so part of the load is supported by the lubricant film and part by direct asperity contact (18,19). Due to the partial asperity contact, friction and wear in mixed regime are larger compared to hydrodynamic regime. Both lubricant properties, like viscosity, and surface topography, like roughness and asperity geometry, play a critical role in defining the lubricant performance. Due to this dependence on various conditions, operation in Mixed regime is not recommended, as the control of friction is difficult.

2.2.3. Boundary Regime

Boundary lubrication regime occurs when a lubricant film of sufficient thickness is not formed. The contact surfaces are in direct contact with applied load being entirely supported by the asperities (15,20). This happens under high loads, low sliding speeds or with low-viscosity lubricants that cannot produce enough pressure to separate the surfaces. Friction and wear in Boundary lubrication are controlled by the interactions between the contact surfaces and the lubricant. The use of chemical or physical modifications of the surface can reduce friction wear in the boundary regime. This can be achieved by adsorbing molecules from the lubricant to the surface to form protective layers, by creating reaction films, by using solid particulates or by incorporating coatings or surface textures (20,21). Boundary lubrication is considered the most challenging regime to optimise the tribological performance, due to the dependence on complex surface interactions between the contacting surfaces and lubricant.

2.3. Tribological Mechanisms in Boundary Regime

In the Boundary lubrication regime, the direct contact of surfaces dominates. The reduction of friction and wear relies solely on interfacial phenomena, arising from both the lubricant and the contacting surfaces. A variety of mechanisms are known to improve the lubrication performance in the Boundary regime. These include:

- Adsorbed layers
- Solid lubricants
- Surface texturing
- Hydration lubrication

Most of these mechanisms aim to create a protective film at the interface using the physical and chemical properties of certain substances present in the lubricant. Most research on these mechanisms is carried out using mineral oil-based lubricants. However, the focus of this thesis is on natural lubricants, specifically water-based lubricants and natural oils. Therefore, the mechanisms in the following sections will be explained from the perspective of these natural lubricants.

2.3.1. Adsorbed Layers

Adsorbed layers form when the molecules from the lubricant adhere to contact surfaces through physical (e.g., van der Waals forces) or chemical interactions. These films are typically formed in mono- or multilayers from long-chain organic molecules, like fatty acid chains in plant oils (22,23), proteins in synovial fluid (24–26) and polysaccharides in water-solutions (27–29). The presence of these films significantly reduces the shear strength at the interface, therefore reducing friction and wear. Although adsorbed films can be disrupted or removed during operation, they are typically replenished continuously from the lubricant.

2.3.2. Particle Lubrication

Particle lubrication utilises the addition of particles to the base lubricant. These particles can improve lubrication through a range of particle-related mechanisms. Figure 2 visualises several examples of such mechanisms: rolling, mending and polishing (30–32). During rolling the particles take some of the applied load and, as seen in Figure 2a, by rolling between the contact surfaces reduce the coefficient of friction (31,33–35). As shown in Figure 2b, the mending effect is characterised by filling the worn gaps and defects in the surfaces to smoothen the surface (31,33–35). Figure 2c illustrates polishing, which reduces the surface roughness. Due to the presence of sharp and hard debris, the peaks and asperities on the contact surfaces can be removed, which can lead to lower friction and wear (30,31). Common nanoparticle types include carbon-based materials, like graphite and graphene, metal oxides from titanium, aluminium and silicon and other engineered nanostructures (30,31).

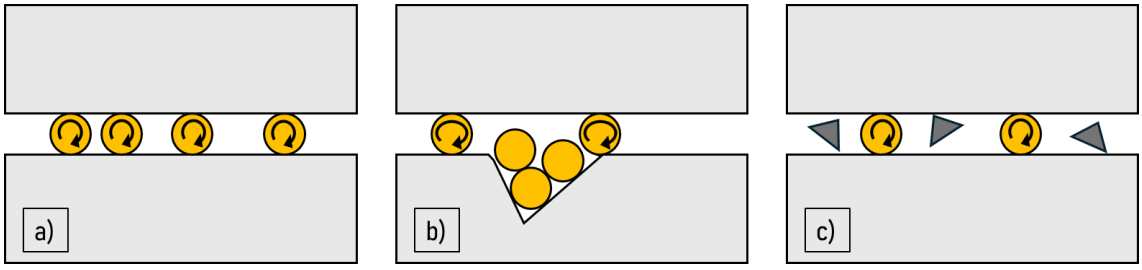


Figure 2. Solid lubrication mechanisms: a) rolling, b) mending and c) polishing.

2.3.3. Surface Texturing

Surface texturing techniques modify the surface structure by introducing micro- or nanopatterns. By introducing different patterns, texturing can trap lubricant or debris within the introduced features, as shown in Figure 3. Trapping the lubricant reduces the real contact area and promotes film formation even after cutoff of external lubricant supply, thus improving tribological performance (36).

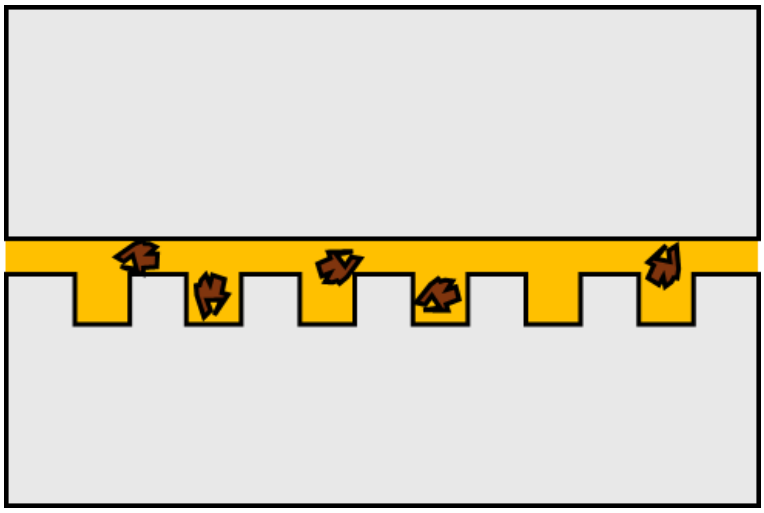


Figure 3. Example of textured surface, entrapping debris.

2.3.4. Hydration Lubrication

Hydration lubrication is a mechanism unique to lubrication strategies that contain water. Water molecules adsorb to the surface via ionic interactions due to water dipole structure (37–40). The resulting structure forms a hydration layer, sometimes called shell, which can sustain high loads (38–40). Both friction and wear are reduced, as the hydration layer can be easily sheared in a fluid-like manner (39).

2.4. Wear Mechanisms in Boundary Lubrication

Boundary lubrication is typically associated with a higher amount of wear due to the absence of a stable lubricant film, separating the surfaces. There are four types of wear that are primarily associated with the boundary regime: abrasive wear, adhesive wear, surface fatigue and tribochemical wear (15,20,41).

2.4.1. Abrasive Wear

Abrasive wear occurs when hard asperities on the opposing surface or hard particles slide across the surface, removing material and potentially affecting surface roughness (41–43).

This wear type can be split further into 2-body and 3-body abrasion types (42,43). In 2-body abrasion only two surfaces are in contact, meaning that asperities from each surface are interacting or the hard added particles are embedded into the surface, as shown in Figure 4a. In 3-body abrasion the particles are not embedded into the surface and are free to roll or slide, thus the material removal is slower than in 2-body type. This case is shown in Figure 4b. In both cases, the movement of these surfaces would lead to the production of scratches and grooves (43).

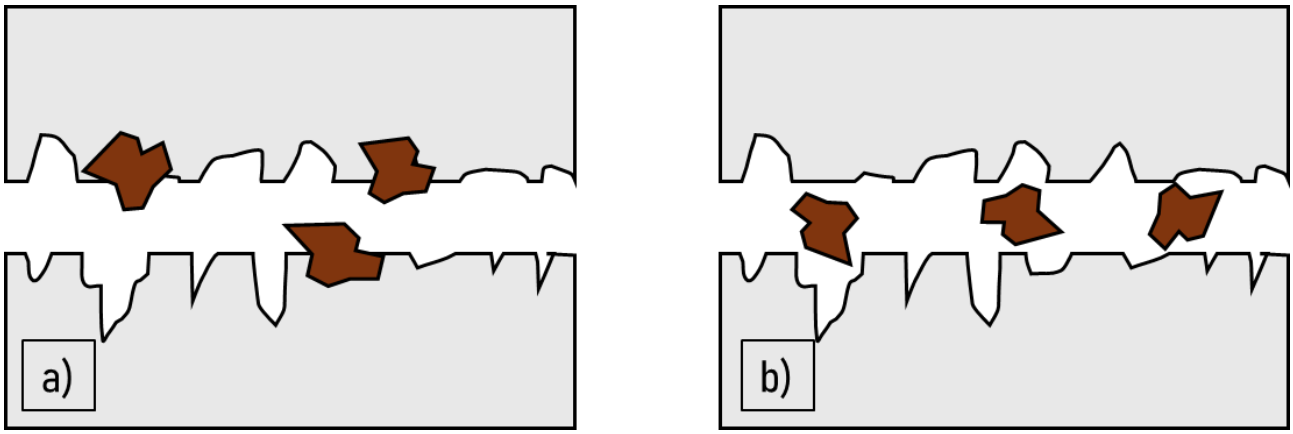


Figure 4. Abrasive wear types: a) 2-body and b) 3-body type.

2.4.2. Adhesive Wear

The asperities from both contact surfaces may form adhesive junctions stronger than the internal bonds within the material. When sheared, these adhesive bonds, if strong enough, may lead to a detachment of material from the weaker surface, causing adhesive wear (15,17,43). The resulting material may transfer to the countersurface or become loose debris, as shown in Figure 5.

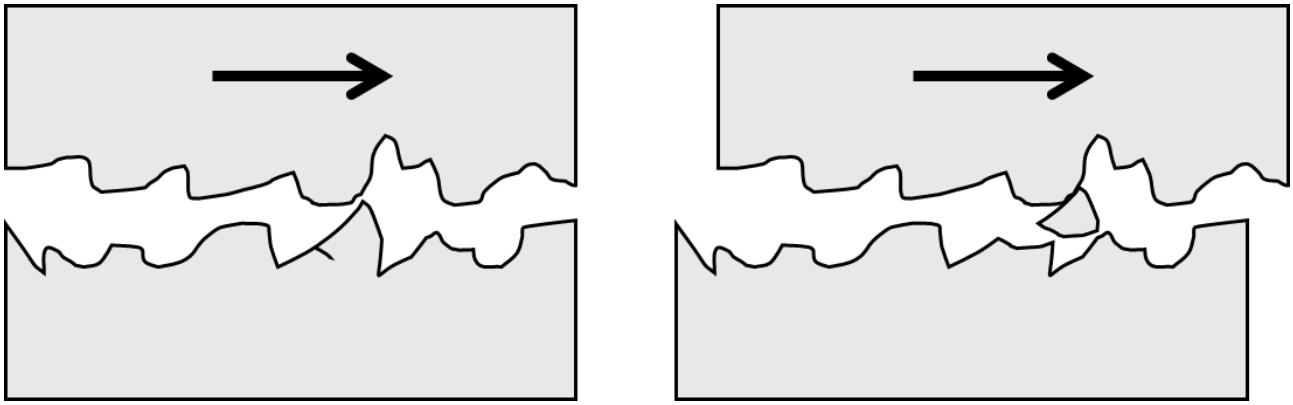


Figure 5. Adhesive wear during asperity contact.

2.4.3. Surface Fatigue Wear

Surface fatigue wear arises from repetitive loading of the surface, which propagates subsurface defects deeper into the material (17). Micro-cracks, pitting, spalling and other internal defects promote and lead to a mechanical failure of the material (42).

2.4.4. Tribochemical Wear

Tribochemical wear is a chemical type of wear, where the chemical reactions degrade the surface material. An example could be the corrosion of steels in humid conditions, which oxidises the steels in the contact, leading to material loss (44). The main problem with tribochemical wear is that once the outer layer is mechanically removed during operation, fresh material is exposed to further chemical reaction, accelerating the loss of material.

2.5. Bio-Lubrication

The need for sustainable and biodegradable lubricants has led to a growing interest in Bio-Lubrication. In contrast to mineral oil-based lubricants, biological systems reduce friction and wear by implementing mechanisms that are fundamentally different. They rely on renewable molecules, water-rich environments and surface-active biopolymers that operate effectively under boundary and mixed lubrication regimes. These regimes are typically dominated by surface interactions, adsorption and hydration effects, which are directly relevant to the systems investigated in this thesis.

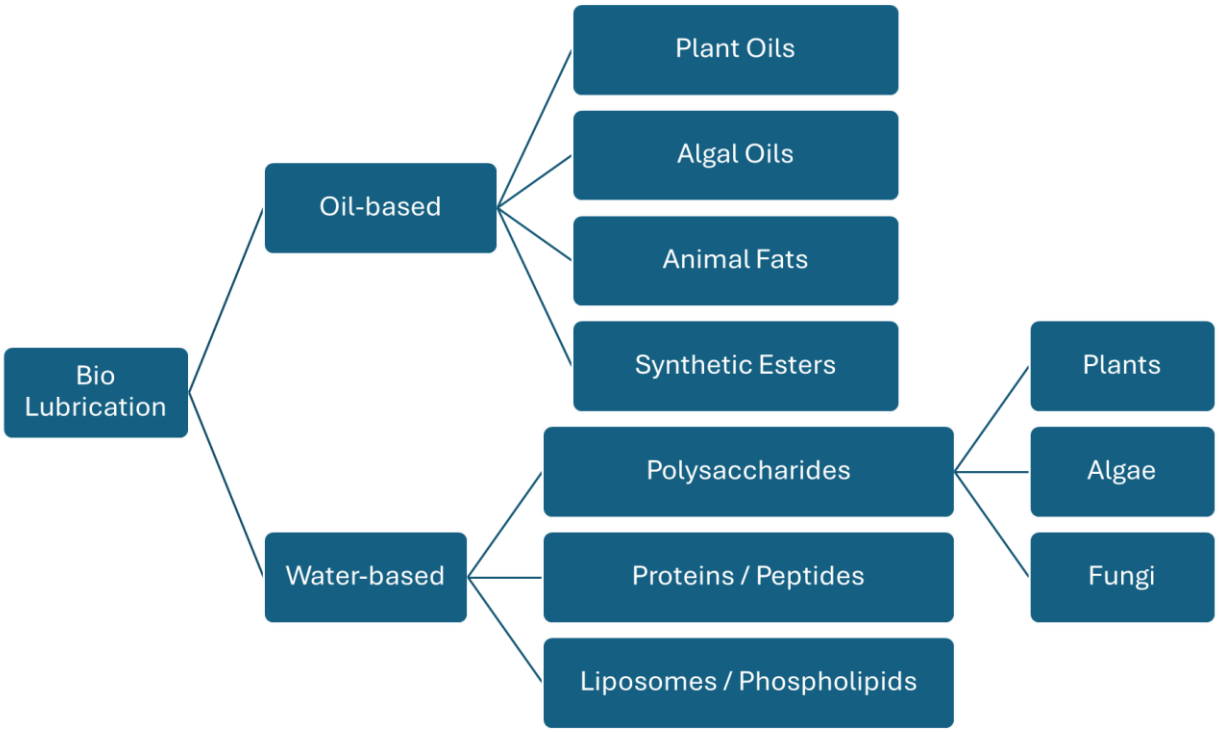


Figure 6. Classification of Bio-Lubrication systems.



Figure 7. Bioinspired (nature) inspiration influencing various tribological conditions: (a) drag reduction in shark skin; (b) adhesion switch in gecko foot; (c) club of mantis shrimp; (d) flexibility of pangolin scales; (e) scorpion back; (f) drag reduction in penguin skin; (g) turtle shell; (h) fibered hierarchical layer of bamboo; (i) dung beetle back; (j) adhesion shift in sea horse tail; (k) friction anisotropy in snakeskin; (l) layered structure of Venus flower basket; (m) antibacterial cicada wings; (n) seashell; (o) hydrophobicity of lotus leaf; (p) trabecular bone network; (q) honeycomb cells; (r) adhesion manipulation in tree frog paw; (s) self-sharpening of maize leaf; and (t) hierarchical structure of softwood. (45).

Bio-Lubrication can be broadly divided into oil-based and water-based systems, as shown in Figure 6. Oil-based bio-lubricants rely on triglycerides from plant oils, algal oils or animal fats (46). Their functional components include long-chain fatty acids that adsorb strongly to metal surfaces and form protective boundary films. In contrast, water-based bio-lubricants rely on biopolymers such as polysaccharides, proteins, peptides, liposomes and phospholipids, that adhere to the surface and form the boundary film, or through mechanism, such as hydration lubrication (47,48).

Biological systems provide extensive inspiration for modern bio-lubricants. Many organisms optimise friction, adhesion and wear protection through hierarchical structures, surface chemistry or hydration layers. Representative examples are shown in Figure 7, adapted from Kumar et al. (2024), illustrating nature-derived solutions such as drag-reducing textures, reversible adhesion, hydration-based lubrication and wear-resistant composites (45). Such natural mechanisms motivate the study of plant-oil triglycerides and biopolymer-based aqueous lubricants presented in this thesis.

In the following sections of this chapter, current developments in bio-lubrication are reviewed, with an emphasis on natural and nature-inspired systems. For each category, existing findings are summarised and the research gaps relevant to this thesis are identified. These gaps directly motivate the experimental studies presented in following chapters, where the performance of plant oils, mushroom-derived polysaccharides and natural hydrogels is systematically investigated under controlled boundary-lubrication conditions.

2.6. Oil-based Bio-Lubrication

2.6.1. Plant Oils

Plant oils are among the most extensively studied bio-lubricants due to their renewable origin and known historical use before the emergence of mineral oils (49). Plant oils are composed of long-chain triglycerides, which consist of a glycerol head that connects three fatty acid chains, like shown in Figure 8 (7,50). The structure of these fatty acids, like chain length, degree of saturation and presence of functional groups, determine the properties and performance of plant oils (7,50,51).

The length of the fatty acid corresponds to the number of carbon atoms in its backbone. Longer chains generally provide higher viscosity and improved load-bearing capacity at the cost of reduced fluidity (52,53). The degree of unsaturation is determined by the presence and position of the double-carbon bonds in the fatty acid chain. In Figure 8, examples of

saturated, monounsaturated and polyunsaturated fatty acids are shown. Saturated fatty acids, like palmitic acid (C16:0), have no double bonds and form straight chains, that can pack tightly. Monounsaturated fatty acids, like oleic acid (C18:1), contain only a single double bond, which improves adsorption on metal surfaces and enhances fluidity. When a fatty acid contains more than one double bond, it is called polyunsaturated, like α-linolenic acid (C18:3).

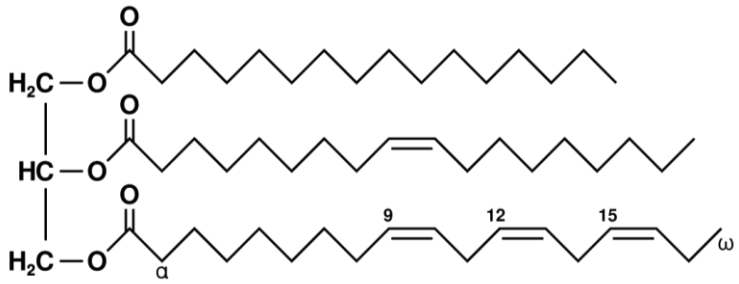


Figure 8. Triglyceride with fatty acids of different chain lengths and saturations: palmitic acid, oleic acid and α-linolenic acids, from top to bottom respectively (54).

The type and proportion of these fatty acids affect the properties of the plant oils. The level of saturation of fatty acids is linked to oxidative stability and fluidity at low temperatures, as shown in Figure 9 from Bart et al. (2012) (7).

Fatty acids reduce friction primarily through the formation of an adsorbed boundary film on metallic surfaces. Their polar carboxyl (–COOH) groups have strong affinity for oxide layers on steels, allowing the molecule to attach to the surface and form close-packed mono- or multilayers (23,55,56). This adsorbed boundary film separates the opposing surfaces, reducing direct metal–metal contact and thereby lowering friction and wear (23,57). The effectiveness of this protective film depends on the structure of the fatty acid. Long-chain C18 fatty acids such as oleic acid are particularly effective because they combine strong adsorption with sufficient chain length to form coherent, shear-resistant films (23,57,58). Highly polyunsaturated chains are more prone to oxidative degradation, which can compromise film stability over time (50,59). Saturated long-chain fatty acids can form dense, tightly packed layers that provide good surface protection, but offer less fluidity at low temperatures compared to unsaturated fatty acids (23,56,58). Through these mechanisms, fatty acids act as surface-active friction modifiers, lowering shear stress at the sliding interface and reducing wear under boundary lubrication conditions.

Reeves et al. (2015) examined a link between the level of unsaturation in triglycerides and their tribological performance (57,60). The analysis concluded that oils with larger amounts of unsaturated fatty acids, like oleic acid, form denser boundary films at the sliding interfaces, thus reducing friction and wear (57). When compared to mineral oil-based

lubricants, plant oils often exhibit advantages of higher viscosity index and friction reduction (60,61). However, their triglyceride structure imposes limitations, such as poor oxidative stability and reduced thermal resistance (50,53).

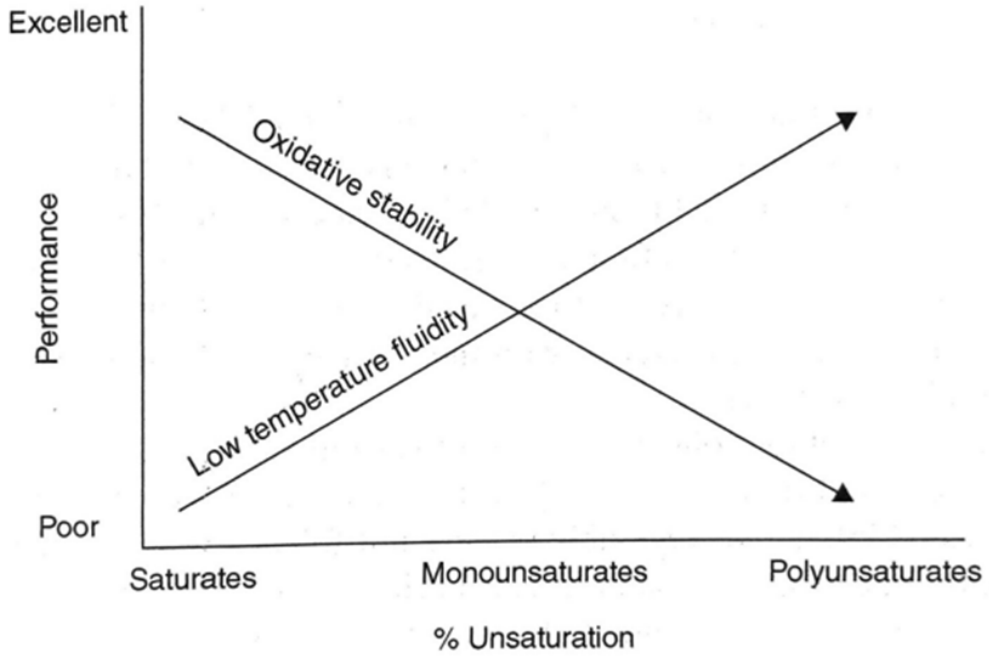


Figure 9. Oxidative stability vs fluidity of plant oils (7).

These limitations restrict the direct use of unmodified plant oils in industrial applications, which operate at high temperatures (61). Chemical modifications, such as transesterification and epoxidation, can improve oxidative stability and extend the lubricant service life, but these processes increase production costs and reduce the sustainability (46,51,61).

In summary, both chain length and degree of unsaturation govern the balance between oxidative stability, viscosity, and tribological behaviour. Although the research on plant oils focusses on investigating new sources under a range a tribological conditions, systematic comparison between unmodified plant oils remains limited (60). This molecular-level understanding forms the basis for evaluating specific plant oils in Chapter 4.

2.6.2. Algal Oils

An alternative renewable source of triglycerides is provided by algae. The composition of algal oils is similar to plant oils. Algal oils tend to be richer in the unsaturated fatty acids (62,63). As in plant oils, a higher degree of unsaturation promotes the boundary film formation but compromises of oxidative stability. The research on algal oils for lubrication remains limited. Primarily the research efforts are focussed on the development of biofuels from algal oils (64). At the same time large scale production of algal biomass faces

significant technological and economic challenges (64). Nevertheless, friction and wear reduction upon addition of algal oil to low-viscosity mineral oil was recently reported by Rubio-Hernandez et al. (2025) (63). These findings indicate that algal oils can become a useful additive and potentially a biolubricant on its own. However, the use of algal oils as biolubricants is constrained by production scalability and limited tribological research (64).

2.6.3. Animal Fats

Animal fats, such as tallow and lard, were historically used as lubricants in traditional machinery (49). Their chemical structure is the same as plant and algal oils. In contrast to plant and algal oils, animal fats have higher proportions of saturated fatty acids (65,66). This composition improves oxidative stability but reduces flow properties at low temperatures (65). Chemical modifications as for plant oils could be applied to animal fats to improve their performance of animal fats (65–67). Modern research on animal fats for tribological applications is scarce, as plant oils have replaced them due to better availability and fewer ethical concerns.

2.6.4. Synthetic Esters

Synthetic esters are chemically engineered lubricants derived from natural triglyceride-based oils (68,69). Through targeted modifications of base structure, like esterification, transesterification and polyol ester synthesis, improvements in viscosity index, oxidative stability and low-temperature properties can be achieved (69). From tribological perspective, synthetic esters generally outperform unmodified plant oils, providing lower friction and wear in addition to improved thermal resistance (70). However, the altered composition may lead to compromised biodegradability and an increased toxicity in synthetic esters (71,72). In addition, the chemical alterations substantially increase the production cost of the lubricant (68,70,73). Consecutively, the main challenge for synthetic esters lies in balancing tribological performance with economic feasibility and environmental compatibility (71).

2.7. Water-based Bio-Lubrication

2.7.1. Polysaccharides

Polysaccharides are natural polymers widely available in plants, algae and fungi. Their long-chain structures strongly interact with water, modifying the viscosity of the resulting solutions (27,28). Such structures consist of repeating monosaccharide blocks, shown in Figure 10 (74). Even at low concentrations of 1-5 %, polysaccharides in water can form viscous

solutions (27,28). In the contact, polysaccharide solutions form boundary films at the sliding interfaces (27).

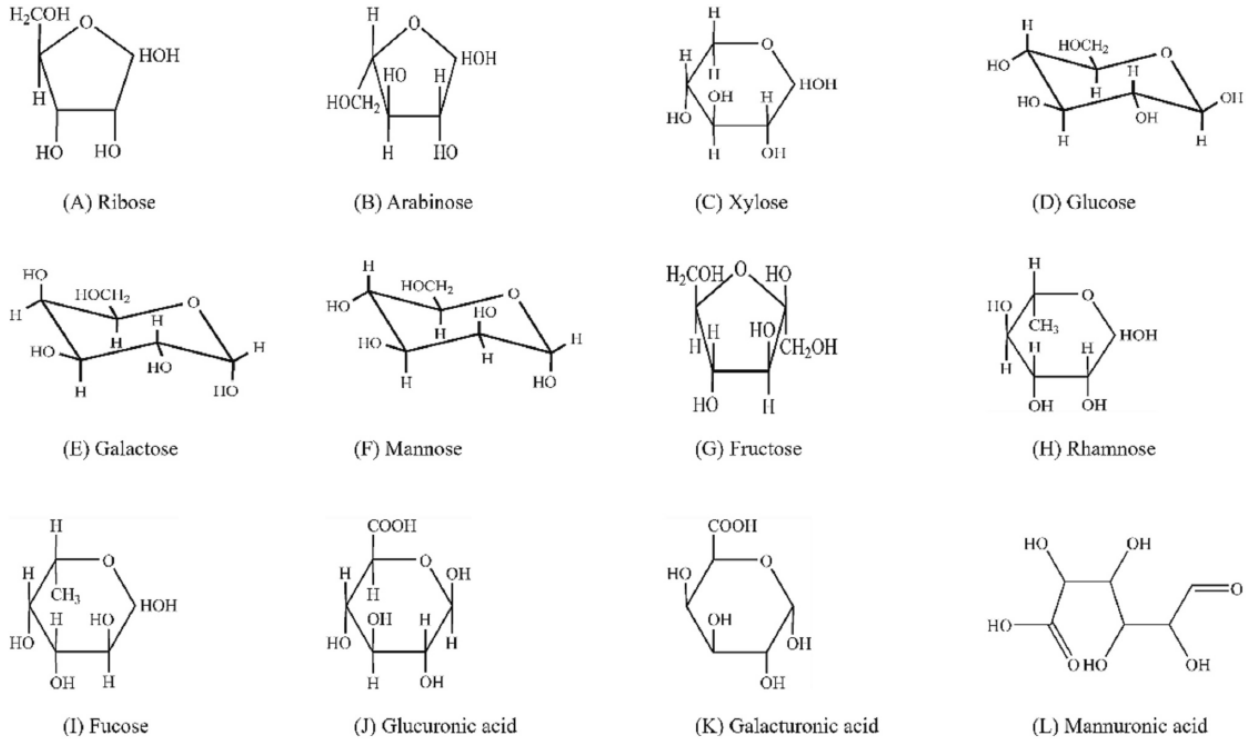


Figure 10. Main types of monosaccharides composed in polysaccharides (74).

In hydrogel form, polysaccharides form three-dimensional crosslinked networks that can retain large amounts of water (75,76). Hydrogels are particularly relevant for boundary lubrication, as their hydration layers mimic the natural biological systems such as cartilage (77). The crosslinking mechanisms of polysaccharide hydrogels may involve addition of ions to tune gel stiffness (75,78,79). However, the effect of ions on tribological properties of polysaccharide hydrogels was not explored.

Polysaccharides from plants and algae were extensively studied as biolubricants, however fungal polysaccharides remain underexplored in tribological applications. Compounds such as β-glucans are well known in medicinal and nutritional applications (80–85). Yet, their tribological performance was not investigated, presenting a novel and promising research direction.

Overall, the ability of polysaccharides to act as viscosity modifiers in solutions and to form water-retaining hydrogels provides a wide range of opportunities for bio-based lubrication. The renewable origin and biocompatibility of polysaccharides further support their potential use in environmentally sensitive and biomedical applications.

2.7.2. Proteins and Peptides

Proteins and peptides are central to biological lubrication in joints and mucosal surfaces. Molecules, such as lubricin, were extensively studied for their ability to adsorb to the interfaces to form protective films (24,26).

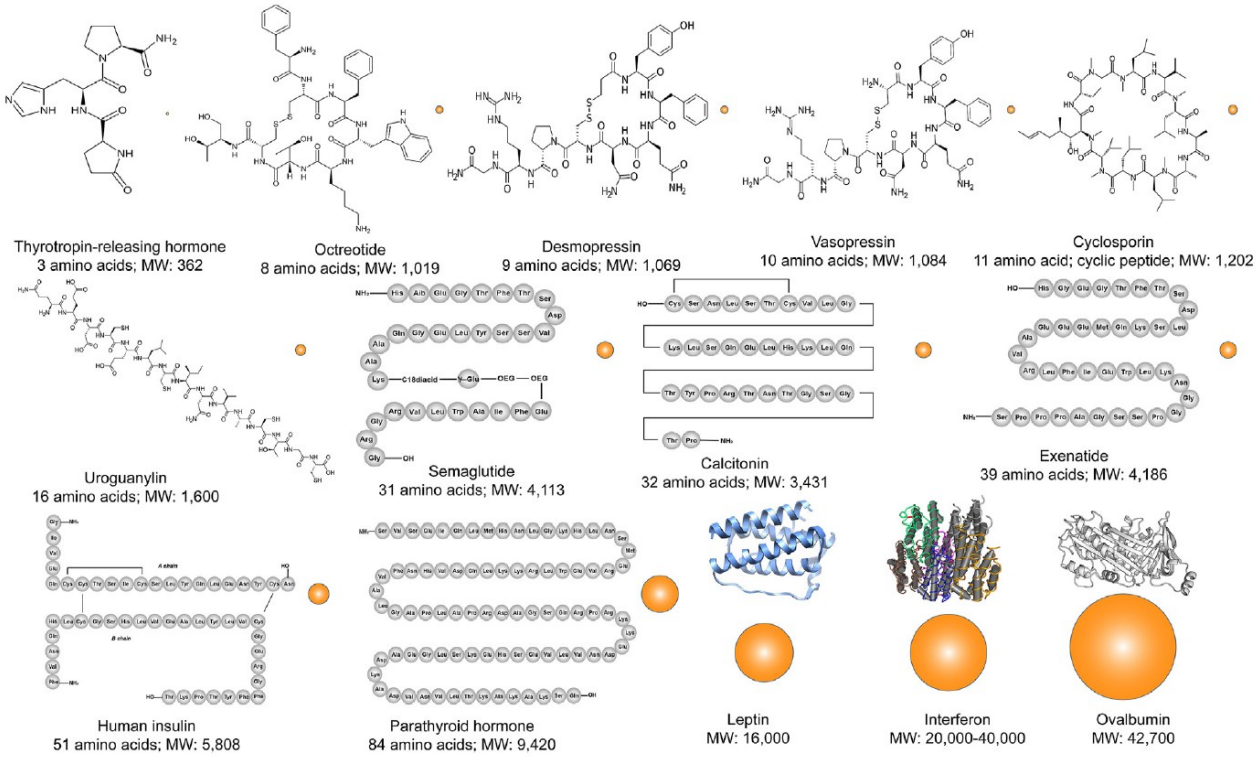


Figure 11. Typical molecular size and structures of proteins and peptides (86).

Synthetic peptides were designed to mimic the functionality of natural proteins and demonstrated their effectiveness in reducing friction in aqueous environments (87,88). However, their tribological performance is strongly dependent on their structure, particularly the presence of polar groups (87). Figure 11 illustrates a range of different protein and peptide structures with their respective molecular sizes (86). Thus, the design of effective peptide-based lubricants is challenging, as minor changes would result in a loss of functionality (88).

While protein-based lubrication is well established in biological systems, replicating these mechanisms in engineering systems remains challenging. Future research should therefore focus on identifying the specific protein properties that are key for effective lubrication, followed by replicating these features on more robust molecules.

2.7.3. Phospholipids and Liposomes

Phospholipids and liposomes provide lubrication through the formation of hydration shells around polar headgroups (26,38). The structure of the liposome and phospholipids is shown in Figure 12 (89). These molecules are key components of synovial fluid lubrication, where they contribute to extremely low friction (25,90). Trunfio-Sfarghiu et al. (2008) first demonstrated that lipid bilayers can achieve coefficients of friction as low as 0.002 (91,92). Despite the effectiveness of phospholipids and liposomes in biological systems, their application in industry remains limited. Phospholipids and liposomes are structurally fragile and are destroyed under high loads and shear stresses (92,93). Their production is costly and requires the development of standard procedures (92). These factors limit their use in large-scale applications.

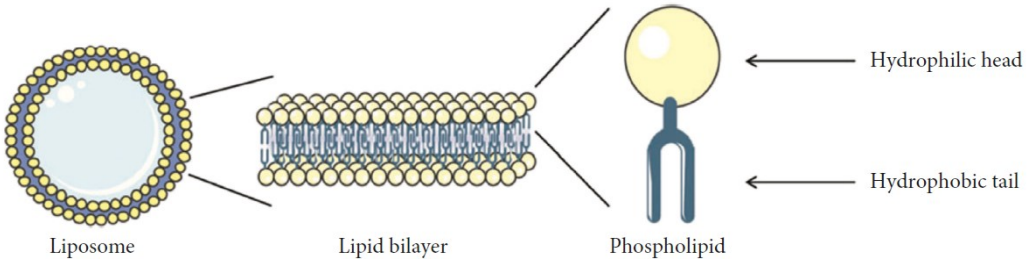


Figure 12. Diagram of a liposome including the amphiphilic phospholipid component that forms its concentric lipid bilayers (89).

2.8. Intended Applications and Operating Conditions

In this thesis the investigated biolubricants are intended for applications where environmental compatibility, non-toxicity and biodegradability are prioritised over extreme load-carrying capacity. Such applications are typically characterised by low to moderate contact pressures, low sliding speeds, operation predominantly within the boundary lubrication regime and ambient or near-ambient operating temperatures.

Representative examples include cosmetic and personal-care formulations, biomedical and bio-contact systems, food-processing and packaging equipment, and environmentally exposed mechanical components where lubricant loss to the surroundings is unavoidable. In cosmetic and biomedical applications, such as skin-contact devices, prosthetic interfaces and soft tissue interactions, contact pressures typically lie in the range of 0.1-20 MPa, sliding velocities are low (often < 10 mm/s), and lubrication is governed by boundary or hydration-dominated mechanisms (39,94,95). In such systems, control of friction and material compatibility are more critical than resistance to wear under high loads (96). In food-processing and packaging machinery, lubricants are frequently used in conveyors, chains, bush bearings, guide rails and sliding seals, where incidental contact with food products is

possible. These components typically operate under low normal loads (0.1-10 N), local Hertzian contact pressures of approximately 50-500 MPa and low sliding speeds (<0.1 m/s), resulting in boundary-dominated lubrication conditions (17). Lubricants used in these environments must be non-toxic, biodegradable and effective under boundary lubrication, as full hydrodynamic films are rarely sustained during intermittent motion or start-stop operation (71). In industrial applications where lubricant release to the environment is expected, such as agricultural machinery and forestry, maximum Hertzian contact pressures remain below 900 MPa, while sliding speeds remain low to moderate (7,17).

In these systems, lubricant performance is dominated by surface interactions, adsorption and boundary-film formation rather than viscosity-driven film thickness. Across these applications, boundary lubrication is the dominant regime, particularly during start-up, reciprocating motion or low-speed operation. The test conditions adopted in this thesis were therefore selected to reproduce boundary-lubricated contacts with controlled severity. This enabled systematic comparison of lubricants rather than optimisation for a single industrial component.

2.9. Summary

This chapter provided a review of bio-lubricants, based on oil and water. Oil-based lubricants, such as plant and algal oils, animal fats and synthetic esters, demonstrate the effectiveness of naturally occurring triglyceride-based systems in lubrication. Plant oils have been extensively studied and provide clear tribological benefits. However, their poor oxidative stability and limited thermal resistance restrict their industrial use. Algal oils and animal fats, while sharing the triglyceride structure, provide advantages from altered chemical composition, but their application in industry is constrained by production scalability, raw resource availability and ethical considerations. Synthetic esters overcome many limitations of natural triglycerides through chemical modification at the expense of biodegradability and environmental compatibility. The research gap lies in identifying environmentally sustainable oils that balance tribological performance, cost and thermal stability. This motivated the work in Chapter 4, where a range of pure plant oils were systematically tested to evaluate their tribological performance.

Water-based lubricants provide a different pathway by mimicking biological lubrication systems. Polysaccharides, proteins, peptides and phospholipids are present in natural systems providing an effective lubrication. Among the mentioned molecules,

polysaccharides stand out due to their ability to form both viscous aqueous solutions and hydrogels. Their role as viscosity modifiers and promoters of hydration layers makes polysaccharides promising molecules for water-based lubrication. While plant and algal polysaccharides were studied extensively, fungal polysaccharides remain unexplored in tribological applications. This research gap is addressed in Chapters 5 and 6, where fungal β-glucans are evaluated as a novel source of water-based biolubricants.

Hydrogels from polysaccharides provide stable lubrication systems with tuneable properties. The addition of ions to modify the properties of hydrogels was explored to provide improved gelation properties. However, the effect of metal ions on the tribological performance of hydrogels was not evaluated for different crosslinking mechanisms. This gap is addressed in Chapter 7, where algal and plant-derived polysaccharide hydrogels with different crosslinking mechanisms were doped with metal ions and their tribological performance was evaluated.

Other natural water-based bio-lubricants: proteins, peptides, phospholipids and liposomes, provide an outstanding friction reduction as part of synovial fluid in human joints. However, their replication in engineering systems is limited by high cost, structural instability and complexity in synthesis. In this thesis such systems were not tested and are highlighted as inspiration for other bio-lubrication strategies.

Finally, the intended application space for the biolubricants reviewed in this chapter is defined by low-load, low-speed and ambient temperature contacts, where boundary lubrication dominates and environmental compatibility is critical. These conditions are representative of cosmetic, biomedical, food-processing and environmentally exposed mechanical systems and they form the basis for the experimental test conditions adopted throughout this thesis.

To summarise, this chapter provides a range of diverse bio-lubrication strategies and reveals clear knowledge gaps, addressed in this thesis. Plant oils need a systematic evaluation of their tribological performance. Water-based lubrication requires exploration of fungal polysaccharides and systematic assessment of the role of ions on tribological performance of hydrogel crosslinking mechanisms. By addressing these research gaps, this thesis contributes to understanding the tribological behaviour of bio-lubricants and supports their potential use in environmentally sensitive applications.

3. Methods

This chapter outlines the experimental methods used in this thesis. Each method is described in detail by specific test conditions and procedures for obtaining experimental data. The steps taken to process raw data and the analysis and interpretation are also provided to ensure reproducibility and reliability of the results.

3.1. Tribological Assessment

The key aim of this thesis is the evaluation of tribological performance of tested lubricants under controlled conditions in the boundary lubrication regime. Tribological performance is assessed through measurements of friction and wear, as these parameters reflect a lubricant's ability to reduce energy losses and prevent surface damage (17,97). In this thesis two categories were investigated: liquid lubricants (plant oils and water-based solutions) and soft solids (hydrogels from natural polysaccharides).

A High Frequency Reciprocating Rig (HFRR), an industry-standard instrument for assessing performance of oils and fuels, was selected for testing liquid lubricants, as it provides well-established, standardised boundary-lubrication conditions (17,98,99). The technique is widely used in both academic and industrial tribology due to its high repeatability, controlled contact geometry and its ability to generate boundary conditions reliably through a combination of small stroke length, high reciprocation frequency and low lubricant volume. These characteristics make the HFRR most suitable for evaluating lubricants where surface interactions and film-forming behaviour dominate tribological performance. This method allows continuous measurement of friction and evaluation of wear after the test. A Biotribology Machine (BTM) was employed for tribological assessment of hydrogels, as the BTM was specifically designed to tested soft, hydrated materials, that may significantly deform under load. Due to the delicate nature of hydrogels and the limitations of wear scar measurements in such systems, only frictional behaviour was assessed for the hydrogels. These approaches were selected to ensure that each lubricant type was tested under appropriate test conditions, while allowing comparison to previous studies.

3.1.1. High Frequency Reciprocating Rig (HFRR)

Friction and wear tests were performed using a High Frequency Reciprocating Rig (PCS Instruments Ltd., UK). The HFRR operates by sliding a ball specimen against a flat disk in reciprocating motion under a controlled normal load, stroke length and frequency, providing

data on frictional and wear behaviours of tested lubricants (100–102). The entrainment velocity in an HFRR test is inherently not constant. As the motion is sinusoidal, the instantaneous entrainment velocity is zero at each end of the stroke and increases to a maximum of $\frac{\pi}{2} \times mean\ entrainment\ velocity$ at mid-stroke. This variation affects the local lubrication conditions, with boundary lubrication dominating close to the edges. Therefore, reported 'mean entrainment velocity' values represent the average velocity determined by the stroke length and reciprocation frequency. A schematic of the test setup is shown in Figure 13.

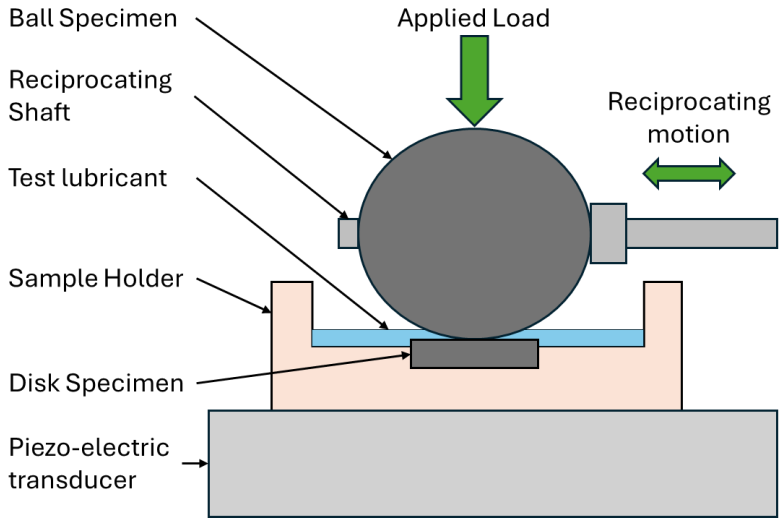


Figure 13. Schematic of the used setup.

Although the HFRR is capable of measuring electrical contact resistance to assess lubricant film formation, this parameter was not used in this thesis. While such measurements can provide useful insight into film formation, reliable interpretation of contact resistance data is restricted by the presence of conductive and non-conductive additives in several tested lubricants and the lack of prior calibration for these specific systems. Consequently, in this thesis the tribological performance of tested lubricants was evaluated based on the analysis of friction and wear.

In this thesis two distinct test conditions were employed, summarised in Table 1. In Chapter 4, standard AISI E-52100 steel specimens with Brinell hardness of 248 from PCS Instruments Ltd. (UK) were used to model steel-on-steel contacts found in engineering systems (17,97). The upper specimen was a 6 mm diameter ball, polished to a surface roughness of $R_a = 0.05$ µm, and the bottom specimen was a standard 9 mm diameter disk, polished to a surface roughness of $R_a = 0.02$µm. The supplied ball and disc specimens are manufactured with an intentional mismatch of hardness, where the ball is slightly harder

than the disc. This design ensures that most of the wear occurs on the disc, allowing more reliable measurement of wear scar geometry. During the test a constant load of 2 N was applied on the ball, resulting in a maximum Hertz contact pressure of 825 MPa. These conditions were selected to promote operation in the boundary lubrication regime, where the lubricant film thickness is smaller than surface roughness. Importantly, the chosen contact conditions closely follow the ASTM D6079 standard for HFRR lubricity testing, which is widely used for benchmarking boundary lubrication performance of fuels and lubricants (101). The only deviation from the standard is the reduced test duration of 20 minutes instead of 75 minutes, chosen to limit excessive wear while retaining comparability of friction and wear trends. Dowson-Hamrock equation, provided in Equation 1, was used to estimate the minimum film thickness h_m (103).The associated dimensionless parameter are provided in Equation 2, where α is the pressure-viscosity coefficient, E' the Reduced Young's modulus, R' the reduced radius, u_m mean entrainment velocity, η lubricant viscosity at ambient pressure and P the applied load (103).

$$h_m = 3.63\, R'\, G^{0.49}\, U^{0.68} W^{-0.073}\, (1 - e^{-0.68}) \quad \text{(Equation 1)}$$

$$G = \alpha E' \qquad U = \frac{u_m \eta}{E' R'} \qquad W = \frac{P}{E' R'^2} \quad \text{(Equation 2)}$$

Based on these equations and using contact conditions and plant oil data, the estimated minimum film thickness of the plant oils are in a range of 13-20 nm, which is much smaller than the surface roughness of the test specimens. These calculations confirm that testing occurs in boundary lubrication. In contrast, castor oil is estimated to provide a minimum film thickness of ≈130 nm due to its much higher viscosity, thus indicating a mixed lubrication regime. To ensure compatibility with literature, ASTM D6079 and ISO 12156-1 standards, stroke length of 1 mm, frequency of 50 Hz and test duration of 20 minutes were chosen (99).

In Chapters 5 & 6, AISI 304 stainless steel specimens (PCS Instruments Ltd., UK) were used instead of AISI E-52100 steel to prevent corrosion in water-based lubricant testing. Larger upper balls (19.05 mm diameter) and a reduced load of 1 N were chosen to reduce the maximum Hertz contact pressure to 289 MPa. These conditions were chosen to better represent low-load, low-speed contacts relevant to bio-tribological, cosmetic and biomedical applications, where lubrication is dominated by boundary lubrication mechanisms. Lower frequency (10 Hz) and shorter test duration (5 minutes) were selected to avoid excessive material removal under water-based conditions, while still enabling clear comparison of

lubricant performance. Such parameters are representative of soft sliding contacts, intermittent motion and start-stop operation commonly encountered in biomedical devices and skin-contact interfaces, where contact pressures are moderate. A PEEK (polyetheretherketone) sample holder replaced the standard steel holder to prevent corrosion and unwanted chemical interactions with water-based lubricants.

Table 1. Test conditions for HFRR Tribological assessment.

Test Parameter	*Chapter 4*	*Chapters 5 & 6*
Load	2 N	1 N
Maximum Hertz pressure	825 MPa	289 MPa
Stroke length	1 mm	1 mm
Stroke frequency	50 Hz	10 Hz
Mean entrainment velocity	0.1 ms^{-1}	0.02 ms^{-1}
Test duration	20 min	5 mins
Temperature	23 ºC	23 ºC
Sample holder	Standard metal holder	Custom PEEK holder
Test specimens	AISI E-52100 Steel Ball: 6 mm diameter, Ra < 50 nm Disk: 9 mm diameter, Ra < 20 nm	AISI 304 Stainless Steel Ball: 19.05 mm diameter, Ra < 50 nm Disk: 9 mm diameter, Ra < 50 nm

Before each test 3 ml of fresh lubricant was placed into the sample holder. Each lubricant was tested 3 times, using new specimens for every repeat, to ensure reproducibility. Between repeats the sample holder was cleaned using deionised water and isopropanol to prevent mixing between tested lubricants.

3.1.1.1. Friction Measurement

Friction force was continuously recorded during each test, and coefficient of friction (COF) was calculated as the time-averaged ratio of friction force to applied load for the total duration of the test run, as shown in Figure 14. The reported values represent the average of 3 test repeats.

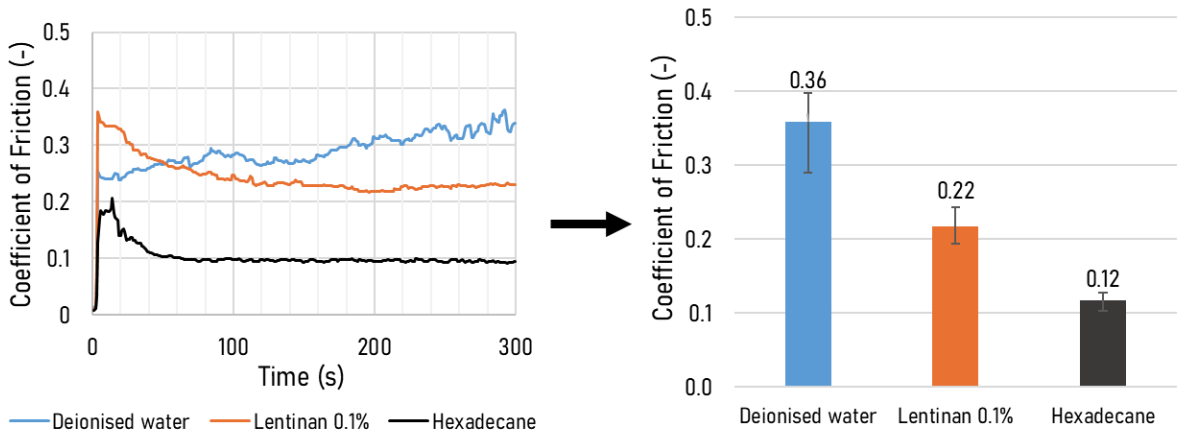


Figure 14. The coefficient of friction values from the test measurements. Error bars indicate minimum and maximum obtained values.

3.1.1.2. Wear Measurement

To analyse the wear performance of tested lubricants, after the test specimens were cleaned using deionised water and wear scars on both ball and disk were inspected and the size was measured, using a Hirox RH-2000 (Hirox, Japan) digital microscope. Depth profiles on the disc were measured using White Light Interferometer (WLI) from Bruker Ltd, USA. The instrument provides a vertical resolution of approximately 1 nm and a lateral resolution of approximately 0.4 µm, ensuring that the depth and the shape of the measured surfaces can be measured with sufficient precision. For each test run 3 line profiles in the central part of the disk wear scar were obtained, as shown in Figure 15. Disk wear scar cross-sectional area was calculated by numerically integrating the line profiles using the trapezoidal rule.

The ball wear scar volume V_{ball} was approximated by the volume of hemispherical cap, following the standard procedure (98,99). The calculation is shown in Equation 3, where D is the diameter of the ball specimen and d is the ball wear scar diameter.

$$V_{ball} = (\pi / 24)\left(D - (D^2 - d^2)^{1/2}\right)\left(2D + (D^2 - d^2)^{1/2}\right) \quad \text{(Equation 3)}$$

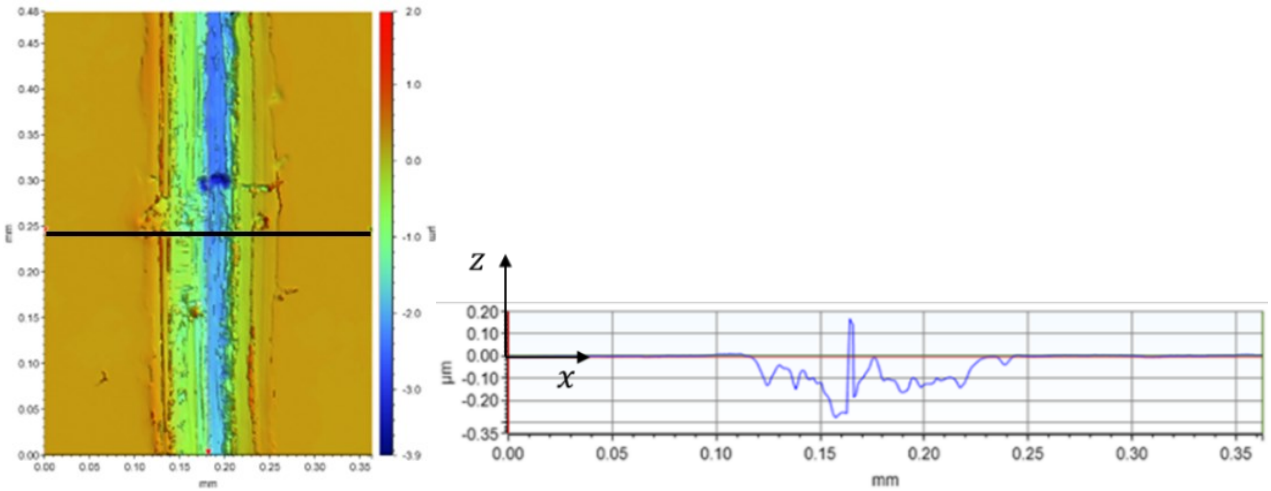


Figure 15. The example of obtained disk wear scar cross-section from WLI.

3.1.2. Biotribology Machine (BTM)

In Chapter 7 the tribological performance of hydrogels was assessed using the BioTribology Machine (BTM) from PCS Instruments Ltd (UK), designed for assessing frictional properties of soft solids (104,105). The used setup is shown in Figure 16. The specimen holder was made using a 20 mm diameter glass PCX lens (#47-892, Edmund Optics, UK) with a radius of curvature of 77.52 mm. The lens was reciprocating at a constant frequency of 1 Hz and a stroke of 10 mm for 10 cycles. All tests were conducted at room temperature of 25°C under a constant loading of 1 N. These low-frequency, low-load conditions were selected to avoid structural damage to hydrogels and ensure reproducibility, consistent with previous studies (104,105).

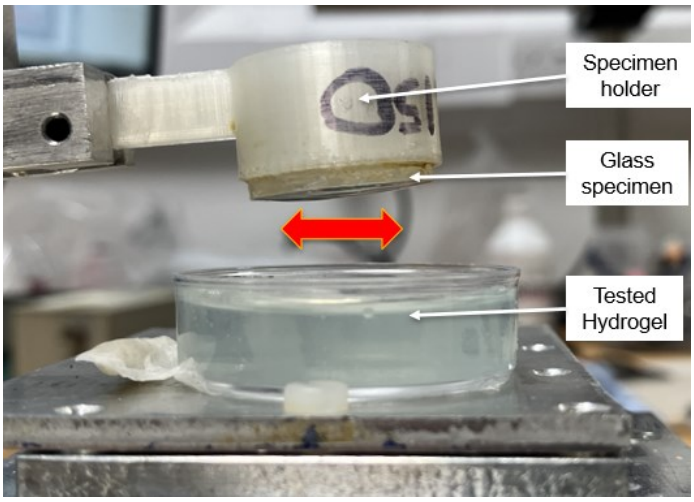


Figure 16. BTM operational setup before applying the load.

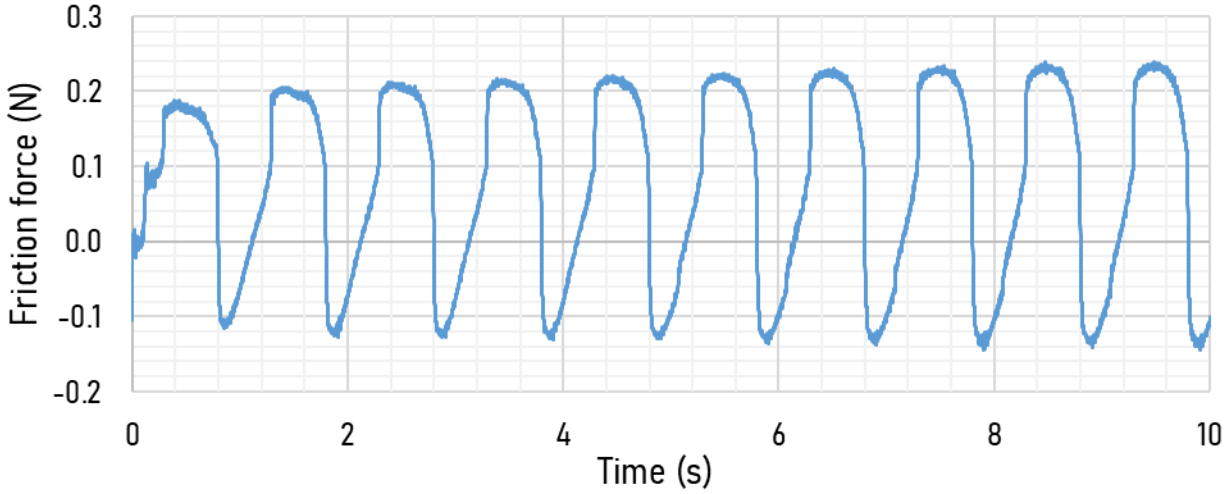


Figure 17. The measured frictional force for 10 cycles for alginate Ca hydrogel.

During the test the friction force was continuously measured for 10 full cycles, as shown in Figure 17. The raw friction-time signal was first normalised by dividing the friction force by the applied normal load, providing instantaneous coefficient of friction. To account for variations between cycles, the coefficient of friction was averaged over the full 10

reciprocating cycles. The resulting mean value is reported as the representative coefficient of friction for each hydrogel sample.

3.2. Rheological Assessment

Rheological properties were evaluated to compliment tribological analysis, as viscosity and viscoelastic moduli influence lubrication (106). All rheological measurements were conducted using a TA Discovery Hybrid Rheometer (DHR-1) from TA Instruments (USA) with parallel plate geometry.

3.2.1. Viscosity Evaluation

Dynamic viscosity of tested lubricants was assessed in Chapters 4 and 6. In Chapter 4 viscosity of plant oils was measured to examine its correlation with tribological behaviour. In Chapter 6 the viscosity of water-based solutions was examined to confirm stability of the solutions and ensure that changes in friction were not due to bulk viscosity changes.

For both assessments a parallel plate rheometer geometry was employed with appropriate gap and plate sizes chosen to minimise edge effects and ensure reliable measurements (107). This configuration was selected instead of a cone-plate geometry because it provides greater flexibility across a wider viscosity range and is less sensitive to alignment errors. Each measurement was repeated 3 times under a constant shear rate of 100 s^{-1} for 30 seconds. Shear rates in boundary lubrication contacts can exceed $10^3 - 10^6$ s^{-1}, which cannot be reproduced in a rotational rheometer (108). Therefore, the chosen shear rate represents a practical compromise, allowing comparison between samples under controlled conditions while approximating the behaviour relevant to boundary lubrication. Table 2 provides a summary of test conditions for these measurements.

Table 2. Rheological test conditions for the respective chapters.

Parameters	*Chapter 4*	*Chapter 6*
Diameter of the parallel plates	25 mm	40 mm
Gap size	0.2 mm	1 mm
Shear rate	100 s^{-1}	100 s^{-1}
Test temperature	25°C	25°C

3.2.2. Hydrogel Assessment

In Chapter 7 hydrogel rheological behaviour was evaluated to measure their viscoelastic properties: Storage and Loss moduli, which play important role in their mechanical and lubrication performance (75,109,110). The Storage modulus G' represents the elastic

component of the material response to loading and quantifies the amount of energy stored and recovered during deformation. The Loss modulus G'' reflects the viscous component, corresponding to the energy dissipated, and indicates how fluid-like the material behaves under shear. Together, these moduli characterise the balance between elastic and viscous behaviour. Hydrogel disks of 2 mm thickness and 25 mm diameter were positioned between two grated parallel plates to prevent slip at the interfaces, as shown in Figure 18. The gap between the plates was adjusted to 1.95 mm to ensure full contact between test sample and plates, while avoiding excessive compression.

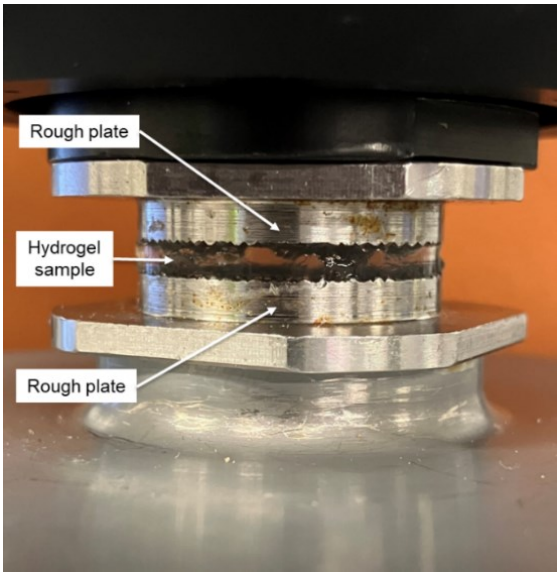


Figure 18. Rheology test setup on DHR-1 with loaded hydrogel sample.

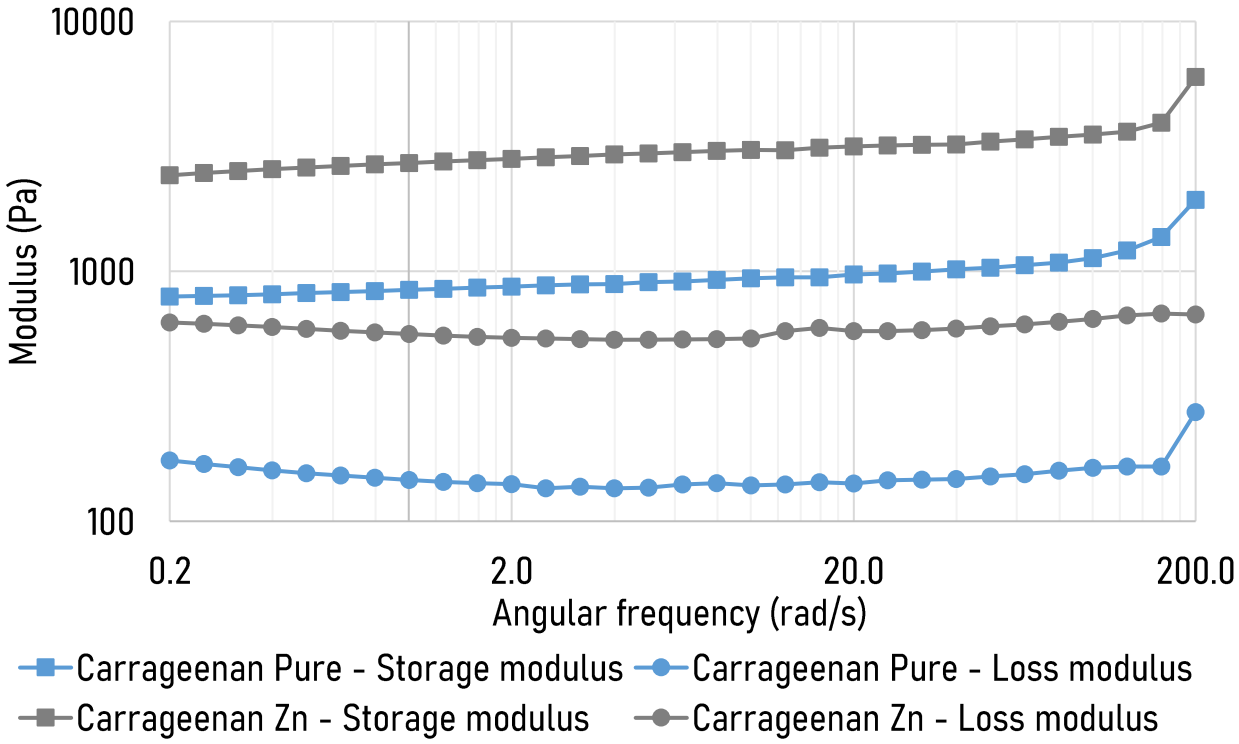


Figure 19. Storage and Loss moduli distributions with frequency for carrageenan hydrogels.

The frequency sweep tests were carried out at a constant strain of 10% over a range of frequencies from 0.2 rad/s to 200 rad/s at a temperature of 25°C. Frequency sweeps for soft solids are usually done at smaller strains of 0.1%-1% (111–113). However, the larger strain value of 10% was chosen to approximate the relatively large deformations induced during friction testing, thus a larger strain value is preferred to obtain the closer estimate of functional hydrogel rheological properties (114–116). Both storage and loss moduli were recorded to obtain the distributions like shown in Figure 19 for two carrageenan hydrogels: Pure and doped with Zn ions. The addition of Zn ions was used as an example of altering the hydrogel structure and mechanical properties. The broader role of metal ions in tuning hydrogel properties is discussed in detail in Chapter 7.

3.3. Indentation Testing

3.3.1. Hydrogel Indentation

To evaluate the elastic behaviour of hydrogels, indentation tests were performed using a Biomomentum Mach-1 test device (Biomomentum, Canada). Indentation testing is a widely used method for soft materials, as it provides an estimate of material properties and preserves structural integrity (117).

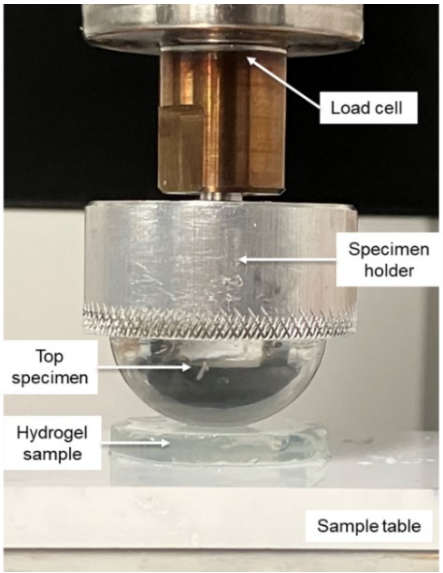


Figure 20. Biomomentum Mach-1 setup for evaluating mechanical properties of hydrogels.

The experimental setup is shown in Figure 20. The hydrogel samples were prepared as 20 mm diameter disks with a thickness of 2 mm. A spherical acrylic indenter with a radius of 10 mm was used, because acrylic is chemically inert with respect to hydrogels and is sufficiently rigid to be treated as non-deformable. The relatively large radius was selected to minimise stress concentrations and ensure the sample response remained within the elastic

regime under test contact conditions (117,118). After placing the hydrogel disk on sample plate, a pre-load of 1 g was applied to define the point of zero indentation depth. The indenter was then moved at a constant velocity of 0.1 mm/s until reaching an indentation depth of 0.2 mm. The maximum displacement was held for 10 seconds. After that the sample is unloaded at the same velocity as during loading. For the duration of the test, force response was continuously measured by the load cell, and the corresponding force-indentation graphs were produced, as shown in Figure 21.

The maximum indentation depth was kept below 10% of the sample thickness to satisfy the assumptions of Hertz contact model, which was used for analysing the force-indentation data. Prior to analysis, the raw indentation data was processed to extract the indentation response after preload, as shown in Figure 21. Then a linear approximation of the loading segment was applied and the reduced elastic modulus $E^* = \frac{E}{1-\nu^2}$ of the hydrogel was calculated by fitting the Hertz contact equation for spherical indentation to the experimental data. The used Hertz contact equation is represented by Equation 4, where F_z is the indentation force, δ the indentation depth and R the radius of the spherical indenter (119):

$$F_z = \frac{4}{3} E^* R^{1/2} \delta^{3/2} \quad \text{(Equation 4)}$$

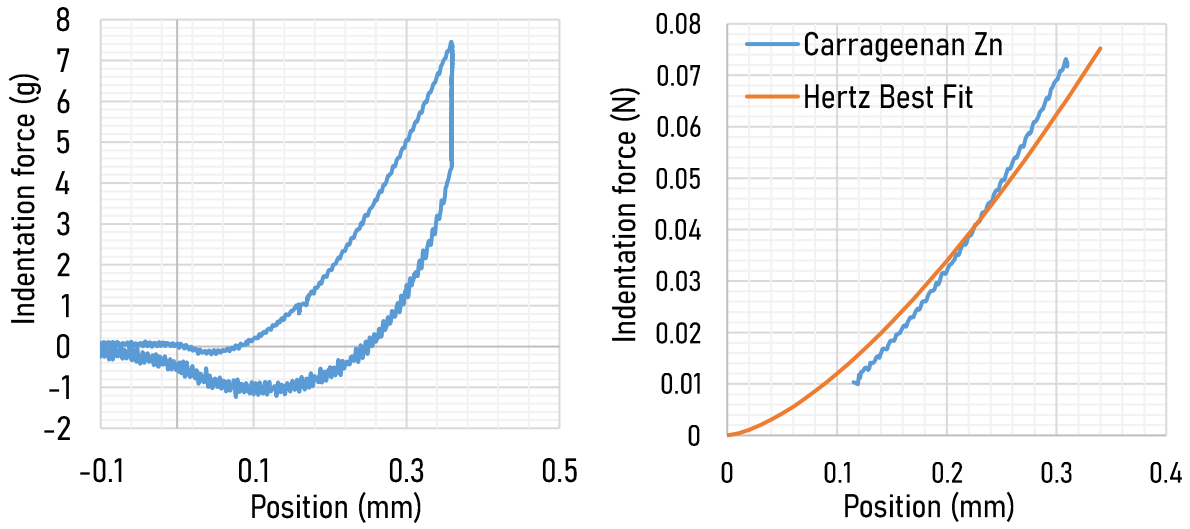


Figure 21. Raw (left) and filtered (right) force-displacement data for carrageenan Zn hydrogel for Hertz model.

The fitting was performed in an iterative manner, where the reduced elastic modulus value was refined across the fitting range and was updated until the R^2 -value between experimental and model data reached its maximum. Figure 21 shows an example of such fitting for a Carrageenan Zn hydrogel.

3.3.2. Indentation Model Validation

In Chapter 9 the Biomomentum Mach-1 test device was used to validate the proposed indentation model through static testing tests. Tests were conducted on square silicone samples (25 mm x 25 mm) of uniform thickness adhered to a rigid metal substate using double-sided adhesive tape. The spherical acrylic indenter, described in the previous section, was used for all tests. Each test condition was repeated 3 times, and samples rested for at least 3 minutes between each repeat to ensure reproducibility.

During static tests, the indenter was driven vertically into the sample at one of four constant speeds (0.005, 0.01, 0.1 or 1 mm/s) until a maximum indentation force of 100 N was reached. This maximum force was chosen to ensure sufficient deformation of both soft and hard silicone samples while remaining within the instrument's safe operating range. For the duration of the tests both indentation force and displacement were continuously recorded. The examples of obtained force-indentation graphs are shown in Figure 22.

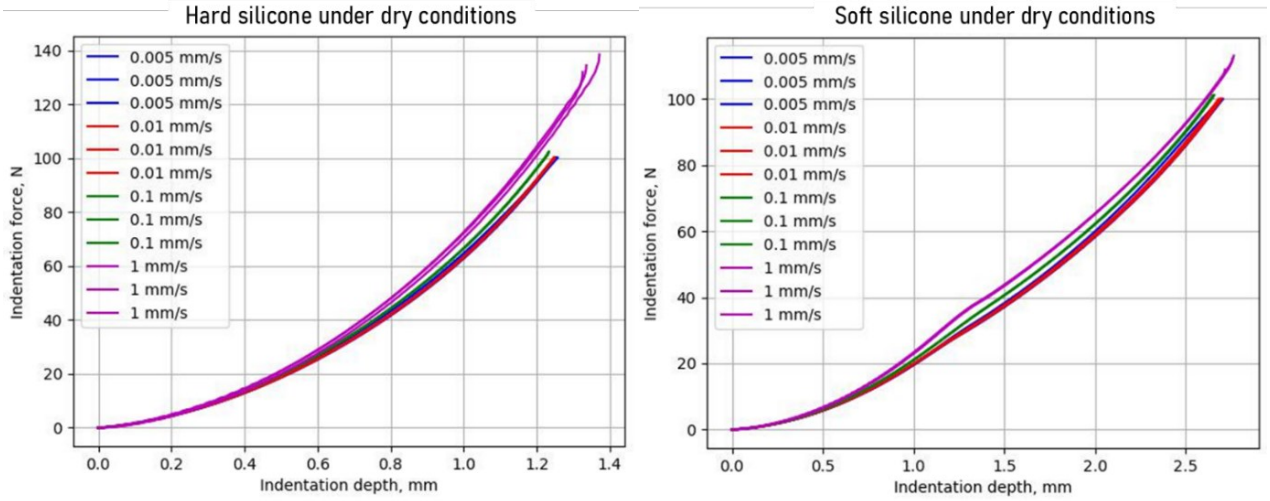


Figure 22. Static scenario: force-indentation graphs of hard and soft silicones under dry conditions.

3.4. Dynamic Light Scattering (DLS)

In Chapter 6 particle size distributions of fungal powders in water were measured using Dynamic Light Scattering (DLS). The DLS technique estimates hydrodynamic diameter from Brownian motion-induced light scattering (120). Measurements were performed using Zetasizer Pro-ZS (Malvern Instruments, UK) at 25 °C. 12 µl samples were scanned with 5 repeats to obtain the intensity graphs of particle sizes, like the one shown in Figure 23. Peaks in the obtained distribution correspond to a dominant particle size populations in the tested solution. In the case of Lentinan solutions, two main particle populations were

detected: a smaller population with a particle diameter of ≈50 nm and a larger population with a particle diameter of ≈500 nm. The sharpness of the peaks indicates that the particle populations are relatively uniform in particle size.

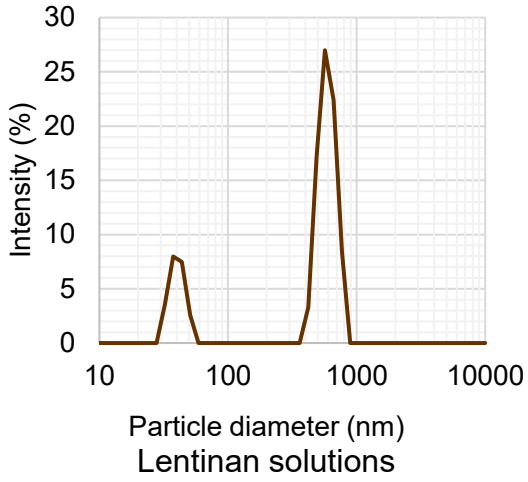


Figure 23. The particle size distribution of Lentinan solutions.

3.5. Summary

This chapter has outlined the experimental methods used in this thesis to evaluate the tribological, mechanical and rheological performance of natural and nature-inspired lubricants. Tribological tests were conducted using the High Frequency Reciprocating rig (HFRR) for boundary lubrication contacts and the BioTribology Machine (BTM) for soft materials, allowing systematic assessment of friction and wear. Rheological characterisation was carried out to correlate lubricant viscosity and structure with tribological performance. Indentation testing provided the mechanical properties of hydrogels and validation data for the development of the novel indentation model for soft matter mechanics. Dynamic Light Scattering was used to determine particle size distributions in fungal solutions. Together, these methods provide a consistent experimental framework for the studies presented in the following chapters.

4. Plant Oils as Direct-Use Bio-Lubricants

This chapter explores the direct-use approach to environmentally friendly lubrication, where unmodified or minimally processed natural materials, like plant oils, are applied directly as lubricants. The historic perspective of using animal and plant oils as lubricants, their subsequent displacement in the late 19th century by mineral oils and the recently renewed interest in bio-based lubricants is presented. Selected plant oils were tested to assess their tribological performance and a mixing strategy was explored to further improve the performance. The results confirm both the potential and limitations of the direct-use approach. The chapter concludes by highlighting these challenges and introducing a more advanced biomimetic approach.

4.1. Introduction

Modern industry relies on functional lubricants to ensure the efficient and reliable operation of machinery. Lubricants reduce friction and wear between the contacting surfaces, thus minimising power losses and extending the service life of machine elements. Due to low cost, good performance and wide availability petroleum-based lubricants became widespread at the end of 19th century (49).

However, petroleum-based oils impose environmental and sustainability issues. Mineral oils are extracted from finite fossil fuel reserves (8). Their extraction, production and use contribute to greenhouse gas emissions. Mineral oils are toxic to most life forms, and spills or leaks contaminate soil and water (4,5). These concerns have driven a renewed interest in environmentally friendly alternatives that maintain tribological performance while reducing environmental effect.

The direct-use approach has attracted attention in the search for sustainable lubrication. This approach involves using naturally occurring lubricants directly with little or no chemical modifications. The main objective of the direct-use approach is to exploit the inherent lubricating properties of natural materials while maintaining simplicity, renewability and biodegradability. The direct-use approach aligns with the principles of Green Tribology, which emphasise the use of renewable and non-toxic materials in tribological applications (121,122).

Although the direct-use approach is attractive from an environmental perspective, it faces significant challenges in meeting the demanding performance requirements of modern

industry. For example, natural oils exhibit poor oxidation stability and limited thermal resistance, which limit their effective use in excessively hot or cold operating conditions (3,7,61,123). Understanding these limitations is essential when considering solutions. In the case of natural oils, blending or further chemical modifications could resolve some of the mentioned issues (3,61,123,124).

To understand the potential and limitations of direct-use lubricants, their historical context needs to be examined. The philosophy behind the direct-use approach has been utilised long before the emergence of mineral and synthetic oils. The next section therefore provides a historical perspective on the direct-use approach, showing how unmodified natural materials were effectively used for centuries and how they were replaced with refined and synthetic alternatives.

4.2. Historical Perspective of Direct-use

The direct-use approach in lubrication has deep historical roots. For thousands of years, civilisations used readily available natural materials to manage friction and wear problems. In Ancient Egypt, water, natural oils and animal fats were used to reduce the force required to move heavy building blocks on sledges, and to lubricate chariot axles to prolong their life (49,125). These substances were applied in their natural state, without modification, highlighting the core principles of the direct-use approach: simplicity, accessibility and minimal processing.

One of the earliest records of lubricants was produced by Pliny the Elder (A.D 23-79), who listed the lubricants available in his times (49). Most of the listed lubricants are plant-based oils that are widely available today. During the Middle Ages and into the early modern period, plant oils, animal fats and water continued to be used as lubricants (49). Their consistent use over centuries highlights their advantages: plant oils and animal fats are abundant, biodegradable and provide adequate performance for the mechanical demands of pre-industrial machinery.

Early scientific studies of friction also relied on direct-use lubricants. In 1699 Amontons conducted friction tests using pork fat, while Leupold (1735) recommended using vegetable oils and tallow for lubricating rough surfaces (49). Such practices reveal that these direct-use lubricants were sufficient for the needs of pre-industrial and early industrial machinery until the mid-19th century. Instead of modifying the oils to improve their performance, the appropriate oil types for each application were chosen based on experience and availability.

The discovery of mineral oil in the 1850s marked a turning point in lubrication history. Interestingly, the initial use of petroleum was consistent with the direct-use approach. Mineral oil was simply replacing animal fats and plant oils. However, as industrial machinery evolved to operate at higher loads and speeds, the need for better lubricant performance emerged. Refining techniques were developed to improve stability and purity of mineral oils, providing more robust and effective lubricants. Within a few decades, mineral oils displaced natural lubricants in most applications. This transition was driven by three key factors:

1. Cost and availability: petroleum was cheaper and more abundant than natural oils
2. Better performance: mineral oils withstand higher temperatures and pressures
3. Refinability: mineral oil could be tailored to the needs through chemical processing

The subsequent emergence of synthetic lubricants, which are produced by chemically altering petroleum-derived oils, marked a further departure from the direct-use approach. Synthetic products offered exceptional performance under extreme conditions at the expense of biodegradability and simplicity. By the mid-20th century direct-use lubricants were used only in niche roles, like forestry and food-grade applications (7).

In recent decades, the growing awareness of environmental damage of using petroleum promoted a renewed interest in bio-based lubricants. The direct use of plant oils aligns with sustainability goals by offering renewable and biodegradable alternatives to mineral oils. However, the inherent limitations of plant oils under harsh operating conditions continue to present challenges. Current research therefore focuses either on modifying or mixing plant oils to improve stability or on developing nature-inspired strategies, which are investigated in later chapters of this thesis.

4.3. Modern Eco-Friendly Lubricants

In response to growing environmental concerns, stricter regulations on pollution and sustainability, the lubricant industry has looked for alternatives to conventional mineral oil-based lubricants in recent decades. The main objective of such alternatives is to reduce the environmental impact of lubricants while maintaining adequate tribological performance. Particular attention is given to sensitive environments where spills and leakages can cause severe consequences, like marine ecosystems, agriculture and forestry (7).

To address these challenges, a range of eco-friendly lubricants emerged, offering a balance between tribological performance and environmental compatibility. These modern eco-friendly lubricants can be categorised in three groups.

The first group consists of Environmentally Acceptable lubricants (EALs). EALs are derived from mineral oils but formulated to minimise their environmental effect by using environmentally safer additives and better refinement (6,17). EALs are often formulated to meet the environmental regulations, such as United States Environmental Protection Agency Vessel General Permit (13). These permits outline the minimum requirements for parameters, like biodegradability and non-toxicity (13). Although an environmental improvement over conventional mineral oils is achieved, EALs cannot be considered fully sustainable, due to their reliance on fossil resources and incomplete biodegradability. Their main advantage is compatibility with existing equipment in applications, like marine and hydraulic systems (126).

The second group contains chemically modified vegetable oils and synthetic esters. In these lubricants complex chemical transformations are introduced to change the structure of natural triglycerides, thus overcoming limitations like poor oxidative stability and thermal degradation (7,46,127). Examples of such transformations are transesterification and epoxidation. Transesterification produces esters by replacing glycerol in the base plant oil with alcohols (7,22,127). This change reduces the lubricant viscosity and improves fluid flow at lower temperatures. Epoxidation targets unsaturated fatty acids, by eliminating their double bond. As this double bond is prone to oxidation, thermal and oxidative stability are improved upon its removal (7,22,50). Targeted modifications combine improved tribological performance with the biodegradability and renewability of base plant oils (7,46,127). Also chemically modified esters can be tuned for specific applications, like automotive, aerospace and industrial needs (7,126).

The third group aligns closely with the philosophy of direct-use approach, as it employs natural oils in their minimally processed form. This approach employs the inherent properties of plant oils, while avoiding the costs and environmental effects of chemical modifications. Common examples of currently used plant oils include rapeseed, soybean and castor oils. These oils demonstrated acceptable lubricating performance under moderate conditions, and their environmental comparability allows their safe use in agriculture, forestry and other applications where environmental impact is a concern (7). However, the direct use of plant oils comes with significant limitations. Unmodified plant oils suffer from oxidative instability, poor low-temperature flow and limited thermal resistance (7,50,53). While blending and formulation improvements have been explored to mitigate these shortcomings, the inherent chemical structure of plant oils constraints the performance.

Although these limitations are well documented, there is still a need to evaluate the performance of plant oils under controlled conditions. Such testing provides quantitative data on their friction and wear performance to identify the most promising oils and to establish a baseline for comparison with more advanced solutions. Moreover, it helps to assess if simple strategies, such as mixing, can improve the performance sufficiently to meet practical demands. The present work seeks to explore the extent to which the performance of direct-use lubricants can be mitigated within the direct-use framework.

4.4. Testing Direct Use of Plant Oils

Although plant oils have been extensively investigated as potential bio-lubricants, most existing studies focus on chemically modified esters or on specific industrial oils such as rapeseed, soybean and castor (51,53,72), to achieve a lubricant with high oxidative resistance. Considerably fewer studies provide direct, comparative benchmarking of unmodified plant oils under controlled boundary-lubrication conditions, meaning that the link between fatty-acids chemistry and tribological performance is not explored. Reported results also vary widely as different studies employ different test geometries, loads, temperatures, and interface materials, making systematic comparison difficult, if not impossible (22,61,63). The present work therefore contributes to this existing research by providing a controlled, side-by-side evaluation of six structurally distinct plant oils, enabling clearer links between fatty-acid composition and friction and wear behaviour.

Before evaluating the performance of direct-use plant oils, it is useful to consider how bio-lubricants perform relative to conventional petroleum-based lubricants. Mineral oils typically provide good oxidative stability, thermal resistance, and consistent viscosity profiles, which make them effective under demanding industrial conditions (7,17,50). However, their boundary-lubrication performance often relies heavily on additive packages (17,126). Lee et al. (2022) and Reeves et al (2015) show that plant oils can achieve equal or lower friction coefficients due to their strong fatty-acid adsorption onto metal surfaces (22,57,60). With respect to wear performance, unmodified plant oils may perform comparably or even better in mild boundary lubricated contacts, but mineral oils outperform them at elevated temperatures and in oxidising environments (50,53). This context highlights the importance of systematically evaluating plant oils under controlled conditions to determine their operational window.

To evaluate the potential of direct-use plant oils as modern eco-friendly lubricants, it is essential to assess their performance in key tribological aspects: viscosity, friction and wear. Although plant oils were extensively used historically, modern machinery operates under more demanding conditions, which requires a clear understanding of capabilities and limitations of plant oils under controlled testing.

As described in the Section 2.6.1, the chemical structure of triglycerides in plant oils determines the lubricant effectiveness. The distribution of fatty acids plays the main role in the formation of adsorbed layers on metal surfaces (23,50,128). Table 3 summarises how chain length and saturation of fatty acids influence viscosity, adsorption and the resulting performance in the boundary regime. Long-chain fatty acids provide an increased viscosity and a closer molecule packing, leading to stronger adsorption and formation of stronger boundary films (55,58). In contrast, shorter fatty acid chains have reduced viscosity and weaker adsorption, limiting the ability to form protective layers (58). The degree of unsaturation is directly related to viscosity of the oil. Saturated fatty acids, without double carbon bonds, generally exhibit lower viscosities than unsaturated ones (59,129). The opposite trend is observed with adsorption, where saturated fatty acids provide stronger adsorption and better surface protection due to more efficient molecule packing on the surfaces (56). Monounsaturated fatty-acids provide a moderate adhesion in combination with medium viscosity, resulting in the development of a film that, however, is not as dense or well-developed as for saturated fatty acids.

Table 3. Role of fatty acid types on plant oil tribological performance.

Property	*Viscosity*	*Adsorption*	*Boundary film characteristics*	*References*
Short Chain Length	Low	Weak	Limited film formation	(55,58,59)
Long Chain Length	High	Strong	Strong film formation	
Saturated	Low	Strong	Dense monolayer	(56,59,129)
Monounsaturated	Medium	Medium	Moderate film formation	
Polyunsaturated	High	Weak	Limited film formation	

Based on these considerations, six plant oils were selected for their diverse fatty-acid compositions that are known to influence the tribological performance (50). Tested oils included avocado, broccoli seed, castor, jojoba, lemon kernel and macadamia nut oils. Their dominant fatty acids are summarised in Table 4.

Together, these oils capture a wide range of structural chemistries: avocado oil combines saturated and monounsaturated fatty acids, broccoli seed oil represents a long-chain

monounsaturated fatty acid, jojoba contains chemically distinct wax esters, lemon kernel oil contains a mix of unsaturated fatty acids, macadamia nut oil is rich in purely monounsaturated fatty acids and castor oil represents a hydroxylated fatty acid. This selection covers a range of different fatty acid types and allows the evaluation of how chain length and degree of unsaturation influence the tribological behaviour of plant oils.

Table 4. Features of chosen plant oils.

Plant oil	*Dominant fatty acids*	*Reason for selection*	*References*
Avocado	Oleic (C18:1) Palmitic (C16:0)	Mostly monounsaturated and saturated fatty acids	(57)
Broccoli Seed	Erucic (C22:1)	Long chain monounsaturated fatty acid	(130)
Jojoba	Wax esters (C20-C22) Gondoic (C20:1)	Chemically distinct Long chain monounsaturated	(53)
Lemon Kernel	Oleic (C18:1) Linoleic (C18:2) Linolenic (C18:3)	Medium chain mono- and polyunsaturated fatty acids	(131)
Macadamia Nut	Oleic (C18:1) Palmitoleic (C16:1)	Medium chain monounsaturated fatty acids	(132)
Castor	Ricinoleic (C18:1-OH)	Medium chain Hydroxylated Monounsaturated fatty acid	(53)

It is important to note that oxidative and thermal stability, although recognised as critical limitations of plant oils (46,127), are not investigated in this study. The focus is solely on assessing the effect of fatty acids on the tribological behaviour under controlled conditions.

The viscosities of these plant oils were evaluated using a parallel-plate rheometer geometry with a gap size of 0.2 mm at a constant shear rate of 100 s^{-1}. The detailed procedure is described in the 3.2 Rheological Assessment section.

Figure 24 presents the dynamic viscosities of the tested oils at ambient conditions. Most plant oils exhibited viscosities in range from 38 mPas and 64 mPas. Exceptionally, castor oils exhibited the highest viscosity value of 700 mPas. This is a direct consequence of the high content of ricinoleic acid, which contains a hydroxyl functional group, increasing intermolecular hydrogen bonding and thus internal resistance to flow (53,133–135).

All tested oils were obtained from NHR Organic Oils Ltd. (UK). These oils were tested as received following procedures described in the 3.1 Tribological Assessment section.

Tribological performance was assessed using the High Frequency Reciprocating Rig (HFRR) under a constant load of 2 N, at a frequency of 50 Hz and a stroke length of 1 mm.

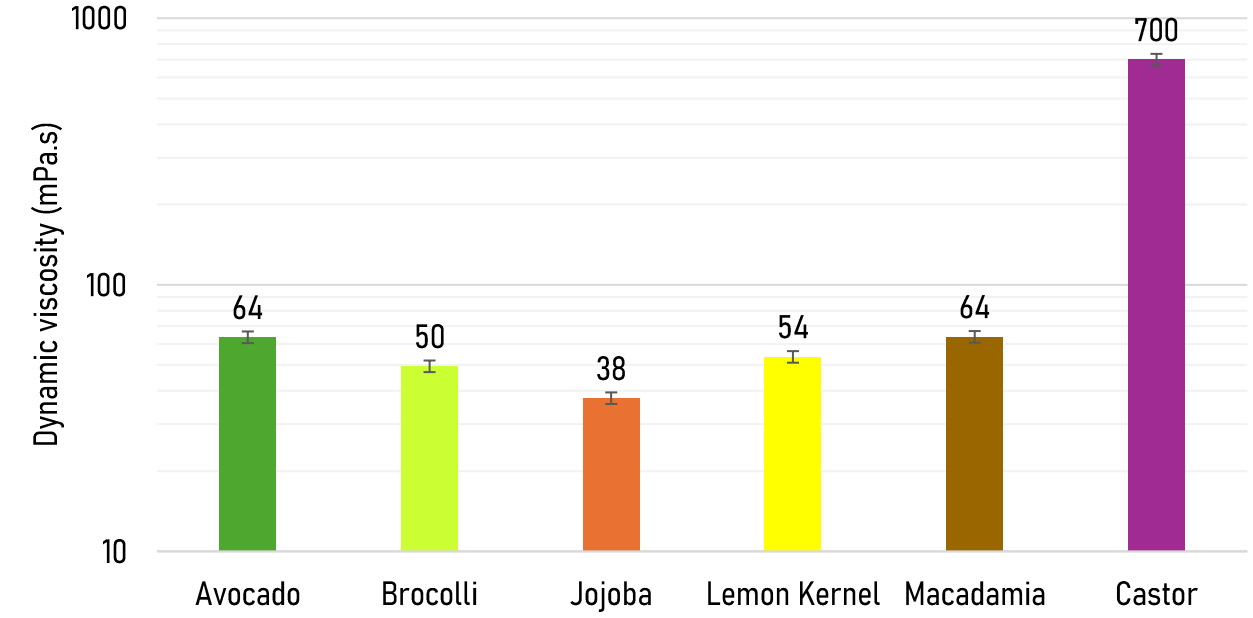


Figure 24. Obtained dynamic viscosities for tested plant oils.

Film thickness values calculated under the test conditions are shown in Figure 22. Most oils provide the film thicknesses in the range of 13–20 nm, placing them firmly in the boundary lubrication regime. Castor oil, however, produced a minimum film thickness of ≈128 nm, corresponding to the mixed lubrication regime. This distinct behaviour is linked to the much higher viscosity, arising from the hydroxyl functional group of ricinoleic fatty acid.

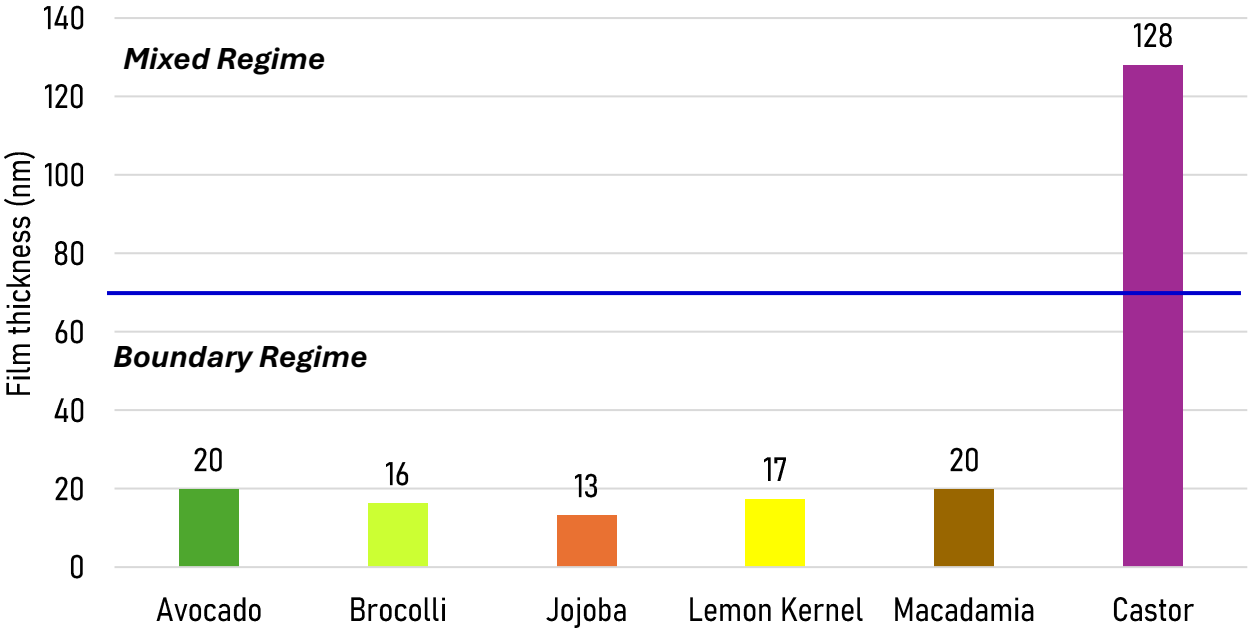


Figure 25. Calculated film thicknesses of tested plant oils with lubrication regimes.

The measured coefficients of friction for selected plant oils are shown in Figure 26. Among the tested oils, the lowest coefficient of friction value of 0.042 was observed with macadamia nut oil, followed by broccoli seed oil with coefficient of friction of 0.046. In contrast, Lemon kernel and castor oils exhibited higher coefficient of friction values of 0.060. The observed differences in friction coefficients could be linked to the fatty acid composition of the oils, in line with the trends summarised in Table 3.

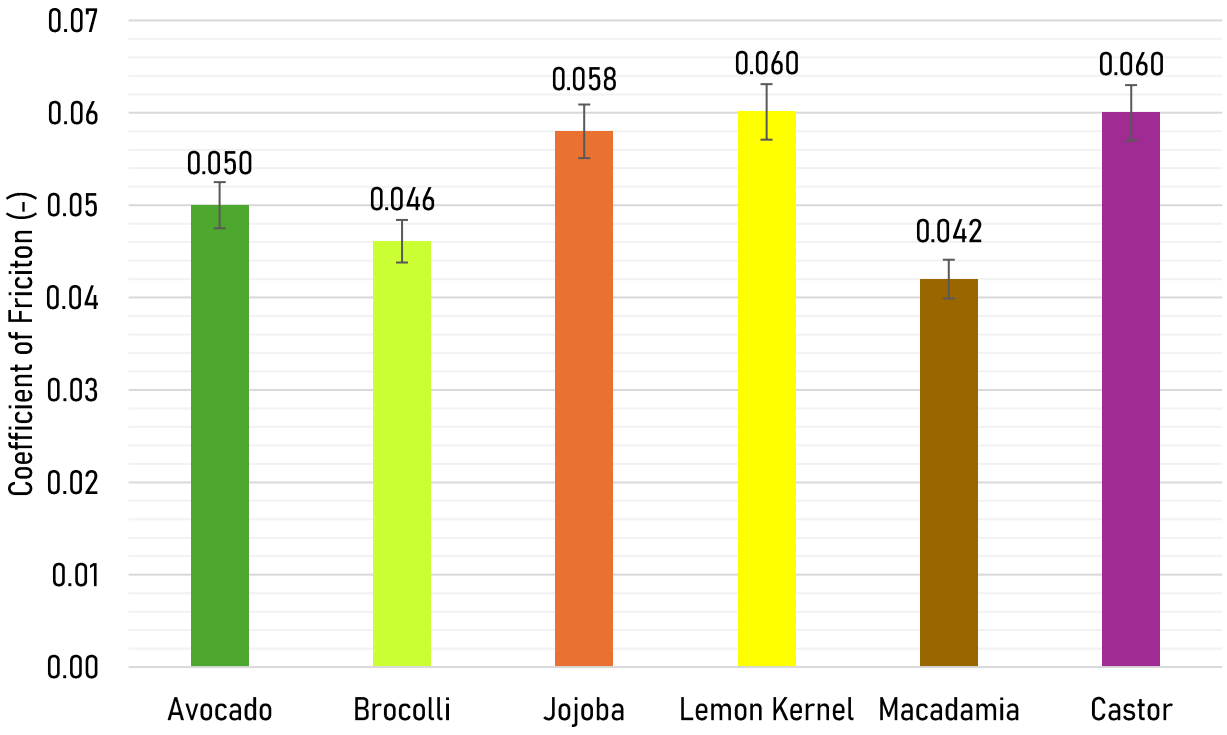


Figure 26. Average coefficients of friction for tested plant oils. Error bars indicate minimum and maximum obtained values.

Although the friction coefficients obtained in this study fall within the commonly reported ranges for plant oil-based lubricants, it is important to compare these values with those published under similar tribological conditions. Under the present HFRR conditions, outlined by ASTM D6079, the measured coefficients of friction ranged from 0.042 to 0.060. Al Sulaimi et al. (2023) reports friction coefficients of 0.08-0.11 for mostly monounsaturated plant oils tested under boundary conditions (10 N load, 1.4 mm stroke, 2 Hz) (53). Reeves et al. (2015), using the same 10 N load and higher sliding velocity of 36 mm/s, reports coefficient of friction values of 0.02-0.10 for mostly monounsaturated plant oils, like avocado, olive and canola oils, and larger values of 0.30-0.50 for mostly polyunsaturated plant oils, like corn and soybean oils (57). Despite methodological differences, which would generally increase friction, the friction coefficients measured in this study lie at the lower end of the reported ranges for monounsaturated plant oils and well below those observed for

polyunsaturated oils. Taken together, these comparisons confirm that the tested plant oils perform in a manner consistent with established trends in the literature and achieve competitive friction levels under boundary lubrication.

To place these friction results in the context of petroleum-based lubricants, a direct comparison can be made with studies that used similar HFRR conditions. Knothe & Steidley (2005), using the ASTM D6079 protocol, which is identical to the testing procedures of present work, but with longer test duration, reported coefficients of friction between 0.112 and 0.528 for fully formulated diesel fuel and their petroleum-derived lubricity components (136). These values are substantially higher than the range of 0.042-0.060, measured for plant oils in present study. Their testing of individual fatty species further confirms this trend: oleic acid – 0.067, triolein – 0.041 and linoleic acid – 0.086 fall around the measured range of friction coefficient values for the tested plant oils (136). Therefore, the unmodified plant oils evaluated in this thesis operate at a lower end of friction values reported for boundary-lubricating organic compounds and far below those of petroleum-based baselines.

Further comparison with fully formulated petroleum lubricants may be drawn from the work of Biresaw (2018), who evaluated petroleum-derived and bio-based polyalphaolefins (PAOs) under boundary lubrication at higher temperature (75°C) and higher load (10 N) (137). Even under these harsher conditions, petroleum-derived PAO exhibited friction coefficients of 0.09-0.39, whereas bio-based PAO performed in the range of 0.08-0.11 (137). Although the operating conditions differ, these values again exceed or match only the very upper bound of the friction coefficients measured for the unmodified plant oils in this study.

Taken together, these comparisons show that all six plant oils tested here deliver frictional performance equal to or substantially better than petroleum-based lubricants under boundary lubrication, despite the absence of chemical modification or additive packages.

Oils with higher contents of monounsaturated fatty acids, like macadamia and avocado oils, are expected to provide balanced boundary films. Their ability to form stable adsorbed layers on metallic surfaces explains the observed low friction coefficients (50). Particularly, the high palmitoleic acid content in macadamia oil combines improved surface adsorption with moderate viscosity, resulting in the lowest coefficient of friction (132,133). Broccoli seed oil also provided a low value of coefficient of friction, consistent with the presence of erucic acid. This long-chain monounsaturated acid allows the formation of thick boundary films while maintaining relatively low shear resistance (53). In contrast, jojoba oil's wax-ester

structure did not match the expected behaviour of triglyceride-based plant oils. Even though, the stronger surface adsorption was promoted by the presence of long-chain fatty acids, the resulting film may be less mobile, resulting in the higher coefficient of friction (53). Castor oil with its ricinoleic fatty acid, does not follow the prediction from Table 3. Its high viscosity supports the formation of a thick lubricating film. This lubricating film separates the contact surfaces but leads to higher friction (7,53). Lemon kernel oil, with a relatively high proportion of polyunsaturated fatty acids produced one of the largest friction coefficients, compared to the other oils. This outcome is consistent with the weaker adsorption and lower film stability, associated with polyunsaturated fatty acids (131).

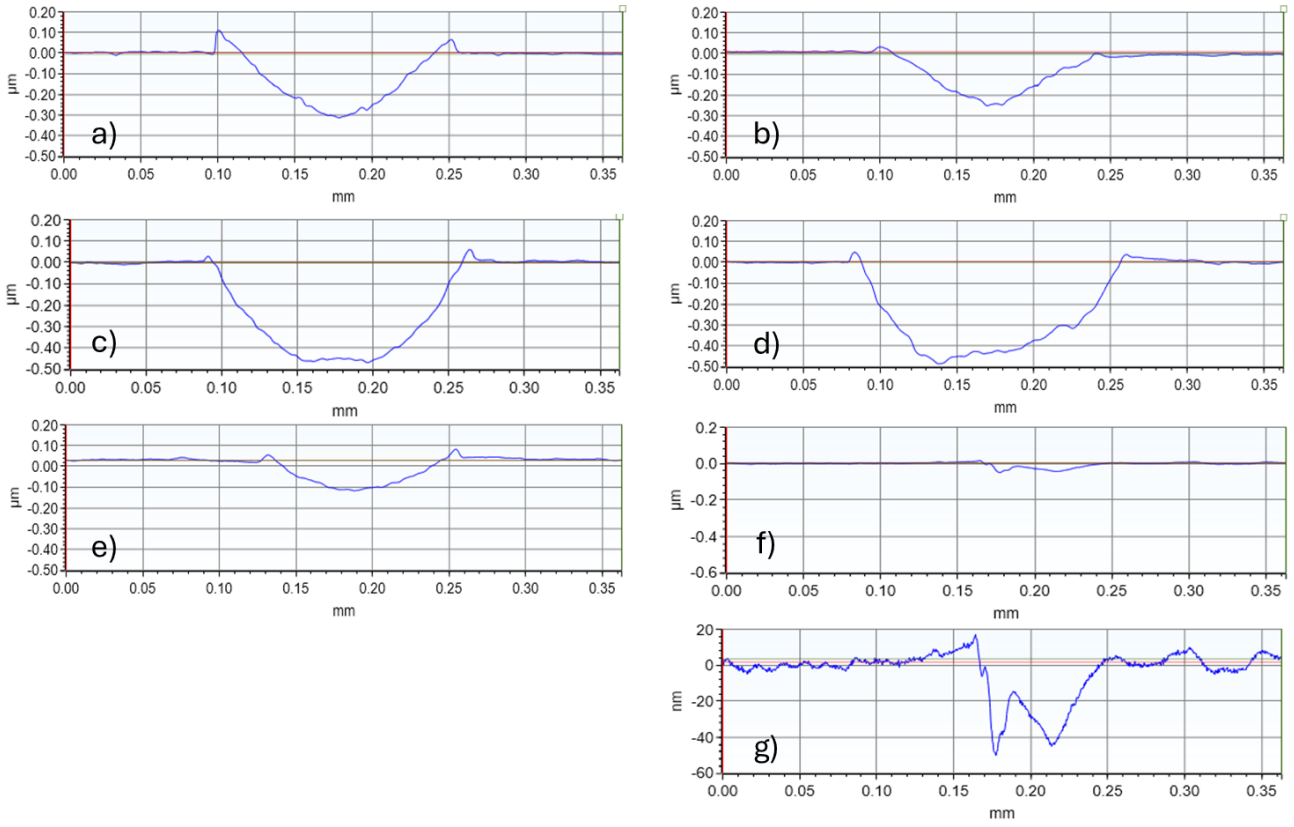


Figure 27. Disk wear scar profiles for a) Avocado, b) Broccoli, c) Jojoba, d) Lemon Kernel, e) Macadamia and f,g) Castor oils. Note height scale for g) is different for clarity.

Figure 27 presents the disk wear scar depth profiles obtained using White-Light interferometer (WLI) for each of the tested plant oils. After 20 minutes of testing, distinct differences in both depth and shape of the scars can be observed. Avocado (Figure 27a) and broccoli seed oil (Figure 27b) produced shallow scars of similar depth and width. Jojoba (Figure 27c) and lemon kernel oils (Figure 27d) resulted in significantly deeper and wider scars, indicating larger material removal. Macadamia oil (Figure 27e) produced a relatively shallow and narrow scar, reflecting good protection against wear. Castor oil (Figure 27f and

Figure 27g) exhibited only minimal wear, with the wear scar barely visible on the disk surface.

Figure 28 shows the corresponding disk wear scar cross-sectional areas measured after the friction tests. Among the tested oils, castor oil exhibited the lowest average disk wear scar cross-sectional area of 1 μm^2, followed by macadamia nut oil with 11 μm^2. The largest wear on the disk was produced by jojoba and lemon kernel oils, reaching 52 μm^2 and 57 μm^2, respectively.

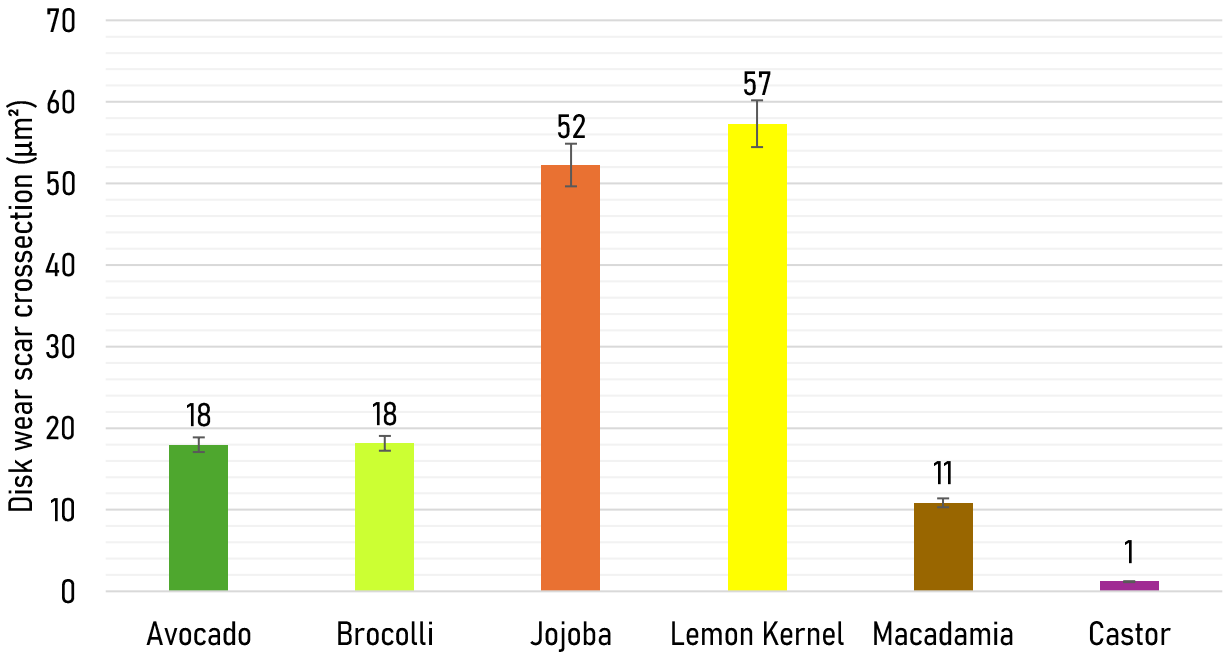


Figure 28. Average disk wear scar cross-sectional values for tested plant oils. Error bars indicate minimum and maximum obtained values.

To enable a more quantitative comparison of wear performance, disk wear coefficient k_{disk} were calculated using the following formula:

$$k_{disk} = \frac{A_{disk} \times s \times H}{P \times L} \qquad \text{(Equation 5)}$$

where A_{disk} is the measured disk wear scar cross-sectional area, H is Brinell hardness of the specimen, s is stroke length, P is the normal load and L is the total sliding distance. These coefficients, provided in Table 5, normalise the wear response to the test conditions, allowing direct comparison between oils and follow the same trends as in Figure 28.

Table 5. Wear coefficients of tested plant oils for disk wear.

Plant Oil	*Avocado*	*Brocolli*	*Jojoba*	*Lemon Kernel*	*Macadamia*	*Castor*
$k_{disk} \times 10^6$ $\left(\frac{mm^3}{Nm}\right)$	9.0	7.1	15.1	17.3	3.7	0.7

Figure 29 shows representative optical images of the ball wear scars after testing with several plant oils. A clear difference in the ball wear scar sizes can be observed. Broccoli oil (Figure 29a) produced a medium-sized oval scar with visible wear marks. Jojoba oil (Figure 29b) produced a larger and darker scar, indicating larger removal of material and strong surface activity. In contrast, castor oil (Figure 29c) produced a very small and shallow scar, barely visible compared to the other ball wear scars. This observation confirms excellent anti-wear performance of castor oil.

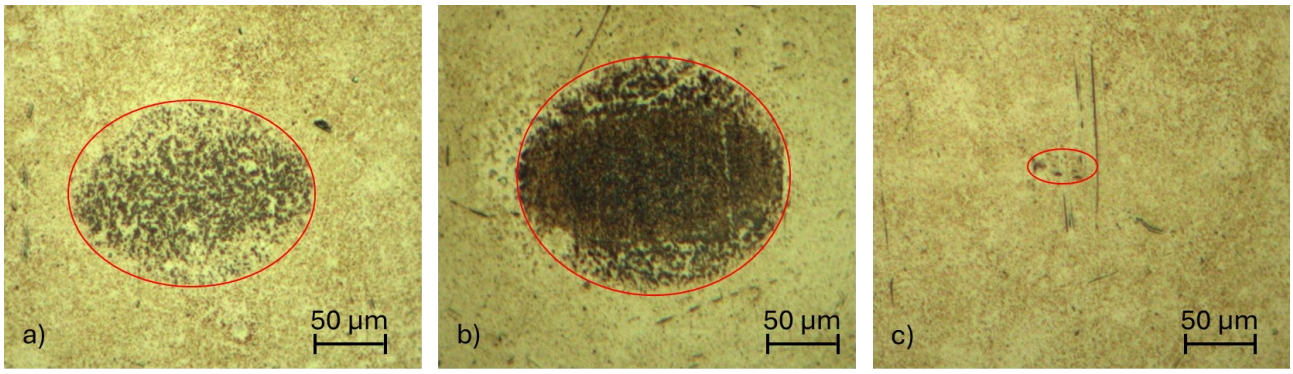


Figure 29. Images of ball wear scars of a) Broccoli, b) Jojoba and c) Castor oils.

The corresponding ball wear scar volumes are shown in Figure 30. As expected, castor oil provided the smallest ball wear scar volume of just 643 µm^3. In contrast, jojoba and lemon kernel oils produced the largest ball wear scars of 14400 µm^3 and 16500 µm^3, respectively. Avocado and broccoli oils showed intermediate wear values of 8600 µm^3 and 6730 µm^3, while macadamia oil exhibited relatively low ball wear scar volume of 3520 µm^3.

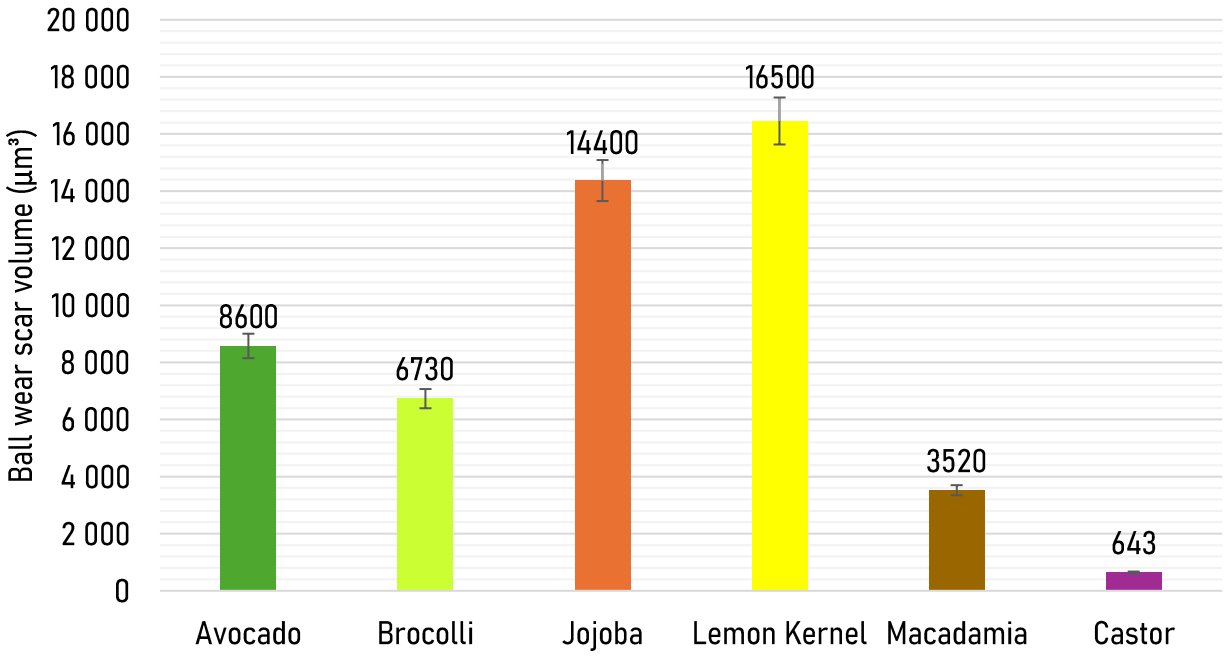


Figure 30. Average ball wear scar volumes for tested plant oils. Error bars indicate minimum and maximum obtained values.

To compliment the disk-wear analysis, ball wear coefficient k_{ball} was calculated from:

$$k_{ball} = \frac{V_{ball} \times H}{P \times L} \quad \text{(Equation 6)}$$

where V_{ball} is the measured ball wear scar volume. The obtained values of ball wear coefficients are provided in Table 6. The observed trends align with those seen in the distribution of ball wear scar volumes in Figure 30.

Table 6. Wear coefficients of tested plant oils for ball wear.

Plant Oil	*Avocado*	*Brocolli*	*Jojoba*	*Lemon Kernel*	*Macadamia*	*Castor*
$k_{ball} \times 10^6$ $\left(\frac{mm^3}{Nm}\right)$	18.6	18.7	54.0	59.2	11.2	1.2

A comparison with literature studies on unmodified plant oil further supports the wear trends observed in present work. Al Sulaimi et al. (2023), using a pin-on-disc configuration under boundary lubrication conditions (10 N, 1.4 mm stroke, 2 Hz), reported the wear rates of $2.5 - 4.0 \times 10^{-9}\ mm^3/Nm$ for several unmodified plant oils, with castor oil exhibiting the lowest value (53). When converting the present ball wear coefficients to ball wear rates, castor oil again shows the lowest value of $2.7 \times 10^{-9}\ mm^3/Nm$, confirming its well-established anti-wear behaviour. In contrast, jojoba oil shows a substantially higher wear rate of $6.1 \times 10^{-8}\ mm^3/Nm$ in the present study, which is an order of magnitude above the values reported by Al Sulaimi et al. (2023). This difference is expected due to the harsher contact conditions in the present work due to higher reciprocating frequency and longer sliding distance per unit time. The observed wear performance: excellent wear protection of castor oil, poor protection for jojoba oil and intermediate performance for other tested plant oils, is consistent with the published behaviour, even though the absolute wear rates vary with the test severity.

Although the wear values obtained in this study cannot be compared directly with petroleum-derived lubricants due to the shorter test duration of 20 minutes rather than the 75 minutes specified in ASTM D6079, ball wear scar diameters measured under identical HFRR geometry and load still allow meaningful qualitative benchmarking. Knothe & Steidley (2005), using the same HFRR configuration and load as in present study, reported ball wear scar diameters of 302-746 μm for petroleum-derived lubricity additives and 153-672 μm for fully formulated diesel fuels (136). In contrast, the unmodified plant oils tested in this thesis produced substantially smaller wear scars, ranging from 79 μm for castor oil to

178 µm for lemon kernel oil with most results falling within the narrow interval of 121-172 µm. Even when acknowledging the shorter test duration, these values lie at or below the lower end of the ranges reported for petroleum-based lubricants. Additionally, Al Sulaimi et al. (2023) reported wear rates of $3 \times 10^{-8}\, mm^3/Nm$ for commercially available PAOs, placing them above the castor wear rate observed in present study and comparable to the other plant oils. Taken together, these comparisons indicate that the tested unmodified plant oils can provide comparable wear performance under boundary lubrication conditions.

While castor oil showed the highest coefficient of friction, exceptional wear protection on both disk and ball surfaces was provided. This matches the expectation, where high viscosity resulted in the formation of thick lubricating film, which effectively shielded the surfaces from direct asperity contact despite relatively higher friction. In contrast macadamia oil, having the lowest coefficient of friction, also demonstrated low wear on both disk and ball specimens. This behaviour aligns with predictions in Table 3 for monounsaturated fatty acids, which provide a balance between viscosity and adsorption.

On the other hand, jojoba and lemon kernel oils showed relatively poor wear protection. For jojoba, Table 4 highlights its wax ester structure, which deviates from typical triglyceride behaviour. This structural difference is potentially crucial for the film formation, as indicated by both higher friction and larger wear values, compared to other tested plant oils. For lemon kernel oil, the dominance of polyunsaturated fatty acids corresponds to the weak adsorption noted in Table 3. These films are more susceptible to rupture, explaining the large wear scars observed on both disk and ball specimens (131). Avocado and broccoli seed oils showed moderate wear performance, consistent with their mixed fatty acid composition. Oleic acid in avocado oils and the long chain erucic acid in broccoli both promoted the formation of stable boundary films, preventing excessive material removal. Taken together, the disk and ball wear results confirm the mechanistic predictions outlined in Table 3: oils dominated by monounsaturated fatty acids, like macadamia and broccoli, provide the most effective wear protection. In contrast, oils with high polyunsaturated content or chemically distinct wax esters perform less effectively.

To summarise, tribological and rheological evaluation of the six plant oils revealed clear differences in their performance. The fatty acid properties, like chain length and saturation, as well as the viscosity are the main factors responsible for the observed tribological performance of plant oils. Among the tested oils, macadamia nut oil provided optimal performance in both friction and wear. Due to its high monounsaturated fatty acid

composition and moderate viscosity, the lowest coefficient of friction and low wear were achieved. Castor oil, while producing higher friction, delivered exceptional wear resistance through its hydroxylated fatty acid structure and high viscosity.

4.5. Optimisation

Building on the tribological performance results of macadamia and castor oils from the previous section, blends of these two oils were tested to determine whether their combined use could optimise both friction reduction and wear protection. Blends were prepared by mixing macadamia and castor oils with macadamia oil concentrations of 10, 25, 40, 50, 60, 75 and 90 wt.%. The mixtures were stirred for 30 minutes at room temperature to obtain visually homogeneous solutions. Consecutively, these blends were tested following the same procedures described in previous section. The tribological performance of blends was compared to the performance of pure macadamia and pure castor oils. Figure 31 presents the results for the coefficient of friction, disk wear scar cross-sectional area, and ball wear scar diameter, respectively, plotted as a function of macadamia oil wt.% fraction.

As shown in Figure 31a, the coefficient of friction decreased with increasing macadamia content, reaching a minimum value of 0.039 at 50 wt.%. At larger concentrations of macadamia oil, the coefficient of friction remained relatively stable in the range of 0.040–0.045. This plateau suggests that the boundary film is formed prevalently by macadamia nut oil. Even small concentrations of macadamia reduced friction compared to pure castor oil. Such an effect is likely due to displacement of less mobile castor oil molecules by more ordered and mobile macadamia oil structures.

The wear results show an opposite trend, highlighting the trade-off between friction and wear in boundary lubrication. As seen in Figure 31 b) and c), both disk and ball wear remained low for blends with less than 50 wt.% of macadamia oil. Above that concentration, wear significantly increased, approaching the levels observed for pure macadamia oil. These findings clearly demonstrate the trade-off between friction and wear within the blends. At low macadamia fractions (0–25 wt.%), the blend maintains castor's excellent wear resistance while slightly reducing friction. At high macadamia fractions (>50 wt.%), the blend achieves the lowest friction but sacrifices wear protection. The optimal performance occurs at 25–50 wt.% macadamia, where both friction and wear are simultaneously minimised. At this composition, the blend combines the strong, protective film of castor oil with the low-shear boundary film of macadamia oil. This study demonstrates that mixing oils with

complementary tribological properties is a practical strategy to tailor lubricant performance to achieve low friction and low wear.

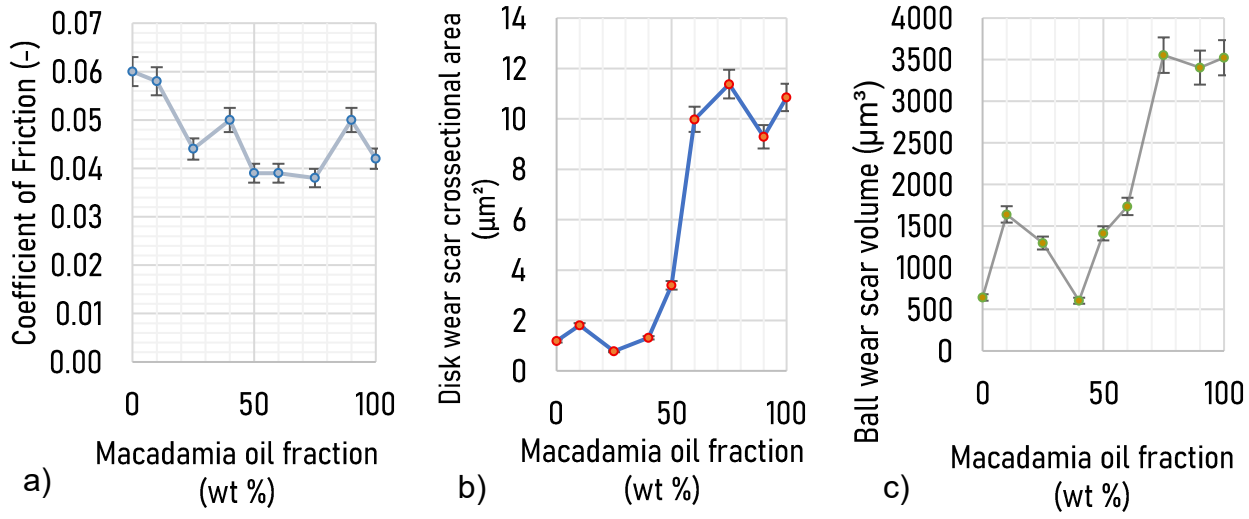


Figure 31. Obtained performance of mixing castor and macadamia oils in a) COFs, b) Disk wear scar cross-sectional areas and c) Ball wear scar volumes.

4.6. Critical Overview

The direct-use approach, as examined in this study, offers distinct advantages for environmentally friendly lubrication in low and moderate duty applications. Its main strengths are simplicity, sustainability, and environmental compatibility. Within the direct-use framework, plant oils represent the most widely available and accessible materials. Their inherent lubricating properties can be applied with minimal processing, avoiding energy-intensive refining and synthesis processes. This can significantly reduce the overall energy consumption and environmental effects of lubricant production. As renewable and biodegradable materials, plant oils impose a much lower environmental impact upon leakage and spillage, compared to mineral oils (72). The chemical composition of plant oils provides certain advantages for tribological performance. For example, plant oils generally exhibit good lubricity, high viscosity indices and high flash points, making them competitive in certain moderate-duty or niche applications (7,50,51,72,124).

However, the historical context and experiments reveal the fundamental limitations of the direct-use approach, particularly when applied to modern machinery operating under high loads, elevated temperatures, and high speeds. While mixing two oils with good tribological performance, as shown in this study, can partially mitigate these issues and improve performance metrics, like friction and wear resistance, the fundamental limitations of triglyceride structures of plant oils remain (138).

These observations suggest that the direct-use approach provides a strong foundation for sustainable tribology. Plant oils can already provide practical solutions in moderate-duty and niche applications, where their simplicity, renewability and biodegradability are most advantageous. To broaden the scope of sustainable lubrication, additional strategies are needed that address conditions beyond the reach of direct-use oils without undermining their strengths. One such strategy is the biomimetic approach, which draws inspiration from nature. By studying the functional mechanisms of biological lubrication systems, biomimetic solutions combine the environmental benefits of natural materials with functionality for low- and mild-duty applications. In this way, biomimetic lubrication complements the direct-use approach: while plant oils offer sustainable solutions in oil-based systems, biomimetic strategies extend these principles to aqueous systems, together creating a complete framework for Green Tribology.

4.7. Conclusions

This chapter examined the direct-use approach to lubrication by reviewing its history, assessing its current relevance, and experimentally evaluating the performance of selected plant oils. The direct-use approach prioritises simplicity, minimal processing, and the use of naturally occurring materials, offering clear sustainability and environmental benefits. However, both historical evidence and experimental results demonstrate that this approach is limited by the structural properties of lubricants. This constrains their functionality in demanding modern applications. Although mixing strategies can improve certain properties, they cannot fully overcome these fundamental limitations. These observations reinforce the need for more advanced approaches that build upon the principles of direct-use approach, while addressing its weaknesses.

Plant oils demonstrate the potential of direct-use lubricants. However, their chemical structure imposes limitations that cannot be fully resolved by mixing. Water shares the same sustainability advantages as plant oils, being abundant, non-toxic and renewable. Yet, water on its own performs poorly as a lubricant. To overcome this, biomimetic strategies have been developed to enhance the tribological performance of water. These strategies extend the principles of direct-use lubrication while offering a pathway towards sustainable and functional aqueous systems. The next chapter therefore turns to water-based lubrication through a biomimetic framework, building on the insights gained from plant oils and expanding them into new environments.

5. Biomimetic Approach in Water-Based Lubrication

A biomimetic approach is explored in this chapter. Its origins and main steps are outlined. A biomimetic approach is applied to improve the water-based lubrication. The novelty of this chapter lies in applying this biomimetic framework to fungal mucilage, which has not previously been studied in a tribological context. The chapter provides details on the choice of useful mushroom species, based on their biological descriptions, availability and presence of beta-glucans. Tribological performance of modelled mucilage is evaluated and used to choose perspective beta-glucans.

5.1. Introduction

Biomimetics entails the study of natural systems, their abstraction into models and their application to solve engineering problems (139). By studying and drawing inspiration from biological structures, processes, and principles, engineers and designers can propose innovative concepts to solve various technological challenges. The adoption of such concepts supports sustainability principles by encouraging the use of renewable resources and minimising environmental impact. Various examples of the use of Biomimetics include bird and insect designs to improve the shape of airplane wings (140), snake-like robots for search and rescue (141), self-cleaning surfaces modelled after lotus leaves (142), building with termite mound-inspired ventilation systems (143), gecko-inspired tapes (144), and shark scale texturing for drag reduction (145). Together these examples represent only a fraction of many bioinspired solutions, highlighting the relevance of biomimetics across engineering.

In the field of Tribology, biomimetics also plays a significant role. Much research has been done on trying to mimic synovial fluid – a natural lubricating solution in the joints (24–26,146,147). Another source of inspiration was found in insect joints, where lipid-based waxes act as boundary lubricants reducing friction in insect joints (148,149).

In 2011 the concept of “Green Tribology” was introduced by Nosonovsky and Bhushan (121). They defined it as “the science and technology of the tribological aspects of ecological balance and environment and biological impacts” (121,122). In addition to this term, 12 principles of Green Tribology were outlined to define the main aspects of the discipline (121,122). The focus of these principles lies in reduction of friction, minimising wear and

reducing environmental effects, like using natural lubrication and sustainable chemistry (121).

One of the principles underlying the concepts of Green Tribology is the use of a Biomimetic approach (121). This involves several steps to get from an understanding of the problem to developing a solution, using existing natural principles. The following steps are defined as key to Biomimetic approach:

1. Define the engineering problem to solve
2. Define the existing limitations causing the problem
3. Find existing natural solutions to the problem overcoming such limitations
4. Explore the principles behind the natural solution's performance
5. Introduce these principles to your problem
6. Optimise the natural principle for the best performance in your problem

In tribology, one of the current challenges is the environmental damage caused by petrochemical lubricants. Mineral oil-based lubricants, while providing excellent lubrication, are derived from finite fossil resources and impose significant ecological hazards (5,150). One of alternatives to mineral oil-based lubricants are water-based lubricants, which avoid biodegradability and toxicity issues of mineral oils and have minimal environmental effect (48). However, water as a lubricant exhibits poor tribological performance under boundary lubrication conditions, leading to increased friction and wear.

In this study the outlined biomimetic methodology was applied to address the environmental issues caused by mineral oil-based lubricants. Water-based lubrication was chosen as a sustainable alternative, offering clear environmental benefits. However, practical use is limited by the poor tribological performance of water. To improve the tribological performance of water, fungi species were explored as a novel source of biological inspiration. Extracts from fresh mushrooms and mushroom powders were obtained and tested using an HFRR setup (PCS Instruments Ltd., United Kingdom). Their tribological performance was evaluated by continuous measurements of friction force and assessment of wear scars after test runs.

5.2. Biomimetic Approach to Water-Based Lubrication

In this study the biomimetic approach was used to identify suitable mushroom species and evaluate their extracts as potential additives for improving water-based lubrication. Mushrooms were chosen because their fruiting bodies often provide a water-based mucilage

(151). This mucilage makes mushroom surface naturally slippery, suggesting a potential lubrication improvement. An example of a fungal mucilage on *Gomphidius Glutinosus* is shown in Figure 32. Following the steps outlined in previous section, the selected mushroom species were identified, and their extracts were tested to assess lubrication performance and investigate the underlying tribological mechanisms of this water-based system.



Figure 32. Slimy Spike (Gomphidius Glutinosus) (152).

5.2.1. Step 1. The Problem

Modern industrial lubricants are typically petrochemically based, composed of carbon-hydrogen bonds. Their tribological performance is excellent, providing low friction and wear prevention under a wide range of conditions. Such lubricants implement mineral oil as a base oil, while additives, like phosphorus, sulphur and other compounds are introduced to further improve their tribological performance. However, mineral oil is a limited natural resource with very poor degradability. Spills, leaks and improper disposal introduce an irreversible ecological damage to the environment (5,150). Given these risks there is a need for alternative environmentally friendly lubricants. Water is a promising alternative, as it is renewable, non-toxic and biodegradable (48).

5.2.2. Step 2. Limitations

The tribological performance of water on its own is not satisfactory. One of main limitations is the low viscosity of water, which prevents the formation of sufficiently thick lubricating films (48,153). As a result, contact surfaces are more likely to experience direct asperity contact and are in the boundary regime, leading to increased friction and wear in the contact.

The other major limitation is corrosion, which limits the choice of materials in the contact (44,48,153). Solutions described in literature depend on the use of additives to the water to improve its performance. Examples include amines to supress foaming and corrosion, glycols to control friction (154), and metal nanoparticles to control wear (153). However, many of these additives are petrochemically derived or non-biodegradable, which conflicts with the principles of environmentally friendly lubrication. This is specifically important for loss-systems, where the lubricant is lost to the environment during operation and its replenishment is needed, like chainsaw oils, hydraulic oils for agricultural equipment (4,7,9). Another critical area is submerged systems, where lubricants can leak directly to the environment during operation (4,9).

5.2.3. Step 3. Natural Solutions

In many natural systems, water is the main source of lubrication. However, pure water is almost never used, and various natural additives, like polysaccharides and proteins, are employed to improve tribological performance. For example, in animal and human joints synovial fluid is present. Synovial fluid contains hyaluronic acid (high molecular weight polysaccharide) and lubricin (glycoprotein), which together form two types of films on cartilage surfaces: boundary film and full film. The full film is sometimes called separating film (24–26,146,147). The formation of these films results in extremely low coefficients of friction (around 0.03) and minimal wear even under high loads, due to a combination of several mechanisms: hydration lubrication, increased viscosity and formation of a protective layer on the articulating surfaces (38,39,155,156).

While in joints' lubrication it is a primary function, in plants and algae the production of mucilage helps to retain water, prevent early seedling and drought stress (157–159). Mucilage is a slimy hydrated material rich in polysaccharides (151,160). A friction reduction is achieved by mucilage through one of two strategies: either by creating adsorbed surface layers or acting as high viscosity lubricant (161,162). Similar lubrication mechanisms were observed in aqueous solutions of polysaccharides derived from plants, algae and bacteria. Examples include pectin from plants, carrageenan from algae, and gellan gum from bacteria. Polysaccharides form hydrated networks, which provide increased viscosity and soft hydrated layers, reducing friction and wear (27,28,163,164). Polysaccharides have been widely explored in the development of hydrogels, where their ability to form 3D networks is used to create soft elastic materials with high water content (75,165). A detailed investigation of mechanical and tribological performance of chosen polysaccharide hydrogels with ion

doping is presented in Chapter 7. The main applications of hydrogels involve lubricious coatings or bulk materials for biomedical applications (77,166,167). Even at concentrations lower than 1% these polysaccharides increase solution viscosity and can produce stable boundary films, typically 5-40 nm thick, which reduce friction and wear (27,164).

A similar mucilage phenomenon, seen in plants and algae, is also observed in fungi: mushrooms often become slippery when wetted. Certain species produce mucilage either natively or upon contact with water. In fungi mucilage prevents desiccation and protects reproductive structures (168). Although not all fungal species show such behaviour, the slimy nature of fungal mucilage makes it a promising biomimetic model for aqueous lubrication.

5.2.4. Step 4. Exploration

To identify potentially interesting fungal species, descriptions of mushrooms from Phillips et al. (1981) and Jordan (2006) were used (169,170). The species that contained descriptions like ‘slimy’, ‘sticky’, ‘viscid’ and ‘glutinous’ were noted down, as these terms indicate the presence of mucilage. The obtained species were combined into respective genera, and the summary is shown in Table 7. It is evident that the order *Agaricales* contains many species with desired behaviour. A significant number of these mushroom species are widely produced worldwide. The most industrially produced genera in recent years are highlighted in orange in Table 7 (171,172). Most of them have been widely used in the pharmaceutical industry and as a food source (171,172).

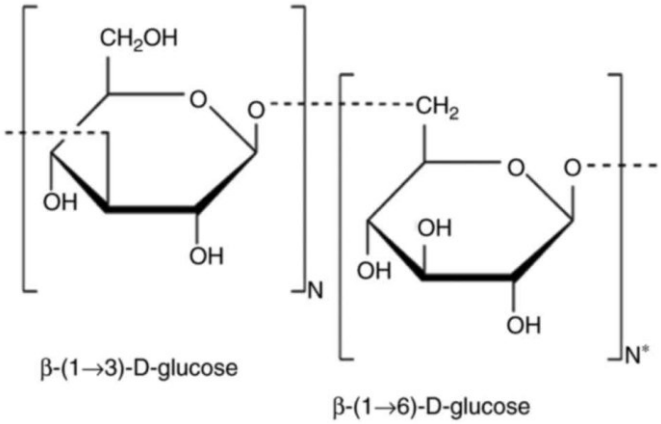


Figure 33. Schematic representation of the basic molecular structure of glucan molecule. N and N represent the number of specific repetitions of each structure (173).*

The fungal mucilage is attributed to the presence of β-glucans and proteins in fungal cell walls (174,175). β-glucans are complex polysaccharides composed of repeating blocks of glucose rings, shown in Figure 33 (82). Most scientifically identified β-glucans are utilised in various medicinal applications, due to having immuno-regulatory, antibacterial and antiviral

effects, as well as influencing cholesterol, blood pressure and diabetes (80,82,176). Due to their gelling capacity and ability to increase viscosity of aqueous solutions, β-glucans from plants are used as stabilisers and thickeners in the dairy industry, as fat replacement in meat products and as texture modifiers in solid, semi-solid and liquid foods, like noodles, yogurts and milk drinks (80,83,84,177–180). Their application in lubrication is not entirely novel. Kripp et al. (2015) patented the use of a maximum 10% w/w β-glucans in base oils, optionally with addition of water, to reduce the friction coefficient (181). However, the use of fungal β-glucans in water-based lubrication has not been reported in scientific literature, where their role has been mainly explored in medicinal applications (81,182,183).

Table 7. Cladogram of identified mushroom genera.

Order	Family	Genus
Agaricales	Amanitaceae	Amanita
	Cortinariaceae	Cortinarius
	Hygrophoraceae	Hygrocybe
		Hygrophorus
	Hymenogastraceae	Hebeloma
	Omphalotaceae	Lentinula
	Physalacriaceae	Flammulina
		Oudemansiella
	Pluteaceae	Volvariella
	Strophariaceae	Agrocybe
		Pholiota
	Tricholomataceae	Tricholoma
Boletales	Boletaceae	Boletus
	Gomphidiaceae	Chroogomphus
		Gomphidius
	Suillaceae	Suillus
Phallales	Phallaceae	Phallus
Polyporales	Irpicaceae	Meruliopsis
Russulales	Russulaceae	Lactarius
		Russula

To explore the tribological performance of the fungal mucilage, two widely cultivated species were chosen: Shiitake (*Lentinula edodes)* and Enoki (*Flammulina velutipes*). These species were chosen because their respective genera exhibit the desired mucilage production, as highlighted in Table 7, and due to their worldwide cultivation, ensuring industrial availability (183–186). Furthermore, both species are known for their β-glucans, as bioactive compounds, which are extensively used in food and health industries, as anti-inflammatory, immune-modulatory and anti-cancer treatments (82,176).

5.2.5. Summary of Biomimetic Phase

In this study a biomimetic approach was applied following the proposed methodology. In Step 1 the problem was identified: the environmental impact of mineral oil-based lubricants. As a sustainable alternative, water-based lubricants were proposed. Step 2 identified the limitations of water as a base lubricant, including poor tribological performance, low viscosity and corrosion. This highlights the need for additives to achieve acceptable performance. Drawing inspiration from natural systems, Step 3 focused on naturally occurring compounds improving lubricating properties of water. In both animals and plants, polysaccharide-rich compounds were identified as key in reducing friction and wear. Fungal mucilage present on fruiting bodies of certain mushroom species was identified as a promising biomimetic model. In Step 4 a review of literature was presented and descriptions of fungal species identified fungal genera exhibiting mucilage-producing characteristics.

β-glucans were recognised as the main components of fungal mucilage and were hypothesised to be essential for improving water tribological performance. Two widely cultivated mushrooms Shiitake (*Lentinula edodes*) and Enoki (*Flammulina velutipes*) were selected for the next steps due to their availability, known mucilage production, and high β-glucan content. This selection completes the biomimetic phase of the study. The next step involves preparation of fungal mucilage and evaluation of its tribological performance. The aim of this step is to understand whether the mechanisms of fungal mucilage can improve the frictional performance of water.

5.2.6. Step 5. Evaluation of Principle

To evaluate the frictional performance of mushroom mucilage, two approaches in mucilage preparation were implemented: using fresh mushrooms and using commercially available mushroom powders. The use of both sources allows a comparison between natural extract and a more standardised, reproducible material.

5.2.6.1. Materials

Fresh mushrooms: shiitake (*Lentinula edodes)* and enoki (*Flammulina velutipes*) were obtained from Merit Mushrooms (Prodac Ltd, UK). The polysaccharide powders of shiitake and enoki were provided by The Shroom Shop (Prodac Ltd, UK).

5.2.6.2. Mushroom Extract Preparation

For the fresh mushrooms, extraction was done by soaking 150 g of fresh full-sized mushrooms in 300 ml of deionised water from a Milli-Q purification system (Millipore, Canada) at room temperature for 1 hour. The extract was obtained by compressing the soaked mushrooms for 30 minutes between two clean glass petri dishes by putting weights on the dishes, resulting in an applied pressure of 7 kPa. The collected extract was filtered using 70 mm diameter KA1 filter paper (Whatman plc.) with a pore size of 7 µm to remove solid residue and large particulates.

Although conventional extraction methods for fungal polysaccharides involve elevated temperatures to increase yield, a room-temperature extraction was chosen to avoid denaturation of proteins, which would affect the mucilage properties (80,176,187,188). However, this approach inevitably results in a lower and more variable yield of extractable biopolymers. The composition and concentration of the extract also vary as fresh mushrooms are a natural product with biological variability (water content, maturity, protein content and polysaccharide distribution), and the extraction process amplifies these differences. Consequently, repeatability between batches is limited.

5.2.6.3. Mushroom Powder Solutions' Preparation

To overcome the extraction limitations and to improve the repeatability and quality of the samples, water solutions using commercially available mushroom powders were produced. These powders have a polysaccharide content of 30% and provide a controlled and consistent base material. Test lubricants were made by dissolving powder from shiitake and enoki, respectively, in deionised water at a concentration of 1 wt.%, based on previous lubrication studies on polysaccharides implementing concentrations in the range of 0.5-5% (29) and around 1% (27). At lower concentrations (<0.5 wt.%) the lubrication performance of polysaccharide solutions is typically limited by insufficient surface coverage and weak boundary film formation (29). Higher concentrations (>2 wt.%) can significantly increase viscosity, which affects tribological performance (29). A concentration of 1 wt.% was chosen as an optimal compromise between film-forming capability and solution viscosity. To prepare a 1 wt.% solution 0.1 g of respective powder was added to 10 g of deionised water. The

mixture was stirred for 30 minutes at room temperature to ensure complete dispersion and a visually homogeneous solution.

5.2.6.4. Tribological Testing

The tribological performance of the obtained solutions was evaluated using a High Frequency Reciprocating Rig (HFRR) under a constant load of 1 N at room temperature and a mean sliding speed of 0.02 mm/s, resulting in a maximum Hertz contact pressure of 289 MPa. AISI 304 stainless steel specimens were used to minimise corrosion effects, which would otherwise occur rapidly with standard steel in aqueous solutions. Using the Dowson and Hamrock equation, provided in Equation 1, the minimum film thickness of water at 20°C is predicted to be 0.71 nm, which is much smaller than the surface roughness of the test specimens. This confirms that during tribological testing the contact is always in the boundary lubrication regime. Full details of the tribological test are provided in section 3.1.1 on page 41.

5.2.6.5. Results

Figure 34 shows the time-dependent coefficient of friction of the tested lubricants for the duration of the friction test. For deionised water a continuous rise in coefficient of friction is observed for the duration of the test, starting from an initial value of 0.30 and reaching a final value of 0.44.

A different time-dependent behaviour compared to water was observed for mushroom extracts. Both shiitake and enoki extracts showed a sharp initial increase in coefficient of friction, followed by a drop value and subsequently a gradual rise till the end of the test. Both extracts performed similarly with the only difference being the time required for the coefficient of friction to stabilise after the initial peak. Shiitake extract's coefficient of friction settled within 25 seconds from the test start, while enoki extract required a longer time of around 60 seconds. No further significant differences between the two extracts were observed in their frictional behaviour.

In comparison, the tested powder solutions show a clear difference in behaviour between the species. The shiitake powder solution (yellow line) showed similar time evolution to the shiitake extract (brown line), including the initial rise followed by stabilisation of the coefficient of friction. However, the peak coefficient of friction value was reduced from 0.30 for extract to 0.22, and the settling time was much shorter, with coefficient of friction stabilising in less than 10 seconds. In contrast, the enoki powder solution behaved more like

deionised water with a continuous rise in coefficient of friction for the whole duration of the test. However, the magnitude of the increase was smaller, ranging from 0.26 to 0.30.

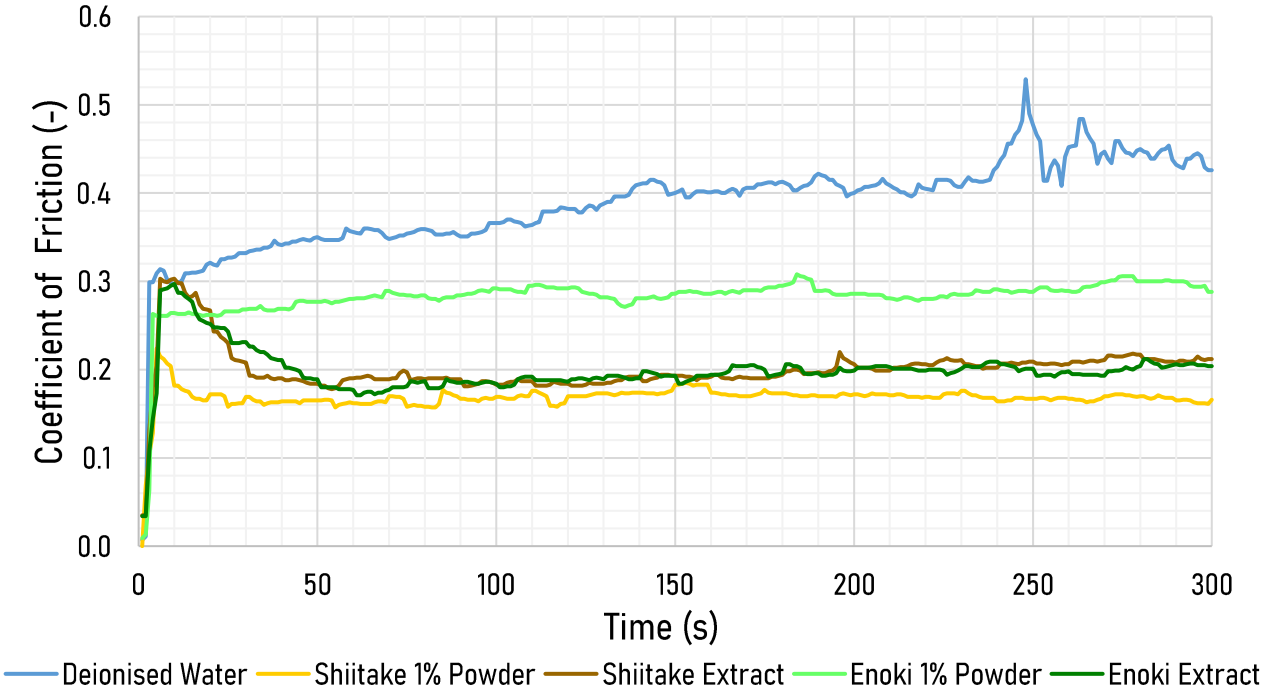


Figure 34. Obtained coefficients of friction during the friction tests.

The observed time-dependent coefficient of friction trends could be linked to the formation of a boundary film at the sliding interface. The initial rise in coefficient of friction occurs prior to the development of any stable lubricating layer and in the absence of polysaccharides the rise continues throughout the test, as seen with deionised water.

Figure 35 shows the average coefficients of friction (COF) obtained for deionised water and the mushroom-derived lubricants, prepared as fresh extracts and 1% powder solutions. Each provided value represents the average of three repeats, and error bars indicate minimum and maximum obtained values.

For water, the coefficient of friction is 0.36. Both shiitake and enoki extracts reduced the coefficient of friction to 0.21, demonstrating that fungal extracts can effectively lower friction compared to pure water. 1% powder solutions for both species also reduced the coefficient of friction relative to water. However, a clear difference between Shiitake and Enoki species was observed. The shiitake 1% powder solution achieved the lowest coefficient of friction of 0.19, while enoki 1% powder solution showed a higher coefficient of friction value of 0.28. Comparing the results of extracts and powders for each of the fungal species, opposite trends are seen. For shiitake, the powder solution showed a lower coefficient of friction than the extract, while for enoki, the extract showed a lower coefficient of friction.

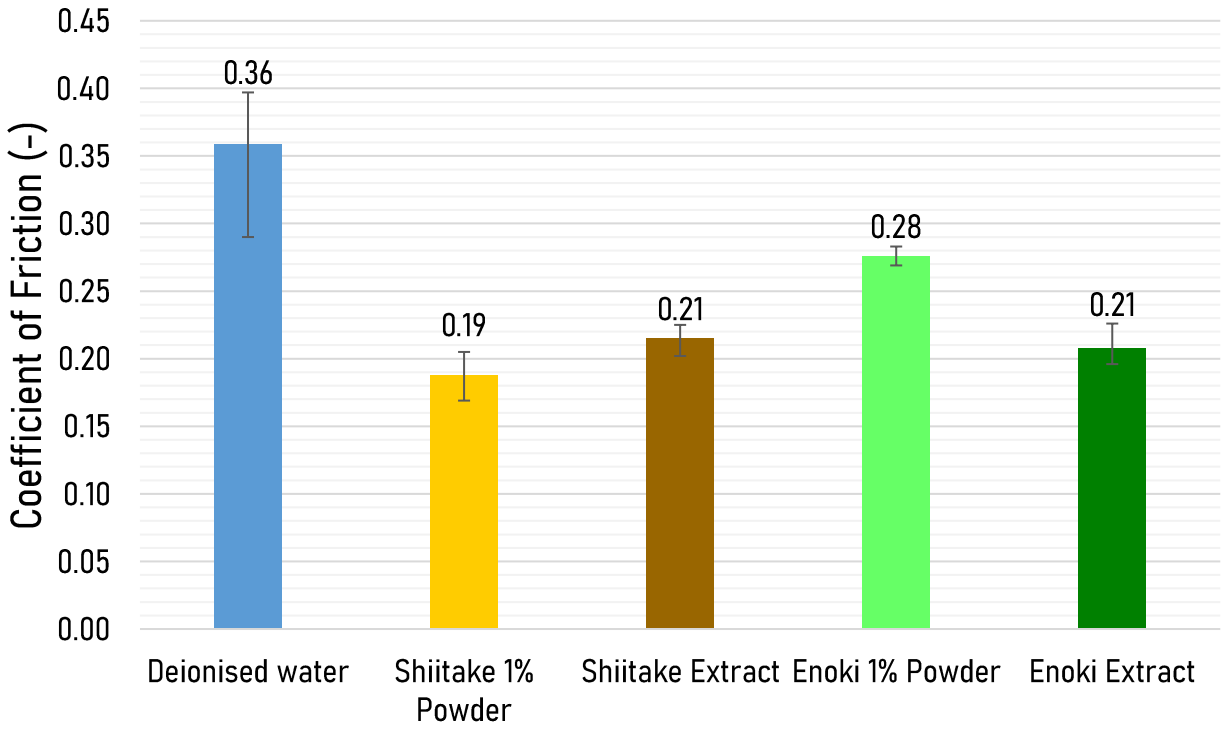


Figure 35.Obtained coefficients of friction for deionised water and tested mushroom solutions. Error bars indicate minimum and maximum obtained values.

The difference between performance of the powder solutions could be attributed to the variations in the structure, composition or molecular weight of β-glucans and other bioactive components, such as polysaccharides and proteins. Studies of plant and algal polysaccharides in aqueous solutions have identified that higher concentration of polysaccharides in water increases viscosity and promotes the formation of more stable boundary films (27–29). This trend could explain the observed frictional behaviour of shiitake-based solutions. The shorter settling time and lower peak coefficient of friction of powder solution, compared to the extract, suggest better adsorption and formation of a boundary film. In contrast, enoki powder solution did not exhibit the same pattern, displaying a water-like frictional behaviour with only a modest reduction in the coefficient of friction. This may indicate that β-glucans and polysaccharides in Enoki either do not form a stable boundary film or interact differently with the contact surfaces with the observed reduction of friction.

5.3. Conclusions

In this study a structured biomimetic approach was applied to improve the frictional performance of water-based lubrication by drawing inspiration from natural fungal mucilage. Two widely available fungal species: Shiitake (*Lentinula Edodes)* and Enoki (*Flammulina velutipes),* were selected based on their mucilage-producing behaviour and accessibility.

A clear reduction in friction compared to pure water was achieved by all tested fungal-derived lubricants, confirming that fungal β-glucans, like other polysaccharides, can form boundary films at the interface. The time-dependent friction data further support this mechanism, showing film development after an initial running-in phase. The differences between shiitake and enoki powder solutions and their corresponding extracts indicate the influence of species-specific properties on boundary film formation, however the specific effect of concentration of polysaccharides could not be fully determined within this study.

These findings demonstrate the potential of fungal β-glucans for use as renewable and environmentally friendly additives for water-based lubrication. Such bio-derived lubricants align with the principles of Green Tribology, offering sustainability and achieving significant frictional reduction. However, the dependence on species and effects of concentration require further investigation and optimisation before implementing in practical applications.

Overall, this work introduces fungal mucilage as a novel and promising biomimetic pathway to improve water-based lubrication by introducing naturally occurring polysaccharides. Chapter 6 builds on the outcomes of this work by examining pure polysaccharide solutions, specifically Lentinan from Shiitake mushrooms. By comparing lentinan solutions, the next chapter provides a detailed evaluation of concentration and particle size effects on tribological performance of water-based solutions.

6. Water-Based Lubricants from Mushrooms

Based on the findings from the previous chapter, the use of the mushroom-based substances in water lubrication is further investigated. The chosen mushrooms species, outlined earlier, were used to obtain mushroom-based solutions. The tribological performance of the tested solutions highlighted the substantial changes in the tribological contact, which are described in this chapter. The novelty of this chapter lies in providing the first systematic tribological assessment of fungal β-glucans in water lubrication, including the effect of concentration and particle size on both friction and wear. These phenomena were further explored and criteria for the performance with least wear and smallest friction were outlined.

6.1. Introduction

There is a need for an environmentally friendly lubricant, as an alternative to petroleum-based ones, which are finite and harmful for the environment. Water is a cheap and safe base, both environmentally and operationally, for a functional lubricant. However, pure water has poor tribological performance and to enhance it additives are required (153).

Currently the focus in introducing water-based lubrication lies in optimising water-oil emulsions and implementing various petroleum-based additives (153,189,190). Alternatively, use of nanoparticles from metal oxides or ceramics is considered (32,191). These approaches, while improving the tribological performance, introduce pollutants and cannot meet sustainability requirements (153). In order to resolve environmental issues, while still improving tribological performance of water, addition of biomolecules is considered (47,153,154).

Water-based lubrication is prevalent in natural lubricated systems, like animal or human joints. Various additives are utilised to improve the tribological performance of water, an example being proteins found in human synovial fluid. Protein aggregation on metal surfaces provides an adsorbed layer, which improves the frictional performance of synovial fluid (24–26,156).

Nature has alternative ways to change the tribological performance of water. Fungi and plants have developed similar strategies to produce mucilage to prevent early seedling development and drought stress (157). Fungal mucilage is either present naturally on the mushroom surface or is produced upon contact with water. For example, Enoki mushroom

(*Flammulina velutipes*) is described as having smooth and slimy surface (169,170), but Poria (*Poria cocos)* has dry surface (192). The fungal mucilage is associated with the presence of β-glucans and proteins in fungal cell walls (174,175). β-glucans are complex polysaccharides composed of repeating blocks of glucose rings, as shown in Figure 33 (82). It is hypothesised that the presence of pure β-glucans instead of the fungal extracts can improve the tribological performance of the water-based lubricant by reducing friction and wear.

In this study the effect of 3 mushroom species on the tribological performance of water is evaluated. Shiitake (*Lentinula edodes*), Enoki (*Flammulina velutipes*) and Poria (*Poria cocos*) were chosen for this study due to their use in pharmaceutical industry and being highly cultivated mushrooms worldwide (172,193). Shiitake and Enoki were discussed in the previous chapter. In this chapter Poria has been included as, unlike Shiitake and Enoki, it produces a structurally distinct β-glucan (Pachyman) that is water-insoluble. This allows assessing whether differences in β-glucan solubility influence lubrication performance, providing a broader comparison across fungal polysaccharide types. The main point of interest for these mushrooms are their β-glucans. Shiitake and Poria mushrooms produce well-defined β-glucans, water-soluble Lentinan and non-soluble Pachyman, respectively. Enoki mushrooms contain a wide range of β-glucans, that have not been individually isolated yet. Due to these implications, this study focuses on the use of Lentinan, β-1,3 beta-glucan with a high molecular weight of 400-800 kDa, and powdered extracts from the chosen mushrooms to improve the lubrication performance of water (194).

This research investigates the potential of fungal-based lubricants in improving tribological performance of water. Lubricants were made from powdered mushroom extracts and from pure lentinan. The tribological performance of obtained lubricants was assessed using a laboratory scaled-tribometer (HFRR, PCS Instruments). To further characterise the lubricants their viscosity and particle size distributions were evaluated. It is hypothesised that pure β-glucans improve tribological performance of water by forming an adsorbed layer, like polysaccharides from plant and algal sources, or through physical action of introduced organic particles.

6.2. Lubricant Preparation and Characterisation

Lubricants from three different mushroom species were characterised using rheology and particle size analysis. Their tribological behaviour was evaluated using a friction test by

measuring a friction force during the test and assessing wear on specimens after the test. The mushroom powders used in this experiment are commercially available food supplements containing a range of components naturally present in the respective mushrooms. The pure β-glucan solution was produced by mixing the pure powdered β-glucan with deionised water. The concentration of the solutions was chosen to minimise the viscosity differences compared to pure deionised water, thus ensuring that the observed tribological effects are not attributed to the viscosity effects. To achieve that, a 1 wt.% concentration was used to produce the solutions, which corresponds with the reported concentrations of 0.5-5 wt.% from the studies of plant and algal polysaccharide aqueous solutions (27,29). A 0.1 wt.% Lentinan solution was also tested to evaluate the effectiveness of smaller amounts of pure β-glucan.

The tribological performance of the fungal-based water solutions was compared to the performance of pure deionised water, hexadecane and 30% bovine serum solution. Deionised water was chosen as the base fluid without any modifications. A well-characterised hydrocarbon Hexadecane was chosen as a model low friction performance lubricant, allowing comparison with oil-based systems. The 30% bovine serum solution was included as a biomimetic benchmark. Its common use in biotribological testing allows comparison with the other bio-based lubricant solutions. Overall, this work provides insight in use of fungal-derived solutions as water-based lubricants and a new application of fungi.

6.2.1. Materials

Polysaccharide powders of shiitake, enoki and poria cocos were obtained from The Shroom Shop (Prodac Ltd, UK). Pure polysaccharide Lentinan (FL33321) was provided by Biosynth (Slovakia). Its molecular structure is shown in Figure 36. Pure deionised water was obtained from a Milli-Q purification system (Millipore, Canada). Hexadecane (99% purity, 296317) was obtained from Sigma Aldrich, UK and was used as supplied. Bovine calf serum (SH30073) was obtained from Hyclone Laboratories Inc, USA and was stored frozen. Prior to use it was defrosted to room temperature.

6.2.2. Fungal Solutions Preparation

Mushroom-based solutions were prepared by dissolving the appropriate amount of powder in deionised water. To prepare a 1 wt.% solution 0.1 g of respective powder was added to 10 g of deionised water. A 0.1 wt.% wt. Lentinan solution was obtained by adding 0.01 g of

Lentinan to 10 g of pure deionised water. The mixtures were stirred for 30 minutes at room temperature to ensure complete dispersion and a visually homogeneous solution.

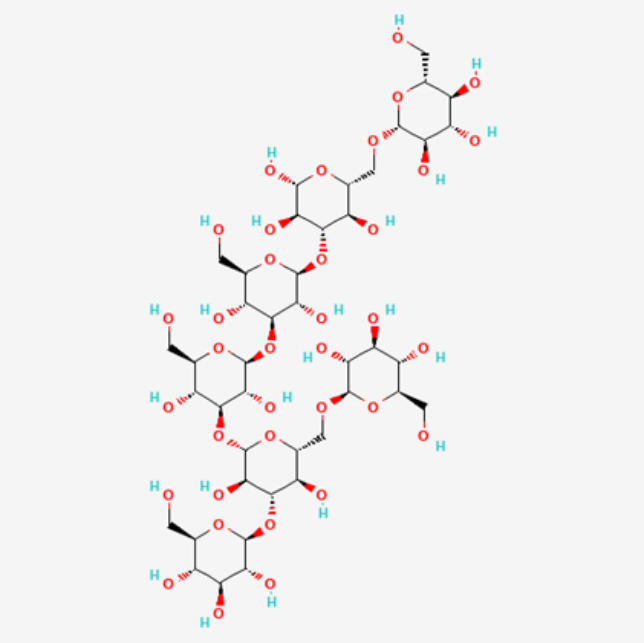


Figure 36. Structure of Lentinan (195).

6.2.3. Lubricant Characterisation

6.2.3.1. Viscosity

The dynamic viscosity of fungal-based solutions was measured using the parallel plate rheology method, described in Section 3.2, at a constant shear rate of 100 s-1 and at 25°C. Figure 37 presents the results, where dynamic viscosities of deionised water and fungal-based solutions are compared.

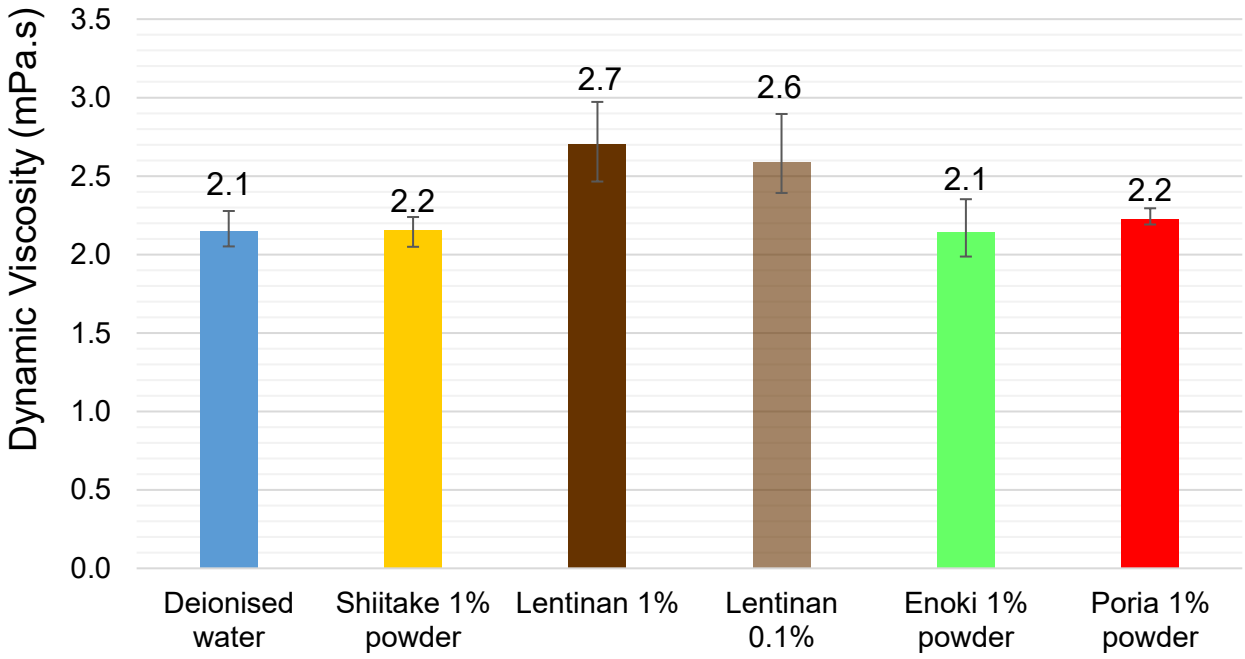


Figure 37.Dynamic viscosities of tested fungal-based water lubricants.

The obtained dynamic viscosity of deionised water is higher than the commonly cited value of 1 mPas. Such effect is consistent with observations of Dakhil and Wierschem (2014), who reported a water dynamic viscosity of 3.5 mPas at a 1 mm gap size and shear rate of 100 s- 1 (196). The lower value of 2.1 mPas, obtained in this study, is attributed to the difference in the used plate diameters. In this study a 40 mm diameter plate was used instead of 50 mm diameter plate in Dakhil and Wierschem (2014) study (196).

Most mushroom solutions exhibited similar viscosities to the pure deionised water. Notably, only lentinan solutions showed slightly higher viscosities of 2.6-2.7 mPas. These results confirm that the chosen concentrations of mushroom powders and of β-glucan maintained the viscosity within a close range of deionised water baseline, thus minimising the effect of viscosity on tribological performance.

6.2.3.2. Particle Sizes

Dynamic Light Scattering (DLS) was used to evaluate the size distribution of particles in the tested solutions, following the procedure described in Section 3.4 on page 51. The obtained intensity-weighted distributions of particle sizes are shown in Figure 38.

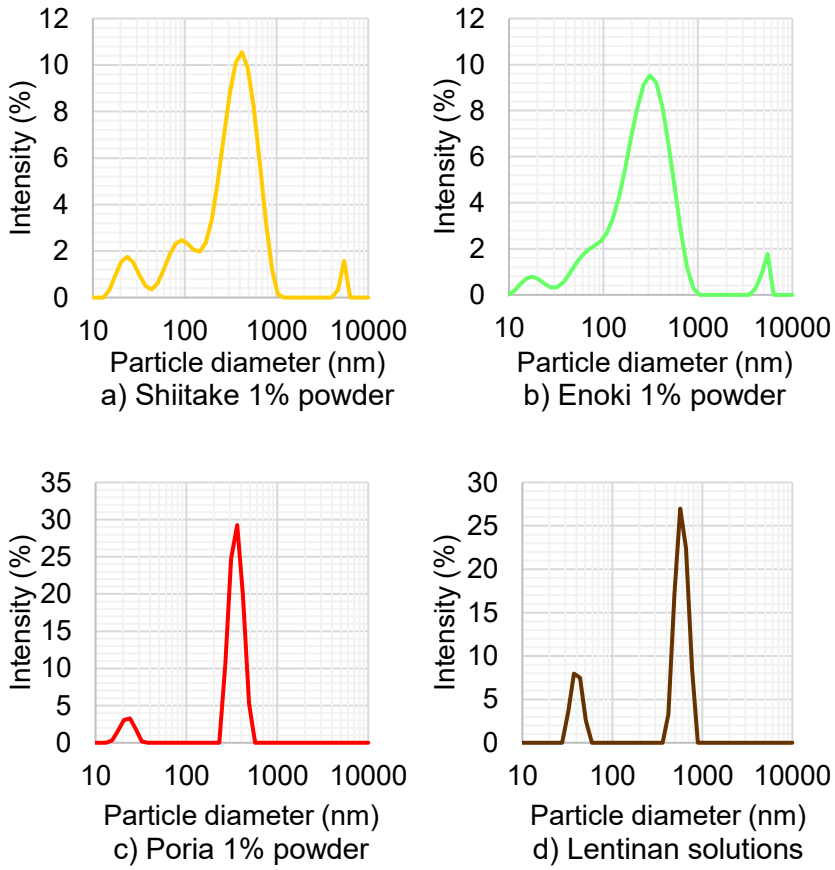


Figure 38. Obtained DLS intensity graphs of tested water-based lubricants.

For all samples, the DLS results indicate the presence of particles in a region up to 1 micron diameter. Shiitake and Enoki powder solutions show broad distributions with small populations below 30 nm, intermediate peaks at ≈100 nm and significant peaks around ≈200-500 nm. Poria powder solution exhibits a sharper peak at ≈300-400 nm, suggesting a more uniform distribution. Lentinan solutions showed same distributions at both concentrations with two distinct peaks at ≈50 nm and ≈500 nm.

These observations confirm that mushroom-derived solutions contain stable suspensions of particles and aggregates, which can contribute to lubrication performance by forming boundary films or acting as rolling elements in the contact (197).

6.3. Results

In this section, the outcomes of the tribological testing are presented and the comparison of both frictional and wear performance of the tested fungal-based solutions to the performance of three benchmarks is made. The chosen benchmarks are pure deionised water, hexadecane and 30% bovine serum solution. All tests were carried out using the High Frequency Reciprocating Rig (HFRR) under the same conditions as in previous chapter. The full description of test procedure and test parameters is provided in section 3.1.1 on page 41. To minimise corrosion effects, specimens from AISI 304 stainless steel were used. The applied test parameters were a constant load of 1 N, a frequency of 10 Hz and a stroke length of 1 mm. These conditions ensure operation within the boundary regime for aqueous systems, allowing direct comparison across all tested lubricants.

6.3.1. Tribological Performance

6.3.1.1. Coefficient of Friction

In Figure 39 the obtained time distributions of coefficient of friction (COF) for the chosen benchmarks and some test solutions are shown. Deionised water showed a steady rise of coefficient of friction during the whole test. Such behaviour is consistent with the lack of boundary film formation in water. In contrast, bovine serum almost immediately reached a stable coefficient of friction, which was maintained over the entire test duration. This behaviour is consistent with the described mechanisms of adsorbed film layer, reducing friction (24–26). Hexadecane showed an initial rise in coefficient of friction, followed by gradual decline until its minimum value, which remained stable for the rest of the test duration. This behaviour is indicative of the boundary film formation during running-in, followed by the stabilised lubrication conditions (100).

Among the fungal-based solutions, most of the tested species followed similar distributions as Hexadecane, as seen for Shiitake 1% powder and Lentinan 1% powder solutions. In fungal-derived solutions time to reach stable film region is much lower. These observations suggest that fungal-based solutions allow relatively quick formation of boundary layers in the contacts, stabilising the friction. However, Enoki 1% solution could not form a stable boundary layer, as seen in friction behaviour similar to deionised water with a reduced value of coefficient of friction. This highlights that individual mushroom-dependent composition influences the film formation.

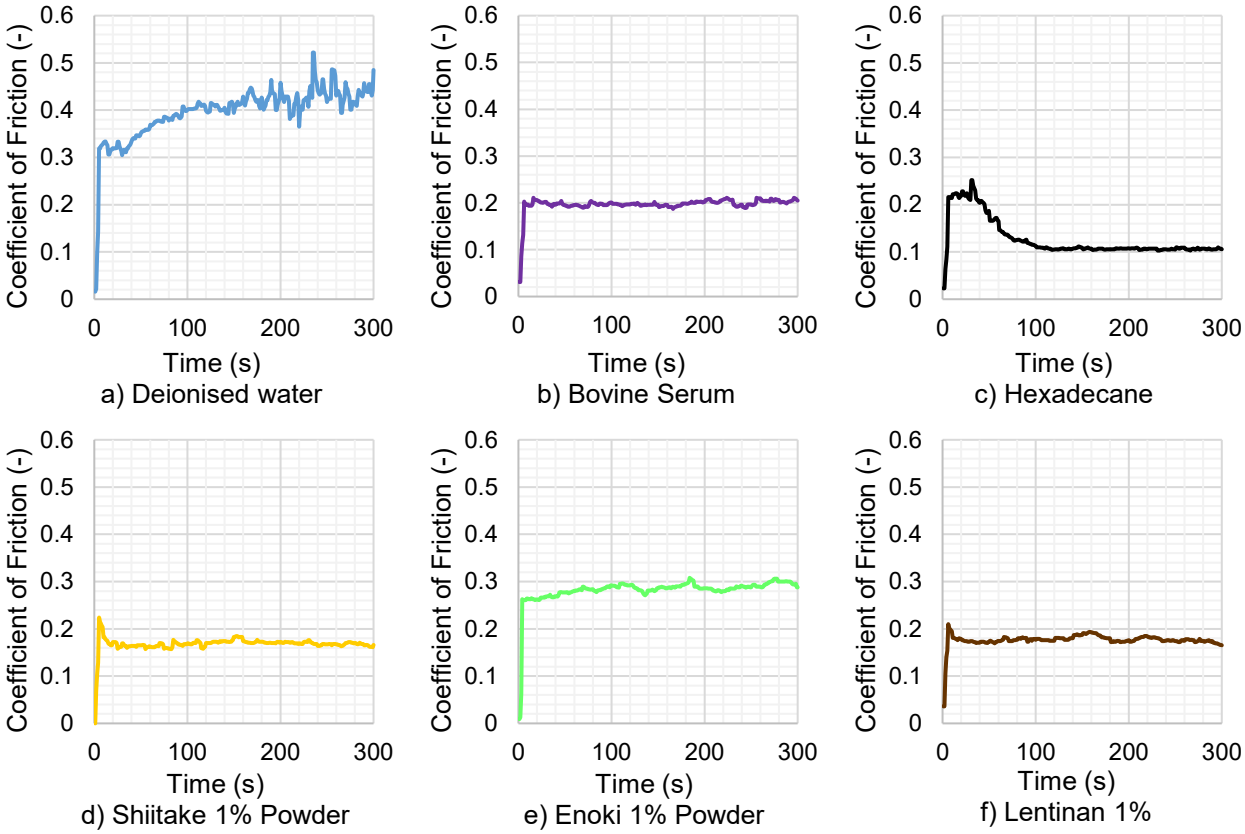


Figure 39. The time-dependant coefficients of friction from HFRR.

The average coefficients of friction, measured in this study, are provided in Figure 40. Deionised water showed the highest friction value of 0.36, and the lowest value of 0.12 was achieved by hexadecane. A useful comparison can be made with Murali et al. (2025), who conducted HFRR tests under similar boundary lubrication conditions using stainless steel specimens, a load of 0.5 N and a reciprocating frequency of 50 Hz, resulting in a higher Hertzian contact pressure of 515 MPa, compared to 289 MPa in present work (93). Coefficients of friction of 0.21 and 0.11 were reported for deionised water and hexadecane respectively (93). The close agreement in hexadecane friction across both studies indicates that its behaviour is insensitive to the changes in severity of contact in boundary regime. In contrast, the higher coefficient of friction of water in present study is consistent with

increased load and reduced entrainment speed, which both promote the greater asperity interaction and thus higher friction. This comparison confirms that the frictional trends observed for water and hexadecane in this study are aligned with those reported in literature under comparable boundary lubrication conditions. All tested fungal-based solutions and bovine serum showed coefficients of friction in a range of 0.17-0.28. Notably, the Shiitake-derived solutions achieved lower coefficients of friction than Enoki and Poria solutions. These observations support the hypothesis that mushroom-derived solutions can improve water-lubrication by mechanisms found with other polysaccharides without changing viscosity of water. As powder solutions were tested at a single concentration of 1 wt.%, differences between species should be attributed to composition and particle characteristics rather than concentration.

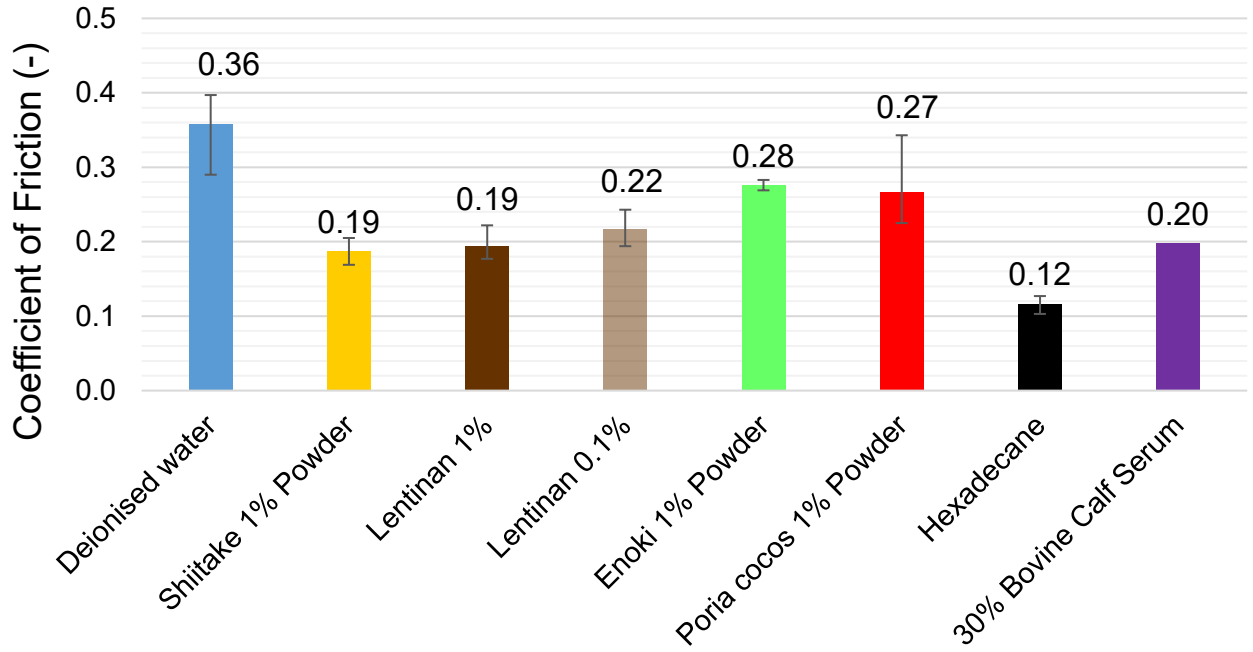


Figure 40. Coefficients of friction of fungal-based water solutions. Average of 3 repeats, error bars indicate minimum and maximum obtained values.

6.3.1.2. Wear

The average disk wear scar cross-sectional areas are shown in Figure 41. Among the benchmarks, hexadecane exhibited the largest wear cross-sectional area of 147 μm^2. This behaviour is consistent with its chemical structure: non-polar hydrocarbons lack functional groups capable of adsorbing onto steel surfaces and therefore provide almost no boundary-film protection, leading to severe asperity contact and large wear scars (100). A direct comparison of disk wear scar cross-sectional areas can be made with Murali et al. (2005), who tested hexadecane under higher contact pressure (515 MPa vs 289 MPa) and longer sliding distance. Under these conditions, the reported disk wear scar area was only 0.18 μm^2

(93). The much larger wear obtained in the present study therefore reflects differences in the test geometry and operating conditions. The larger ball radius and lower entrainment speed promote greater asperity interaction in the absence of boundary film. In contrast, deionised water produced a relatively small disc wear scar area of 11 μm^2. Murali et al. (2005) reported a substantially higher disk wear scar area of 56 μm^2 (93). The lower wear measured in the present study is consistent with the reduced contact pressure, shorter sliding distance and lower overall mechanical severity.

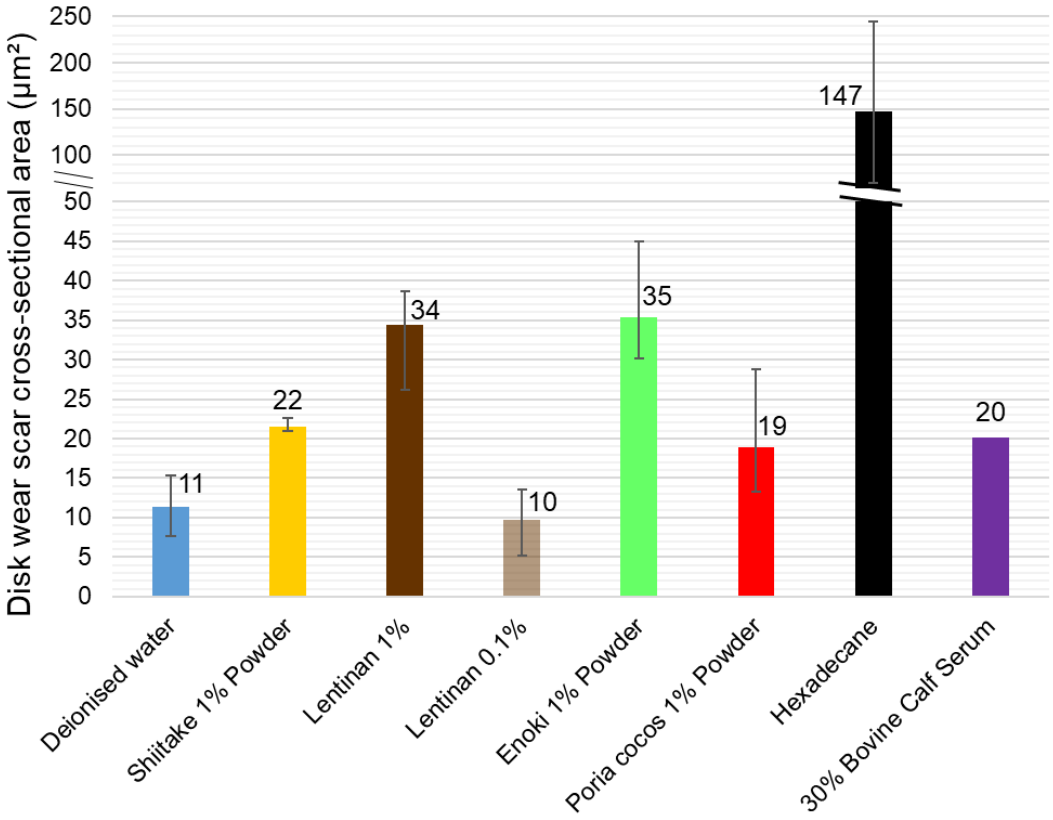


Figure 41. Disk wear scar cross-sectional areas of fungal-based water solutions. Average of 3 repeats, error bars indicate minimum and maximum obtained values.

Only 0.1% Lentinan solution showed similar disc wear cross-sectional area to deionised water. Other mushroom-based solutions, showed higher disk wear scar cross-sectional areas, suggesting that the introduced particles promoted wear, while reducing friction.

Figure 42 shows representative optical images of the disk wear scars produced by deionised water and mushroom powder solutions. The wear scar generated by deionised water (Figure 42a) appears wider and is surrounded by many loose debris. A strong darkening of the wear track indicates oxidative or corrosive wear, which is expected in water-mediated contact. In contrast, the wear scars produced by Shiitake, Poria and Enoki 1 wt.% powders (Figure 42b-d) exhibit smaller wear tracks with noticeably less scattered debris. These mushroom-based lubricants produced visually cleaner wear scars, indicating reduced extent of oxidation. The

clear visual differences between water and the mushroom solutions suggest that the addition of mushroom powders alters the nature of the wear process, reducing corrosion-related damage.

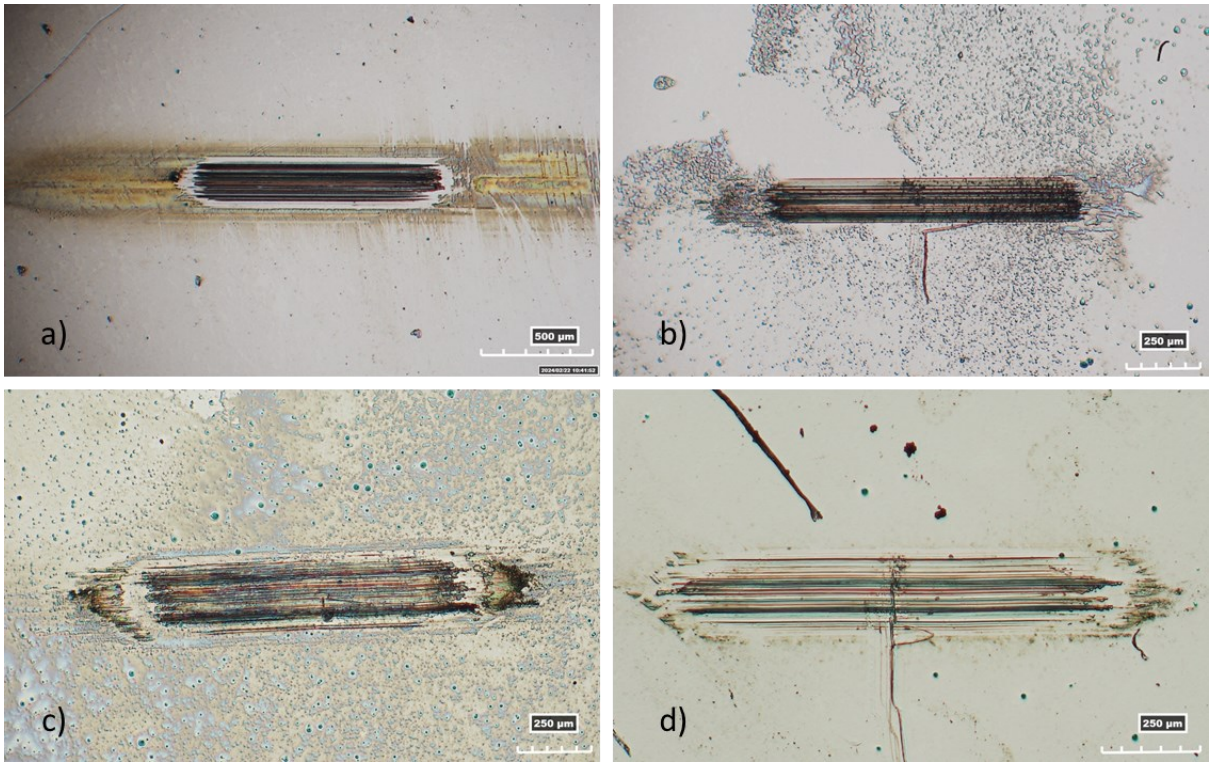


Figure 42. Disk wear scar images of a) deionised water, b) Shiitake 1% powder, c) Poria 1% powder and d) Enoki 1% powder. Note, scales are different for clarity.

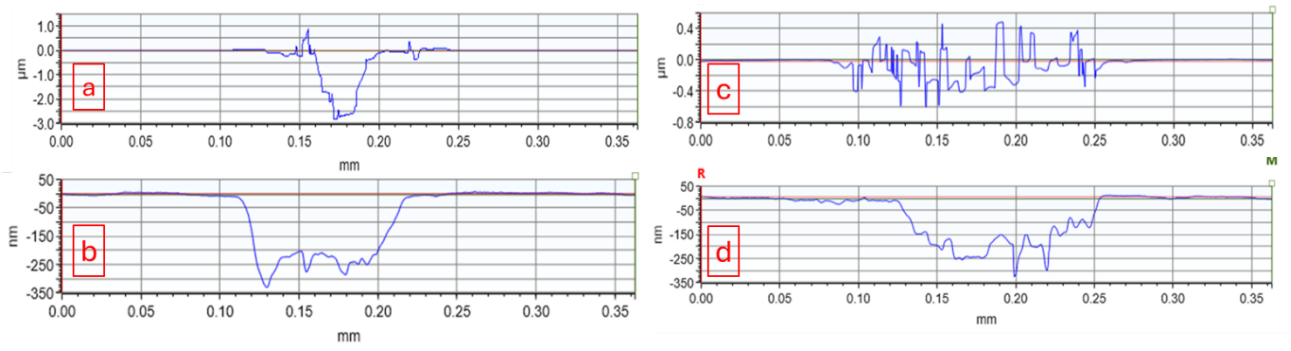


Figure 43. Cross-sectional profiles of a) Hexadecane, b) Bovine serum, c) Deionised water and d) Shiitake 1% powder. Note, height scales for samples are made different for clarity.

The observations of the disk wear scar cross-sections show a significant change in wear scar shapes between the different lubricants, which affects the size of cross-sectional areas. In Figure 43, several typical disk wear scar cross-sections are shown. Hexadecane (a), bovine serum (b) and Shiitake 1% powder (d) show relatively deep well-defined grooves, which are mostly smooth. Such behaviour is not seen in deionised water (c). Its wear scar cross-section is very rough with significant peaks and multiple grooves. This suggests a change in the wear pattern.

Previously, similar changes in appearances of wear scars were observed and described by Kayaba et al. (1986) (41). Three main types of abrasive wear were identified: ploughing, cutting and wedge formation. Characteristic wear scar in ploughing has multiple grooves of different sizes, but without significant material removal. On the other hand, single grooves with large removal of material from the contact are characteristic for cutting mode of abrasive wear (41). The change in modes is dependent on various properties of abrasive particles, like their concentration, particle size, shape and hardness (42,198,199). Most of the available literature focuses on particles, which are harder than their surrounding contact materials, like diamond particles in steel/glass contact or quartz in metal/metal contact (42,198,199). However, organic particles used in this work are much softer and thus cannot be abrasive particles themselves.

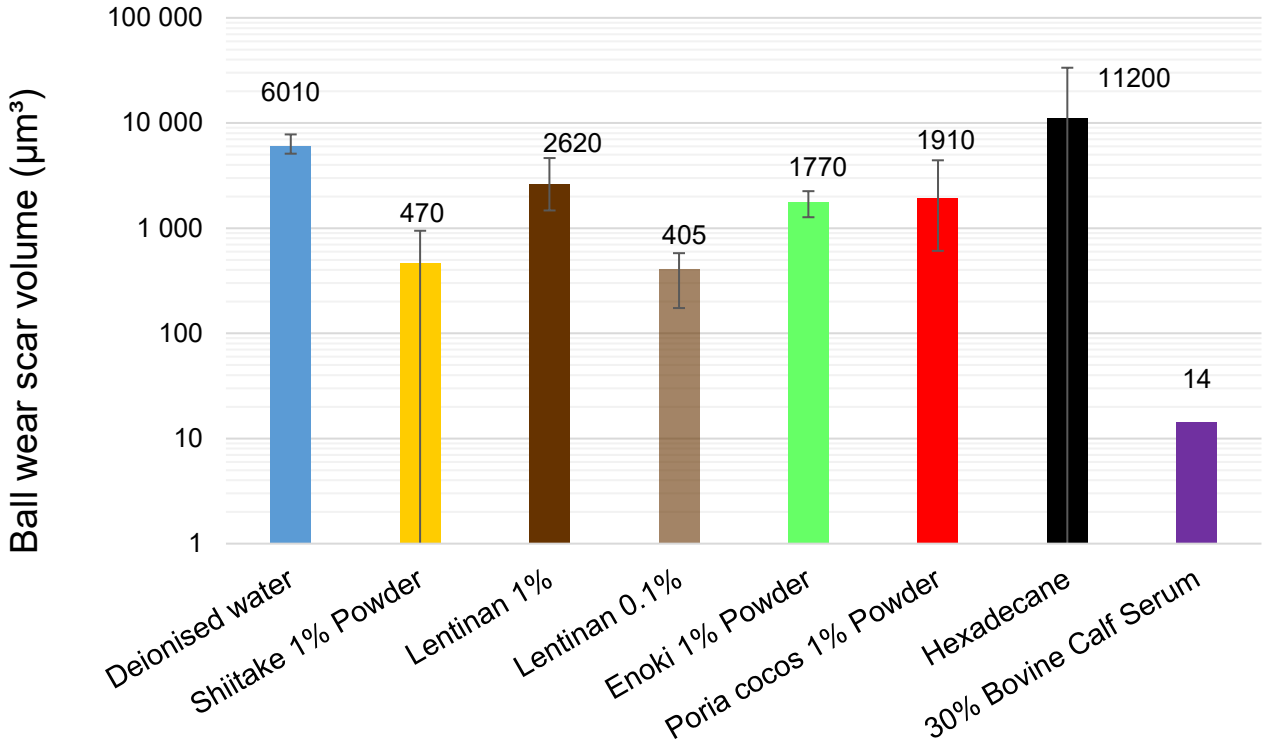


Figure 44. Ball wear scar volumes of fungal-based water solutions. Average of 3 repeats, error bars indicate minimum and maximum obtained values.

Compared to deionised water, most fungal-based water solutions showed a reduction in ball wear volume, as seen in Figure 44. 30% bovine calf serum solution showed the lowest ball wear volume of all tested lubricants, just 14 µm³. This is consistent with its ability to form robust protein layers, protecting the surface (24,25). Shiitake 1% powder and Lentinan 0.1% solutions also provided reduced ball wear volumes, 470 µm³ and 405 µm³, respectively.

These observations indicate that fungal-based lubricants can effectively protect the surfaces from wear, although not as effectively as bovine serum.

These findings suggest that fungal-derived lubricants can influence both friction and wear performance of water. A combination of mechanisms could be responsible for such behaviour: adsorption of β-glucans to the surfaces, like seen in plant- and algae-based polysaccharides, and the presence of soft organic particles, acting as rollers, thus reducing friction and wear.

6.3.2. Effect of Lentinan Concentration

To further investigate these mechanisms without the influence of different fungi species, Lentinan solutions with different concentrations of 0.1 wt.%, 1 wt.%, and 5 wt.% were tested. Figure 45 presents the resulting coefficients of friction, disk wear scar cross-sectional areas and ball wear scar volumes for the mentioned solutions. The coefficient of friction of lentinan solutions decreased with increasing concentration of Lentinan, reaching the minimum of 0.18 for 5 wt.% solutions. This suggests that higher concentrations of β-glucans provide a more effective formation of boundary film. The opposite trend is seen with disk wear scar cross-sectional area, which increased with higher concentrations of lentinan, reaching a maximum of 57 μm^2. The ball wear volume remained substantially lower for all concentrations. This suggests than Lentinan effectively protects the ball surface independent of concentration.

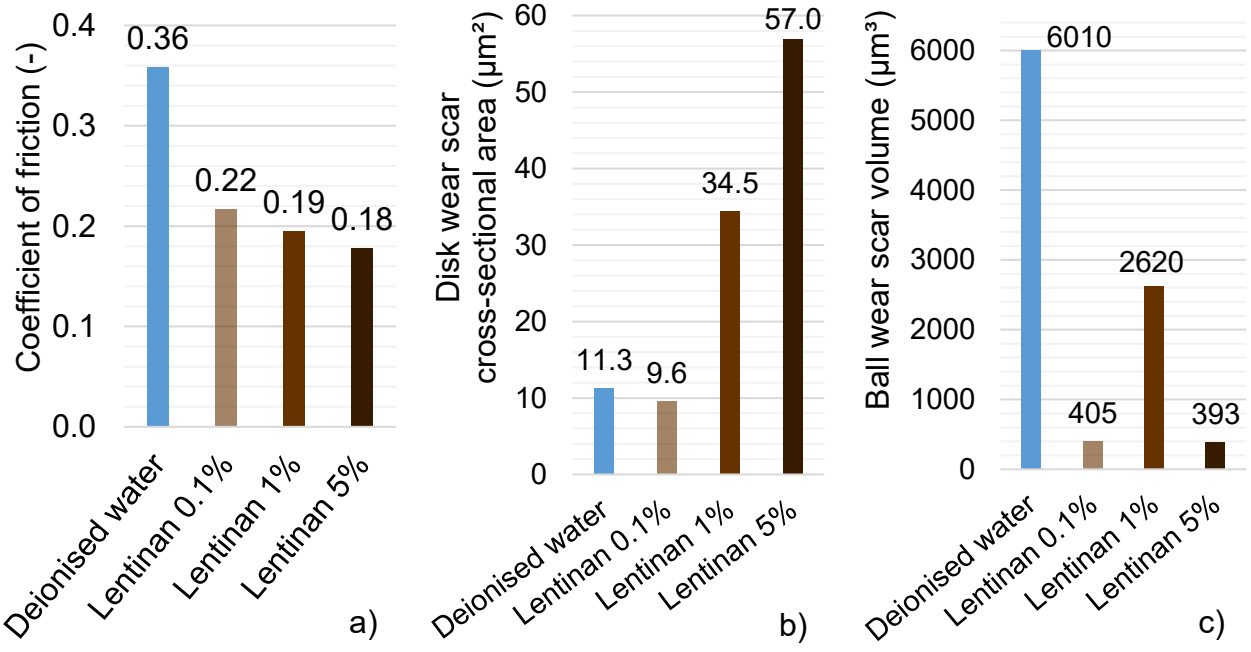


Figure 45. Tribological performance of Lentinan solutions: a) Average coefficients of friction, b) Disk wear scar cross-sectional areas and c) Ball wear scar volumes.

The changes in the shapes of disk wear scar cross-sectional areas, outlined earlier, were also observed by comparing deionised water and solutions with different concentrations of

Lentinan. Disk wear scar profile of deionised water in Figure 46a shows a formation of many grooves of a range of sizes. The surface is significantly distorted, but limited material is removed, resulting in relatively low wear volume. Different behaviour is observed with Lentinan solutions. The wear scars b)-d) in Figure 46 show a transition from multiple grooves to a single groove of larger amount of material removed. These observations align with Dwyer-Joyce et al. (1994), who also observed an increase in wear with the increase in concentration of particles (198).

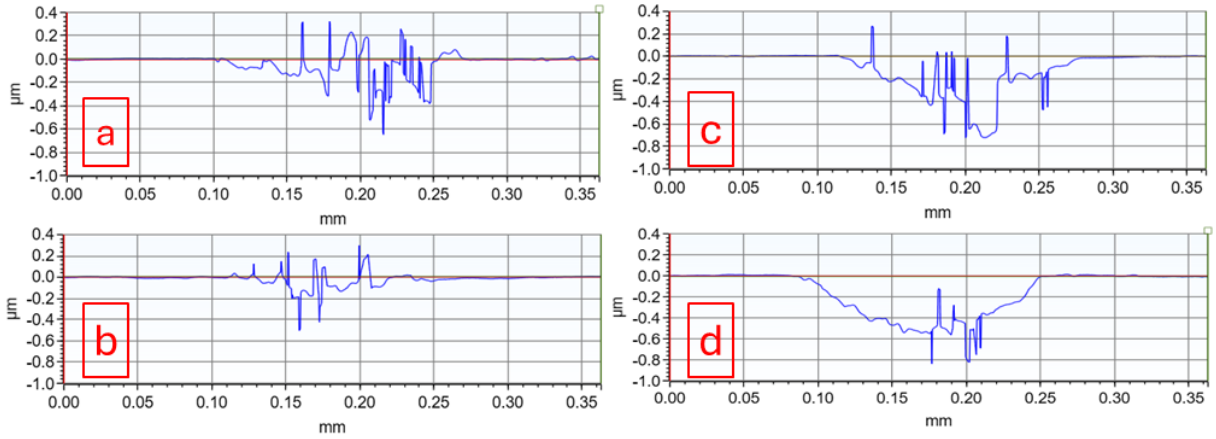


Figure 46. Disk wear scar cross-sections of a) deionised water, b) 0.1% Lentinan, c) 1% Lentinan and d) 5% Lentinan.

6.4. Discussion

Mushrooms-derived substances introduce particles of different sizes, as seen by DLS measurements in Figure 38. Figure 47 shows an example of particles from 0.1% Lentinan solution, observed using Scanning Electron Microscope (SEM). Instead of triple-helix structure of Lentinan in deionised water, aggregates were observed, as the critical aggregation concentration of 0.26 mg/ml of water was exceeded (186). The applied Lentinan solutions showed two distinctive particle diameters: around 50 and 500 nm, which was observed earlier in Section 6.2.3.2 (186,187). Lentinan solutions have shown a decrease in measured friction force, compared to water, as shown in Figure 45. Similar effect has been observed by Cann (2006) in rolling-sliding contact, where the plant leaves produced an adhesive viscous layer, improving the lubricity (200).

Initially it was hypothesised, that similar mechanism emerges with addition of mushroom-derived substances. In this study it was identified that the particles may have caused such reduction. Similar behaviour was reported in water solutions with other types of nanoparticles, metal and ceramic ones (30). It is suspected, that in the contact the mushroom particles either physically separate the contact surfaces or produce a tribofilm

with low resistance to shear, thus reducing the direct metal-metal contact and reducing the coefficient of friction (32,191,201).

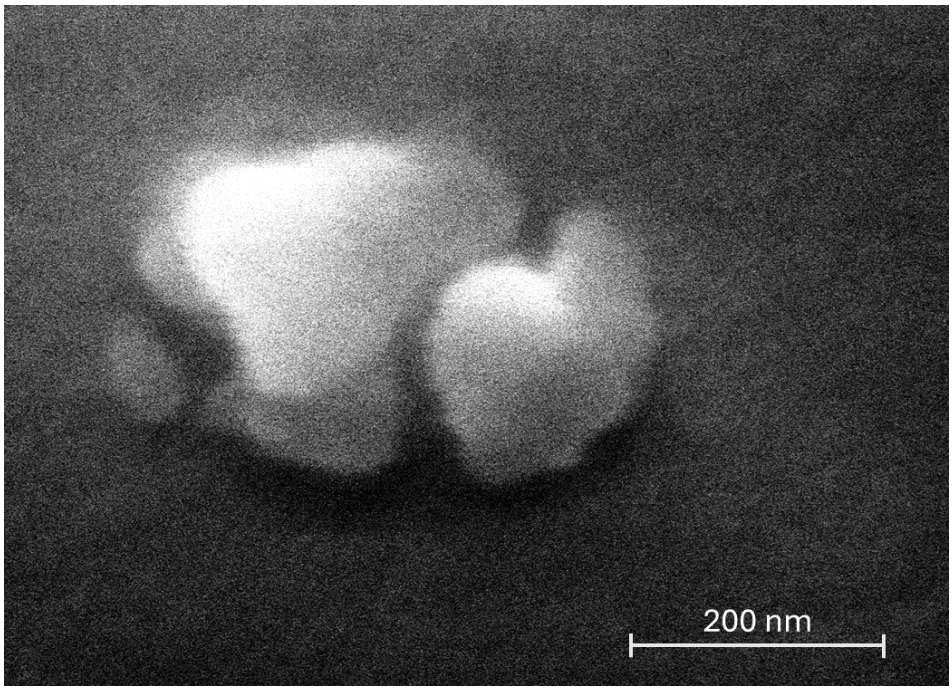


Figure 47. SEM image of particles in 0.1% Lentinan solution on stainless steel disk after Cr-coating.

The tribological behaviour of Lentinan in aqueous solutions was evaluated across three concentrations - 0.1 wt.%, 1 wt.%, and 5 wt.%. As shown in Figure 45, a reduction in coefficient of friction, compared to deionised water, was seen for all Lentinan solutions. The change of disk wear shapes and depths was observed.

0.1% Lentinan has smaller wear scar, but without a significant change in average wear depth from deionised water. This is indicative of partial surface adsorption of lentinan molecules forming a boundary layer. Such behaviour is consistent with previous findings on polysaccharide-based lubricants, where adsorbed layers, govern interfacial friction (27,200). Waller et al. (2013) similarly demonstrated that adsorbed glycoproteins in synovial systems substantially reduce boundary friction, even in the absence of rheological changes (156).

In contrast, in 5% lentinan solution the wear depth increased significantly. The wear scar changed character, as it appears smoother, but deeper, consistent with cutting rather than ploughing. The observed reduced friction and increased wear suggest that excess lentinan, particularly the ~500 nm particles may be interfering with the contact interface. Similar effects were observed by Chern et al. (2022), who showed that larger third-body particles, even when soft, reduce real contact area and increase contact pressure, ultimately promoting wear (202). Chojnicka et al. (2008) also found that protein aggregates larger than

300 nm can disrupt boundary lubrication by acting as entrained third bodies that mechanically disturb the sliding interface (203).

To summarise, these results suggest that at low concentrations, Lentinan acts primarily through a surface adsorption mechanism, forming a protective boundary layer that reduces friction. However, at higher concentrations, the presence of larger particles promotes wear through three-body interaction, despite further reducing friction.

To further investigate the tribological role of Lentinan particle size, a 0.1% Lentinan solution was filtered using Millipore Express 40 membrane filter with 0.22 µm pore size (Merck, Germany). During this process larger particles were removed from the 0.1% Lentinan solution, as seen in Figure 48, while retaining the smaller ~50 nm polysaccharide structures. This further reduced the actual concentration of Lentinan in the solution.

The tribological performance of the filtered 0.1% Lentinan solution was evaluated and the comparison of friction coefficients and wear volumes with unfiltered 0.1% Lentinan solution and deionised water is provided in Figure 49. The filtered solution showed a further decrease in coefficient of friction to 0.14, compared to 0.36 and 0.22, for deionised water and unfiltered 0.1% Lentinan solution, respectively. This observation provides strong evidence that the smaller Lentinan chains are primarily responsible for effective boundary lubrication, consistent with previous findings on the adsorption-controlled nature of hydrated biopolymer films (27,156).

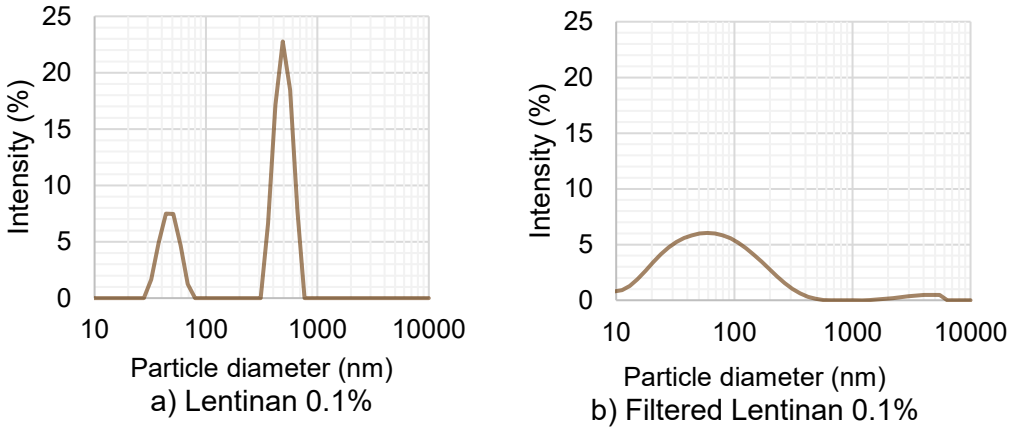


Figure 48. Obtained DLS intensity graphs of a) Lentinan 0.1% and b) filtered Lentinan 0.1% solutions.

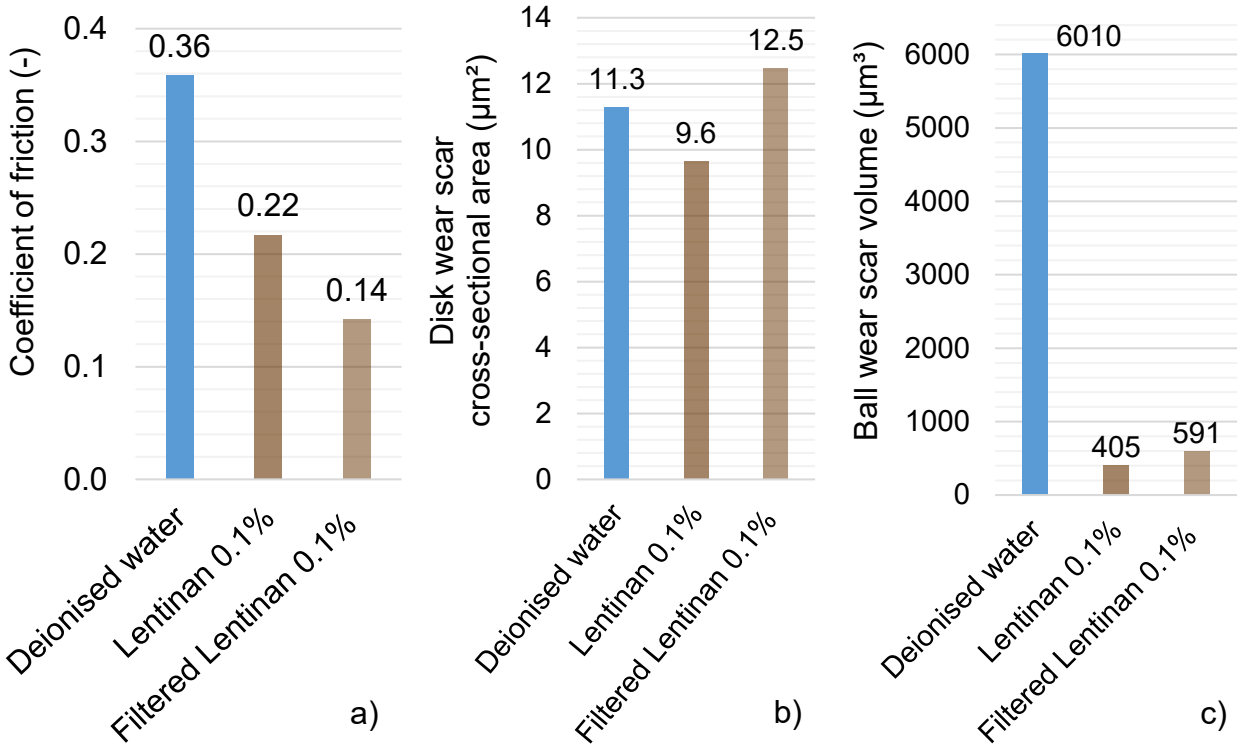


Figure 49. Comparison of tribological performance of deionised water and 0.1% Lentinan solutions: a) Coefficients of friction, b) Disk wear scar cross-sectional areas, c) Ball wear scar volumes.

The filtered 0.1% Lentinan solution showed a slightly larger disk wear scar area compared to the unfiltered solution, 9.6 against 12.5 μm^2. No significant change in ball wear scar volume was observed. The obtained disc wear scar cross-sections are shown in Figure 50. The filtered 0.1% Lentinan solution experienced pure cutting mode of wear, compared to a mixture of cutting and ploughing of the unfiltered 0.1% Lentinan solution, suggesting a shift towards more stable sliding conditions. This suggests that although larger particles are not abrasive, as they are soft and organic, their presence in the contact introduces local instabilities, which can promote irregular wear.

While particle-surface interactions are one possible explanation, several other mechanisms may also contribute to the observed differences in wear. First, water-based solutions are susceptible to corrosive wear, which can deepen wear scars independently of mechanical abrasion (204). However, all tests were conducted over short time periods using stainless steel specimens under identical environmental conditions, and no progressive darkening or surface pitting characteristic of dominant corrosive wear was observed across the different lentinan concentrations. This suggests that corrosion alone cannot account for the systematic differences between tested solutions.

Second, the presence or removal of larger aggregates may influence the local availability of lubricant, resulting in the intermittent lubrication starvation. This could also alter wear behaviour. While this mechanism cannot be fully excluded, the observed friction profiles did not show the large transient spikes typically associated with starvation (200). Moreover, starvation would be expected to increase both friction and wear, whereas the experiments showed reduced friction alongside increased wear at higher concentrations of lentinan.

Third, changes in the surface adsorption of lentinan, such as differences in continuity or stability of boundary layer, may affect how load and shear are distributed across the contact (27,156). Filtration may promote a more uniform adsorption of smaller lentinan particles, resulting in a more continuous boundary layer.

Taken together, these mechanisms' considerations suggest that particle size plays a dominant role in the observed wear behaviour. Larger lentinan aggregates are likely entrained intermittently into the contact, where they act as soft third bodies that locally vary stress distribution and promote irregular material removal without acting as hard abrasives (203,205). Removal of these aggregates stabilises the contact mechanics, leading to a more uniform wear response governed primarily by asperity interaction and boundary-layer lubrication rather than particle-mediated disturbances.

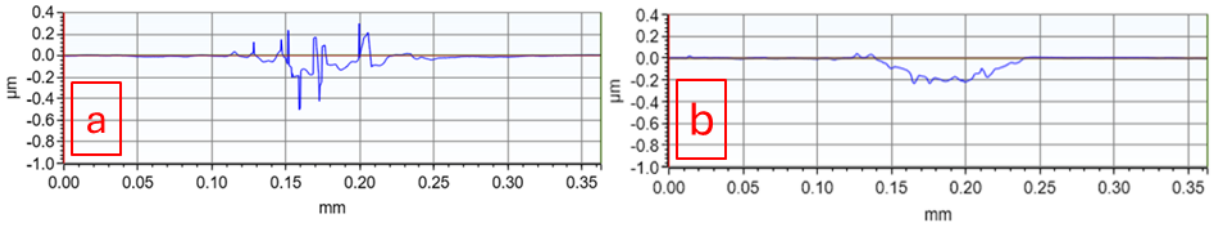


Figure 50. Wear scar cross-sections of a) Lentinan 0.1% and b) Filtered Lentinan 0.1% solutions.

By removing larger particles, the filtered solution avoids such effect, while maintaining sufficient surface adsorption to reduce friction. These findings support the idea that even soft third-body particles can increase wear if they are sufficiently large, consistent with the tribological modelling of Chern et al. (2022) and experimental work by Chojnicka et al. (2008) on soft protein aggregates (202,203). This also confirms that friction and wear are independent in this system: while friction is primarily controlled by molecular-level surface interactions, wear is more sensitive to the presence and behaviour of larger aggregates in the contact.

Overall, these results highlight the importance of controlling not just concentration, but also size distribution of biopolymer additives in water lubrication. Filtering to remove larger

particulates may offer a simple but effective strategy to optimise the tribological performance of lentinan-based water solutions, thus preserving low friction and avoiding aggregation-related wear.

6.5. Conclusions

Water is an environmentally friendly lubricant, forming the base of most natural lubricating systems. It has potential in replacing the petroleum-based lubricants in engineering applications. However, water on its own is a poor lubricant and enhancing its tribological performance typically requires additives of petroleum origin. β-glucans provide a natural alternative to such additives.

In this study, three widely cultivated fungal species: Shiitake (*Lentinula edodes*), Enoki (*Flammulina Velutipes*) and Poria (*Poria cocos*), were used to obtain water-based solutions from powders. Lentinan, a pure β-glucan of Shiitake, was also used to make water-based solutions. The tribological performance of these solutions was evaluated using HFRR and compared to three benchmarks: pure deionised water (solution base), hexadecane (petroleum-based lubricant) and 30% bovine calf serum (biological lubricant).

To summarise, the conclusions are as follows:

a) The addition of fungal-based substances to deionised water reduces the friction in the contact, due to the presence of mushroom particles.
b) The addition of fungal-based substances to deionised water reduces the wear on the ball surface.
c) Increasing concentration of Lentinan in water solutions reduces the friction.
d) Higher concentration of particles, particularly larger ones, increases the amount of wear removal on the disk by promoting 3-body interactions.
e) The removal of larger particulates from the Lentinan solutions improves stability of the boundary lubrication, thus reducing the friction and avoiding irregular wear.
f) Particle size determines the preferred mechanism of lubrication: larger particles promote 3-body interactions and smaller particles produce an adsorbed layer, leading to stable boundary lubrication.

These findings demonstrate that water-based lubrication can be improved by addition of fungal-derived β-glucans. The resulting tribological performance is controlled by concentration and particle size distribution of the added β-glucans.

7. Hydrogels from Natural Polysaccharides

The previous chapter examined water-based polysaccharide solutions, while this chapter investigates their solid counterparts in the form of hydrogels derived from plant and algal polysaccharides. Hydrogels are soft solids composed of crosslinked polymer networks that retain large amounts of water. Their structure and performance are sensitive to the presence of divalent metal ions, which are encountered in both biological and engineering environments. To assess the influence of ions on material properties and frictional behaviour, hydrogels from plant and algal polysaccharides were prepared and systematically characterised.

7.1. Introduction

The current lubricant market is predominantly composed of products derived directly from mineral oil or synthetic oils based on petrochemical products. While biolubricants are employed in niche applications, such as metalworking oils, chainsaw and gear oils, they represent a small portion of the industry (3,7,61). In most cases, lubricants are lost to the environment either during operation or through leakage. This highlights the need for biodegradable and environmentally friendly alternatives to minimise the environmental impact.

One promising candidate for such alternatives are hydrogels derived from natural polymers. They are known for high biocompatibility, which led to their extensive use in the food industry, biomedical, agricultural, and sanitary fields (165). Typically, hydrogels are utilised for controlled release of substances or as an efficient absorbent, examples being medical drug delivery, antimicrobial treatments, and removal of dyes and heavy metals at water treatment sites (75,77,165). Furthermore, hydrogels are used as the base for medical injectable gels, pharmaceuticals, cosmetics and as gelling agents, emulsifiers, and stabilisers in food products (75,165,167,206).

Hydrogels are three-dimensional polymer networks, which can absorb and retain significant amounts of water (75,110,166). Depending on the system, hydrogel can contain 70-99 wt.% water and still behave as soft solid (110,166). Hydrogel structures are formed through crosslinking, which can be achieved using either natural or synthetic polymers. Polymer chains are stabilised into a continuous network, either by chemical or physical crosslinking (207,208). Chemically crosslinked hydrogels are formed by addition of crosslinking agents,

that provide covalent bonds, usually resulting in a permanent, irreversible hydrogel structure (166). In contrast, physical crosslinking involves mechanical entanglement of the polymer chains without addition of a special crosslinking agent (75,209). The resulting hydrogels usually have weaker mechanical properties compared to chemically crosslinked hydrogels, but physical crosslinking processes provide reversible structures (166,209).

Hydrogels can be prepared from both natural and synthetic polymers. Synthetic hydrogels, such as polyacrylamide-based, offer precise control over mechanical strength and chemistry, and are widely used in engineered biomedical applications (167,210). However, production of synthetic hydrogels relies on petrochemical feedstocks, and may not be environmentally friendly (211). In contrast, hydrogels made from natural polysaccharides, such as carrageenan, agar, alginate, pectin and gellan gum, are renewable, biodegradable and inherently biocompatible (75,77). Their network formation relies on physical crosslinking mechanisms, such as helix aggregation, hydrogen bonding or ionic coordination (75,77). Even though, physically crosslinked hydrogels are weaker than chemically crosslinked ones, natural hydrogels provide dynamic networks that are responsive to environmental conditions. These properties make natural hydrogels attractive for sustainable lubrication and soft-matter applications.

In this study the chosen polysaccharides: carrageenan, agar, gellan gum (phytagel), alginate and pectin, represent a diverse set of natural gelling agents derived from algae and plants. These polysaccharides were chosen for three main reasons. First, all selected polysaccharides are widely used in food, biomedical and pharmaceutical industries, ensuring established safety profiles and availability (77,211). Second, this set spans distinct physical gelation mechanisms, including helix aggregation (carrageenan, agar), ion-mediated junctions (alginate, pectin) and mixed helix-junction networks (phytagel). This diversity enables systematic comparison between non-ionic and ionic crosslinking mechanisms, allowing to isolate the influence of network structure on friction and interfacial shear. Third, all selected hydrogels can be formed at relatively low polymer concentrations: 0.5 wt.% for phytagel, 1 wt.% for carrageenan and agar, 2 wt.% for alginate, and 5 wt.% for pectin (212–216). This is essential for maintaining high water content and boundary-lubricated conditions relevant to bio-tribological applications. Beyond these practical considerations, this selection was designed to span a wide range of mechanical stiffness, viscoelastic dissipation and interfacial behaviour while keeping chemistry and preparation routes comparable. This approach ensures that observed differences in friction arise

primarily from network structure and ion-polymer interactions. Consequently, the chosen hydrogels provide a robust framework for establishing structure-tribology relationships in natural polysaccharide-based lubrication systems.

Carrageenan is a family of galactans that occur naturally in the cell walls of red algae *Rhodophyceae* (75,217,218). This type of polysaccharides is made of a backbone composed of alternating α-D-1,3 galactose and β-D-1,4 galactose with some branches substituted by sulfate groups (217,218). This results in three main types of carrageenan: kappa (κ), iota (ι), and lambda (λ), which differ by the number of sulfate groups per repeating unit. The resulting structures are shown in the Figure 51. In this study only κ-carrageenan is used, as it is the most abundant and produces the strongest hydrogel networks (75,218).

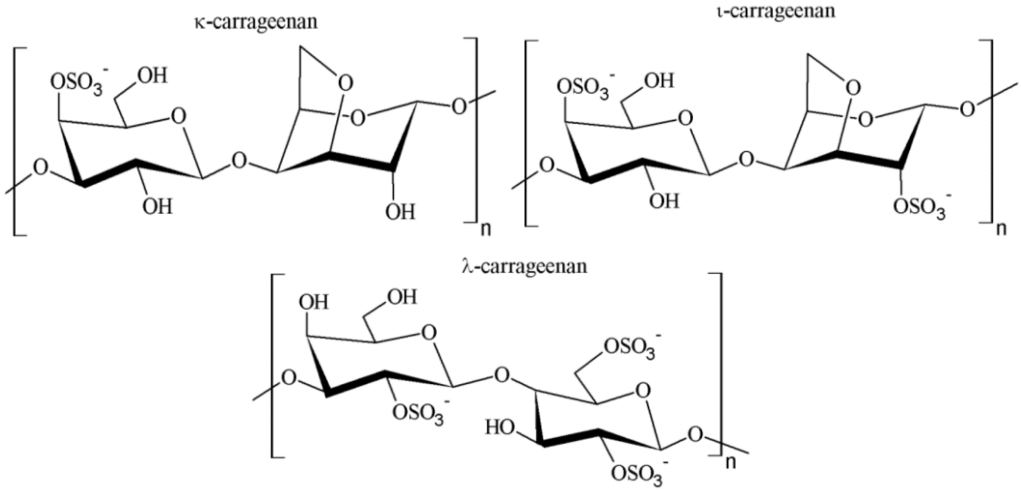


Figure 51. Chemical structures of carrageenans (218).

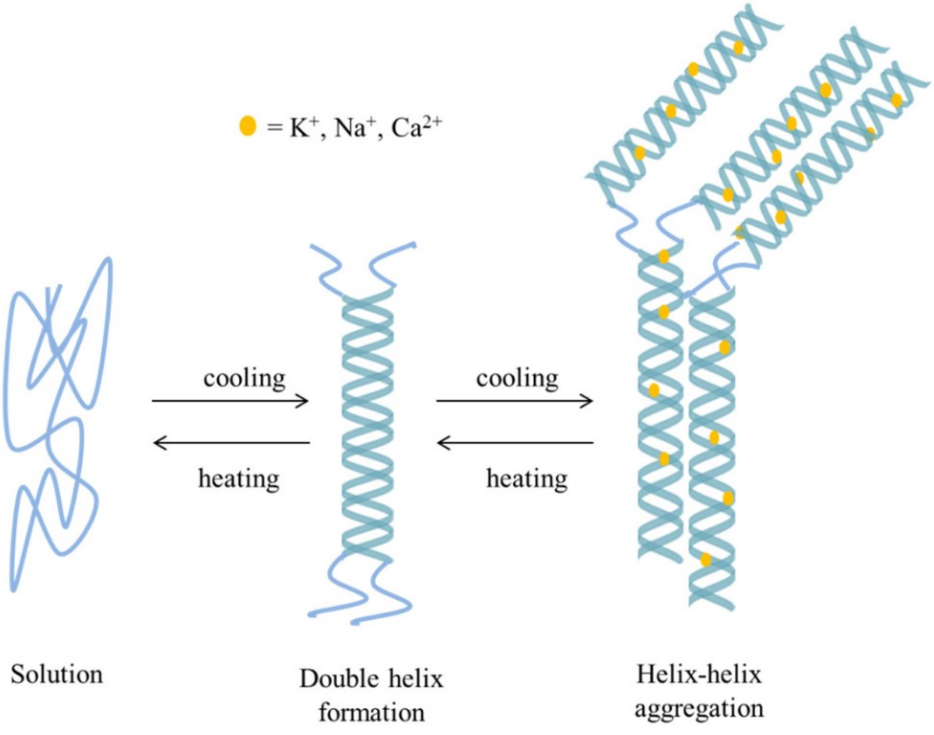


Figure 52. Scheme of carrageenan gel formation (218).

The gelation mechanism of carrageenan is characterised as a coil-to-helix transition of polymer chains upon cooling, followed by aggregation of the double helices into the structured network (217,218). The scheme of carrageenan gel formation is shown in Figure 52. Several ions, particularly K^+, Na^+ and Ca^{2+}, are known to crosslink the helical aggregates by fitting into inter-helix sites, reinforcing the resulting hydrogel network (214,218). The mentioned characteristics, together with abundance of red algae, make carrageenan hydrogels a well-defined system to evaluate the effect of external ions on the frictional and mechanical responses of hydrogels.

Agar is a polysaccharide mixture extracted from the cell walls of red algae, like carrageenan (75,219). This mixture consists of two main fractions: agarose and agaropectin. Agarose is the main gelling component, built of the repeating units of β-D-galactose and 3,6-anhydro-L-galactose units, shown in Figure 53 (219). Agaropectin has similar structure as agarose, but contains several additional side groups, such as sulfate, methyl and pyruvic acid acetyl groups (75,220). These groups reduce the gelling ability of agar and influence the structural properties of resulting hydrogel.

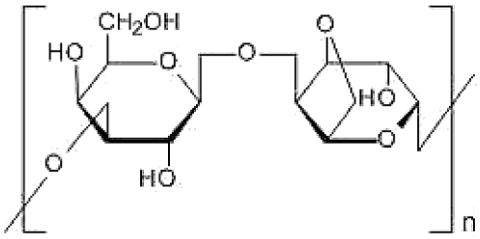


Figure 53. Chemical structure of agar (221).

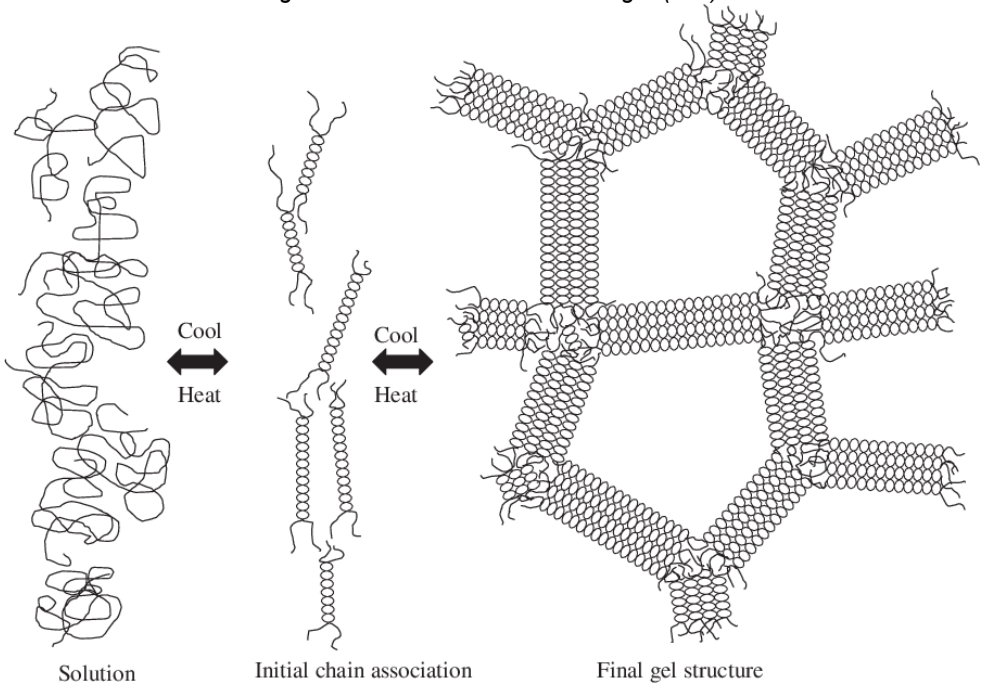


Figure 54. Scheme of agar hydrogel formation (222).

The gelation of agar follows a similar mechanism to carrageenan. Upon cooling a coil-to-helix transition occurs, followed by aggregation into a three-dimensional network, as visualised in Figure 54 (75,220,222). Unlike carrageenan, the resulting structure is reinforced only by hydrogen bonding between helices (220). This makes agar gels highly dependent on stability of hydrogen-bonds, especially in the presence of other ions (75).

Gellan gum is a linear polysaccharide secreted by the bacterium *Sphingomonas elodea* (75,212). Its repeating unit consists of two β-D-glucose, one β-D-glucuronic acid and one α-L-rhamnose (223). Commercially, gellan gum is available in high acyl (HA) and low acyl (LA) forms, which are shown in Figure 55 (75,212). Low acyl gellan gum, marketed as Phytagel, was used in this study due to its ability to form strong, transparent gels (212).

The gelation mechanism of gellan gum involves a temperature-dependent transition from coils to double helices, followed by helix-helix aggregation through junction zones (223,224). The formation of junction zones is promoted by cations, particularly divalent ones, like Ca^{2+} (223,225). These ions serve as ionic bridges between carboxylic groups of neighbouring helices (224). In the absence of ions, gellan gum solutions do not form stable hydrogels (212).

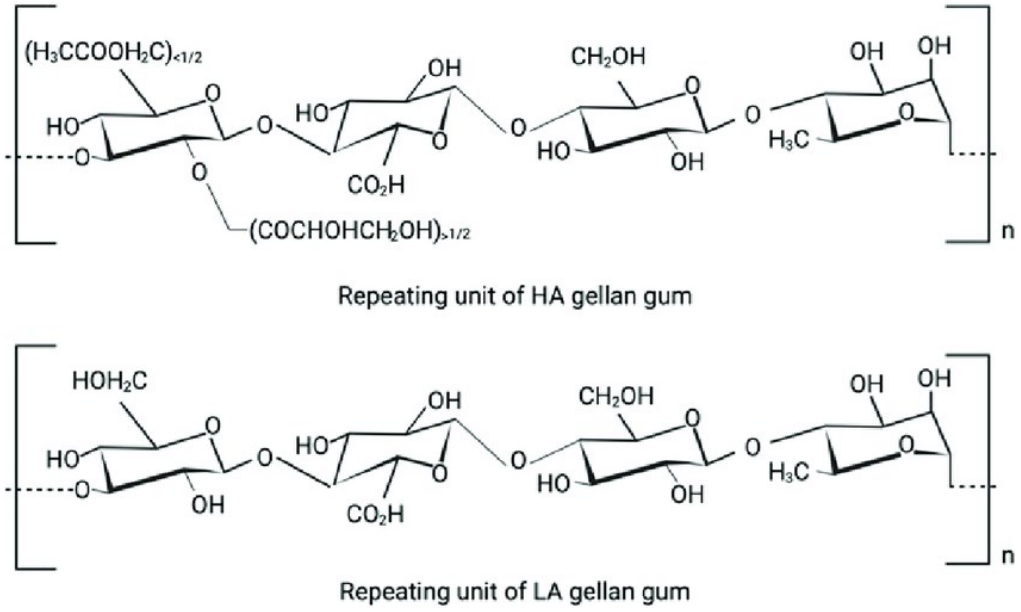


Figure 55. Structures of high (HA) and low acyl (LA) gellan gum (75).

Alginate is a family of polysaccharides extracted from brown algae such as *Laminaria* (75,226). Its structure is composed of β-D-mannuronate (M) and α-L-guluronate (G), which are arranged in consecutive M- and G-blocks and alternating MG-blocks, as illustrated in Figure 56 (75,220,226). The ratio and distribution of M- and G- blocks depend on the algal source and influence the stiffness and gelation capacity of the alginate hydrogels (226).

Gelation of alginate occurs through ionic crosslinking via “egg-box” model, visualised in Figure 57 (75,220). In this mechanism, divalent ions, such as Ca^{2+}, fit into cavities formed by G-blocks, crosslinking adjacent chains and reinforcing the hydrogel structure (78,220). Alginate hydrogels can be prepared from different ions, and the resulting properties of hydrogels are directly dependent on ion type and concentration (78,220). This ion-sensitive gelation makes alginate a well-suited model to study the effect of ions on the mechanical and tribological properties of resulting hydrogels.

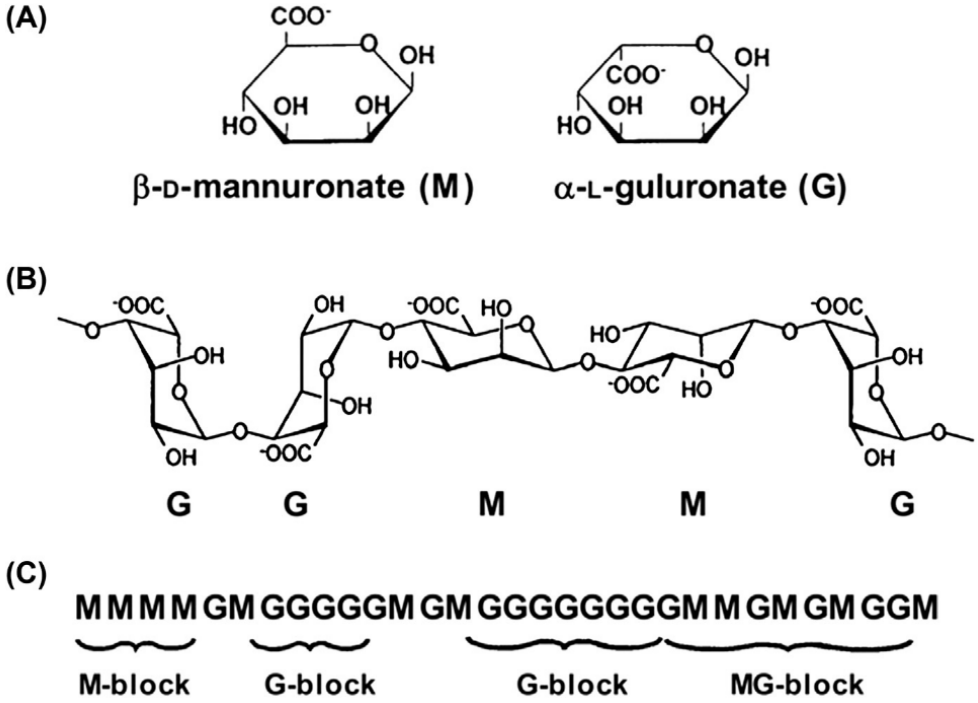


Figure 56. Structures of alginates: (A) - monomers, (B) – chain conformation, (C) – block distribution (226).

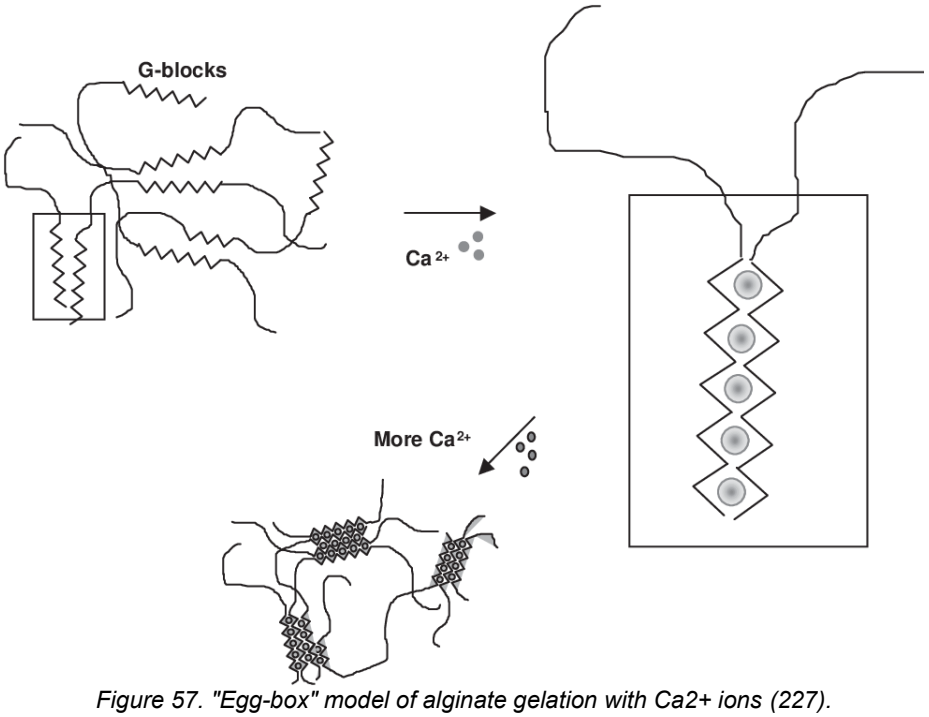


Figure 57. "Egg-box" model of alginate gelation with Ca2+ ions (227).

Pectin is a complex polysaccharide consisting of linear regions of α-(1,4)-linked D-galacturonic acid units, partly esterified with methoxyl groups, as illustrated in Figure 58 (14,75,216). Depending on the degree of esterification, pectin is classified into low-methoxyl (LM) and high-methoxyl (HM) types (75,216,228). HM pectin forms gels under acidic conditions through hydrophobic associations between methyl-ester groups and hydrogen bonding between adjacent chains (75,216,228). In contrast, LM pectin requires ions for gelation, forming ionic crosslinks between carboxyl groups via the “egg-box” mechanism (14,75,228). Both gelation mechanisms are shown in Figure 59.

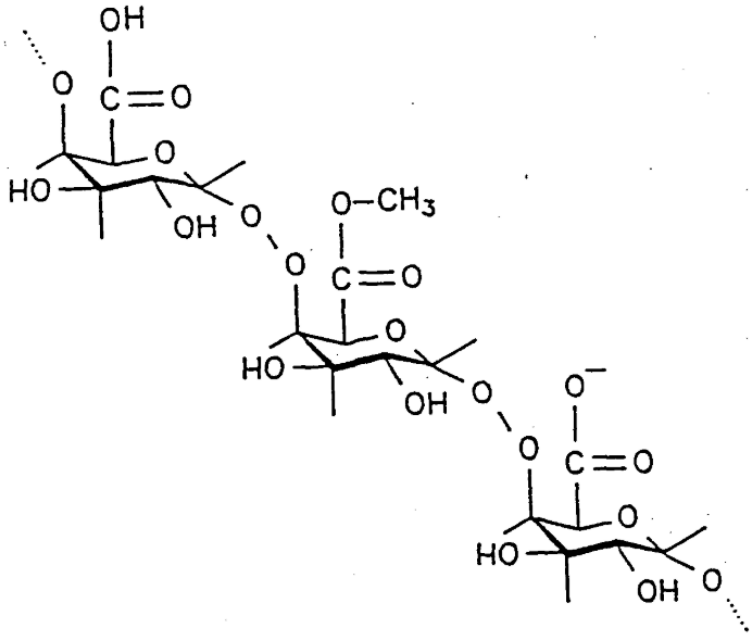


Figure 58. Structure of repeating segment of pectin (228).

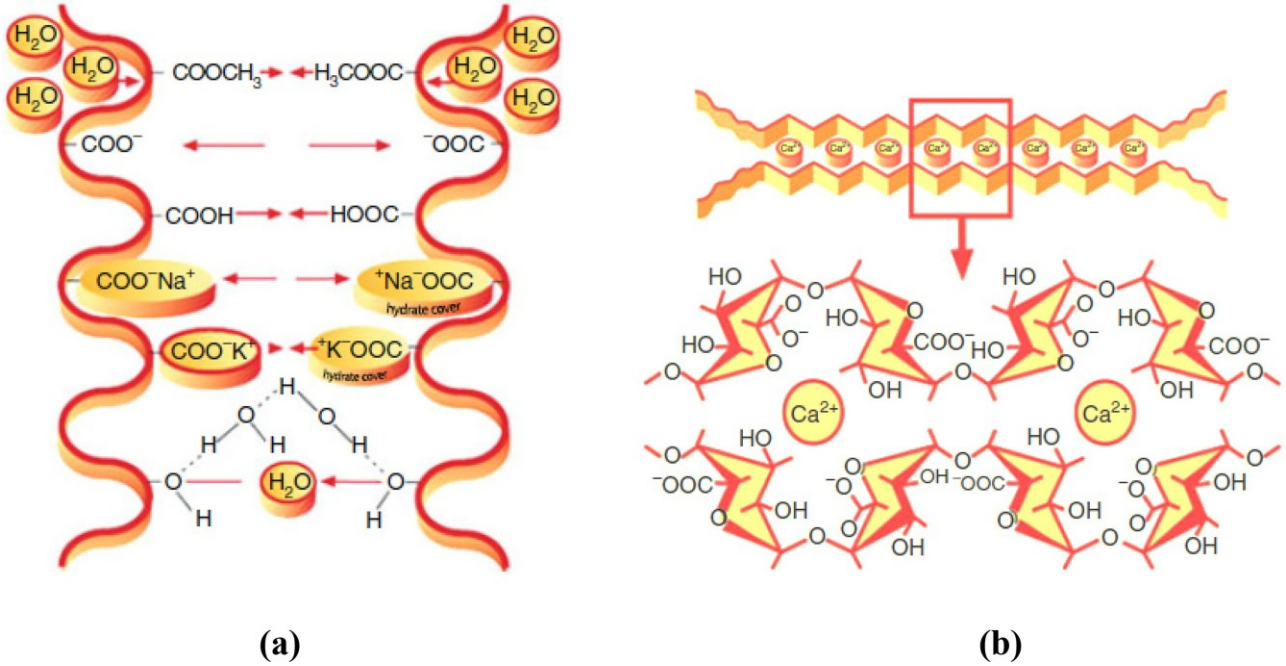


Figure 59. Gelation mechanisms of a) high-methoxyl and b) low-methoxyl pectin (14).

In this study, gels were obtained only in the presence of divalent ions and under neutral aqueous conditions, indicating the material behaved as low-methoxyl pectin. The added ions crosslinked the pectin chains, forming stable hydrogels, whose properties were strongly dependent on the ion type.

The mentioned hydrogels that form natural polysaccharides can be divided into two main groups. Non-ionic hydrogels, such as carrageenan and agar, do not require ions to form their structures, but ions may be used to modify these structures. Ionic hydrogels, such as alginate, phytagel and pectin, rely directly on the presence of ions to form the hydrogels using ionic crosslinking. In both cases, the interaction between polymer networks and added ions can affect the mechanical and tribological performance of the resulting hydrogels.

To investigate these effects systematically, this study investigates the addition of four divalent ions to the mentioned natural polymers. The chosen ions were iron Fe^{2+}, copper Cu^{2+}, zinc Zn^{2+} and calcium Ca^{2+}. Calcium is a widely used cation in food processing, water treatment, and construction, and it also represents the classical ion for alginate gelation through the “egg-box” model (112,223,225). Zinc has extensive applications in galvanisation, alloys, and biomedical products, reflecting its strong affinity for coordination with carboxyl groups (229). Copper is indispensable in electrical and electronic industries, as well as catalysis and antimicrobial systems (230). Iron is the most abundant and industrially significant transition metal, central to steelmaking, catalysis, and environmental remediation, and thus particularly relevant for applications where hydrogel–metal interactions may occur (231,232). Together, these four ions provide a diverse set of industrially and biologically important divalent metals, allowing systematic comparison of how ion-polymer interactions can shape the properties of non-ionic and ionic hydrogels.

Despite their versatility, hydrogels are not suited for harsh tribological environments such as bearings or gear systems, where high contact pressures, shear rates, and temperatures exceed their mechanical and thermal stability (233). Their high water content also restricts their use in conventional mechanical systems due to the risk of corrosion. Nevertheless, hydrogels remain highly relevant in the fields, where softer contacts, biocompatibility and water-rich conditions dominate (233). Applications in medicine, cosmetics and food processing demonstrate their value as functional soft solids rather than as direct substitutes for industrial lubricants.

One of the most widely studied applications of hydrogels is biomedical lubrication, particularly in cartilage repair and osteoarthritis treatment (234–236). Blends of polyvinyl alcohol and hyaluronic acid have already been applied to restore lubrication in synovial joints (210). In addition, research by Hu et.al. (2020) demonstrated that natural hydrogels in combination with microgels from proteins can provide low friction coefficients (237). The effectiveness of hydrogels in these contexts is linked to hydration lubrication. In this mechanism a low-shear layer from the water within the polymer network is formed, reducing friction (38,39). The stability of this hydration layer depends strongly on the polymer–ion interactions within the hydrogel network. Divalent ions can interact with the polymer network, reinforcing the structure and offering a potential for improving hydrogels' lubricating properties (238). By understanding how divalent ions affect hydrogel behaviour, it may be possible to optimise lubricating properties of hydrogels and potentially tailor their behaviour in tribological contacts.

Despite the widespread use of natural hydrogels in food, biomedical and cosmetic applications, their tribological behaviour remains poorly understood. Existing studies usually examine a single hydrogel type or investigate the effect of polymer type or ion concentration in isolation. This creates a gap in understanding how hydrogel stiffness, viscoelasticity and ion-polymer interactions together influence lubrication in soft hydrated contacts. To address this gap, this study investigates five natural hydrogels and evaluates how their mechanical and tribological properties are modified by the addition of four industrially relevant divalent ions. A summary of the measured properties and their relevance is provided in Table 8.

Table 8. Summary of measured hydrogel properties.

Measured Parameter	*Method*	*Relevance*
Storage Modulus G'	Oscillatory rheology	Elastic resistance to shear
Loss Modulus G''	Oscillatory rheology	Viscous energy dissipation
Reduced Elastic Modulus E^*	Indentation testing	Network stiffness
Coefficient of Friction	Biotribology Machine	Frictional response

In this study frictional behaviour was measured experimentally and analysed using a two-term non-interacting model from Adams et al. (2007) (239). According to this model, the friction force F is a sum of deformation friction F_{def} and interfacial friction F_{int} terms, as shown in the equation below (239):

$$F = F_{def} + F_{int} = \beta \left(\frac{9}{128R}\right)^{\frac{2}{3}} \frac{P^{4/3}}{E^{*1/3}} + \tau A_{contact} \quad \text{(Equation 7)}$$

where $A_{contact}$ is the area over which adhesion forces operate. In this study this area was approximated by the contact area evaluated by Hertz contact model:

$$A_{contact} = \pi a_{Hertz}^2 , \quad a_{Hertz} = \left(\frac{3PR}{4E^*}\right)^{\frac{1}{3}} \quad \text{(Equation 8)}$$

Adams et al. (2007) suggests evaluating parameter β using the relationship $\beta = \pi \tan\delta$ (239). The loss ratio $\tan\delta$ is defined by a ratio of Loss modulus over Storage modulus and is evaluated experimentally for each hydrogel using rheological testing. In this study the moduli used for calculation of β were taken at an angular frequency of 2π rad/s, corresponding to the frequency of 1 Hz, used in the friction testing. Since β represents the fraction of energy dissipated through viscoelastic hysteresis, its value cannot exceed unity. Therefore, in the cases where $\pi \tan\delta > 1$, the value of β is capped at 1. The radius R and applied load P are constants, set out in the friction test procedure. The reduced elastic modulus E^* is evaluated individually using indentation testing. All the mentioned testing procedures are described in detail in Chapter 3. These calculations are based on a Hertz contact model, assuming that indentation depths during friction tests are negligible compared to the radius of contact and the thickness of the tested hydrogels. In addition, it is assumed that the hydrogel behaves as a linear elastic solid with negligible porosity, thus exhibiting a constant value of E^*. These assumptions are appropriate for the tested hydrogels under the tested conditions. Under applied load of 1 N the resulting indentation depths are only a few micrometres, which is small compared to the radius of curvature of the lens and the hydrogel thickness. Under such deformation, hydrogels behave predominantly elastically, and time-dependent effects are minimal over the short testing times (240). Therefore, treating hydrogels as linear elastic solids with a constant reduced elastic modulus provides a reasonable approximation for analysing deformation-related friction.

7.2. Non-Ionic Hydrogels

To provide a clear overview of how the gelation mechanism affects the hydrogel behaviour, the results are presented according to gelation type: non-ionic hydrogels (carrageenan and agar) and ionic hydrogels (phytagel, alginate and pectin). This structure allows direct comparison of how the chosen divalent ions (Fe^{2+}, Cu^{2+}, Zn^{2+} and Ca^{2+}) influence material and rheological properties, as well as tribological performance of hydrogel networks formed by two types of physical crosslinking: non-ionic and ionic.

7.2.1. Materials

Natural polymers: agar (A1296), carrageenan (C1013) and divalent ion chlorides: calcium chloride (C1016), zinc chloride (793523), iron (II) chloride (372870) and copper (II) chloride (751944); were all obtained from Sigma-Aldrich, UK.

7.2.2. Non-Ionic Hydrogel Preparation

Due to differences in the crosslinking mechanisms of the chosen natural polymers, the preparation methods distinguish between non-ionic and ionic hydrogels. As non-ionic hydrogels do not require the addition of ions to produce stable hydrogels, a base hydrogel without any ions as well as ion-doped versions were produced.

To produce the hydrogel samples for the tests, custom-made acrylic gel moulds were used. These moulds are shown in Figure 60. Each mould geometry was selected to correspond to the requirements of the tests undertaken:

- Indentation tests: Three samples with a diameter of 20 mm and a thickness of 2 mm were prepared for each tested hydrogel. The 20 mm diameter was chosen to fit securely within the indenter setup, while minimising edge effects. The thickness of 2 mm ensured the sample remains much smaller than the indenter radius of 10 mm, supporting the assumptions of the Hertz contact model as closely as possible.
- Rheological tests: Three samples with diameter of 25 mm and thickness of 2 mm were prepared for each tested hydrogel. The chosen diameter matched the rheometer plate diameter, ensuring full contact between the hydrogel and the plates.
- Friction tests: acrylic Petri dishes of 35 mm diameter were used to cast hydrogel layer large enough to cover the sliding contact region. The larger surface area and thickness reduced edge effects during the reciprocating motion. The Petri dish design enabled direct mounting on the top of the load cell, ensuring accurate measurement of the friction force.

The use of acrylic moulds provided smooth surfaces and allowed easy demoulding, thus reducing the number of surface defects that could affect the measurements.

The pure non-ionic hydrogels were produced by mixing the needed amounts of natural polymer into deionised water from a Milli-Q purification system (Millipore, Canada). The mixing weights for each gelling polymer were chosen to be 1 wt.% of the hydrogel solution and are shown in Table 9 (75,219,241). The hydrogel solution was obtained by stirring the required amount of powder and deionised water in a 60 ml capped borosilicate bottle for two

hours on IKA® C-MAG HS hotplate stirrer, which was kept at a constant temperature of 80°C. After mixing, the hot hydrogel solution was poured into custom-made acrylic forms and petri dishes, shown in Figure 60. The forms with hydrogels were left in fridge at a constant temperature of 4°C overnight to ensure complete gelation.

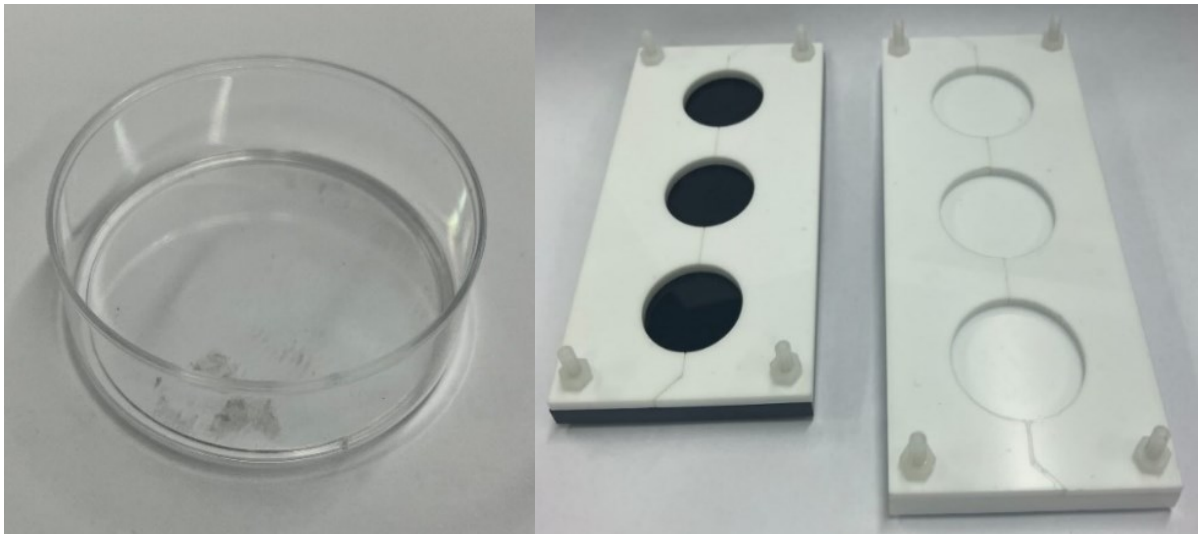


Figure 60 Acrylic gel forms for hydrogel preparation: Petri dish (left), Ø20 mm and Ø25 mm acrylic forms (right).

The ion-doped non-ionic hydrogels were produced by mixing two solutions: a hydrogel solution and an ion solution. A similar procedure as before was used to obtain the hydrogel solution. The required amount of natural polymer from Table 9 was stirred with 40 g of deionised water in a 60 ml capped borosilicate bottle for two hours on IKA® C-MAG HS hotplate stirrer, kept at a constant temperature of 80°C. The ion solution was produced by mixing 0.05 g of the ion chloride (calcium, iron, copper, or zinc chloride) with the remaining amount of deionised water from Table 9. In the last 30 minutes of stirring the ion solution is added to the hydrogel solution to obtain the ion-doped hydrogel solution. After mixing the hot solution was poured into custom-made acrylic forms, which were left in a fridge at a constant temperature of 4°C overnight.

Table 9 Amounts of polymer and deionised water for base non-ionic hydrogel preparation.

Natural gelling polymer	Agar	Carrageenan
Weight of polymer (g)	0.5	0.5
Weight of deionised water (g)	49.5	49.5
Weight of chosen chloride (g)	0.05	0.05

7.2.3. Results

7.2.3.1. Storage and Loss Moduli

The viscoelastic behaviour of hydrogels was evaluated by oscillatory shear frequency sweeps using a parallel-plate geometry at a constant strain of 10% and frequencies ranging from 0.2 rad/s to 200 rad/s. The detailed procedure is described in the Section 3.2.2 on page 47. In these measurements, the angular frequency (rad/s) corresponds to the rate of oscillatory deformation applied to the sample. Lower angular frequencies represent slower deformations, and higher angular frequencies correspond to fast loading cycles relevant to dynamic conditions.

Figure 61a and Figure 61b show the variation of storage modulus G' with angular frequency for carrageenan and agar hydrogels, respectively. For both polymers, the storage modulus exhibits a near-linear increase with frequency when plotted on a log-log scale. This observation indicates the stiffening of the gels under faster deformations. For carrageenan, addition of ions significantly reinforced the hydrogel structure. The largest values of storage moduli across the measured frequency range were obtained by Ca^{2+}-doped carrageenan. In contrast, pure carrageenan hydrogel exhibited the lowest storage modulus and followed the same linear-increase trend, observed in the doped versions. Agar hydrogels followed the similar trend; however, the storage moduli values are lower than carrageenan ones. Zn^{2+} and Ca^{2+} produced the largest increases in storage modulus. The addition of Fe^{2+} ions resulted in the weakest gel structure with the values of storage modulus being an order of magnitude lower, than of other agar hydrogels.

Figure 61c and Figure 61d show the corresponding loss modulus G'' variation with angular frequency. Carrageenan hydrogels exhibited relatively stable loss modulus values across all tested angular frequencies and followed the same ion-related trends as the corresponding storage moduli. Above an angular frequency of ≈15 rad/s all ion-doped carrageenan samples experienced a noticeable rise, which may reflect instrumental artifacts such as inertia effects, partial slip or edge fracture (107,242). Edge fracture refers to a rheological instability in which the outer rim of the sample fails or tears under shear, causing material at the edge to deform or detach. This leads to distortions in the torque signal and artificially elevated moduli at higher frequencies (107,242). Agar hydrogels displayed a clearer ion dependence with Ca^{2+} and Zn^{2+} ions maintaining the highest loss moduli and Fe^{2+} providing the weakest response.

At angular frequencies, larger than 20 rad/s, several hydrogels exhibited sharp increases and irregular fluctuations in both storage and loss moduli. Such observations appear consistently across different samples and do not align with the expected gel behaviour, meaning that limitations of rheometer-sample interaction are considered the most likely cause (107,242). Therefore, all values used for evaluation of loss ratios were extracted at 6.28 rad/s, which is within the stable region of the moduli sweeps. The chosen frequency also corresponds to a frequency of 1 Hz, used in friction tests.

The combination of storage and loss moduli provides an insight into the relative contributions of elastic and viscous components of the hydrogels. To further quantify these contributions, the loss ratio $\tan\delta$ was calculated for each hydrogel at 1 Hz. These values are summarised in Table 10, and are used for evaluating the interfacial shear strength in the later section.

Table 10. Loss ratio of tested non-ionic hydrogels.

$tan\,\delta$	*Pure*	*Fe^{2+}*	*Cu^{2+}*	*Zn^{2+}*	*Ca^{2+}*
Carrageenan	0.154	0.178	0.180	0.178	0.205
Agar	0.370	0.275	0.272	0.185	0.245

7.2.3.2. Reduced Elastic Modulus

Reduced elastic moduli were obtained from indentation testing, following procedures described in section 3.3.1 on page 49. The obtained values for non-ionic hydrogels are presented in Figure 62. Pure carrageenan hydrogel exhibited a relatively low reduced elastic modulus of 11 kPa. The addition of metal ions led to a significant increase in stiffness, with reduced elastic moduli increasing to 31-46 kPa. The largest increase was achieved by the addition of Zn^{2+} ions. In contrast, Agar hydrogels showed a different response to ion incorporation. The addition of metal ions resulted in inconsistent effects on mechanical stiffness. Cu^{2+} ions showed a reduced elastic modulus of 15 kPa, resembling the one of unmodified Agar hydrogel. Both Zinc and Calcium ions showed an increase of reduced elastic modulus to 23 kPa. Notably, the addition of Fe^{2+} ions reduced the stiffness to just 9 kPa.

7.2.3.3. Friction

The coefficients of friction (COF) obtained from the Biotribology Machine (BTM, PCS Instruments, UK) are shown in Figure 63. The friction tests were conducted under a constant normal load of 1 N, at a reciprocating frequency of 1 Hz and a stroke length of 10 mm. Carrageenan hydrogels have shown an increase in coefficient of friction upon ion addition,

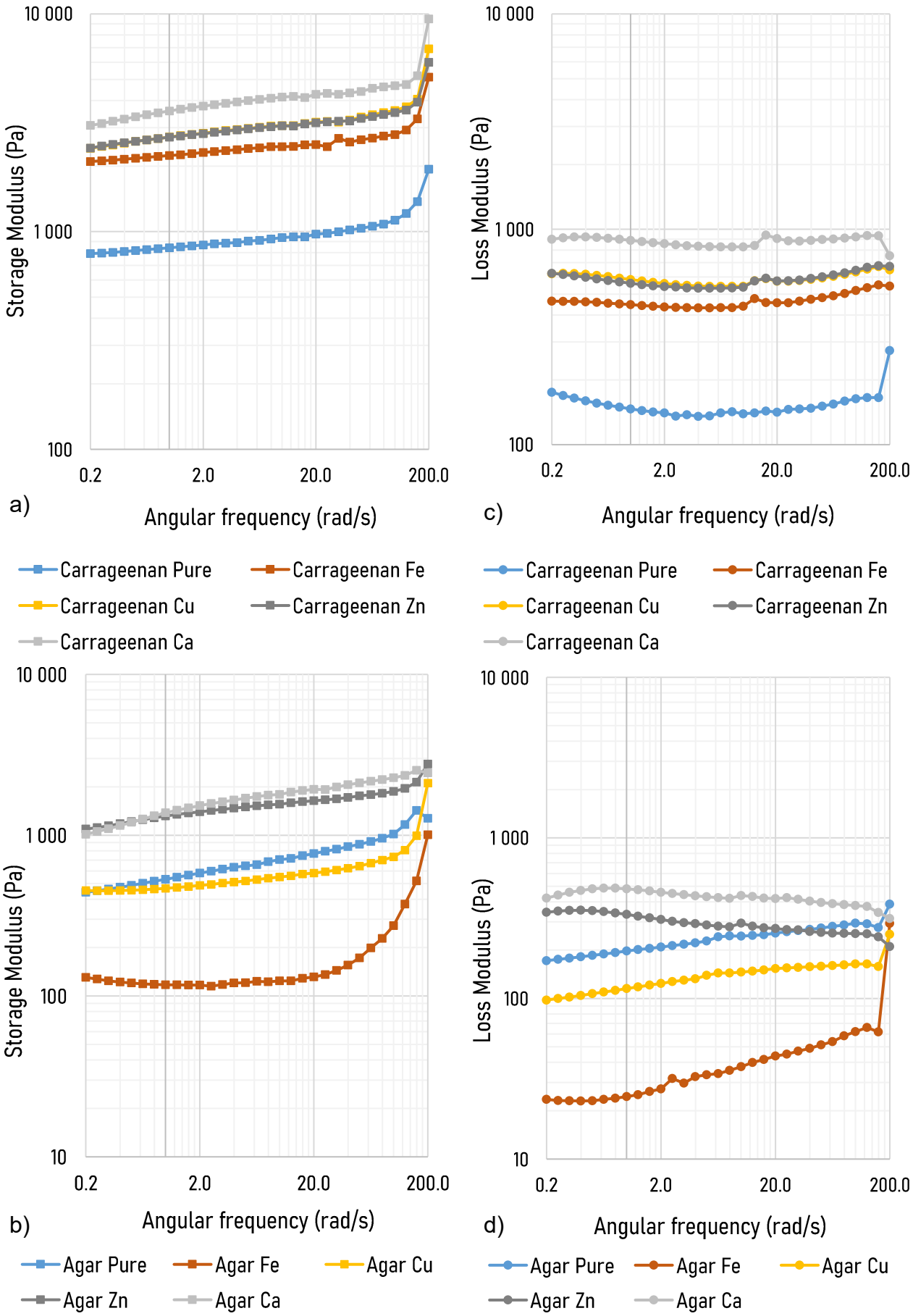


Figure 61. Obtained storage and loss moduli distributions for non-ionic hydrogels.

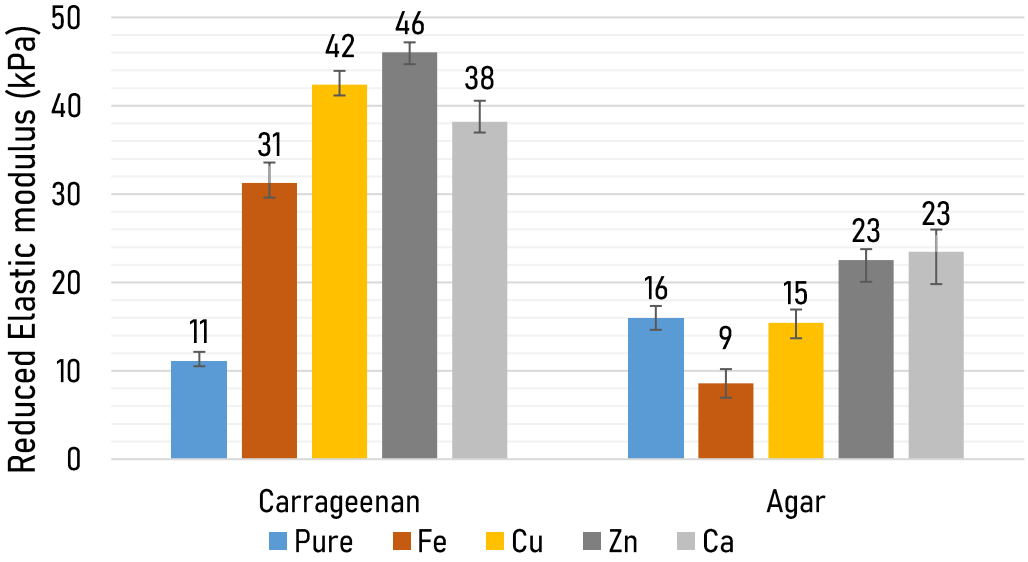


Figure 62. Obtained reduced elastic moduli for non-ionic hydrogels.

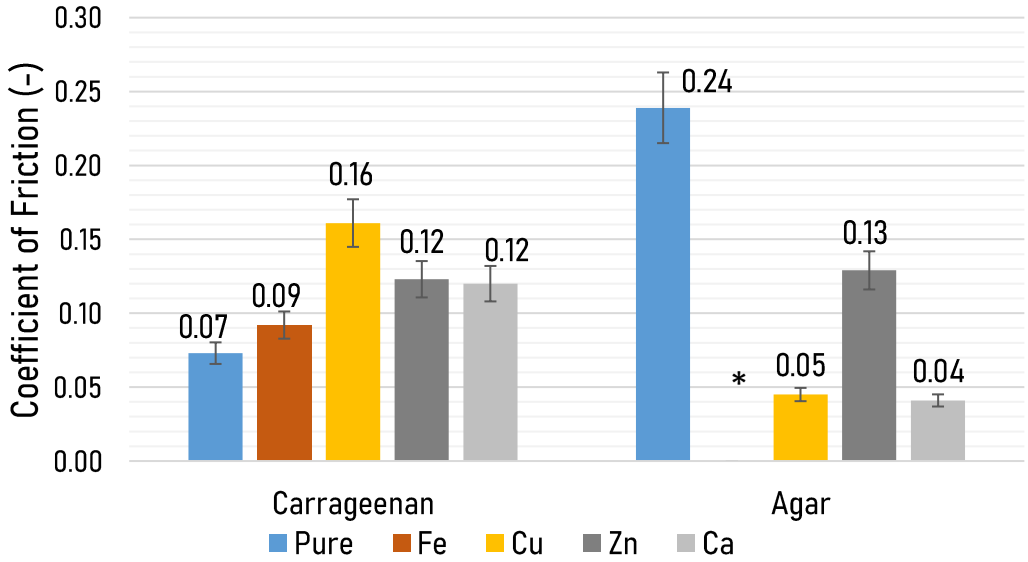


Figure 63. Obtained coefficients of friction for non-ionic hydrogels. Agar Fe (star) was not assessed due to lack of structural integrity.

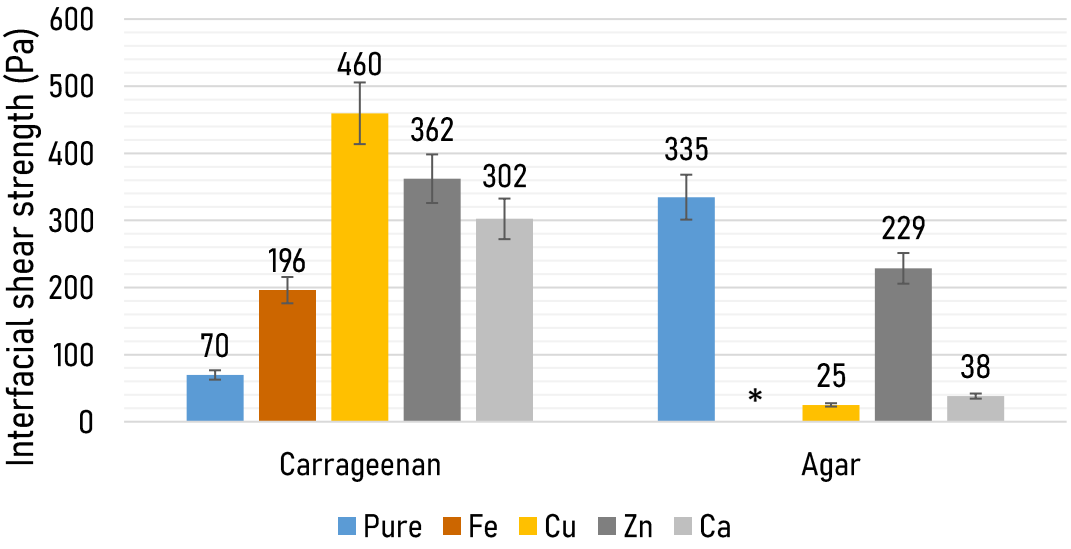


Figure 64. Interfacial shear strength of non-ionic hydrogels. Agar Fe (star) was not assessed due to lack of structural integrity.

rising from 0.07 for pure hydrogel to a maximum of 0.16 for copper-doped one. In contrast, agar hydrogels demonstrated the opposite trend. The coefficient of friction of pure agar was reduced through addition of ions from 0.24 to the minimum value of 0.04 for calcium-doped agar. The frictional testing of agar hydrogel with Fe^{2+} ions could not be conducted, as these samples were mechanically unstable and collapsed during the friction test.

7.2.3.4. Interfacial Shear Strength

By rearranging Equation 7 for interfacial shear strength (τ) and inputting the obtained coefficients of friction, reduced elastic moduli and loss ratios from Table 10, the values of τ are evaluated and are provided in Figure 64. For carrageenan hydrogels, the addition of ions significantly enhanced interfacial shear strength, increasing from 70 Pa for pure hydrogel to values ranging between 196 Pa and 460 Pa. The largest shear strength was observed with addition of copper ions. In contrast, agar hydrogels demonstrated a decrease in τ upon addition of ions. The pure hydrogel exhibited the shear strength of 335 Pa, while addition of Cu^{2+} and Ca^{2+} ions resulted in lower values of 25 Pa and 38 Pa, respectively. As agar hydrogel with Fe^{2+} collapsed during friction testing, its interfacial shear strength could not be calculated and was excluded.

7.2.4. Summary

The tested non-ionic hydrogels demonstrated contrasting behaviours in response to the addition of divalent metal ions. Carrageenan hydrogels showed consistent reinforcement with all ions. Compared to the pure carrageenan hydrogel, the reduced elastic moduli, storage moduli and loss moduli increased upon addition of ions. The largest increase in storage and loss moduli was observed with addition of Ca^{2+} ions. The highest reduced elastic modulus was achieved with Zn^{2+}. These changes accompanied by the increase in friction and interfacial shear strength. The highest values of coefficient of friction and τ were obtained with Cu^{2+}-doped carrageenan hydrogel. Overall, ion addition improved stiffness of the carrageenan hydrogel and promoted stronger resistance to shear during sliding.

In contrast, agar hydrogels provided a less uniform response to ion addition. Zn^{2+} and Ca^{2+} ions promoted modest increases in reduced elastic modulus as well as in storage and loss moduli. Doping with Fe^{2+} ions resulted in mechanically weak hydrogels, that collapsed during friction testing. However, a reduction of friction was experienced by all tested ion-doped agar hydrogels compared to the pure agar. The lowest coefficient of friction was

achieved with addition of Ca^{2+} ions. Interfacial shear strengths of agar hydrogels consistently decreased with addition of ions, in clear contrast to carrageenan's response.

To summarise, ion addition caused stiffening and higher friction in carrageenan hydrogels, while agar hydrogels did not stiffen to the same extent but achieved reduced friction when doped with ions. These opposite trends reflect the different gelation mechanisms of carrageenan and agar, establishing a clear distinction of non-ionic hydrogel response to modification with ions.

7.3. Ionic Hydrogels

7.3.1. Materials

Natural polymers: sodium alginate (71238), pectin citrus (P9135), phytagel (P8169); and divalent ion chlorides: calcium chloride (C1016), zinc chloride (793523), iron (II) chloride (372870) and copper (II) chloride (751944); were all obtained from Sigma-Aldrich, UK.

7.3.2. Ionic Hydrogel Preparation

The ionic hydrogels were produced by mixing two solutions: hydrogel solution and ion solution. The hydrogel solution was obtained by mixing the required amount of natural polymer from Table 11 with 40 g of deionised water in a 60 ml capped borosilicate bottle for two hours on IKA® C-MAG HS hotplate stirrer, kept at a constant temperature of 80°C. The ion solution was produced by mixing of the ion chloride (calcium, iron, copper, or zinc chloride) with the rest of required deionised water from Table 11. The differences in polymer and chloride weights across ionic hydrogels reflect their distinct minimum gelling concentrations and ion-binding requirements for stable hydrogel formation (78,212,243).

Table 11 Weights of natural polymers, deionised water and ion chlorides for ionic hydrogel preparation.

Natural gelling polymer	Pectin from citrus fruit	Sodium Alginate	Phytagel
Weight of polymer (g)	2.5	1.0	0.25
Weight of deionised water (g)	47.5	49.0	49.75
Weight of chosen chloride (g)	2.0	1.0	0.05

To produce the hydrogel specimens, the volumes of both hydrogel and ion solutions, shown in Table 12, were put into the moulds using a micropipette, stirred to obtain the uniform mixture and left in a fridge at a constant temperature of 4°C for a minimum of 2 hours or overnight.

Table 12. The volumes of hydrogel and ion solutions used for filling the respective acrylic forms.

Acrylic forms	Ø20 mm diameter	Ø25 mm diameter	Acrylic Petri dish
Hydrogel solution (ml)	0.51	0.79	5.23
Ion solution (ml)	0.12	0.19	1.28

7.3.3. Results

7.3.3.1. Storage and Loss Moduli

The same procedure, described in the Section 3.2.2 on page 47, was followed to obtain the viscoelastic properties of ionic hydrogels. The obtained distributions of storage and loss moduli for ionic hydrogels are shown in Figure 65a-c and Figure 65d-f, respectively.

All Cu^{2+}-doped ionic hydrogels exhibited the irregular distributions of moduli with sharp fluctuations and values several orders of magnitude below the moduli of the other tested samples. These observations reflect the poor contact between the hydrogel and rheometer plates, leading to a consistent slip during testing. The mismatch between the stable visual appearance of the samples and the measured rheological behaviour further support the presence of slip. Therefore, the obtained rheological distributions for Cu^{2+}-doped ionic hydrogels were not considered reliable and were not used for further calculations.

Across most tested samples, the storage modulus follows a near-linear increase with angular frequency on the log-log scale, same as observed with non-ionic hydrogels. Clear ion-dependent effects were observed in the tested ionic hydrogels. Alginate hydrogels doped with Ca^{2+} ions produced the largest storage modulus values across all tested hydrogels. Phytagel hydrogels exhibited moderate storage moduli with less pronounced ion-dependent effects. Pectin hydrogels provided the highest storage modulus upon addition of Zn^{2+} ions. The corresponding distributions of loss modulus are provided in Figure 65d-f. The same trends outlined for storage modulus were observed in the distributions of loss modulus.

Similarly to non-ionic hydrogels, at angular frequencies larger than 20 rad/s fluctuations in moduli behaviour were observed. As discussed in Section 7.2.3.1, such behaviour is most likely caused by rheometer artifacts, including inertia effects, partial slip or edge fracture (107,242). In addition, alginate hydrogels with Ca^{2+} and Zn^{2+} experienced a dip in storage modulus, which is attributed to local network rearrangements or water redistribution (244).

As with the non-ionic hydrogels, the loss ratio was calculated for each ionic hydrogel at a frequency of 6.28 rad/s (1 Hz). The obtained values are summarised in Table 13 and are used for the evaluation of interfacial shear strength in later section.

Table 13. Loss ratios of tested ionic hydrogels.

$tan\,\delta$	Fe^{2+}	Zn^{2+}	Ca^{2+}
Phytagel	0.428	0.387	0.568
Alginate	0.239	0.432	0.568
Pectin	0.399	0.417	0.205

7.3.3.2. Reduced Elastic Modulus

Reduced elastic moduli were obtained from indentation testing, following procedures described in section 3.3.1 on page 49. The obtained values of reduced elastic moduli are shown in Figure 66. For phytagel hydrogels, the addition of different ions resulted in values of reduced elastic modulus ranging from 29 kPa with Ca^{2+} ions to 41 kPa with Zn^{2+} ions. This narrow range suggests a less pronounced ion-specific effect on hydrogel stiffness. In contrast, Alginate hydrogels exhibited a strong ion-specific response. The addition of Fe^{2+} and Cu^{2+} ions resulted in relatively low reduced elastic moduli of 12 and 13 kPa, respectively. A significantly larger reduced elastic modulus of 102 kPa was obtained with addition of Ca^{2+} ions. For Pectin hydrogels, a preference for Cu^{2+} and Zn^{2+} ions was observed, resulting in reduced elastic moduli of 95 kPa and 61 kPa, respectively. In contrast, Fe^{2+} and Ca^{2+} ions produced weaker hydrogels, with reduced elastic moduli of 23 kPa and 19 kPa, respectively.

7.3.3.3. Friction

As for non-ionic hydrogels, friction tests were conducted under a constant normal load of 1 N, at a reciprocating frequency of 1 Hz and a stroke length of 10 mm. The obtained coefficients of friction for ionic hydrogels are presented in Figure 67. Phytagel hydrogels exhibited coefficients of friction ranging from 0.06 for Zn^{2+}-doped hydrogel to 0.14 for Ca^{2+}-doped one. In contrast, alginate-based hydrogels showed larger variation, with Fe^{2+} ions showing friction coefficient of 0.27. Alginate hydrogels with Zn^{2+} and Ca^{2+} ions showed significantly lower coefficients of friction of 0.10 and 0.11, respectively. Pectin hydrogels with the tested divalent ions showed coefficients of friction, ranging from 0.19 to 0.25. Hydrogel from pectin with Ca^{2+} ions was mechanically unstable and collapsed during the friction test, preventing the measurement.

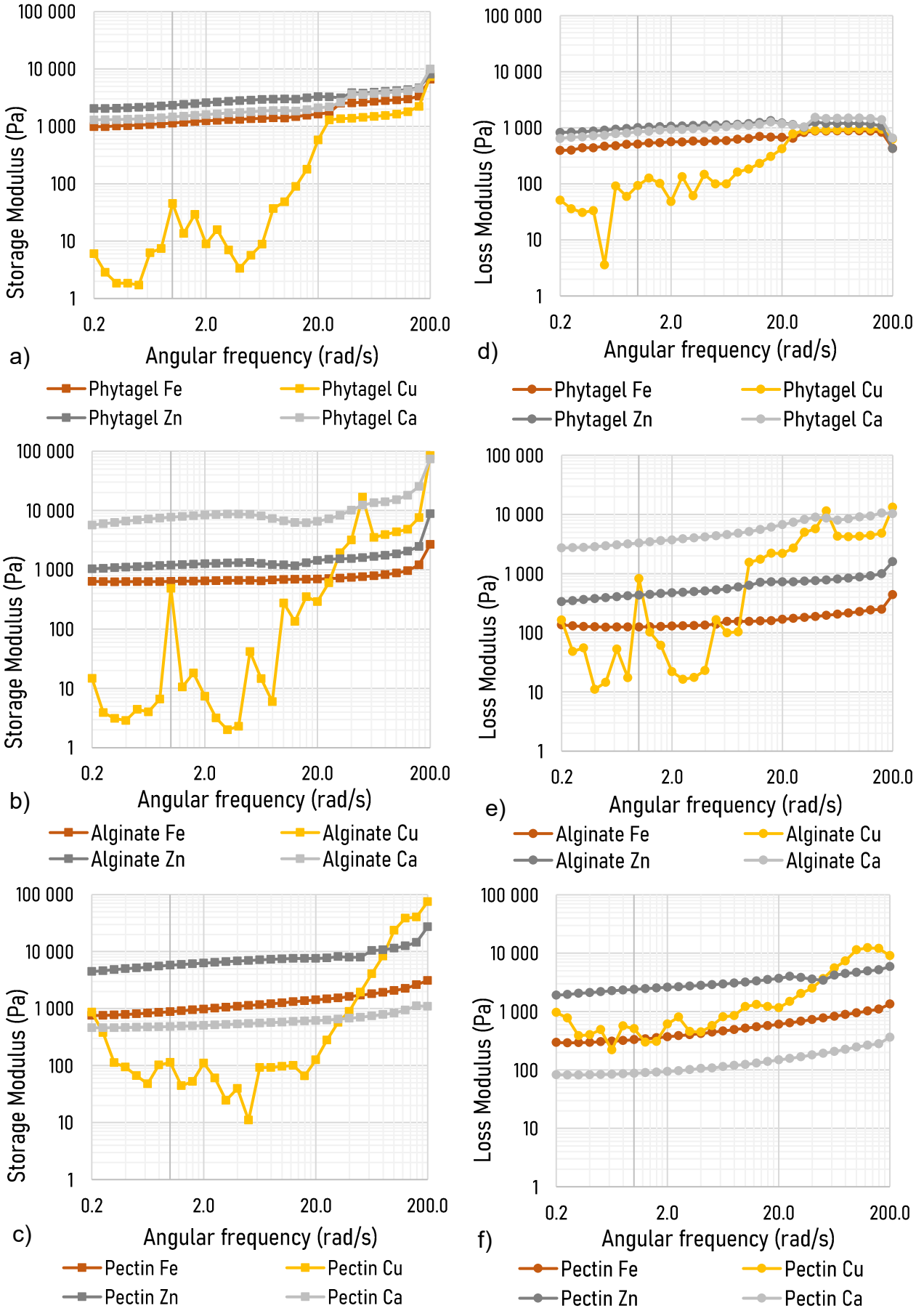


Figure 65. Obtained storage and loss moduli distributions for ionic hydrogels.

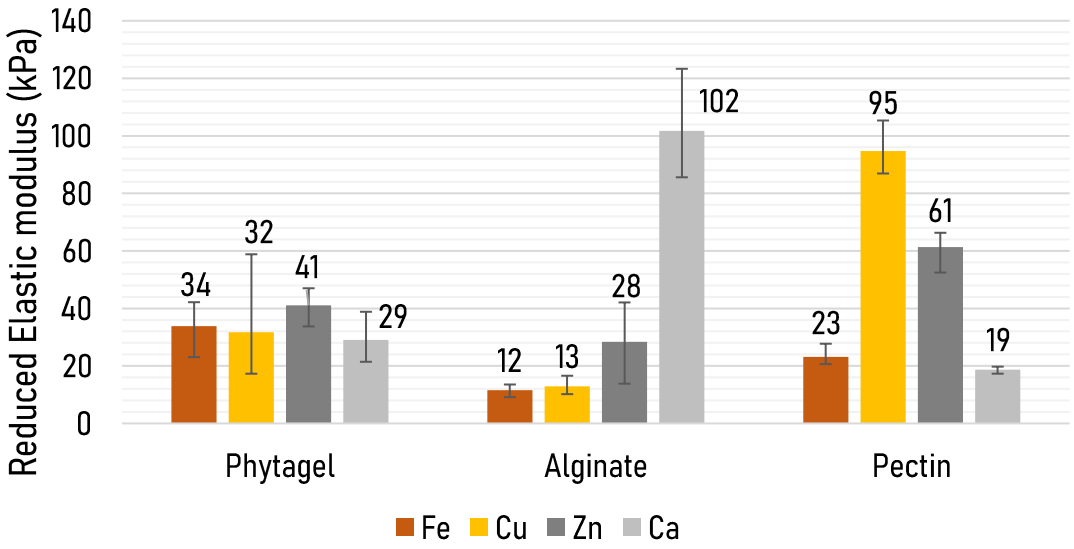


Figure 66. Obtained reduced elastic moduli for ionic hydrogels.

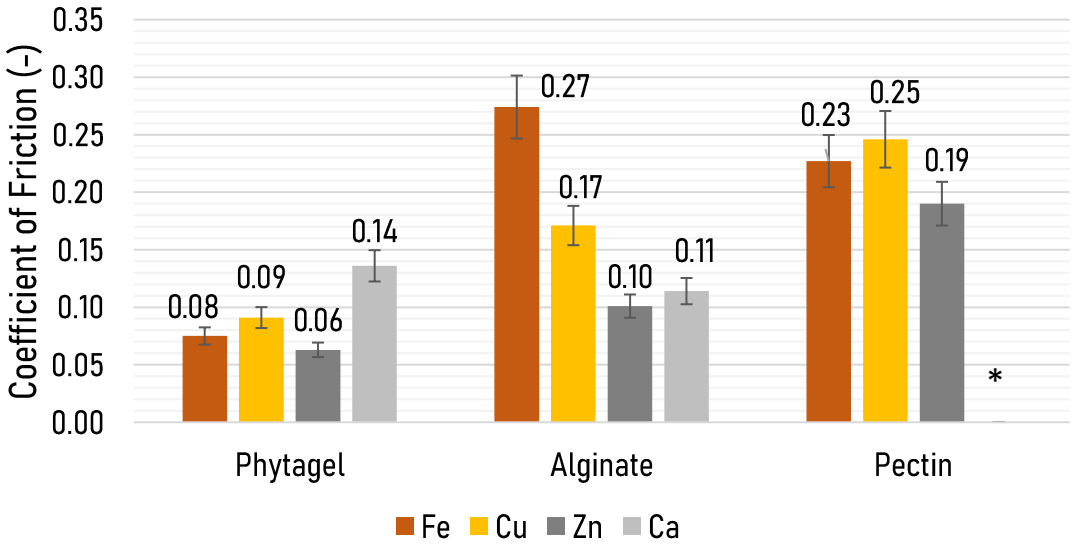


Figure 67. Obtained coefficients of friction for ionic hydrogels. Pectin Ca (star) was not assessed due to lack of structural integrity.

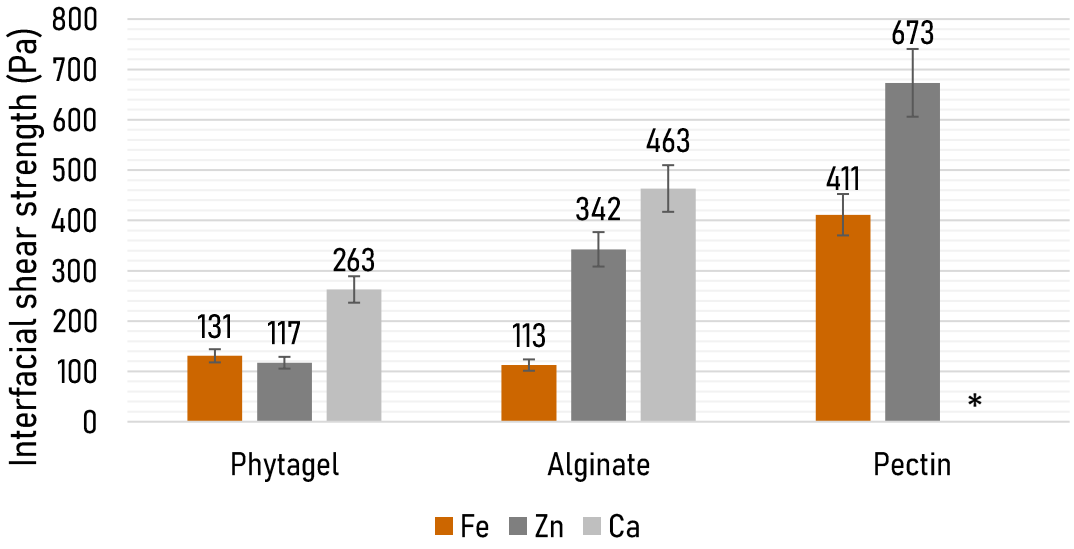


Figure 68. Interfacial shear strength for ionic hydrogels. Pectin Ca (star) was not assessed due to lack of structural integrity.

7.3.3.4. Interfacial Shear Strength

Using the same procedure as outlined in the section 7.2.3.4, the values of interfacial shear strength (τ) were evaluated for ionic hydrogels and are shown in Figure 68. Due to consistent slip during rheological assessment, the values of τ for Cu^{2+}-doped ionic hydrogels could not be calculated and are not included. Similarly, the Ca^{2+}-doped pectin hydrogel is excluded due to failure during frictional testing. Phytagel hydrogels with Fe^{2+} and Zn^{2+} ions showed relatively low values of τ, 131 Pa and 117 Pa, respectively. A higher value of 263 Pa was obtained for phytagel hydrogel with addition of Ca^{2+} ions. Alginate hydrogels demonstrate stronger shear strengths with values of 463 for Ca^{2+} ions, 342 Pa for Zn^{2+} ions. A lower shear strength of 113 Pa was obtained for Fe^{2+}-doped phytagel. Pectin hydrogels show one of the highest interfacial shear strength values: 411 Pa for Fe^{2+} ions and a maximum of 673 Pa for Zn^{2+} ions.

7.3.4. Summary

The tested ionic hydrogels demonstrated distinct ion-specific behaviours across their rheological, mechanical and tribological properties. Phytagel hydrogels did not exhibit pronounced changes in properties upon addition of ions. The obtained friction coefficients remained low across all ions, ranging from 0.06 to 0.14, and the highest interfacial shear strength was 263 Pa for Ca^{2+}-doped phytagel hydrogel.

Alginate hydrogels exhibited a strong dependence on the added ion. Ca^{2+} doping produced the stiffest hydrogel with the highest reduced elastic modulus of 102 kPa and a low friction coefficient of 0.11. In contrast, the addition of Cu^{2+} and Fe^{2+} ions resulted in weaker hydrogels with reduced elastic moduli of 12-13 kPa and significantly higher coefficients of friction, up to 0.27 for Fe^{2+}.

Pectin hydrogels displayed a clear preference for Zn^{2+} and Cu^{2+} ions. Hydrogels doped with Zn^{2+} and Cu^{2+} both resulted in high stiffness of 61 kPa and 95 kPa, respectively, and the highest interfacial shear strength of 673 Pa for Zn^{2+}. However, the coefficients of friction of pectin hydrogels are consistently higher than for phytagel or alginate hydrogels, ranging from 0.19 to 0.25.

In summary, ionic hydrogels displayed a stronger preference for specific ions, compared to non-ionic hydrogels. Alginate provided the optimal reinforcement with Ca^{2+} and pectin formed strong networks with Zn^{2+} and Cu^{2+}. In contrast, phytagel provided a more uniform response across all tested ions. These contrasting behaviours highlight the importance of

polymer-ion interactions in determining the balance between stiffness, friction and interfacial strength in ionic hydrogels.

7.4. Discussion

In this study the material properties and frictional performance of hydrogels made from natural polysaccharides and their response to doping with divalent metal ions were explored. The chosen polysaccharides: carrageenan, agar, phytagel, alginate and pectin, all exhibit physical crosslinking during gelation. Divalent metal ions of Fe^{2+}, Cu^{2+}, Zn^{2+} and Ca^{2+} were selected due to their wide presence in most industrial tribological applications and their ability to alter the hydrogel structure. The results highlight how both mechanical and frictional behaviours are affected by the underlying gelation mechanism, both non-ionic and ionic, and the specific divalent ion added.

7.4.1. Effect of Gelation Mechanisms on Hydrogel Properties

The observed differences in the material and tribological behaviours across the tested hydrogels can be linked to their underlying gelation mechanisms. These mechanisms determine the formation of the polymer network and govern the balance between stiffness, friction and interfacial shear strength.

For the non-ionic hydrogels, carrageenan consistently stiffened with the addition of divalent metal ions. The reduced elastic modulus, storage and loss moduli and interfacial shear strength all increased upon ion addition. Such behaviour is consistent with the coil-to-helix transition mechanism of carrageenan. During gelation, carrageenan chains form double helices, which can be further stabilised by ions occupying inter-helix sites. Previous studies have shown that Ca^{2+} and K^{+} ions promote helix aggregation and increase network density in carrageenan, leading to stiffer gels (245). The present results extend this understanding by demonstrating that other divalent ions, such as Zn^{2+}, Cu^{2+} and Fe^{2+}, can also stabilise carrageenan helices, although with differing magnitudes of stiffness and friction. Moraes et al. (2024) investigated the rheology of κ/ι-carrageenan hydrogels at the same polymer concentration of 1 wt.% in the presence of K^{+} ions, reporting storage moduli from 24 Pa to 21.5 kPa depending on carrageenan composition and strain amplitude (241). In the present study the pure carrageenan hydrogel exhibited storage moduli in the range of 0.8-2 kPa at 10% strain rate, while ion-doped formulations showed increased storage moduli of 2.1-9.5 kPa across the tested frequency range. The storage modulus values from literature span over a broader range due to the differences in the used carrageenan types, ion chemistry

and test protocols. The magnitudes and ion-induced reinforcement trends in the present study are in good agreement with previously reported rheological behaviour of carrageenan hydrogels.

In contrast, agar responded to ion addition with less predictable changes in mechanical properties. In particular, Fe^{2+}-doped agar hydrogel produced a mechanically unstable hydrogel that collapsed during friction testing. Agar hydrogels are formed by thermoreversible hydrogen bonding between helices. The incorporation of divalent ions appears to disrupt hydrogen bonding and helix packing rather than reinforce the hydrogel network. Similar destabilisation of agar hydrogels by metal ions has been reported in earlier studies, where small additions of Li^{+} and Na^{+} salts reduced gel strength and modified the network microstructure (246). Bertasa et al. (2020) reported the storage moduli of 2.5-35 kPa and loss moduli of 0.1-0.4 kPa for 1 w/v.% agar hydrogels tested at low strain amplitudes of 0.05-0.1% (219). In the present study storage moduli ranged from 0.13-2.5 kPa and the loss moduli from 24-480 Pa. While the loss moduli fall within the literature-reported ranges, the lower storage moduli reflect the much higher applied strain amplitude of 10% used in this study. Despite the lack of mechanical reinforcement, ion-doped agar hydrogels exhibited reduced friction. This behaviour is attributed primarily to changes in water-binding capacity and interfacial hydration rather than bulk network stiffening, highlighting the decoupling of friction reduction from elastic modulus in hydrogen-bonded hydrogel systems.

For the ionic hydrogels, the dependence on the type of ion was much stronger. Alginate showed a clear preference towards Ca^{2+} ions, with Ca^{2+}-doped hydrogels showing the highest reduced elastic modulus, storage and loss moduli among all tested alginate formulations. This behaviour is fully consistent with the established egg-box model of alginate gelation, in which Ca^{2+} acts as the most effective crosslinker among common divalent cations (75,220,247). Previous studies on ionically crosslinked alginate hydrogels report the elastic moduli in the 2-100 kPa range, depending on polymer properties, polymer and Ca^{2+} concentrations (247). The elastic moduli obtained in this study (12-102 kPa) fall within this expected range. Moderate reinforcement was achieved with addition of Zn^{2+} ions, while Fe^{2+} and Cu^{2+} ions failed to create strong networks. This ion specific response aligns with previous findings that multivalent ions differ significantly in their binding affinity and coordination geometry with alginate chains, resulting in weaker or heterogeneous crosslinking for non-calcium ions (220,247).

Phytagel, in contrast, forms hydrogel networks by aggregation of double helices with ion-mediated junction zones. The observed weaker ion-specific response indicates that formation of junction zones is less sensitive to the type of added ion, which is consistent with other studies on gellan gum gels (248,249). Zhou et al. (2019) reported values of elastic moduli 15-113 kPa for different concentrations of phytagel polymer in a variety of different salts (250). The same study also reported ranges of 1.5-10 kPa and 0.1-3.5 kPa for storage and loss moduli, respectively (250). In the present study, the reduced elastic moduli ranged 29-41 kPa, which is well within the expected ranges. The storage and loss moduli obtained in present study are within 1.0-10 kPa and 0.4-1.5 kPa, respectively. While both ranges fall within the literature-reported ones, the loss moduli are concentrated towards the lower end of the reported spectrum, indicating reduced viscous dissipation.

Pectin displayed a distinct behaviour, with Zn^{2+} and Cu^{2+} ions producing the strongest networks and highest interfacial shear strengths. The observed response can be attributed to specific interactions between divalent ions and the carboxyl groups of the pectin chains. Previous studies confirm that Zn^{2+} forms strong interfacial complexes with pectin (228). Such binding explains why addition of Zn^{2+} ions promoted high interfacial shear strength despite only moderate storage and loss modulus values. Vancauwenberghe et al. (2017) investigated low-methoxy pectin hydrogels with addition of smaller amounts of Ca^{2+} ions, reporting the storage and loss moduli in 0.8-3.0 kPa and 30-800 Pa ranges, respectively (251). In the present study, the Ca^{2+}-doped pectin hydrogel exhibited storage moduli of 0.5-1.1 kPa and loss moduli of 80-365 Pa, which both fit within the literature-reported ranges.

Overall, the numerical ranges of storage moduli, reduced elastic moduli and loss moduli obtained in this study fall within or close to those previously reported for food-grade polysaccharide hydrogels of comparable concentration and gelation mechanism. While direct one-to-one comparison is limited by differences in strain amplitude, frequency range and ions chemistry between studies, the observed orders of magnitude and ion-dependent trends are consistent with established rheological behaviour reported in literature. These comparisons confirm that the gelation mechanism plays a central role in governing both the mechanical stiffness and tribological response of polysaccharide hydrogels. Helix-stabilising mechanisms, like in carrageenan and alginate, favour the formation of stiffer networks and higher shear strengths upon addition of ions. In contrast, the hydrogen-bonding gelation mechanism of agar is more susceptible to ion-induced disruption. Pectin's carboxyl-based ion coordination highlights how strong interfacial interactions can dominate frictional

behaviour even when hydrogel stiffness remains moderate. This highlights that when designing hydrogel-based biolubricants, it is important to consider material stiffness, bulk rheology and interfacial lubrication mechanisms.

7.4.2. Mesh Size

In addition to the material and rheological characterisations from previous sections, the network structure of the hydrogels was assessed through the calculation of mesh size ξ. The mesh size represents the average distance between crosslinking sites in the polymer network and is an important factor in water retention, load-bearing and interfacial interactions (252–254). Mesh size ξ was evaluated from the storage modulus G' using the adapted formula from Karvinen et al. (2019) (252):

$$\xi = \left(\frac{k_B T}{G'}\right)^{\frac{1}{3}} \quad \text{(Equation 9)}$$

where $k_B = 1.38 \times 10^{-23}\, J/K$ is Boltzmann constant and T is the absolute temperature of hydrogel in degrees Kelvin (252). For consistency, the used storage modulus values for mesh size calculations were taken at an angular frequency of 1 Hz, corresponding to the same frequency used in the calculation of loss ratio and interfacial shear strength. This approach provides a defined reference point across hydrogel types. However, it must be noted that the calculated mesh size values are semi-quantitative, due to the frequency dependence of storage modulus G'. Moreover, the calculation assumes an ideal, isotropic network and purely entropic elasticity, which are significant simplifications for physically crosslinked hydrogels (255,256). These assumptions neglect network defects, chain length distribution and dangling ends, that affect the modulus-derived estimates of mesh size (255–257). Thus, the values of mesh size should be treated as comparative indicators of network density rather than absolute measures of structural spacing.

The calculated mesh sizes for non-ionic hydrogels are shown in Figure 69. Carrageenan displayed a consistent reduction in mesh size upon ion addition from 17 nm in the pure hydrogel to 10-12 nm with divalent ions. This reduction confirms the formation of denser networks, consistent with the increases in stiffness and interfacial shear strength observed in Sections 7.2.3.2 and 7.2.3.4. In contrast, agar showed a range of mesh sizes. Fe^{2+}-doped agar provides the largest mesh size of 32 nm, reflecting a more disrupted hydrogen-bonded structure. Smaller mesh size values of 14 and 13 nm were obtained for agar with Zn^{2+} and Ca^{2+}, respectively.

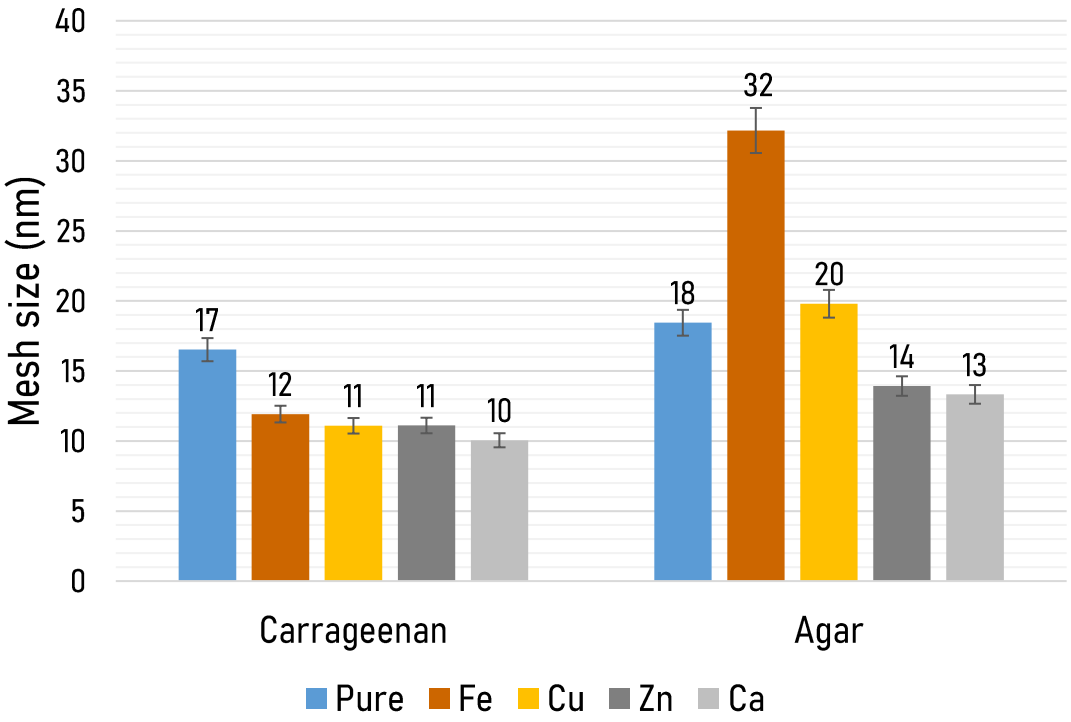


Figure 69. Evaluated mesh sizes for non-ionic hydrogels.

For ionic hydrogels, clear ion-dependent effects are observed, as shown in Figure 70. Alginate hydrogel with Ca^{2+} provided the smallest mesh size of 8 nm. This reflects the optimal “egg-box” crosslinking between Ca^{2+} ions and guluronate blocks (78,220). Other metal ions resulted in looser networks, with mesh size values of 15-19 nm. Pectin doped with Zn^{2+} also produced dense networks, which agrees with its high interfacial shear strength. The addition of Ca^{2+} ions to pectin produced the largest mesh size of 19 nm, indicating weak gelation. Phytagel hydrogels showed relatively similar network densities, with the values of mesh size ranging from 11 to 14 nm.

Figure 71 shows a correlation between the calculated interfacial shear strength and the mesh sizes of the tested hydrogels. A general tendency towards an inverse relationship can be observed, where smaller mesh size values are generally associated with higher τ values. However, this relationship is not consistent across all tested hydrogels and is quite sensitive to outliers. This observation suggests that denser polymer networks may promote higher interfacial shear strength, but other factors, such as water-binding capacity, play a significant role.

These findings demonstrate that mesh size is a valuable parameter linking rheological measurements to tribological performance. Even though absolute values of mesh size evaluation may not reflect the exact dimensions of hydrogel networks, these values provide

a useful comparative insight into the combined effect of gelation mechanisms and added ions on hydrogel behaviour (255–257).

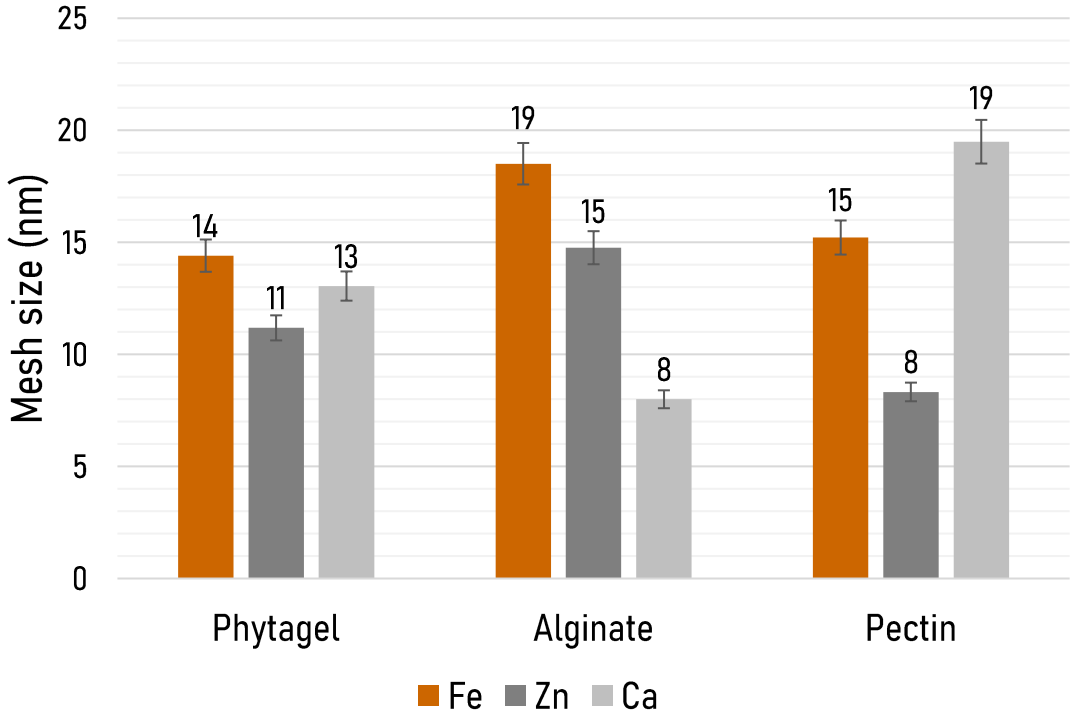


Figure 70. Evaluated mesh sizes for ionic hydrogels.

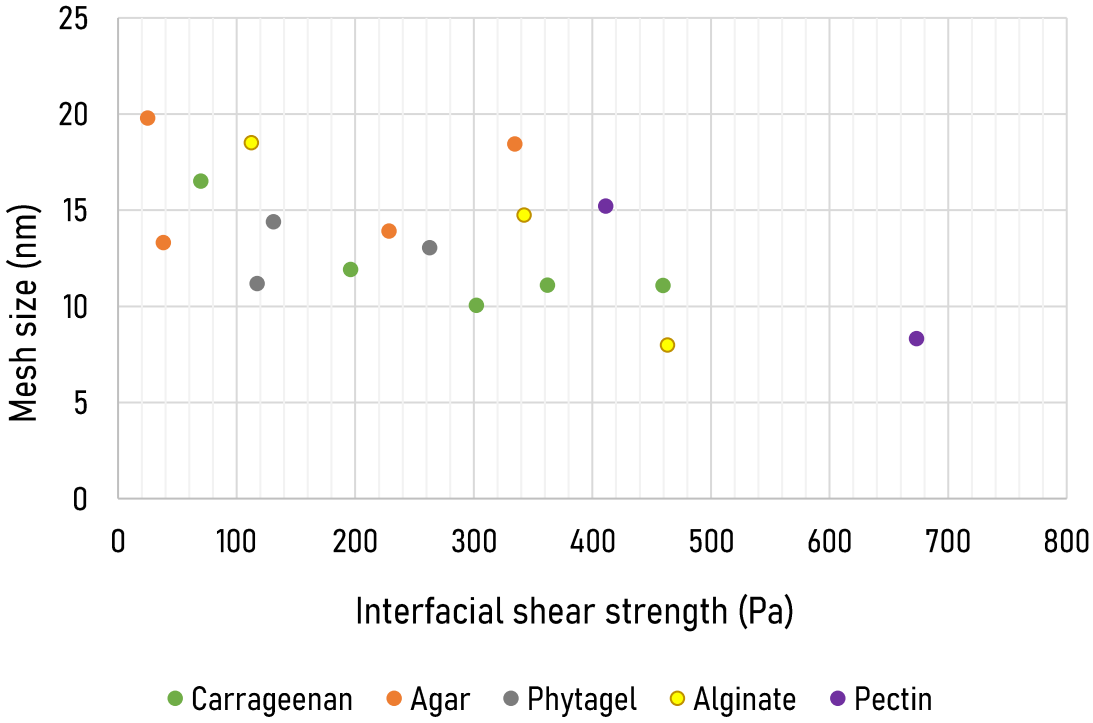


Figure 71. Correlation of interfacial shear strengths and mesh sizes.

7.4.3. Components of Friction Force

To better understand lubrication mechanisms, the measured friction forces were decomposed into deformation and interfacial components using the two-term model from Adams et al. (2007) (239). According to this framework, the total friction force is expressed as a sum of deformation and interfacial components.

The calculated friction components for non-ionic and ionic hydrogels are presented in Figure 72 and Figure 73, respectively. The analysis shows that both components contribute significantly to the total friction. In some cases, the deformational component dominated, reaching up to 65% of the total friction. Previous studies similarly highlighted that deformation-related energy dissipation can lead to substantial frictional losses (40). However, for most tested hydrogels the interfacial component was the primary contributor.

The decomposition highlights that higher stiffness alone does not guarantee lower friction. For example, carrageenan hydrogels got stiffer upon addition of ions, which should reduce deformational component of friction, according to Equation 7. However, the denser networks restrict the release of water, therefore limiting hydration lubrication and increasing interfacial adhesion (38,39,110). These changes led to higher coefficients of friction despite the increased stiffness. Similar behaviour was observed in cartilage-inspired hydrogels, where excessive crosslinking suppressed the fluid release and hindered lubrication (258).

Hydrogels, such as agar and Ca^{2+}-doped alginate, provided sufficient water release. This allowed the formation of hydration layers at the contact interface, which reduced interfacial shear and compensated lower hydrogel stiffness. As a result, these hydrogels provided relatively low coefficients of friction. Comparable findings were reported in alginate hydrogels for biomedical lubrication, where Ca^{2+}-based crosslinks provided water mobility and supported hydration-layer formation, leading to reduced friction (39,259).

To summarise, the analysis of frictional components demonstrates two key points. First, network density plays a dual role: denser structures improve stiffness but reduce water release, creating a trade-off that directly affects lubrication. Second, the polymer type sets the baseline level of interfacial shear strength, which is then modulated by ion-induced changes in network density and water mobility. The calculated interfacial shear strength therefore reflects both the intrinsic adhesive nature of hydrogel and the extent of hydration at the contact. These findings emphasise that a mechanistic understanding of hydrogel lubrication must combine stiffness, polymer-specific adhesion and water retention.

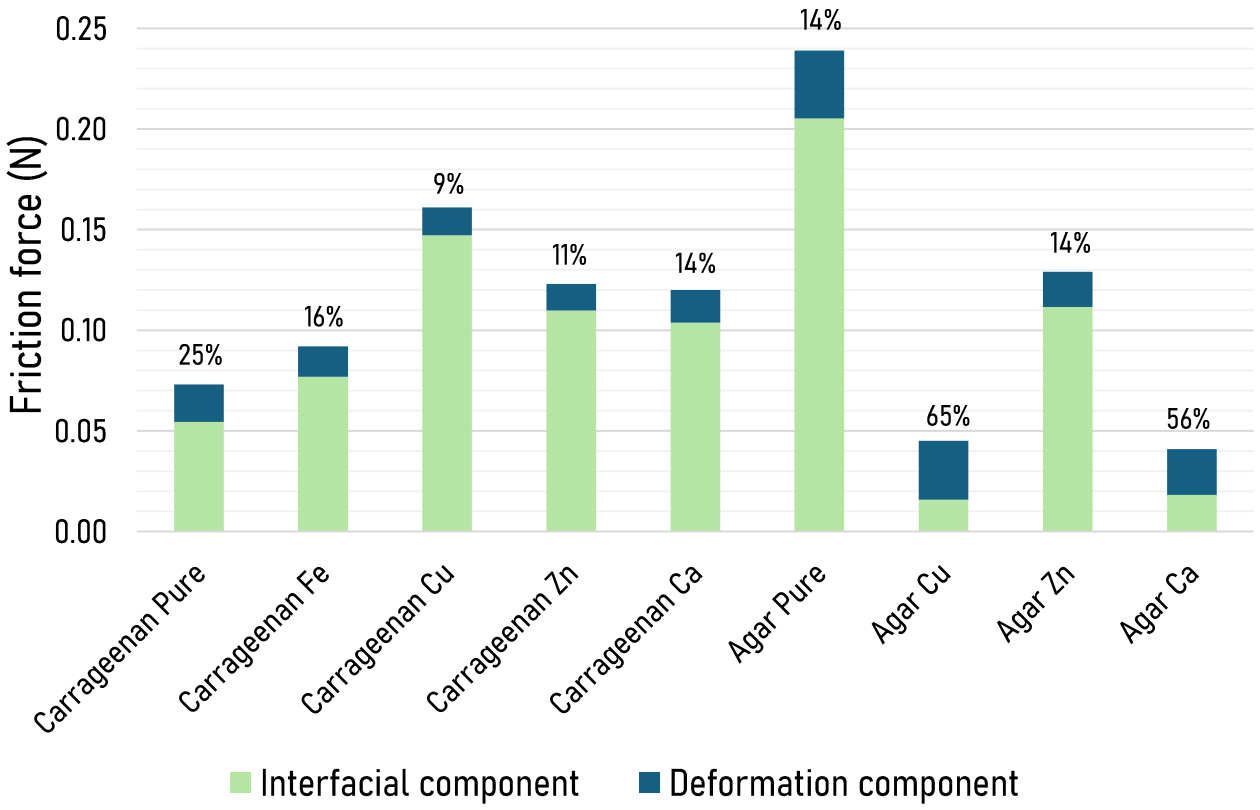


Figure 72. Friction force, separated into deformation and interfacial components, for non-ionic hydrogels. Data labels correspond to the deformational component's percentage of total friction force.

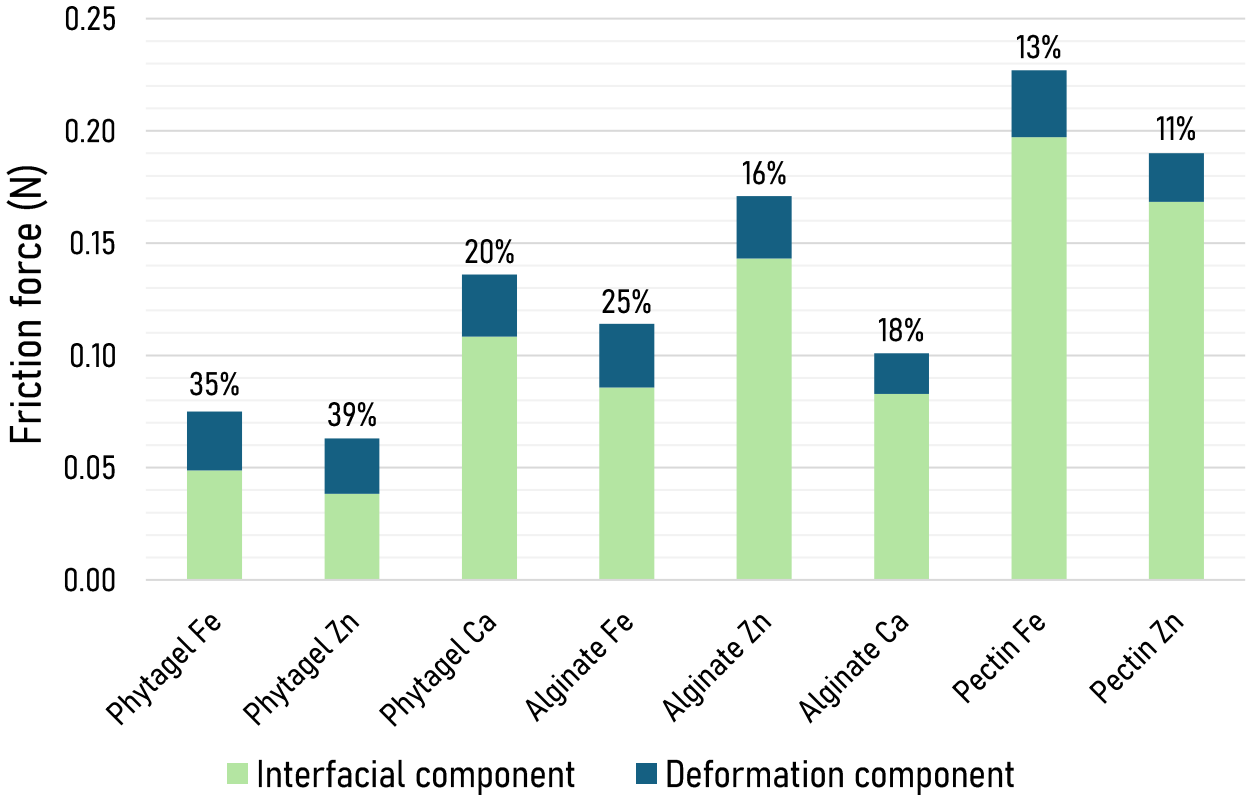


Figure 73. Friction force, separated into deformation and interfacial components, for ionic hydrogels. Data labels correspond to the deformational component's percentage of total friction force.

7.4.4. Guidelines for Tailoring Hydrogels

The findings of this study show that tailoring hydrogel properties requires balancing the mechanical reinforcement provided by ions with the ability of the network to sustain hydration lubrication. Mesh size ξ proved to be a useful comparative parameter. Smaller ξ values were generally associated with higher stiffness and interfacial shear strength, while larger ξ supported improved water mobility and lower friction. This trade-off demonstrates that hydrogels cannot be optimised by a single parameter, and their performance must be tuned according to the intended application.

For non-ionic hydrogels, carrageenan benefited from ion-induced reinforcement, producing dense, stiff networks that resisted shear. However, this came at the expense of lubrication, as water release was suppressed and friction increased. In contrast, agar showed weaker ion-induced stiffening but retained its capacity for hydration lubrication, which allowed friction reduction. These differences highlight that non-ionic gels should be tailored by deciding whether stiffness or lubrication is the primary design target.

Ionic hydrogels exhibited stronger ion-specific behaviour. Alginate demonstrated optimal reinforcement with Ca^{2+} and produced a favourable balance of stiffness and low friction. Pectin showed the strongest interfacial shear with Zn^{2+}, which coincides with higher friction. This suggests that Zn^{2+}-doped pectin forms strong interfacial interactions at the expense of lubrication. Phytagel displayed only modest sensitivity to ions, offering relatively stable but less tuneable properties. These observations underline that the identity of the crosslinking ion must be chosen in connection to the gelation mechanism of the polymer rather than assumed to provide uniform reinforcement.

Taken together, the results provide the following guideline: stiffness, interfacial shear strength and lubrication cannot be optimised simultaneously. Reinforcement by reducing mesh size improves stiffness but limits hydration lubrication. Looser networks improve lubrication at the expense of stiffness. Rational design therefore depends on identifying the application-specific compromise: carrageenan or alginate for high stiffness, agar for low friction, and pectin for strong resistance to interfacial shear. Optimisation will require linking polymer chemistry, ion selection and network density to the desired balance of performance.

Importantly, the absence of a universal trend across all hydrogel types confirms that tailoring cannot rely on generic rule. Each polymer-ion combination follows a distinct pathway, which is determined by its gelation mechanism. Therefore, design strategies must remain system-

specific, as ions that reinforce one network, may destabilise another. At the same time improvements in stiffness may compromise lubrication, depending on the polymer. Such system-dependent behaviour highlights that optimisation of hydrogel performance requires targeted, mechanism-based selection of polymers and ions.

7.5. Conclusions

This study demonstrated that the tribological behaviour of hydrogels is dictated by the interaction between gelation mechanism of the polymer, ion type and network density. Although no universal trend was observed across all hydrogel types, clear system-specific patterns were observed. Non-ionic hydrogels showed contrasting responses to ion addition. Upon ion addition carrageenan hydrogels stiffened at the expense of lubrication, while agar retained low friction without significant stiffening. Ionic hydrogels exhibited stronger ion-specific effects. Alginate was reinforced the most by Ca^{2+}, and pectin achieved the largest interfacial shear strength with Zn^{2+} ions. In contrast, phytagel demonstrated limited sensitivity to ions. Mesh size proved to be a useful comparative parameter, linking network density to both stiffness and interfacial shear strength. However, its relationship with interfacial shear strength is less direct, reflecting the role of hydration in the lubrication. These findings highlight that stiffness, interfacial shear strength and friction cannot be optimised simultaneously. Instead, hydrogel performance must be tailored according to the application requirements.

8. A New Model for Contact of Soft Solids

Following the previously highlighted problems of using existing indentation and friction models for soft matter, this chapter introduces a novel limit radius model. The model focuses on the material deformation and defines a new parameter 'limit radius', which represents the boundary of affected zone. Unlike adhesion-based models, which only incorporate near-contact zone, the limit radius model extends to the finite radius beyond which no surface deformations and stresses occur. This chapter presents the mathematical background of the model and validates its performance using indentation tests.

8.1. Introduction

The classical Hertz model has been widely used to describe elastic indentation problems. However, Hertz model is limited to small deformations and considers only the contact region of direct contact. In addition, Hertz assumes linear elastic material behaviour and frictionless contact (260,261). These limitations make the Hertz model less accurate for soft materials, like hydrogels and elastomers, where large deformations and non-linear effects are present (117). In this thesis, such limitations are critical to polysaccharide hydrogels in Chapter 7, undergoing large deformations and providing the deformation-driven frictional components, that cannot be fully captured by Hertzian analysis. Adhesive models such as the Johnson-Kendall-Roberts (JKR) and Derjaguin-Muller-Toporov (DMT) theories extend the analysis beyond the contact zone by incorporating surface forces in the near-contact zone. These theories focus on adhesive behaviour, and do not account for the deformation profile outside of the contact region and its contribution to the load support and frictional response.

In parallel, a substantial work in numerical modelling of contact, using boundary-element or finite-element analyses, has advanced the understanding of contact mechanics in soft, layered, and viscoelastic materials. For example, finite-element simulations were used to study adhesive and viscoelastic indentation of soft layers, capturing effects such as strain-rate dependence, large deformations and interface adhesion that cannot be described by closed-form analytical elastic contact models (262,263). Boundary-element approaches have also been applied to rough surface contacts and layered materials, enabling efficient evaluation of contact pressures, deformation fields and energy dissipation in systems beyond the reach of closed-form analytical solutions (264,265). More recent studies demonstrate that numerical models accurately predict indentation behaviour of thin viscoelastic layers under confined and unconfined conditions, capturing transient responses

and time-dependent relaxation (266). Together, these numerical approaches demonstrate that computational techniques can accommodate complex geometries, heterogeneities and viscoelastic responses with high accuracy, resulting in reliable models linking the forces and resulting displacements. The aim of the present chapter is to develop an analytical framework that captures the essential physics of indentation of soft elastic layers, while remaining sufficiently tractable to couple directly with experimental tribological measurements. Such a model will be essential to determine the mechanical properties from indentation experiments under large deformations.

This study introduces a novel limit radius model, that extends beyond the contact region by defining a finite limit radius L_0. Within the limit radius deformation is continuous, starting from the contact area. Beyond L_0 all stresses and deformations vanish. The limit radius model is formulated for a rigid sphere indenting an elastic half-space of fixed thickness.

The model enables calculation of surface deformations and of stress and strain distributions in all three spatial directions. The deformations were described using two cases: polynomial displacement profile (Case A) and Boussinesq-type profile (Case B). Validation was performed through indentation tests on silicone samples of different hardness under dry and lubricated conditions. This study aims to evaluate the limit radius model as a framework for understanding deformational behaviour of soft matter.

8.2. Limit Radius Model Definition

The limit radius model is proposed for the case of a rigid sphere of radius R indenting an elastic layer of finite thickness t, supported by a rigid substrate, as shown in Figure 74. The surface of the elastic layer is divided into three distinct regions based on the deformation behaviour. Region AB is the contact region, starting from the central axis (point A) to the edge of the contact area (point B), where $r = a$. In this region, the rigid sphere and the elastic layer are in direct physical contact. Region BC is the transition region, defined between the contact radius $r = a$ and the limit radius $r = L_0$. In this region, there is no direct contact between the sphere and the layer, but the vertical deformation remains non-zero. The outer boundary at point C is defined as the limit radius L_0, beyond which all stresses and displacements vanish. The outmost region beyond point C, where $r > L_0$, is the unaffected region, as the elastic layer remains undeformed, and all stresses are equal to zero. This framework therefore extends the conventional Hertz model, which is limited to the contact region, by including the transition region up to the finite radius of L_0. This finite

affected zone is more realistic for finite-thickness soft layers than the infinite decay of stress and strains provided in Hertz theory (267).

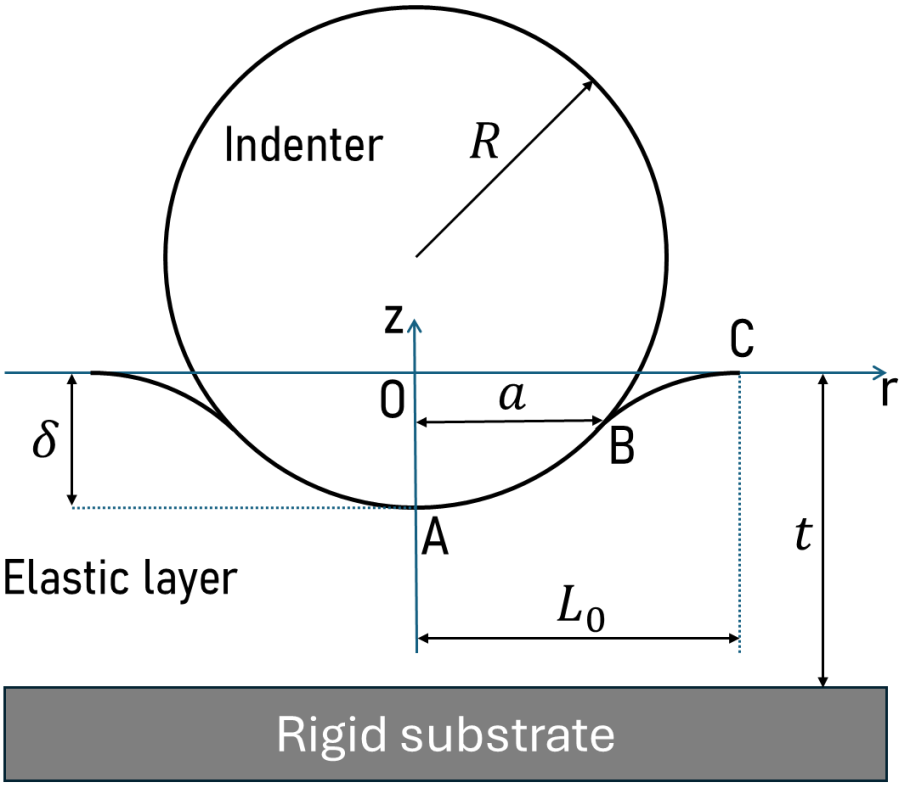


Figure 74. Indentation of a rigid sphere into a soft elastic layer of known thickness.

The normal stress follows a Hertz pressure distribution in the contact region. Beyond the contact radius, for $r \geq a$, the normal stress vanishes. The definition of normal stress is therefore provided by the following formula:

$$\sigma_z(z=0,r) = \begin{cases} -\frac{3F_z}{2\pi a^3}(a^2-r^2)^{\frac{1}{2}} & for\ 0 \leq r \leq a \\ 0 & for\ r \geq a \end{cases} \quad \text{(Equation 10)}$$

The normal displacement u_z on the surface within the contact region is prescribed by the geometry of the rigid sphere:

$$u_z(r) = -\left(\delta - R + \sqrt{R^2 - r^2}\right) \quad for\ 0 \leq r \leq a \quad \text{(Equation 11)}$$

In the transition region $(a \leq r \leq L_0)$, the displacement distribution is not known directly. Instead, it must be prescribed to satisfy several geometrical and physical conditions. To ensure continuity at both the contact radius and limit radius, four geometrical criteria are imposed:

Criterion 1. The deformation at point B is defined as:

$$u_z(r=a) = -\delta_a = -\left(\delta - R + \sqrt{R^2 - a^2}\right)$$

Criterion 2. The gradient at point B is defined as:

$$\frac{du_z}{dr}(r=a)=\frac{d\delta_a}{dr}=\frac{a}{\sqrt{R^2-a^2}}$$

Criterion 3. The deformation at point C is defined as:

$$u_z(r=L_0)=0$$

Criterion 4. The gradient at point C is defined as:

$$\frac{du_z}{dr}(r=L_0)=0$$

A fifth criterion is derived from the Hooke's theory for linear elasticity, using the following standard relations:

$$\begin{cases} E\varepsilon_z=\sigma_z-v(\sigma_r+\sigma_\theta) \\ E\varepsilon_r=\sigma_r-v(\sigma_z+\sigma_\theta) \\ E\varepsilon_\theta=\sigma_\theta-v(\sigma_z+\sigma_r) \end{cases} \quad \text{(Equation 12)}$$

where strains are defined as:

$$\varepsilon_z=\frac{u_z}{t} \quad \text{(Equation 13)}$$

$$\varepsilon_r=\frac{du_r}{dr} \quad \text{(Equation 14)}$$

$$\varepsilon_\theta=\frac{u_r}{r} \quad \text{(Equation 15)}$$

After introducing these relations, rearranging and integrating across the radius from $r=0$ to $r=L_0$, the following integral condition is obtained:

Criterion 5. $$\int_0^{L_0} ru_z\,dr=-\frac{(1+v)(1-2v)}{(1-v)}\frac{F_z t}{2\pi E}$$

This relation provides a link between indentation force, displacement distribution and material parameters. The full derivation of this criterion is provided in Appendix A.

To ensure the model is physically valid, the following criterion is introduced:

Criterion 6. There is no secondary contact outside the contact region.

This criterion could be satisfied in either of two ways:

- The deformed elastic layer does not intersect with the rigid sphere within the transition region, which can be expressed as:

$$u_z<-\left(\delta-R+\sqrt{R^2-r^2}\right) \quad for\ a<r\le R$$

- The normal displacement increases monotonically with radial distance, which can be expressed as:

$$\frac{du_z}{dr} \geq 0$$

To summarise, the limit radius model extends conventional contact models by prescribing a smooth, finite decay of surface deformation in the transition region. Unlike Hertz or adhesive models, which neglect deformation beyond the contact region, this formulation explicitly accounts for the substantial deformations that occur in soft materials. Such inclusion is essential for soft solids and finite-thickness layers, where deformation outside the contact region contributes to load support and frictional response.

8.3. Experimental Validation

8.3.1. Materials and Methods

Two silicone rubber moulded sheets: R4001/60 TRANS and WS.20.1.white, were obtained from Silex Ltd (UK). For clarity, R4001/60 TRANS silicone is referred to as ‘hard silicone’ and has a thickness of 5.6 mm. WS.20.1.white silicone is referred to as ‘soft silicone’ with a thickness of 5.0 mm. Both sheets were cut into 25 mm x 25 mm square samples. Silicone elastomers were chosen for their homogeneity and reproducibility, providing clear benchmarks for model validation.

The Biomomentum Mach-1 test device was used to perform the indentation testing of silicones under dry and lubricated surface conditions. The lubricated condition was obtained by applying 1 ml of deionised water on the specimen surface before testing. The detailed testing protocol is provided in Indentation Model Validation section in Chapter 3. To summarise, two silicone elastomers of different stiffness were indented using a spherical indenter under both dry and water-lubricated conditions using controlled indentation speeds.

8.3.2. Indentation Curves

The resulting indentation curves are shown in Figure 75. Tests were conducted at several indentation speeds to examine the influence on the normal force response. Across both silicones and under both surface conditions, the observed effects were consistent, but relatively small. As expected, larger indentation forces were achieved with higher indentation speeds for a given indentation depth. However, the overall similarity of the curves confirmed the elastic behaviour of the tested materials.

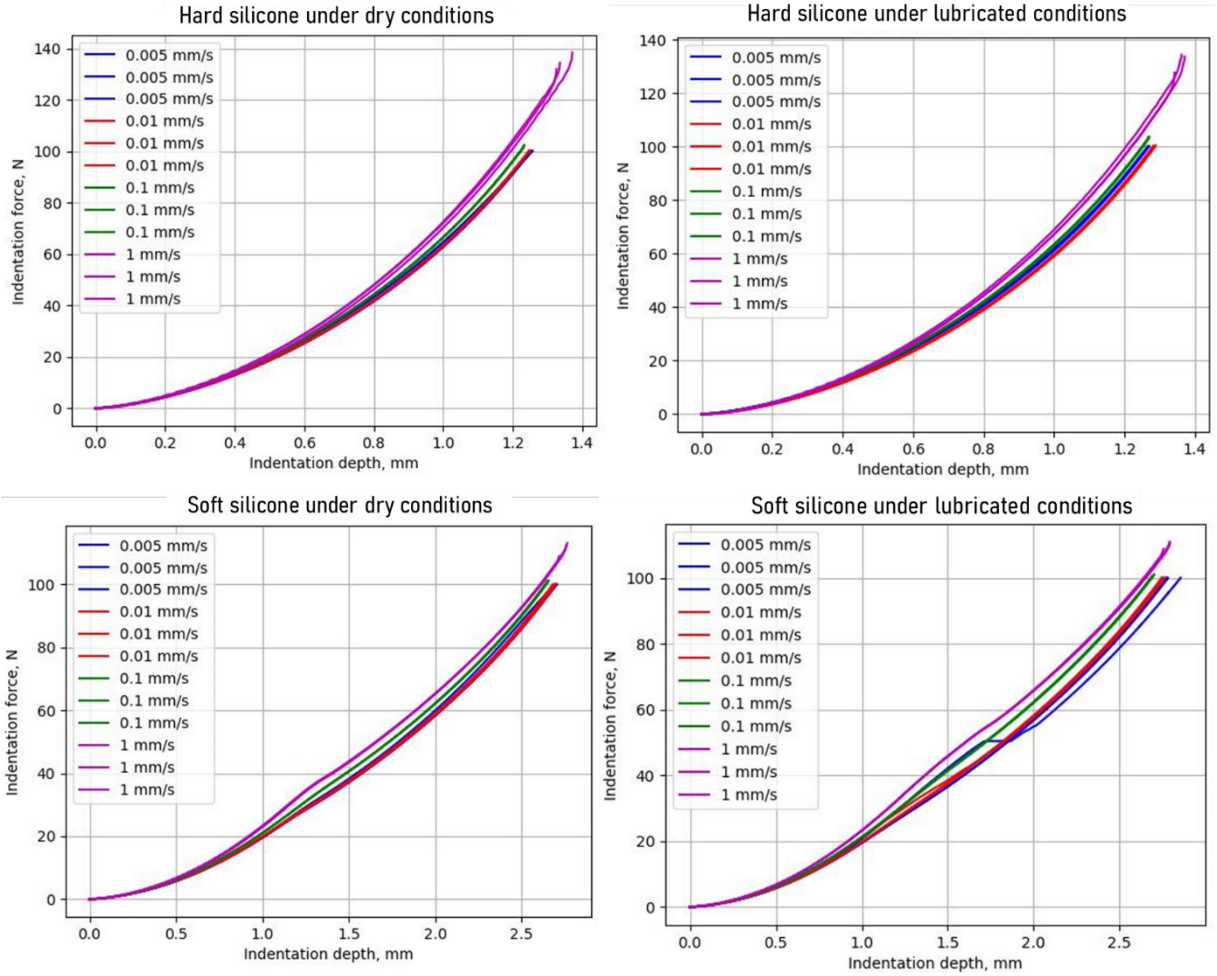


Figure 75. Comparison of force-indentation graphs of indentation speeds for hard and soft silicones with dry and lubricated conditions.

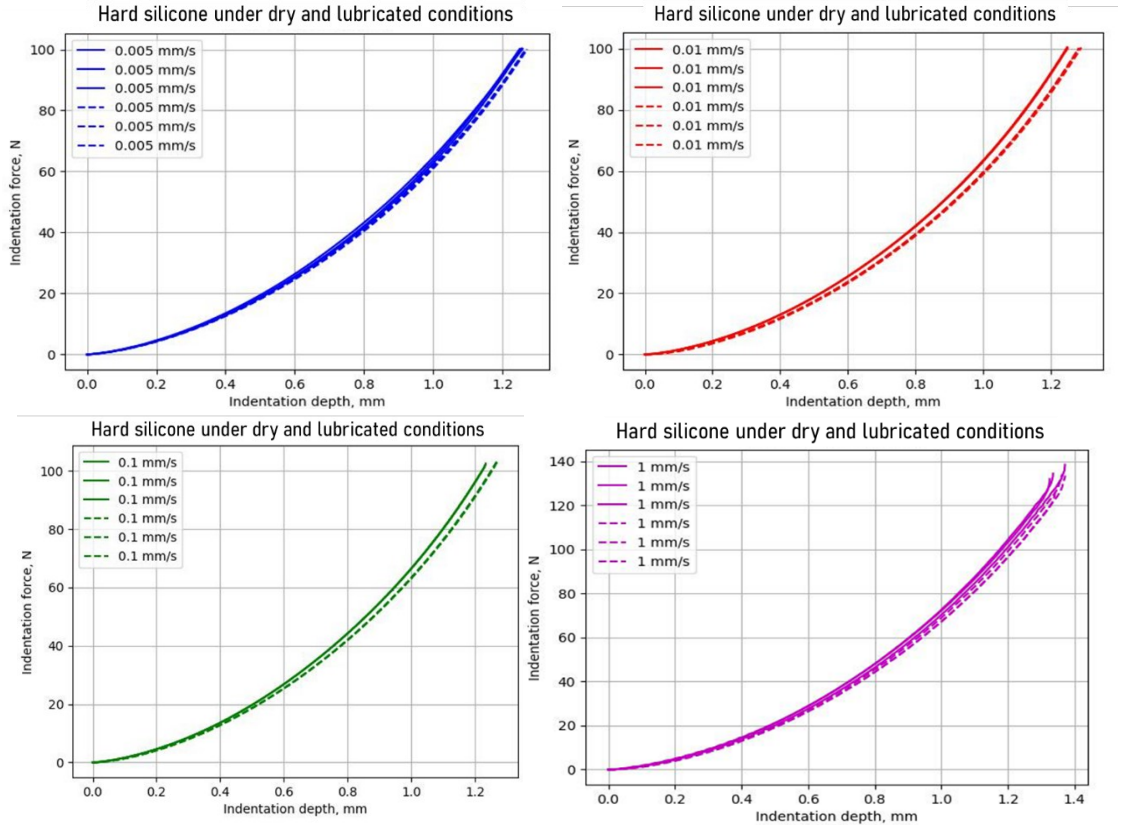


Figure 76. Comparison of force-indentation graphs of dry (solid lines) and lubricated (dashed lines) surface conditions for hard silicone.

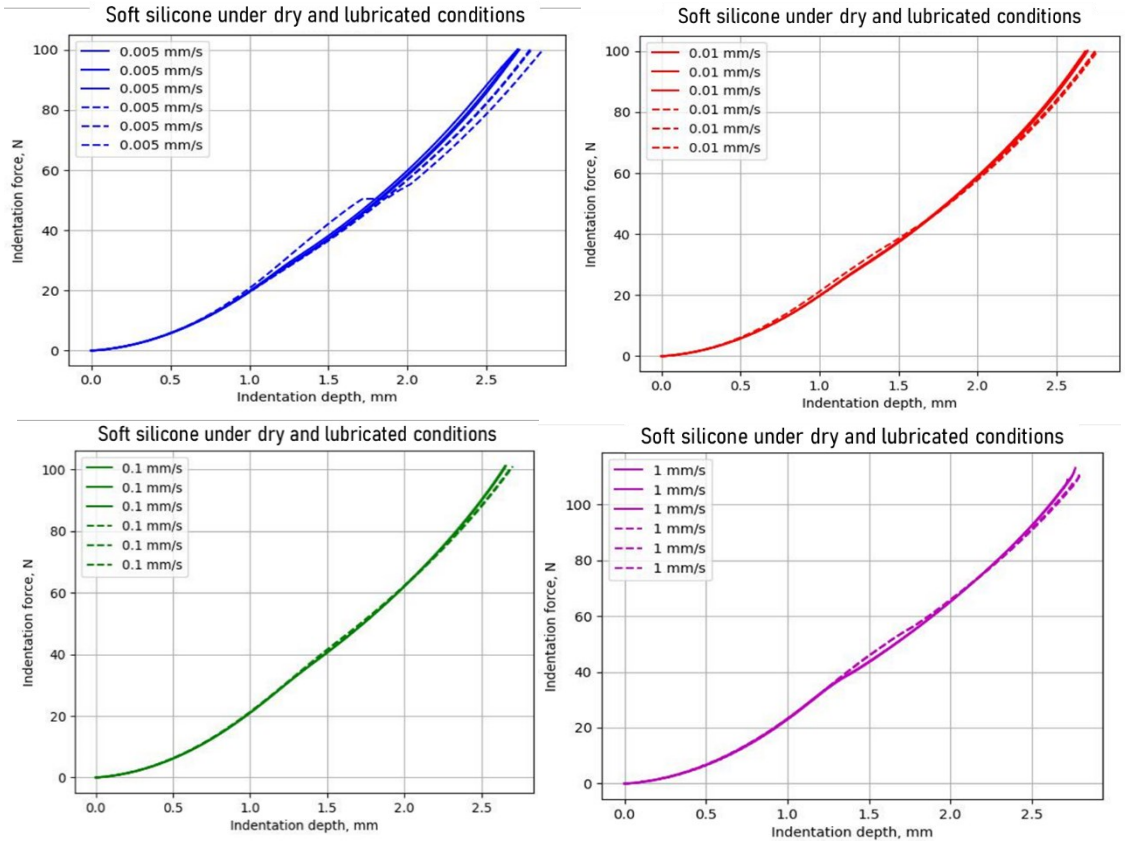


Figure 77. Comparison of force-indentation graphs of dry (solid lines) and lubricated (dashed lines) surface conditions for soft silicone.

Figure 76 and Figure 77 provide a comparison of indentation behaviour under dry (solid line) and lubricated (dashed line) conditions for hard and soft silicones, respectively. For the hard silicone, a clear reduction in indentation force is observed under lubrication for all tested indentation speeds. In contrast, soft silicone showed minimal differences between dry and lubricated surface conditions. These observations suggest that for harder silicones the presence of surface lubrication can significantly reduce the indentation force, while the response of softer silicones is dominated by bulk deformation rather than interfacial effects. This supports the need for an indentation model that accounts for finite thickness geometry, as well as taking in account the interfacial effects.

8.3.3. Elastic Modulus Evaluation

All indentation curves were analysed using the Hertz contact model to estimate the reduced elastic modulus E^*. The Equation 4, provided on page 50, was rearranged to solve for E^* and the elastic modulus E was obtained assuming a Poisson's ratio of $v = 0.48$.

To account for the finite thickness of the tested samples, the correction proposed by Dimitriadis et al. (2002) was applied (118). This correction introduces an additional thickness-dependent term $\chi = \sqrt{R\delta}/t$ to the Hertz equation, improving accuracy for the samples with finite thickness (118). The modified Hertz equation is presented below:

$$F_z = \frac{4}{3}\frac{E}{1-v^2} R^{\frac{1}{2}} \delta^{\frac{3}{2}} (1 + 1.133\chi + 1.283\chi^2 + 0.769\chi^3 + 0.0975\chi^4) \quad \text{(Equation 16)}$$

Figure 78 shows the calculated elastic modulus as a function of indentation depth for all individual tests, provided in previous section. Each line corresponds to one experimental run, plotted for the original Hertz model (red) and the Hertz model with Dimitriadis correction (blue). Near zero indentation depth, large fluctuations appear due to the sensitivity of the modulus calculation to noise in the force and displacement signals at small indentation depths. The original Hertz model (red) exhibits a depth dependence with elastic moduli increasing systematically with indentation depth. In contrast, the Dimitriadis correction (blue) compensates the finite thickness effects, producing more consistent elastic modulus values across the indentation range. This behaviour is expected for silicone elastomers, which are approximately elastic within the tested range. The corrected results indicate that hard and soft silicones have elastic moduli of approximately 6 MPa and 2 MPa, respectively. These values were used in all subsequent calculations of the model.

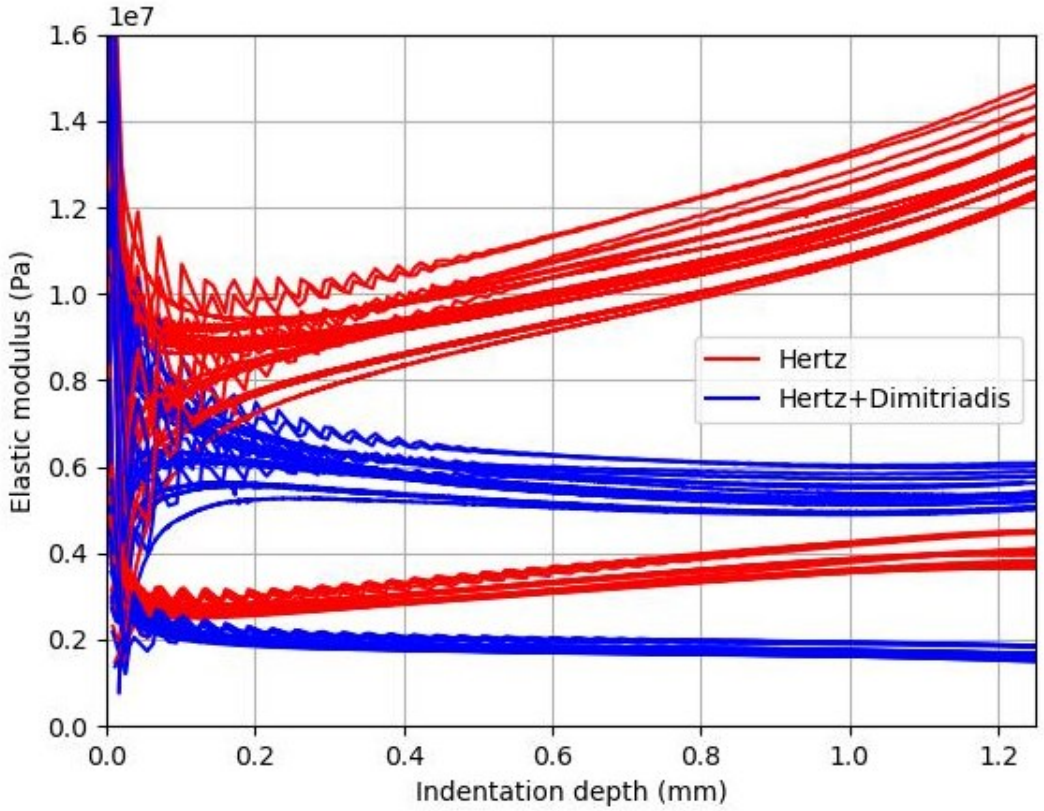


Figure 78. Obtained elastic moduli of hard and soft silicones, using Hertz model and Dimitriadis-corrected Hertz model.

8.4. Static Scenario

During indentation, the applied indentation force F_z is compensated by deformation of the elastic layer in both contact and transition regions. The stress and strain distributions in these regions are obtained by extending the derivation of Criterion 5. The following set of equations is obtained:

$$\varepsilon_\theta = \begin{cases} \frac{(1+v)(1-2v)}{r^2 vE}\left(\frac{F_z}{2\pi a^3}\right)\left((a^2-r^2)^{\frac{3}{2}}-a^3\right)+\frac{1-v}{r^2 vt}\left(\frac{\delta-R}{2}r^2-\frac{1}{3}(R^2-r^2)^{\frac{3}{2}}+\frac{R^3}{3}\right) \\ for\ 0 \le r \le a \\ -\frac{(1+v)(1-2v)}{r^2 vE}\frac{F_z}{2\pi}+\frac{1-v}{r^2 vt}\left(\frac{\delta-R}{2}a^2-\frac{1}{3}(R^2-a^2)^{\frac{3}{2}}+\frac{R^3}{3}\right)-\frac{1-v}{r^2 vt}\int_a^r r u_z\, dr \\ for\ a \le r \le L_0 \end{cases}$$

(Equation 17)

$$\varepsilon_r = -\varepsilon_\theta + \frac{(1+v)(1-2v)}{vE}\sigma_z - \frac{1-v}{vt}\varepsilon_z \quad \text{(Equation 18)}$$

$$\sigma_r = v(\sigma_z + \sigma_\theta) + E\varepsilon_r \quad \text{(Equation 19)}$$

$$\sigma_\theta = \frac{E}{1-v^2}(\varepsilon_\theta + v\varepsilon_r) + \frac{v}{1-v}\sigma_z \quad \text{(Equation 20)}$$

A complete derivation of these equations is provided in Appendix A. For the purposes of the model, the main objective is to link the indentation force F_z, indentation depth δ and the contact radius a by taking in account the limit radius L_0, contact geometry and material properties. Expanding the formulation of Criterion 5 provides:

$$\int_a^{L_0} r u_z \, dr = -\frac{(1+v)(1-2v)}{(1-v)} \frac{F_z t}{2\pi E} + (\delta - R)\frac{a^2}{2} + \frac{R^3}{3} - \frac{(R^2-a^2)^{\frac{3}{2}}}{3} \qquad \text{(Equation 21)}$$

In this equation, the right-hand side (RHS) is dependent on F_z, δ and a. By substituting the experimental data from all indentation tests a family of curves is produced, as shown in Figure 79. Each plotted line corresponds to one experimental test, plotted for different multiples of the Hertz contact radius a_{Hertz} represented by a different colour. The close overlap of curves within each colour confirms that the RHS is independent of speed, material stiffness and surface condition, and therefore is a purely geometric term. This observation justifies treating the model as quasi-static, where deformation depends only on geometry. Therefore, the admissible range of contact radii is determined by the geometry of the deformational profile.

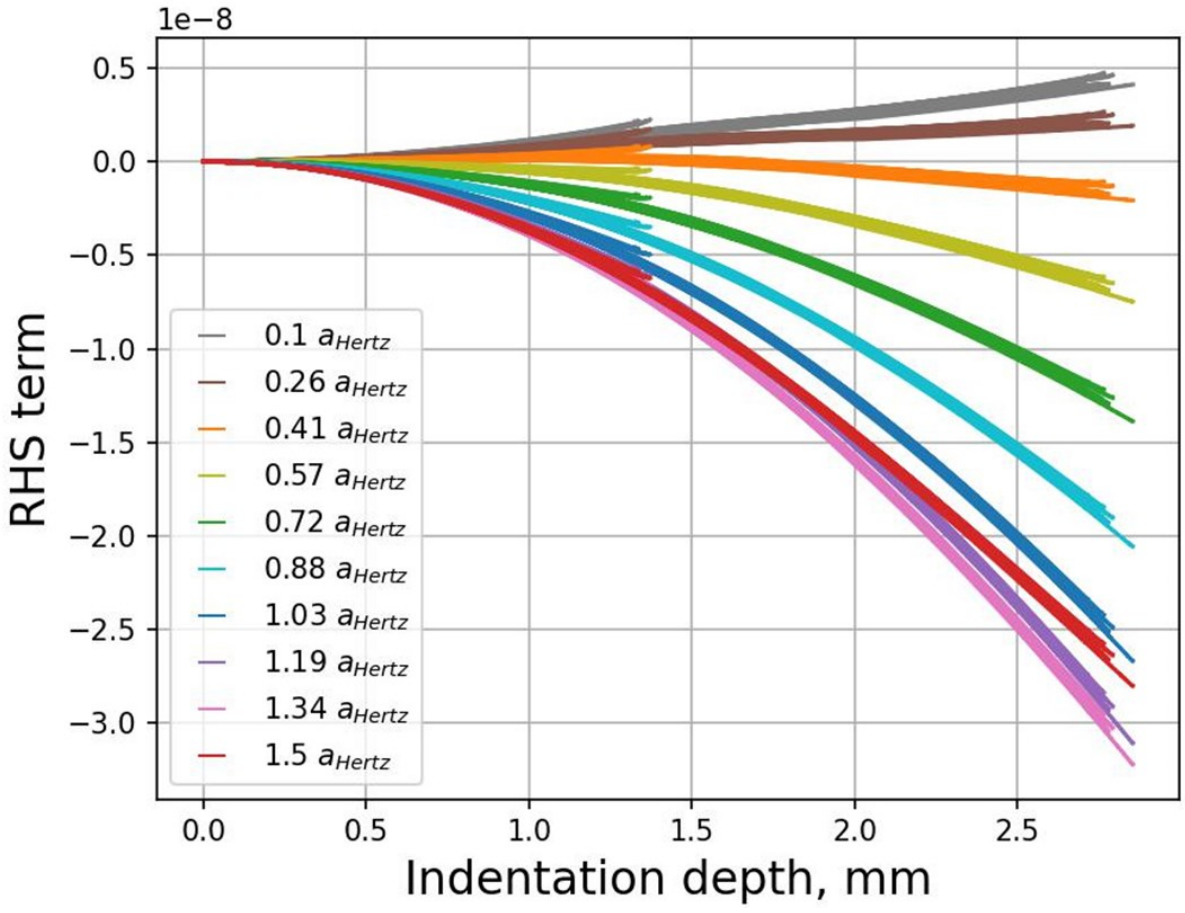


Figure 79. The variation of n-independent term with different multiples of Hertz contact radius at a range of indentation depths.

To solve the left-hand side (LHS) of Equation 21, the deformation profile in the transition region must be assumed. Two functional forms were considered:

- Case A: Polynomial form

$$u_z = Ar^n + Br^{n-1} + Cr^{n-2}$$

  This form is flexible and allows a variety of surface shapes by adjusting the exponent n, but it is not tied to a specific analytical solution.

- Case B: Boussinesq-type form

$$u_z = \frac{A}{r^n} + B$$

  This form is derived from the classical Boussinesq solution for point loading of an elastic half-space, making it a well-known analytical reference (267).

Both forms were constrained by the four geometric criteria, defining values and gradients at the edges of transitional region, and were subsequently tested against Criteria 5 and 6, which impose linear elastic behaviour and prevent the secondary contact, respectively. This procedure allows identification of the pairs (a, n) that simultaneously satisfy all conditions of the model.

8.4.1. Case A: Polynomial

The general form of Case A is a three-term polynomial with a variable power n:

$$u_z = Ar^n + Br^{n-1} + Cr^{n-2}$$

By applying Criteria 1, 3 and 4 the constants A, B and C can be determined, providing a closed form of the normal displacement:

$$u_z = -\delta_a \left(\frac{r}{a}\right)^n \frac{\left(1-\frac{L_0}{r}\right)^2}{(1-K)^2} \quad \text{(Equation 22)}$$

where K is defined as the ratio of Limit radius to the Contact radius. Using Criterion 2, K can be expressed as a function of a and n for a given geometry and indentation depth δ:

$$K = \frac{L_0}{a} = \frac{a\frac{d\delta_a}{dr} + n\delta_a}{a\frac{d\delta_a}{dr} + (n-2)\delta_a} \quad \text{(Equation 23)}$$

The full derivation of the obtained closed forms is provided in Appendix B – Case A Deformation. The variation of the limit radius with indentation depth for a range of n-values and Hertz contact radii are shown in Figure 80. The curves demonstrate that for all values of n the limit radius grows with indentation depth and exceeds the contact radius (dashed line), confirming that deformation extends outside the contact region but remains finite. This behaviour is consistent with the physical expectation that soft materials deform well beyond the contact region.

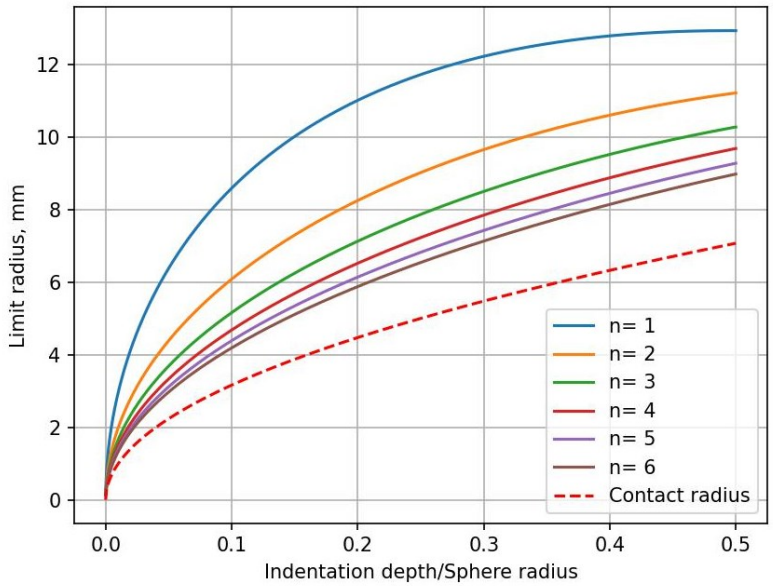


Figure 80. Case A limit radius variation with indentation depth at several n values.

The deformation profiles predicted by Case A are shown in Figure 81 for indentation depths of 0.5 and 1.0 mm. For a Hertz contact radius, a range of n values can be identified that satisfy the geometrical Criterion 6 and provide realistic surface profiles. These profiles decay smoothly to zero slope at L_0.

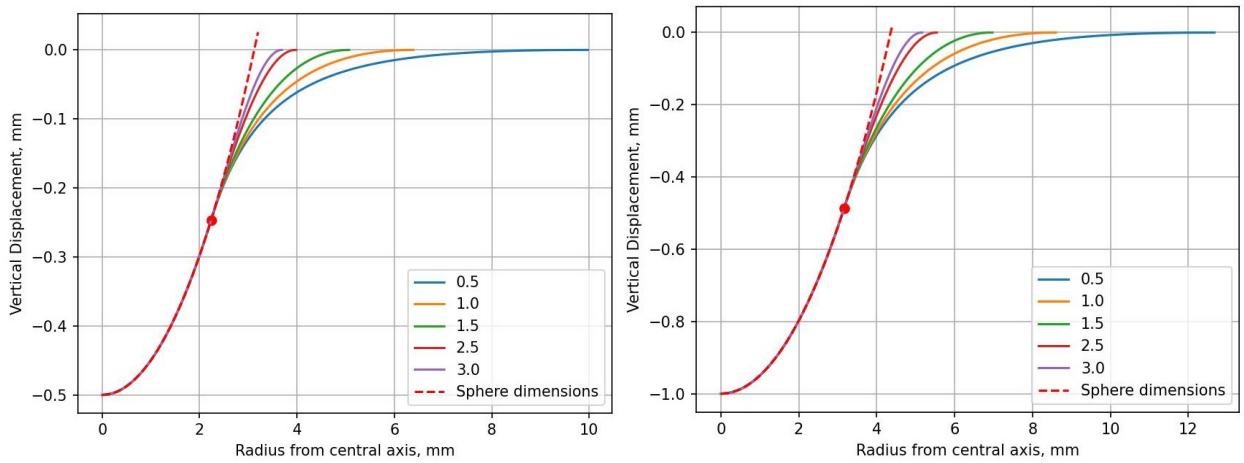


Figure 81. Example Case A displacements at indentation depths of 0.5 and 1.0 mm at different n-values.

The corresponding combinations of a and n that satisfy both Criterion 6 (no second contact) and the requirement of $K > 1$ are shown in Figure 82. Blue regions mark admissible solutions, while the red dot corresponds to the Hertz contact radius for reference. These plots confirm that multiple (a, n) pairs exist for a given indentation depth, allowing flexibility in representing real deformation profiles. Two distinct clusters of solutions appear: the compact region on the left corresponds to the physically realistic deformation profiles, while the wider cluster on the right is non-physical as it predicts contact radii much larger than can occur at these indentation depths.

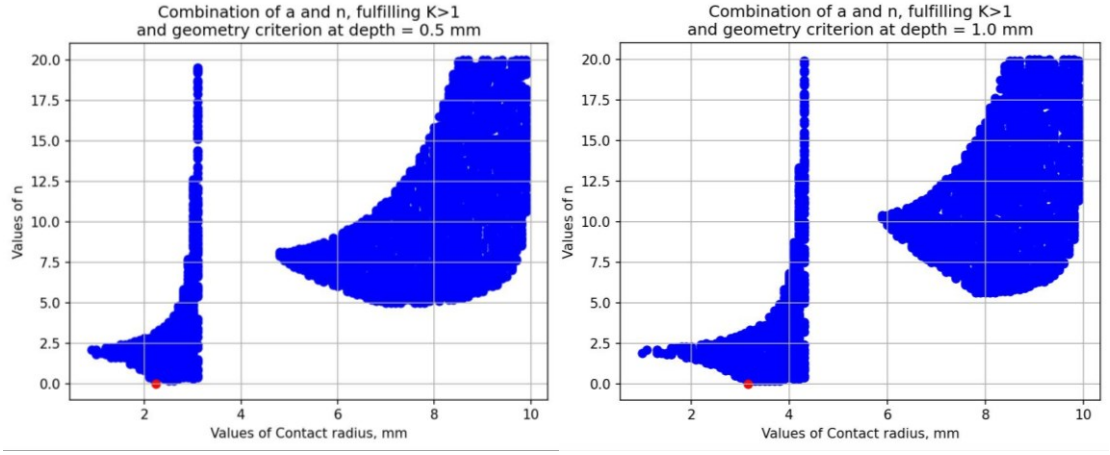


Figure 82. Values of n and contact radii, fulfilling the definition of K and geometry condition, for indentation depths of 0.5 and 1.0 mm, evaluated using Case A.

To further constrain the solution, Criterion 5 (linear elastic compatibility) was applied with a numerical tolerance of 0.1%. Figure 83 provides a comparison of the resulting distribution of contact radii with the Hertz contact radii. The close agreement indicates that Hertz contact radius remains a valid baseline reference with the values tending towards the upper limit within the range of physically realistic contact radii.

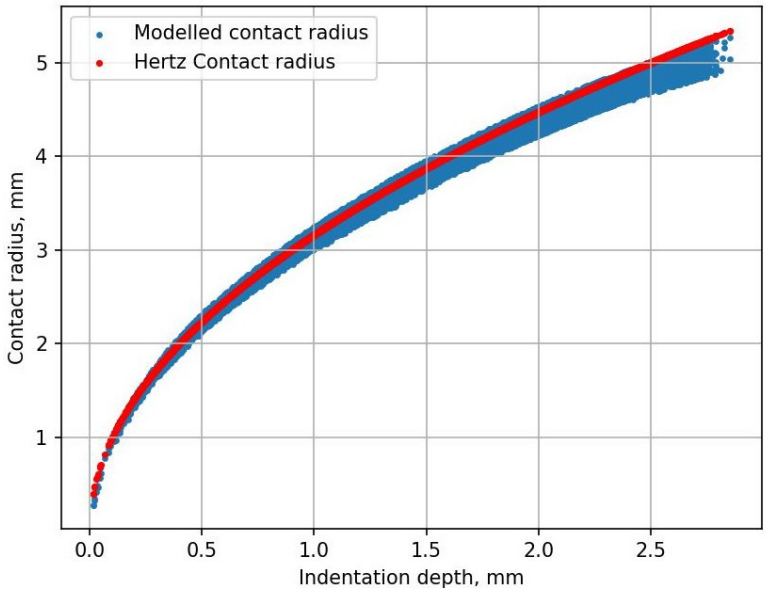


Figure 83. Comparison of Hertz contact radii with acceptable contact radii from limit radius model.

Building on this observation the range of n values that satisfy all six criteria was determined for the Hertz contact radius. The resulting distribution is shown in Figure 84. The graph compiles results from all tests, showing that n rises rapidly at small indentation depths, reaches a peak between 2.4-2.6 at indentation depth of 0.5-0.7 mm, and then gradually decreases towards 2.0 at larger indentation depths. Although some variability is seen between soft and hard silicone samples, both follow the same trend. This consistency suggests that the evolution of n is primarily governed by geometry rather than material properties. Overall, Case A demonstrates that deformation can be represented by a range of Hertz-like contact radii combined with variable n. This flexibility allows to capture realistic deformational profiles beyond the single-solution Hertz framework.

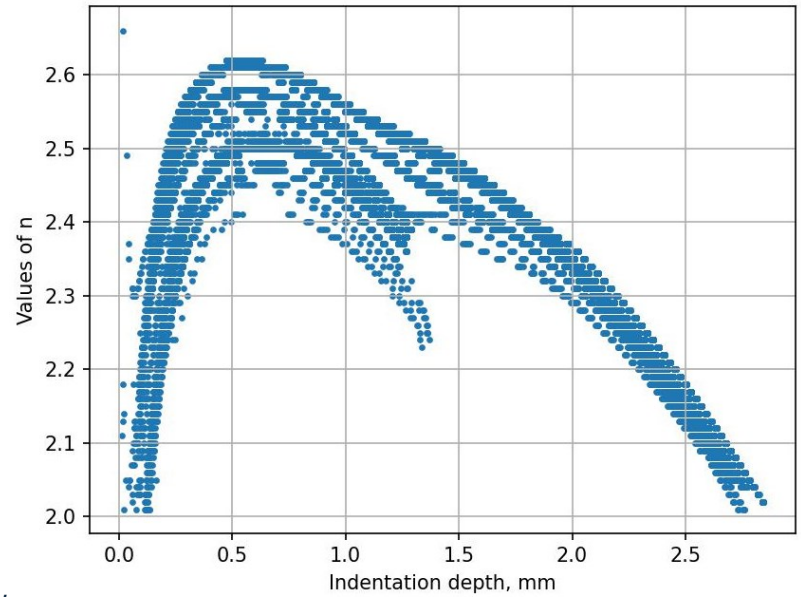


Figure 84. Values of n, fulfilling all conditions, using Hertz contact radius.

8.4.2. Case B: Boussinesq-type

The general form of Case B is a Boussinesq-type two term expression:

$$u_z = \frac{A}{r^n} + B$$

This formulation presents a significant limitation. Gradient of this function cannot vanish, meaning that Criterion 4 (zero slope at limit radius) cannot be satisfied. Therefore, Case B cannot fully comply with model requirements. By applying criteria 1 and 3 the constants A and B can be determined, providing a closed form of the normal displacement:

$$u_z = -\delta_a \frac{\left(\frac{L_0}{r}\right)^n - 1}{K^n - 1} \quad \text{(Equation 24)}$$

where K is the ratio of limit radius to contact radius. By applying Criterion 2, K can be expressed as a function of a and n for a given geometry and indentation depth δ:

$$K = \left(\frac{a\frac{d\delta_a}{dr}}{a\frac{d\delta_a}{dr} - n\delta_a} \right)^{\frac{1}{n}} \quad \text{(Equation 25)}$$

The full derivation of these expressions is provided in Appendix C – Case B Deformation. Figure 85 presents the variation of the limit radius with indentation depth for a range of n-values. As expected, the limit radius is consistently larger than the contact radius. However, for $n > 2$ the limit radius diverges to infinity at shallow indentation depths, which is unrealistic.

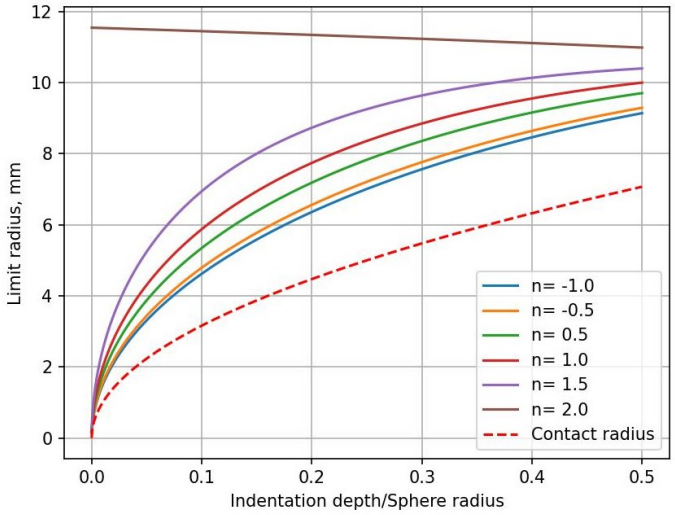


Figure 85. Case B limit radius variation with indentation depth at several n-values.

The deformation profiles predicted by Case B are shown in Figure 86 for indentation depths of 0.5 and 1.0 mm. For the Hertz contact radius, only profiles of $n > 1$ produce more realistic physical displacement profiles. Importantly, none of the curves decay to zero slope at L_0, reinforcing the failure of Criterion 4.

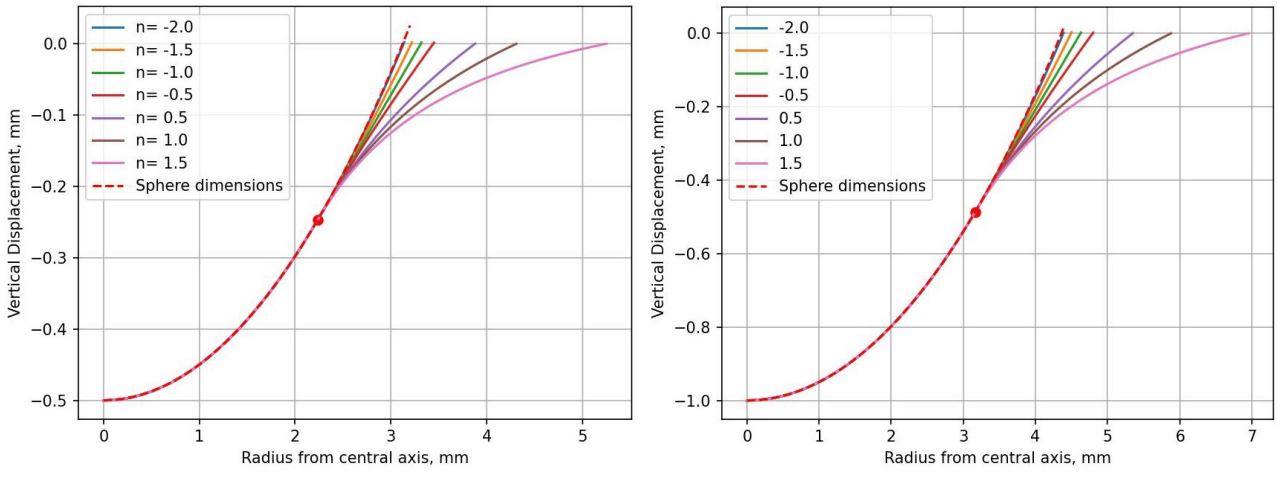


Figure 86. Example Case B displacements at indentation depths of 0.5 and 1.0 mm at different n-values.

The combinations of a and n that satisfy both Criterion 6 (no second contact) and $K > 1$ are shown in Figure 87 for indentation depths of 0.5 and 1.0 mm. These results demonstrate that multiple (a, n) pairs are available for a given indentation depth, providing flexibility in modelling displacement profiles.

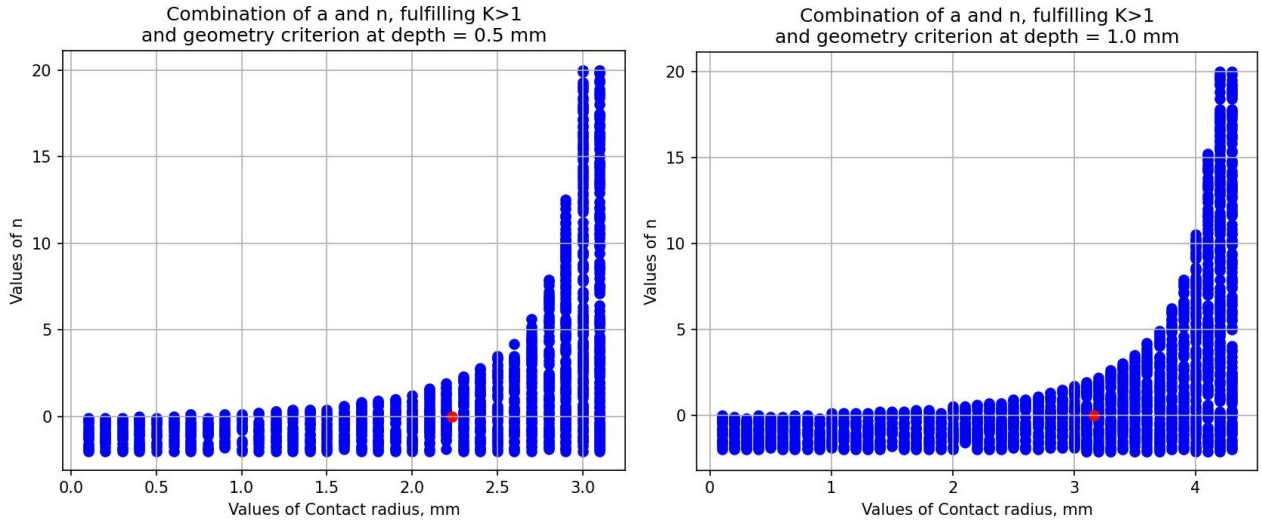


Figure 87. Values of n and contact radii, fulfilling the definition of K and geometry condition, for indentation depths of 0.5 and 1.0 mm, evaluated using Case B.

To further constrain the solutions, Criterion 5 (linear elasticity) was implemented with a numerical tolerance of 1%. The resulting distributions of contact radii are compared against Hertz contact radii in Figure 88. At very shallow indentation depths up to 0.05 mm, Case B provides contact radii that follow closely the Hertz contact radii. However, at larger indentation depths, no admissible contact radii were found. This observation demonstrates that beyond shallow depths Case B fails to satisfy all conditions simultaneously.

Taken together, these findings highlight the limitations of Case B. Even though the Boussinesq-type formulation links back to a known analytical solution, it cannot reproduce realistic deformation profiles across the full depth range. The infinite limit radius predictions for $n > 2$ and the extremely narrow range of valid indentation depths for fulfilling the Criterion 5 (linear elasticity) demonstrate the lack of robustness of Case B

To summarise, Case B is mathematically admissible but physically unrealistic. It offers realistic behaviour only at low indentation depths with lower accuracy. In contrast, Case A provides a more consistent solution, better agreement with Hertz contact radii, and validity at a full range of indentation depths. For these reasons, Case A is recommended as the more reliable framework for modelling and is used in the following sections.

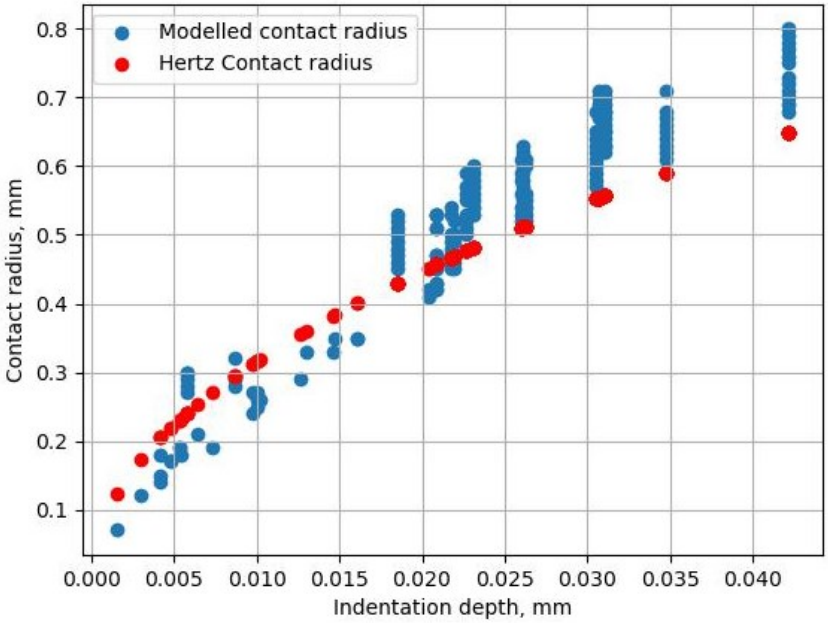


Figure 88. Comparison of Hertz contact radii with obtained contact radii from Case B limit radius model.

8.5. Application of the Model

To apply the limit radius model in practice, the formulation from Case A was used. By combining Equation 21 and Equation 22, the indentation force can be expressed in closed form with K defined by Equation 23:

$$F_z = \frac{(1-v)}{(1+v)(1-2v)}\frac{2\pi E}{t}\left[\frac{\delta_a a^2}{(1-K)^2}\left(\frac{2K^{n+2}}{n(n+1)(n+2)} - \frac{K^2}{n} + \frac{2K}{n+1} - \frac{1}{n+2}\right) + \right.$$

$$\left. + \frac{a^2}{2}(\delta - R) + \frac{R^3}{3} - \frac{(R^2-a^2)^{\frac{3}{2}}}{3}\right] \quad \text{(Equation 26)}$$

This equation provides the general force-displacement relationship of the model, with explicit dependence on the polynomial exponent n.

Three strategies for applying the model are considered:

1. Simplified approach – constant n:

   A practical first step is to assume a constant value of n across all indentation depths while using the Hertz contact radius as a. This approximation provides a straightforward way to produce force-indentation curves. As shown in Figure 89 the use of this approach with $n = 2.5$ already provides an improvement over the Hertz model with Dimitriadis correction. This highlights the potential of limit radius model to extend the classical Hertz analysis with minimal added complexity.

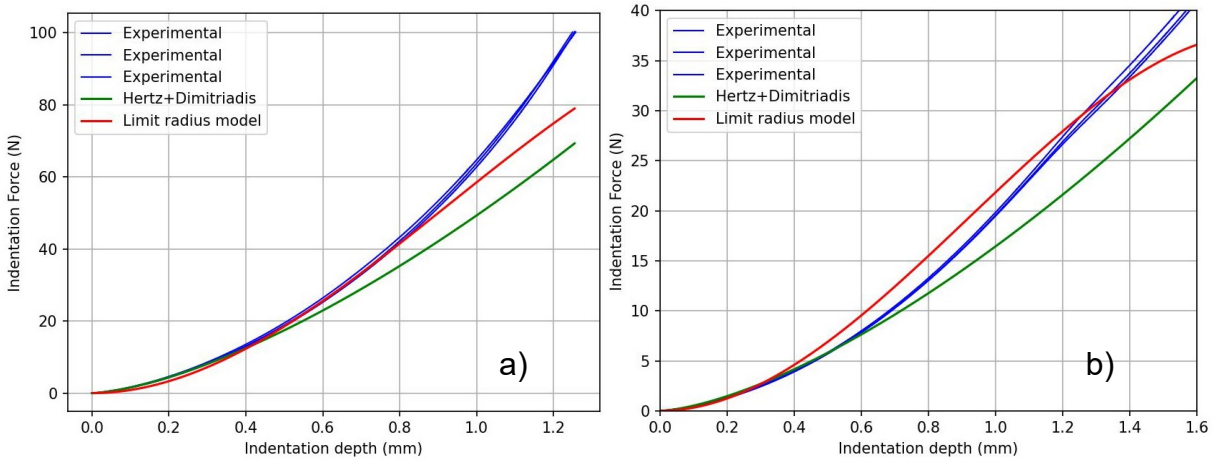


Figure 89. The comparison of force-indentation profile from experiments, corrected Hertz model and limit radius model with n=2.5 for a) hard and b) soft silicones.

Figure 89 compares the experimental force-displacement curves (blue) for hard and soft silicones at the indentation speed of 0.005 mm/s under dry surface conditions with predictions from the corrected Hertz model (green) and the simplified limit radius model (red). For both silicones, the simplified limit radius model aligns more closely with the experimental data than the corrected Hertz model. However, deviations are more pronounced in the softer silicone. This highlights the limitation of the simplified approach to limit radius model.

2. Semi-empirical approach – variable n:

   As shown in Figure 84, the value of n changes with the indentation depth. Although the span of the values is relatively small, its effect is significant as observed in the simplified approach. Variations of n from the indentation tests on hard and soft silicone with an indentation speed of 0.005 mm/s under dry surface conditions were fitted using second-order polynomials, as shown in Figure 90.

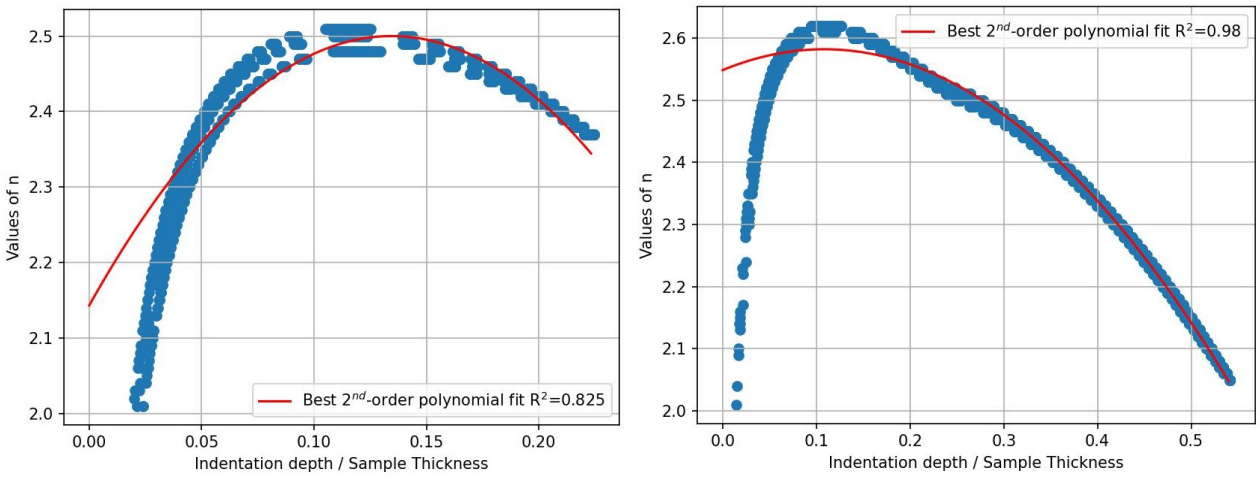


Figure 90. Distributions of n values with respect to indentation depth for a) hard and b) soft silicones.

These polynomial dependences $n(\delta)$ were then used together with the Hertz contact radii to obtain the force-displacement response, shown in Figure 91. A clear improvement upon both the simplified approach and the corrected Hertz model was achieved. These observations confirm that even the simple added variability of n can capture the observed indentation force behaviour.

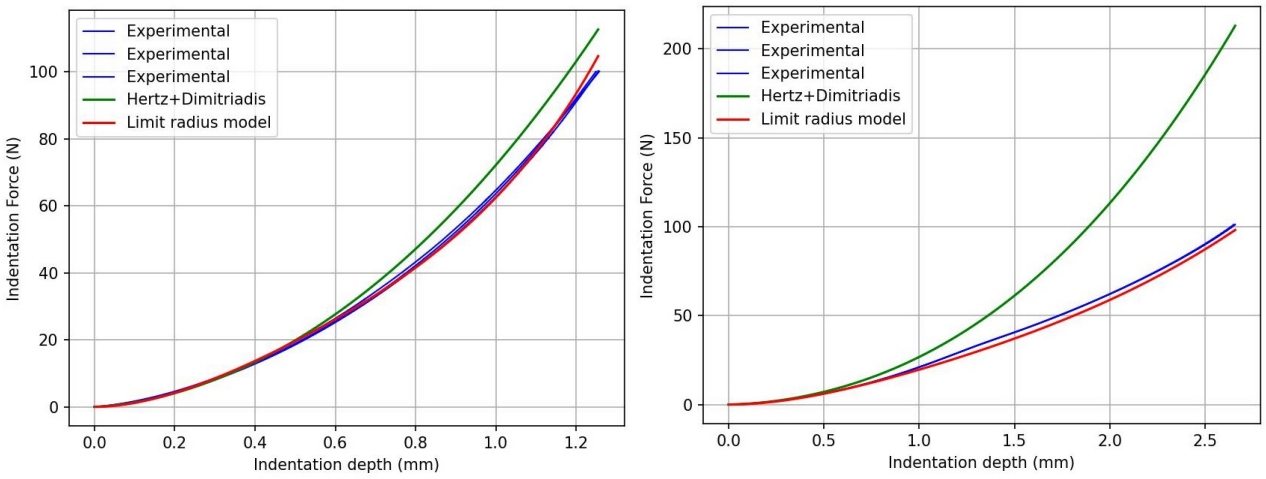


Figure 91. The comparison of force-indentation profiles from experiments, corrected Hertz model and limit radius model with variable n for a) hard and b) soft silicones.

3. Comprehensive approach – depth-dependant n and a:

   The full strength of the limit radius model lies in resolving both n and a as functions of the indentation depth. The admissible values of a for each indentation depth were presented in Figure 83. Establishing universal formulations of $a(\delta)$ and $n(\delta)$ would allow the model to predict deformation profiles independent of material stiffness. This would allow the model to be transferred across different materials.

To summarise, the limit radius model can be implemented at three levels of complexity. The simplified constant-n approach provides a practical improvement over the classical Hertz model. The semi-empirical framework with $n(\delta)$ from experimental data, captures even better force-indentation behaviour. Finally, the comprehensive approach, where both a and n vary with δ, outlines a pathway towards a fully predictive model of indentation mechanics in soft materials.

8.6. Conclusions

In this study the limit radius model was introduced as a novel approach to describing indentation mechanics in soft layers of finite thickness. Classical Hertz contact model focusses just on the contact region and most adhesion-based models, like JKR and DMT,

extend partially into the transition region. Limit radius model includes the entire transition region. The outer boundary of transition region is defined by the finite limit radius L_0, beyond which all displacements and stresses vanish.

The formulation of the model prescribes six criteria, based on the continuity of the deformation profile, force balance and physical feasibility. The deformational profile in the transition region was described by two Cases. Case A is based on a polynomial profile and satisfied all criteria. The distribution of contact radius from Case A agrees with Hertz contact radius prediction for all tested indentation depths. In addition, Case A allows flexibility of the deformation profiles through exponent parameter n. Case B is based on a Boussinesq-type profile. This formulation failed to satisfy all prescribed criteria and could not operate over all tested indentation depths. Therefore, Case B was deemed unsuitable for further application.

Indentation tests on soft and hard silicone samples under dry and lubricated conditions were used to obtain the experimental data for validating the proposed model. The limit radius model with Case A and Hertz contact radius produces a distribution of n values with indentation depth. The obtained distribution revealed consistent trends across both tested materials and both surface conditions. This observation suggests that the relation between n and indentation depth is driven primarily by geometry.

Further refinement of the model should focus on establishing universal functions linking n, contact radius, and indentation depth. Such formulations would enable prediction of the deformation profiles directly from indentation geometry, independent of material stiffness. In addition, direct imaging of the contact and transition regions would provide experimental data for validating both contact radii and limit radii predicted by the model.

To summarise, the limit radius model provides a new perspective on the contact mechanics of soft matter. By introducing the analysis of the deformations to a finite limit radius, the model captures the complex deformation behaviour of soft solids. The limit radius model provides a promising foundation for understanding indentation in challenging systems, like hydrogels, elastomers and biological interfaces.

9. Conclusions and Future Work

This chapter summarises the main outcomes of the studies presented in this thesis. Significance of the obtained conclusions within a broader context of bio-lubrication research as well as limitations of the current work are discussed. Finally, potential future research directions are outlined to further explore and refine the knowledge developed in this thesis.

9.1. Summary of Findings

In this thesis natural and nature-inspired lubrication strategies from plants, fungi and algae were explored. Four principal outcomes can be highlighted:

1. Plant oils were confirmed as effective baseline bio-lubricants. Several oils, such as macadamia nut and broccoli seed oils, provided low coefficients of friction and modest wear. Castor oil exhibited excellent anti-wear performance due to its high viscosity. Mixing of oils demonstrated a simple practical strategy to improve the tribological performance. The mixtures of castor and macadamia oils provided low friction and wear, combining the advantages of the individual oils. However, the triglyceride structure of plant oils imposes limitations in terms of oxidative and thermal stability. Plant oils represent a useful starting point for bio-lubrication, but chemical modifications or compositional tailoring are necessary to match the robust nature of mineral oil-based lubricants.
2. Water-based lubrication with the use of fungal β-glucans was investigated for the first time. Using biomimetic approach, fungal mucilage was identified as a source of inspiration for a novel water-based biolubricant. Several mushroom species were identified, and their extracts were tested to confirm the tribological effects. Consecutively, Lentinan, β-glucan from Shiitake mushrooms, was used to produce aqueous solutions. Even at low concentrations, these solutions achieved a significant reduction in friction and wear compared to pure water. The key findings include the dependence of tribological performance on particle size and concentration of Lentinan in the solutions. Larger particulates seem to act as third bodies in the contact, promoting wear. Smaller Lentinan particles seem to form a stable boundary layer, like polysaccharides from plants and algae. The increased concentration of both particle sizes led to a reduction of friction and an increase in wear. These findings demonstrate that water-based lubrication can be tuned by controlling the particle size distributions.

3. Polysaccharide hydrogels from plants and algae were examined as water retaining soft solids. Frictional behaviour of hydrogels was governed by a balance between deformational and interfacial contributions. Hydration lubrication, attributed to water release at the sliding interface, was identified as key mechanism for reducing shear. In the absence of water, interfacial adhesion dominates, leading to increased friction. The effect of different divalent metal ions on material properties and tribological performance was evaluated. The addition of ions has distinctive effects on each crosslinking mechanism; thus, the performance of hydrogel is individual to a combination of polymer type and ion added. The findings suggest that tribological performance is not determined solely by mechanical stiffness but arises from a combination of network density and water mobility within the hydrogel. Hydrogels with smaller mesh sizes generally exhibited higher interfacial shear strength. The larger mesh sizes supported the water release and reduced interfacial shear strength. As the mesh size was estimated using rubber elasticity theory, the mesh size values should be treated as comparative indicators rather than an absolute measure of structure. Overall, these findings demonstrate that hydrogel lubrication cannot be optimised by a single parameter but must be tailored through system-specific combinations of polymer chemistry, gelation mechanism and ionic environment.
4. A limit radius model was introduced as a new framework for the contact mechanics of soft solids. The model expands the analysis of deformations beyond the contact region by defining a finite limit radius L_0. Beyond the limit radius no stresses and displacements occur. The model introduces several criteria, describing the deformation profile and linking indentation force, contact radius and indentation depth. Two deformation profiles were evaluated against experimental observations. Case A (polynomial type) satisfied all prescribed criteria and produced deformation profiles across all tested indentations depths. Case B (Boussinesq type) failed to satisfy all criteria and was found unsuitable.

9.2. Limitations

This thesis enriched the understanding of natural and nature-inspired lubrication strategies, but several limitations must be acknowledged:

- Scope of tested materials: Only selected plant oils, fungal polysaccharides, and polysaccharide hydrogels were investigated. Other bio-lubricants discussed in literature were not experimentally examined.

- Laboratory test conditions: Tribological tests employed in this thesis do not fully represent typical tribological contacts. The used contact conditions employed lower contact pressures than those in practical engineering applications. Nevertheless, these test setups ensure reproducibility and allow direct comparison of lubricant performance. The resulting outcomes are sufficient for analysis and proposal of future pathways.
- Long-term performance: The study focused on relatively short-duration tests. Long-term effects, like oxidative and thermal degradation of plant oils or fatigue in hydrogels, were not assessed, as the emphasis of this thesis was on assessing the primary tribological performance parameters: friction and wear.
- Boundary film characterisation: Lubrication mechanisms were deduced from the observed tribological behaviours and material characterisation. Direct in situ visualisation or spectroscopic characterisation of the boundary film was not performed.
- Contact model validation: The proposed limit radius model was validated only against static indentation experiments on silicone elastomers. Further validation is needed across different materials and in the dynamic case, where lateral motion of the indenter introduces deformation-related friction.

9.3. Recommendations for Future Work

The tribological potential of natural and nature-inspired systems based on plant oil, fungal β-glucans and polysaccharide hydrogels was established in this thesis. In addition, a new framework for contact mechanics was introduced by the limit radius model. Building on these findings, the following recommendations for future work are proposed:

1. The tribological testing of six plant oils revealed clear differences in friction and wear behaviour. Future work should focus on linking this performance directly to the triglyceride types. Evaluating pure triglycerides, composed of only one fatty acid type, would clarify the individual contributions of fatty acids. Such understanding would allow to blend or modify the plant oils towards improved tribological properties. The most promising plant oils and their blends should then be tested under conditions, relevant to the industrial applications.
2. This thesis provided the first tribological evaluation of fungal β-glucans in water solutions. Further work is needed to confirm the proposed roles of particle size and concentration.

The tribological testing of larger Lentinan particles at low and high concentrations in water should be performed. In parallel, the spectroscopic analysis of the test samples before and after friction tests should be performed to identify adsorbed films and to detect the chemical changes in Lentinan. To evaluate the reported corrosion inhibition of Lentinan (268), testing on standard steel specimens instead of stainless-steel ones should be conducted. Alongside the research depth, a wide scope of β-glucans should be investigated, especially the ones coming from mushrooms species that exhibit the mucilage more strongly. Finally, long-term experiments are required to evaluate the lubricating ability of β-glucans under continuous operation.

3. The observations of plant and algal polysaccharide hydrogels highlighted the crucial role of water retention and mesh size in tribological performance. To strengthen these conclusions, direct quantification of hydration and mesh size should be done using techniques, such as dynamic light scattering or small angle X-ray scattering for mesh size and swelling ratio analysis or gravimetric water content for hydration. The durability of hydrogels under prolonged sliding and cyclic loading should be established to evaluate the performance under dehydration. The next step is to understand whether the hydrogel structure and lubrication behaviour are affected by ions supplied externally, either through aqueous solutions or by transfer from metallic countersurfaces. These studies would further deepen understanding of tuning hydrogel lubrication.
4. The limit radius model introduced in this thesis was validated only in the static indentation case. The next step is to extend the framework to dynamic conditions, where the indenter is displaced laterally at constant velocity while held at fixed indentation depth. Validation should involve comparing predicted deformation profiles with direct experimental observations, using microscopic digital image correlation, and matching the predicted lateral forces with measured values. After validation, the model can be applied to hydrogel friction experiments, enabling direct comparison between predicted and measured frictional responses. This would critically assess the model's ability to link deformation mechanics with friction in soft solids.
5. Finally, the most promising systems should be tested under appropriate conditions linked to application. This includes higher contact pressures, longer test duration and use of engineering materials present in application. In addition to friction and wear, further studies should evaluate other performance metrics, like thermal and oxidative stability and environmental compatibility.

Bibliography

1. Cabrera-Escobar C, Moreno-Gutiérrez J, Rodríguez-Moreno R, Pájaro-Velázquez E, Calderay-Cayetano F, Durán-Grados V. A Review on Global Recovery Policy of Used Lubricating Oils and Their Effects on the Environment and Circular Economy. *Environments - MDPI*. 2025;12(5). https://doi.org/10.3390/environments12050135.

2. Afolalu SA, Onu P, Adediran AA, Samuel A. Green Tribology, Sustainable Lubrication Practices and Environmental Impact: A Mini Review. In: *International Conference on Science, Engineering and Business for Driving Sustainable Development Goals, SEB4SDG 2024*. Institute of Electrical and Electronics Engineers Inc.; 2024. https://doi.org/10.1109/SEB4SDG60871.2024.10630171.

3. Mannekote JK, Kailas S V., Venkatesh K, Kathyayini N. Environmentally friendly functional fluids from renewable and sustainable sources-A review. *Renewable and Sustainable Energy Reviews*. 2018;81: 1787–1801. https://doi.org/10.1016/j.rser.2017.05.274.

4. Bartz WJ. Lubricants and the environment. *Tribology International*. 1998;31(1–3): 35–47.

5. Nowak P, Kucharska K, Kamiński M. Ecological and health effects of lubricant oils emitted into the environment. *International Journal of Environmental Research and Public Health*. 2019;16(16). https://doi.org/10.3390/ijerph16163002.

6. Stavárek P, Jaklová N, Večeř M, Zelenka L, Bernat S, Armada S, et al. The current state of environmentally acceptable lubricants (EALs) in stern tube lubrication: A review. *Journal of Tribology*. 2025; 1–84. https://doi.org/10.1115/1.4069028.

7. Bart JCJ, Cavallaro S, Gucciardi E. *Biolubricants: science and technology*. Biolubricants : science and technology. Cambridge: Woodhead Publishing; 2012.

8. Willing A. Lubricants based on renewable resources - an environmentally compatible alternative to mineral oil products. *Chemosphere*. 2001;43: 89–98.

9. Boyde S. Green lubricants. Environmental benefits and impacts of lubrication. *Green Chemistry*. 2002;4(4): 293–307. https://doi.org/10.1039/b202272a.

10. Shah R, Woydt M, Zhang S. The economic and environmental significance of sustainable lubricants. *Lubricants*. 2021;9(2): 1–11. https://doi.org/10.3390/lubricants9020021.

11. Ahmad U, Naqvi SR, Ali I, Naqvi M, Asif S, Bokhari A, et al. A review on properties, challenges and commercial aspects of eco-friendly biolubricants productions. *Chemosphere*. 2022;309. https://doi.org/10.1016/j.chemosphere.2022.136622.

12. General Assembly. *A/RES/70/1. Transforming our world: the 2030 Agenda for Sustainable Development*. 2015 Oct.

13. US EPA. *Final 2013 VGP Vessel General Permit for Discharges Incidental to the Normal Operation of Vessels (VGP)*. 2013.

14. Padma Ishwarya S, Sandhya R, Nisha P. Advances and prospects in the food applications of pectin hydrogels. *Critical Reviews in Food Science and Nutrition*. 2022;62(16): 4393–4417. https://doi.org/10.1080/10408398.2021.1875394.

15. Davim PJ. *Tribology for engineers: a practical guide*. Tribology for engineers : a practical guide. Oxford: Woodhead; 2011.

16. Wang Q, Chung YW, [eds.]. *Encyclopedia of Tribology*. Springer New York; 2013.

17. Mang Theo, Dresel Wilfried. *Lubricants and Lubrication*.. 2nd ed. Lubricants and lubrication. Weinheim: Wiley-VCH; 2007.

18. Spikes HA. Mixed lubrication - An overview. *Lubrication Science*. 1997;9(3): 221–253. https://doi.org/10.1002/ls.3010090302.

19. Spikes HA, Olver A V. Basics of mixed lubrication. *Lubrication Science*. 2003;16(1): 1–28. https://doi.org/10.1002/ls.3010160102.

20. Hironaka S. Boundary Lubrication and Lubricants. *Three Bond Technical News*. 1984; 1–8.

21. Dowson D. *Thin films in tribology, proceedings of the 19th Leeds-Lyon Symposium on Tribology held at the Institute of Tribology, University of Leeds, U.K. 8th-11th September 1992*. Elsevier; 1993.

22. Adhvaryu A, Erhan SZ, Perez JM. Tribological studies of thermally and chemically modified vegetable oils for use as environmentally friendly lubricants. *Wear*. 2004;257(3–4): 359–367. https://doi.org/10.1016/j.wear.2004.01.005.

23. Fox NJ, Tyrer B, Stachowiak GW. Boundary lubrication performance of free fatty acids in sunflower oil. *Tribology Letters*. 2004;16(4).

24. Fan J, Myant C, Underwood R, Cann P. Synovial fluid lubrication of artificial joints: Protein film formation and composition. *Faraday Discussions*. 2012;156: 69–85. https://doi.org/10.1039/c2fd00129b.

25. Schmidt TA, Gastelum NS, Nguyen QT, Schumacher BL, Sah RL. Boundary lubrication of articular cartilage: Role of synovial fluid constituents. *Arthritis and Rheumatism*. 2007;56(3): 882–891. https://doi.org/10.1002/art.22446.

26. Marian M, Shah R, Gashi B, Zhang S, Bhavnani K, Wartzack S, et al. Exploring the lubrication mechanisms of synovial fluids for joint longevity – A perspective. *Colloids and Surfaces B: Biointerfaces*. 2021;206. https://doi.org/10.1016/j.colsurfb.2021.111926.

27. Stokes JR, Macakova L, Chojnicka-Paszun A, De Kruif CG, De Jongh HHJ. Lubrication, adsorption, and rheology of aqueous polysaccharide solutions. *Langmuir*. 2011;27(7): 3474–3484. https://doi.org/10.1021/la104040d.

28. Ji L, Orthmann A, Cornacchia L, Peng J, Sala G, Scholten E. Effect of different molecular characteristics on the lubrication behavior of polysaccharide solutions. *Carbohydrate Polymers*. 2022;297. https://doi.org/10.1016/j.carbpol.2022.120000.

29. Shi L, Nie S, Ji H, He H, Hong R, Yin F. Excellent lubrication characteristics of green lubricants from yam polysaccharide in reducing friction and wear for water-lubricated environments. *Tribology International*. 2025;209. https://doi.org/10.1016/j.triboint.2025.110755.

30. Wang B, Qiu F, Barber GC, Zou Q, Wang J, Guo S, et al. Role of nano-sized materials as lubricant additives in friction and wear reduction: A review. *Wear*. 2022;490–491. https://doi.org/10.1016/j.wear.2021.204206.

31. Opia AC, Hamid MKA, Samion S, Johnson CAN, Rahim AB, Abdulrahman MB. Nano-Particles Additives as a Promising Trend in Tribology: A Review on their

Fundamentals and Mechanisms on Friction and Wear Reduction. *Evergreen*. 2021;8(4): 777–798. https://doi.org/10.5109/4742121.

32. Huang S, Wu H, Jiang Z, Huang H. Water-based nanosuspensions: Formulation, tribological property, lubrication mechanism, and applications. *Journal of Manufacturing Processes*. 2021;71: 625–644. https://doi.org/10.1016/j.jmapro.2021.10.002.

33. Wu H, Zhao J, Cheng X, Xia W, He A, Yun J, et al. Friction and wear characteristics of TiO2 nano-additive water-based lubricant on ferritic stainless steel. *Tribology International*. 2018;(117): 24–38.

34. Wu H, Jia F, Zhao J, Huang S, Wang L, Jiao S, et al. Effect of water-based nanolubricant containing nano-TiO2 on friction and wear behaviour of chrome steel at ambient and elevated temperatures. *Wear*. 2019;426–427: 792–804. https://doi.org/10.1016/j.wear.2018.11.023.

35. Wu H, Zhao J, Xia W, Cheng X, He A, Authors Hui Wu A, et al. A study of the tribological behaviour of TiO2 nano-additive water-based. *Tribology International*. 2017;(109): 398–408. https://ro.uow.edu.au/eispapers

36. Huang Q, Shi X, Xue Y, Zhang K, Wu C. Recent progress on surface texturing and solid lubricants in tribology: Designs, properties, and mechanisms. *Materials Today Communications*. 2023;35. https://doi.org/10.1016/j.mtcomm.2023.105854.

37. Gaisinskaya A, Ma L, Silbert G, Sorkin R, Tairy O, Goldberg R, et al. Hydration lubrication: Exploring a new paradigm. *Faraday Discussions*. 2012;156: 217–233. https://doi.org/10.1039/c2fd00127f.

38. Klein J. Hydration lubrication. *Friction*. 2013;1(1): 1–23. https://doi.org/10.1007/s40544-013-0001-7.

39. Lin W, Klein J. Hydration Lubrication in Biomedical Applications: From Cartilage to Hydrogels. *Accounts of Materials Research*. 2022;3(2): 213–223. https://doi.org/10.1021/accountsmr.1c00219.

40. Jahn S, Klein J. Hydration Lubrication: The Macromolecular Domain. *Macromolecules*. 2015;48(15): 5059–5075. https://doi.org/10.1021/acs.macromol.5b00327.

41. Kayaba T, Hokkirigawa K, Kato K. Analysis of the Abrasive wear Mechanism by Successive Observations of Wear Process in a Scanning Electron Microscope. *Wear*. 1986;110: 419–430.

42. Stachowiak GB, Stachowiak GW. The effects of particle characteristics on three-body abrasive wear. *Wear*. 2001;(249): 201–207.

43. Kovaříková I, Szewczyková B, Blaškovitš P. *Study and Characteristic of Abrasive Wear Mechanisms*. Institute of Production Technologies, Faculty of Materials Science and Technology, Slovak University of Technology; 2009.

44. Mercer AD, Lumbard EA. Corrosion of mild steel in water. *British Corrosion Journal*. 1995;30(1): 43–55. https://doi.org/10.1179/000705995798114177.

45. Kumar R, Rezapourian M, Rahmani R, Maurya HS, Kamboj N, Hussainova I. Bioinspired and Multifunctional Tribological Materials for Sliding, Erosive, Machining, and Energy-Absorbing Conditions: A Review. *Biomimetics*. 2024;9(209). https://doi.org/10.3390/biomimetics9040209.

46. Salimon J, Salih N, Yousif E. Biolubricants: Raw materials, chemical modifications and environmental benefits. *European Journal of Lipid Science and Technology*. 2010;112: 519–530. https://doi.org/10.1002/ejlt.200900205.

47. Hakala TJ. *Water-based boundary lubrication with biomolecule additives on diamond-like carbon and stainless-steel surfaces*. PhD Thesis. Aalto University.

48. Ahlroos T, Hakala TJ, Helle A, Linder MB, Holmberg K, Mahlberg R, et al. Biomimetic approach to water lubrication with biomolecular additives. *Proceedings of the Institution of Mechanical Engineers, Part J: Journal of Engineering Tribology*. 2011;225(10): 1013–1022. https://doi.org/10.1177/1350650111406635.

49. Dowson D. *History of tribology*.. 2nd ed. History of tribology. London: Professional Engineering Publishing; 1997.

50. Fox NJ, Stachowiak GW. Vegetable oil-based lubricants-A review of oxidation. *Tribology International*. 2007;40(7): 1035–1046. https://doi.org/10.1016/j.triboint.2006.10.001.

51. Berman D. Plant-Based Oils for Sustainable Lubrication Solutions—Review. *Lubricants*. 2024;12(9). https://doi.org/10.3390/lubricants12090300.

52. Yalcin H, Toker OS, Dogan M. Effect of Oil Type and Fatty Acid Composition on Dynamic and Steady Shear Rheology of Vegetable Oils. *Journal of Oleo Science*. 2012;61(4): 181–187. http://www.jstage.jst.go.jp/browse/jos/http://mc.manusriptcentral.com/jjocs

53. Al Sulaimi R, Macknojia A, Eskandari M, Shirani A, Gautam B, Park W, et al. Evaluating the effects of very long chain and hydroxy fatty acid content on tribological performance and thermal oxidation behavior of plant-based lubricants. *Tribology International*. 2023;185. https://doi.org/10.1016/j.triboint.2023.108576.

54. Schaefer W. *Shorthand (line) formula for a typical example molecule of Fat Triglycerides in native fat or oil*. https://commons.wikimedia.org/wiki/File:Fat_triglyceride_shorthand_formula.PNG (Accessed 17 September 2025). 2005.

55. Loehle S. *Understanding of adsorption mechanisms and tribological behaviors of C18 fatty acids on iron-based surfaces: a molecular simulation approach*. Université de Lyon; 2014.

56. Wood MH, Casford MT, Steitz R, Zarbakhsh A, Welbourn RJL, Clarke SM. Comparative Adsorption of Saturated and Unsaturated Fatty Acids at the Iron Oxide/Oil Interface. *Langmuir*. 2016;32(2): 534–540. https://doi.org/10.1021/acs.langmuir.5b04435.

57. Reeves CJ, Menezes PL, Jen TC, Lovell MR. The influence of fatty acids on tribological and thermal properties of natural oils as sustainable biolubricants. *Tribology International*. 2015;90: 123–134. https://doi.org/10.1016/j.triboint.2015.04.021.

58. Jahanmir S. Chain Length Effects in Boundary Lubrication. *Wear*. 1985;102: 331–349.

59. Folayan AJ, Anawe PAL, Aladejare AE, Ayeni AO. Experimental investigation of the effect of fatty acids configuration, chain length, branching and degree of unsaturation on biodiesel fuel properties obtained from lauric oils, high-oleic and high-linoleic vegetable oil biomass. *Energy Reports*. 2019;5: 793–806. https://doi.org/10.1016/j.egyr.2019.06.013.

60. Lee CT, Lee MB, Mong GR, Chong WWF. A bibliometric analysis on the tribological and physicochemical properties of vegetable oil–based bio-lubricants (2010–2021). *Environmental Science and Pollution Research*. 2022;29(37): 56215–56248. https://doi.org/10.1007/s11356-022-19746-2.

61. Mobarak HM, Niza Mohamad E, Masjuki HH, Kalam MA, Al Mahmud KAH, Habibullah M, et al. The prospects of biolubricants as alternatives in automotive applications. *Renewable and Sustainable Energy Reviews*. 2014;33: 34–43. https://doi.org/10.1016/j.rser.2014.01.062.

62. Patel A, Mu L, Shi Y, Rova U, Christakopoulos P, Matsakas L. Single-cell oils from oleaginous microorganisms as green bio-lubricants: Studies on their tribological performance. *Energies*. 2021;14(20). https://doi.org/10.3390/en14206685.

63. Rubio-Hernández CC, Iqbal HMN, González-Meza GM, Pérez-González J, Marín-Santibáñez BM, Resendiz-Calderon CD, et al. Tribological, viscous, and thermal properties of low-viscosity Scenedesmus microalgae oil as a new green and sustainable additive for vehicle lubricants. *Proceedings of the Institution of Mechanical Engineers, Part J: Journal of Engineering Tribology*. 2025; https://doi.org/10.1177/13506501251319964.

64. Farfan-Cabrera LI, Franco-Morgado M, González-Sánchez A, Pérez-González J, Marín-Santibáñez BM. Microalgae Biomass as a New Potential Source of Sustainable Green Lubricants. *Molecules*. 2022;27(4). https://doi.org/10.3390/molecules27041205.

65. Yosief HO, Sarker MI, Bantchev GB, Dunn RO, Cermak SC. Chemical Modification of Beef Tallow for Lubricant Application. *Industrial and Engineering Chemistry Research*. 2022;61(27): 9889–9900. https://doi.org/10.1021/acs.iecr.2c01207.

66. Dhanavel N, Nandakrishnan MH. A Review of Animal Fat: A Great Source for Industrial Applications. *Journal of Chemical Reviews*. 2024;6(2): 115–137. https://doi.org/10.48309/jcr.2024.425819.1276.

67. Hájek M, Vávra A, De Paz Carmona H, Kocík J. The Catalysed Transformation of Vegetable Oils or Animal Fats to Biofuels and Bio-Lubricants: A Review. *Catalysts*. 2021;11(1118). https://doi.org/10.3390/catal.

68. Máximo F, Bastida J, Montiel C, Gómez M, Murcia MD, Barqueros C, et al. Branched saturated esters and diesters: Sustainable synthesis of excellent biolubricants. *Catalysis Today*. 2024;429. https://doi.org/10.1016/j.cattod.2024.114509.

69. Singh Y, Sharma A, Singh N, Singla A, Rastogi PM. Prospects of inedible plant oil-driven bio-lubricants for tribological characteristics–a review. *International Journal of Ambient Energy*. 2020;41(13): 1534–1547. https://doi.org/10.1080/01430750.2018.1517684.

70. Cecilia JA, Plata DB, Saboya RMA, de Luna FMT, Cavalcante CL, Rodríguez-Castellón E. An overview of the biolubricant production process: Challenges and future perspectives. *Processes*. 2020;8(257). https://doi.org/10.3390/pr8030257.

71. Salih N, Salimon J. A Review on New Trends, Challenges and Prospects of Ecofriendly Friendly Green Food-Grade Biolubricants. *Biointerface Research in Applied Chemistry*. 2021;12(1): 1185–1207. https://doi.org/10.33263/briac121.11851207.

72. Salih N, Salimon J. A review on eco-friendly green biolubricants from renewable and sustainable plant oil sources. *Biointerface Research in Applied Chemistry*. 2021;11(5): 13303–13327. https://doi.org/10.33263/BRIAC115.1330313327.

73. Barbera E, Hirayama K, Maglinao RL, Davis RW, Kumar S. Recent developments in synthesizing biolubricants — a review. *Biomass Conversion and Biorefinery*. 2024;14(3): 2867–2887. https://doi.org/10.1007/s13399-022-02438-9.

74. Wang Z, Zheng Y, Lai Z, Hu X, Wang L, Wang X, et al. Effect of monosaccharide composition and proportion on the bioactivity of polysaccharides: A review. *International Journal of Biological Macromolecules*. 2024;254. https://doi.org/10.1016/j.ijbiomac.2023.127955.

75. Chen Y. *Hydrogels based on natural polymers*. Amsterdam, Netherlands: Elsevier; 2020.

76. BeMiller JN. 4 - Polysaccharides: Occurrence, Structures, and Chemistry. In: BeMiller JN (ed.) *Carbohydrate Chemistry for Food Scientists (Third Edition)*. Third Edition. AACC International Press; 2019. p. 75–101. https://doi.org/https://doi.org/10.1016/B978-0-12-812069-9.00004-2.

77. Catoira MC, Fusaro L, Di Francesco D, Ramella M, Boccafoschi F. Overview of natural hydrogels for regenerative medicine applications. *Journal of Materials Science: Materials in Medicine*. 2019;30(10). https://doi.org/10.1007/s10856-019-6318-7.

78. Malektaj H, Drozdov AD, deClaville Christiansen J. Mechanical Properties of Alginate Hydrogels Cross-Linked with Multivalent Cations. *Polymers*. 2023;15(14). https://doi.org/10.3390/polym15143012.

79. BeMiller JN. 14 - Algins/Alginates. In: BeMiller JN (ed.) *Carbohydrate Chemistry for Food Scientists (Third Edition)*. Third Edition. AACC International Press; 2019. p. 293–301. https://doi.org/https://doi.org/10.1016/B978-0-12-812069-9.00014-5.

80. Borchani C, Fonteyn F, Jamin G, Destain J, Willems L, Paquot M, et al. Structural Characterization, Technological Functionality, and Physiological Aspects of Fungal β-D-glucans: A Review. *Critical Reviews in Food Science and Nutrition*. 2016;56(10): 1746–1752. https://doi.org/10.1080/10408398.2013.854733.

81. Xu C, Wang F, Guan S, Wang L. β-Glucans obtained from fungus for wound healing: A review. *Carbohydrate Polymers*. 2024;327(121662). https://doi.org/10.1016/j.carbpol.2023.121662.

82. Zhu F, Du B, Bian Z, Xu B. Beta-glucans from edible and medicinal mushrooms: Characteristics, physicochemical and biological activities. *Journal of Food Composition and Analysis*. 2015;(41): 165–173.

83. Mykhalevych A, Polishchuk G, Nassar K, Osmak T, Buniowska-Olejnik M. β-Glucan as a Techno-Functional Ingredient in Dairy and Milk-Based Products—A Review. *Molecules*. 2022;27(6313). https://doi.org/10.3390/molecules27196313.

84. Nguyen TTL, Gilbert RG, Gidley MJ, Fox GP. The contribution of β-glucan and starch fine structure to texture of oat-fortified wheat noodles. *Food Chemistry*. 2020;324(126858). https://doi.org/10.1016/j.foodchem.2020.126858.

85. Álvarez D, Barbut S. Effect of inulin, β-Glucan and their mixtures on emulsion stability, color and textural parameters of cooked meat batters. *Meat Science*. 2013;94: 320–327. https://doi.org/10.1016/j.meatsci.2013.02.011.

86. Zhu Q, Chen Z, Paul PK, Lu Y, Wu W, Qi J. Oral delivery of proteins and peptides: Challenges, status quo and future perspectives. *Acta Pharmaceutica Sinica B*. 2021;11(8): 2416–2448. https://doi.org/10.1016/j.apsb.2021.04.001.

87. Zhang E, Li W, Wang N, Zhao G, Ma R, Dong J, et al. Peptide from natural source as ecofriendly aqueous lubricant additive. *Tribology International*. 2023;178. https://doi.org/10.1016/j.triboint.2022.108082.

88. Lin CY, Wang YL, Chen YJ, Ho C Te, Chi YH, Chan LY, et al. Collagen-binding peptides for the enhanced imaging, lubrication and regeneration of osteoarthritic articular cartilage. *Nature Biomedical Engineering*. 2022;6(10): 1105–1117. https://doi.org/10.1038/s41551-022-00948-5.

89. Allahou LW, Madani SY, Seifalian A. Investigating the Application of Liposomes as Drug Delivery Systems for the Diagnosis and Treatment of Cancer. *International Journal of Biomaterials*. 2021;2021. https://doi.org/10.1155/2021/3041969.

90. Myant C, Cann P. On the matter of synovial fluid lubrication: Implications for Metal-on-Metal hip tribology. *Journal of the Mechanical Behavior of Biomedical Materials*. 2014;34: 338–348. https://doi.org/10.1016/j.jmbbm.2013.12.016.

91. Trunfio-Sfarghiu AM, Berthier Y, Meurisse MH, Rieu JP. Role of nanomechanical properties in the tribological performance of phospholipid biomimetic surfaces. *Langmuir*. 2008;24(16): 8765–8771. https://doi.org/10.1021/la8005234.

92. Tang L, Winkeljann B, Feng S, Song J, Liu Y. Recent advances in superlubricity of liposomes for biomedical applications. *Colloids and Surfaces B: Biointerfaces*. 2022;218(112764). https://doi.org/10.1016/j.colsurfb.2022.112764.

93. Murali M, Cann P, Masen M. Development of a biomimetic water-based lubricant: Nanoencapsulation of stearic acid using liposomes. *Tribology International*. 2025;201(110238). https://doi.org/10.1016/j.triboint.2024.110238.

94. Dowson D. Bio-tribology. *Faraday Discussions*. 2012;156: 9–30. https://doi.org/10.1039/c2fd20103h.

95. Derler S, Gerhardt LC. Tribology of skin: Review and analysis of experimental results for the friction coefficient of human skin. *Tribology Letters*. 2012;45(1): 1–27. https://doi.org/10.1007/s11249-011-9854-y.

96. Luengo GS, Tanner H, L'Haridon J, Portal J, Leonforte F, Deswarte F, et al. Polymers and the eco-design transformation. A cosmetic perspective. *Green Materials*. 2025; https://doi.org/10.1680/jgrma.24.00187.

97. Bhushan B. *Introduction to tribology*.. Second edition. Introduction to tribology. Chichester: John Wiley & Sons; 2013.

98. *Test Method for Linearly Reciprocating Ball-on-Flat Sliding Wear*. 2016. https://doi.org/10.1520/G0133-05R16.

99. International Organization of Standartization. *ISO 12156-1: Diesel fuel — Assessment of lubricity using the high-frequency reciprocating rig (HFRR)*. 2023.

100. Zhang J, Campen S, Wong J, Spikes H. Oxidational wear in lubricated contacts – Or is it? *Tribology International*. 2022;165. https://doi.org/10.1016/j.triboint.2021.107287.

101. Cores TD. *ASTM D6079–11, Standard Test Method for Evaluating Lubricity of Diesel Fuels by the High-Frequency Reciprocating Rig (HFRR)*. 2012. p. i:1-6.

102. Parkes M, Myant C, Dini D, Cann P. Tribology-optimised silk protein hydrogels for articular cartilage repair. *Tribology International*. 2015;89: 9–18. https://doi.org/10.1016/j.triboint.2014.11.024.

103. Lubrecht AA, Venner CH, Colin F. Film thickness calculation in elasto-hydrodynamic lubricated line and elliptical contacts: The Dowson, Higginson, Hamrock contribution. *Proceedings of the Institution of Mechanical Engineers, Part J: Journal of Engineering Tribology*. 2009;223(3): 511–515. https://doi.org/10.1243/13506501JET508.

104. Porte E, Cann P, Masen M. Fluid load support does not explain tribological performance of PVA hydrogels. *Journal of the Mechanical Behavior of Biomedical Materials*. 2019;90: 284–294. https://doi.org/10.1016/j.jmbbm.2018.09.048.

105. Porte E, Cann P, Masen M. A lubrication replenishment theory for hydrogels. *Soft Matter*. 2020;16(45): 10290–10300. https://doi.org/10.1039/d0sm01236j.

106. Larson RG. *The structure and rheology of complex fluids*. Oxford: Oxford University Press; 1999.

107. Mezger TG. *The rheology handbook : for users of rotational and oscillatory rheometers*.. 4th edition. Hannover: Vincentz Network; 2014.

108. Szeri AZ. *Fluid film lubrication: theory and design*. Fluid film lubrication : theory and design. Cambridge: Cambridge University Press; 1998.

109. Gong JP. Why are double network hydrogels so tough? *Soft Matter*. 2010;6(12): 2583–2590. https://doi.org/10.1039/b924290b.

110. Gong JP. Friction and lubrication of hydrogels - Its richness and complexity. *Soft Matter*. 2006;2(7): 544–552. https://doi.org/10.1039/b603209p.

111. Krivega ES, Kotova SL, Timashev PS, Efremov YM. Mechanical characterization of soft biomaterials: which time and spatial scale to choose? *Soft Matter*. 2024;20(26): 5095–5104. https://doi.org/10.1039/d4sm00530a.

112. Cuomo F, Cofelice M, Lopez F. Rheological characterization of hydrogels from alginate-based nanodispersion. *Polymers*. 2019;11(2). https://doi.org/10.3390/polym11020259.

113. Bianco S, Panja S, Adams DJ. Using Rheology to Understand Transient and Dynamic Gels. *Gels*. 2022;8(2). https://doi.org/10.3390/gels8020132.

114. Keykhaee M, Sorouri F, Rahimifard M, Baeeri M, Forumadi A, Firoozpour L, et al. Polysaccharide-based hydrogel enriched by epidermal growth factor peptide fragment for improving the wound healing process. *Heliyon*. 2023;9(12). https://doi.org/10.1016/j.heliyon.2023.e22749.

115. Shah R, Saha N, Kitano T, Saha P. Influence of strain on dynamic viscoelastic properties of swelled (H2O) and biomineralized (CaCO3) PVP-CMC hydrogels. *Applied Rheology*. 2015;25(3): 1–10. https://doi.org/10.3933/APPLRHEOL-25-33979.

116. Schek RM, Michalek AJ, Iatridis JC. Genipin-crosslinked fibrin hydrogels as a potential adhesive to augment intervertebral disc annulus repair. *European Cells and Materials*. 2011;21: 373–383. https://doi.org/10.22203/eCM.v021a28.

117. Lin DC, Shreiber DI, Dimitriadis EK, Horkay F. Spherical indentation of soft matter beyond the Hertzian regime: Numerical and experimental validation of hyperelastic

models. *Biomechanics and Modeling in Mechanobiology*. 2009;8(5): 345–358. https://doi.org/10.1007/s10237-008-0139-9.

118. Dimitriadis EK, Horkay F, Maresca J, Kachar B, Chadwick RS. Determination of elastic moduli of thin layers of soft material using the atomic force microscope. *Biophysical Journal*. 2002;82(5): 2798–2810. https://doi.org/10.1016/S0006-3495(02)75620-8.

119. Czerner M, Fellay LS, Suárez MP, Frontini PM, Fasce LA. Determination of Elastic Modulus of Gelatin Gels by Indentation Experiments. *Procedia Materials Science*. 2015;8: 287–296. https://doi.org/10.1016/j.mspro.2015.04.075.

120. Stetefeld J, McKenna SA, Patel TR. Dynamic light scattering: a practical guide and applications in biomedical sciences. *Biophysical Reviews*. 2016;8(4): 409–427. https://doi.org/10.1007/s12551-016-0218-6.

121. Nosonovsky M, Bhushan B. Green tribology: Principles, research areas and challenges. *Philosophical Transactions of the Royal Society A: Mathematical, Physical and Engineering Sciences*. 2010;368(1929): 4677–4694. https://doi.org/10.1098/rsta.2010.0200.

122. Freschi M, Paniz A, Cerqueni E, Colella G, Dotelli G. The Twelve Principles of Green Tribology: Studies, Research, and Case Studies - A Brief Anthology. *Lubricants*. 2022;10(6). https://doi.org/10.3390/lubricants10060129.

123. Afonso IS, Nobrega G, Lima R, Gomes JR, Ribeiro JE. Conventional and Recent Advances of Vegetable Oils as Metalworking Fluids (MWFs): A Review. *Lubricants*. 2023;11(4). https://doi.org/10.3390/lubricants11040160.

124. Biresaw G. Vegetable Oils in Lubrication. In: *Bailey's Industrial Oil and Fat Products*. Wiley; 2020. p. 1–29. https://doi.org/10.1002/047167849x.bio055.pub2.

125. Nosonovsky M. Oil as a Lubricant in the Ancient Middle East. *Tribology Online*. 2007;2(2): 44–49. https://doi.org/10.2474/trol.2.44.

126. Rudnick LR. *Synthetics, mineral oils, and bio-based lubricants: chemistry and technology*. Boca Raton: CRC/Taylor & Francis; 2006. https://doi.org/10.1201/9781420027181.

127. Nogales-Delgado S, Encinar JM, González JF. A Review on Biolubricants Based on Vegetable Oils through Transesterification and the Role of Catalysts: Current Status and Future Trends. *Catalysts*. 2023;13(9). https://doi.org/10.3390/catal13091299.

128. Asadauskas S. Lubrication properties of castor oil - Potential basestock for biodegradable lubricants. *Lubrication Engineering*. 1997;53(12): 35–40.

129. Fasina OO, Hallman H, Craig-Schmidt M, Clements C. Predicting temperature-dependence viscosity of vegetable oils from fatty acid composition. *JAOCS, Journal of the American Oil Chemists' Society*. 2006;83(10): 899–903. https://doi.org/10.1007/s11746-006-5044-8.

130. West L, Tsui I, Balch B, Meyer K, Huth PJ. Determination and health implication of the erucic acid content of broccoli florets, sprouts, and seeds. *Journal of Food Science*. 2002;67(7): 2641–2643. https://doi.org/10.1111/j.1365-2621.2002.tb08791.x.

131. Park YS, Kim ID, Dhungana SK, Park EJ, Park JJ, Kim JH, et al. Quality Characteristics and Antioxidant Potential of Lemon (Citrus limon Burm. f.) Seed Oil Extracted by Different Methods. *Frontiers in Nutrition*. 2021;8. https://doi.org/10.3389/fnut.2021.644406.

132. Akhtar N, Ahmad M, Madni A, Sattar M. Evaluation of basic properties of macadamia nut oil. *Gomal University Journal of Research*. 2006;(22): 21–27. https://www.researchgate.net/publication/237671502

133. Ojha PK, Poudel DK, Rokaya A, Maharjan S, Timsina S, Poudel A, et al. Chemical Compositions and Essential Fatty Acid Analysis of Selected Vegetable Oils and Fats. *Compounds*. 2024;4(1): 37–70. https://doi.org/10.3390/compounds4010003.

134. Patel VR, Dumancas GG, Viswanath LCK, Maples R, Subong BJJ. Castor oil: Properties, uses, and optimization of processing parameters in commercial production. *Lipid Insights*. 2016;9(1). https://doi.org/10.4137/LPI.S40233.

135. Yeboah A, Ying S, Lu J, Xie Y, Amoanimaa-Dede H, Boateng KGA, et al. Castor oil (Ricinus communis): A review on the chemical composition and physicochemical properties. *Food Science and Technology (Brazil)*. 2021;41: 399–413. https://doi.org/10.1590/fst.19620.

136. Knothe G, Steidley KR. Lubricity of components of biodiesel and petrodiesel. The origin of biodiesel lubricity. *Energy and Fuels*. 2005;19(3): 1192–1200. https://doi.org/10.1021/ef049684c.

137. Biresaw G. Biobased Polyalphaolefin Base Oil: Chemical, Physical, and Tribological Properties. *Tribology Letters*. 2018;66(2). https://doi.org/10.1007/s11249-018-1027-9.

138. Hashempour-Baltork F, Torbati M, Azadmard-Damirchi S, Savage GP. Vegetable oil blending: A review of physicochemical, nutritional and health effects. *Trends in Food Science and Technology*. 2016;57: 52–58. https://doi.org/10.1016/j.tifs.2016.09.007.

139. Letard A, Potrel M, Graeff E, Petit LM, Saint-Sardos A, Pygmalion MJ, et al. Biomim'Index—A New Method Supporting Eco-Design of Cosmetic Products Through Biomimicry. *Sustainability*. 2025;17(13): 6124. https://doi.org/10.3390/su17136124.

140. Han J, Hui Z, Tian F, Chen G. Review on bioinspired flight systems and bionic aerodynamics. *Chinese Journal of Aeronautics*. 2020;(34): 170–186.

141. Matsuno F. Snake Robots and Their Applications in Harsh Environments - A Review. In: *2025 IEEE International Conference on Mechatronics, ICM 2025*. Institute of Electrical and Electronics Engineers Inc.; 2025. https://doi.org/10.1109/ICM62621.2025.10934914.

142. Samaha MA, Gad-el-Hak M. Slippery surfaces: A decade of progress. *Physics of Fluids*. 2021;33(071301). https://doi.org/10.1063/5.0056967.

143. Kshirsagar M, Kulkarni S, Meena AK, D'costa DC, Bhagwat A, Siddiqui MIH, et al. Biomimicry-Based Design of Underground Cold Storage Facilities: Energy Efficiency and Sustainability. *Biomimetics*. 2025;10(2). https://doi.org/10.3390/biomimetics10020122.

144. Thopate K, Jaiswal KN. Bio-inspired design in healthcare: The gecko-inspired surgical adhesive. In: *Intelligent Decision Making Through Bio-Inspired Optimization*. IGI Global; 2024. p. 111–130. https://doi.org/10.4018/979-8-3693-2073-0.ch008.

145. Bixler GD, Bhushan B. Fluid drag reduction with shark-skin riblet inspired microstructured surfaces. *Advanced Functional Materials*. 2013;23(36): 4507–4528. https://doi.org/10.1002/adfm.201203683.

146. Han Y, Pang X, Pi G. Biomimetic and Bioinspired Intervention Strategies for the Treatment of Rheumatoid Arthritis. *Advanced Functional Materials*. 2021;31(2104640). https://doi.org/10.1002/adfm.202104640.

147. Ateshian GA. The role of interstitial fluid pressurization in articular cartilage lubrication. *Journal of Biomechanics*. 2009;42(9): 1163–1176. https://doi.org/10.1016/j.jbiomech.2009.04.040.

148. Nadein K, Gorb S. Lubrication in the joints of insects (Arthropoda: Insecta). *Journal of Zoology*. 2022;316(1): 24–39. https://doi.org/10.1111/jzo.12922.

149. Oh JK, Behmer ST, Marquess R, Yegin C, Scholar EA, Akbulut M. Structural, tribological, and mechanical properties of the hind leg joint of a jumping insect: Using katydids to inform bioinspired lubrication systems. *Acta Biomaterialia*. 2017;62: 284–292. https://doi.org/10.1016/j.actbio.2017.08.013.

150. Shankar R, Jung JH, Loh A, An JG, Ha SY, Yim UH. Environmental significance of lubricant oil: A systematic study of photooxidation and its consequences. *Water Research*. 2020;168. https://doi.org/10.1016/j.watres.2019.115183.

151. Nazari M, Riebeling S, Banfield CC, Akale A, Crosta M, Mason-Jones K, et al. Mucilage Polysaccharide Composition and Exudation in Maize From Contrasting Climatic Regions. *Frontiers in Plant Science*. 2020;11. https://doi.org/10.3389/fpls.2020.587610.

152. Quark M. *Slimy Spike (Gomphidius glutinosus)*. https://uk.inaturalist.org/photos/461292785.

153. Rahman MH, Warneke H, Webbert H, Rodriguez J, Austin E, Tokunaga K, et al. Water-based lubricants: Development, properties, and performances. *Lubricants*. 2021;9(8). https://doi.org/10.3390/lubricants9080073.

154. Tomala A, Karpinska A, Werner WSM, Olver A, Stoeri H. Tribological properties of additives for water-based lubricants. *Wear*. 2010;(269): 804–810. https://doi.org/10.1016/j.wear.2010.08.008.

155. Seror J, Merkher Y, Kampf N, Collinson L, Day AJ, Maroudas A, et al. Articular cartilage proteoglycans as boundary lubricants: Structure and frictional interaction of surface-attached hyaluronan and hyaluronan-aggrecan complexes. *Biomacromolecules*. 2011;12(10): 3432–3443. https://doi.org/10.1021/bm2004912.

156. Waller KA, Zhang LX, Elsaid KA, Fleming BC, Warman ML, Jay GD. Role of lubricin and boundary lubrication in the prevention of chondrocyte apoptosis. *Proceedings of the National Academy of Sciences of the United States of America*. 2013;110(15): 5852–5857. https://doi.org/10.1073/pnas.1219289110.

157. Tosif MM, Najda A, Bains A, Kaushik R, Dhull SB, Chawla P, et al. A comprehensive review on plant-derived mucilage: Characterization, functional properties, applications, and its utilization for nanocarrier fabrication. *Polymers*. 2021;13(7). https://doi.org/10.3390/polym13071066.

158. Zheng Z, Dong C, Bai X, Yuan C, Cai T. A novel biomimetic strategy for improving lubrication performances of modified UHMWPE inspired by the slippery gel release behavior of chia seeds. *Composites Part B: Engineering*. 2025;301. https://doi.org/10.1016/j.compositesb.2025.112520.

159. Hakala TJ, Saikko V, Arola S, Ahlroos T, Helle A, Kuosmanen P, et al. Structural characterization and tribological evaluation of quince seed mucilage. *Tribology International*. 2014;77: 24–31. https://doi.org/10.1016/j.triboint.2014.04.018.

160. Western TL. The sticky tale of seed coat mucilages: Production, genetics, and role in seed germination and dispersal. *Seed Science Research*. 2012;22(1): 1–25. https://doi.org/10.1017/S0960258511000249.

161. Zhang X, Wei L, Qiu X, Wu T, Zhao Y, Hu B, et al. Probing the adsorption and interaction mechanisms of green bio-lubricants on model surfaces: Using okra mucilage on mica as a model system. *Applied Surface Science*. 2025;686(162207). https://doi.org/10.1016/j.apsusc.2024.162207.

162. Liu P, Liu Y, Yang Y, Chen Z, Li J, Luo J. Mechanism of biological liquid superlubricity of brasenia schreberi mucilage. *Langmuir*. 2014;30: 3811–3816. https://doi.org/10.1021/la500193n.

163. Liu S, Yuan C, Dong C, Liu C. Excellent lubricating performance of a novel polysaccharide lubricant on reducing friction-induced deformation. *Journal of Molecular Liquids*. 2024;401. https://doi.org/10.1016/j.molliq.2024.124593.

164. Liu S, Lv J, Zheng Z, Liu C. The molecular characteristics, hydration actions and anti-wear performances of the bio-extracted polysaccharides. *Wear*. 2025;571. https://doi.org/10.1016/j.wear.2025.205787.

165. H. Gulrez SK, Al-Assaf S, O G. Hydrogels: Methods of Preparation, Characterisation and Applications. In: *Progress in Molecular and Environmental Bioengineering - From Analysis and Modeling to Technology Applications*. InTech; 2011. https://doi.org/10.5772/24553.

166. Asmatulu R, Usta A. Hydrogels in Various Biomedical Applications. In: Mendez-Vilas A, Solano A (eds.) *Polymer science: research advances, practical applications and educational aspects*. 2015. https://www.researchgate.net/publication/311559090

167. Caló E, Khutoryanskiy V V. Biomedical applications of hydrogels: A review of patents and commercial products. *European Polymer Journal*. 2015;65: 252–267. https://doi.org/10.1016/j.eurpolymj.2014.11.024.

168. Moore D, Robson G, Trinci A. *21st Century Guidebook to Fungi*.. 2nd ed. Cambridge: Cambridge University Press; 2020.

169. Phillips Roger, Shearer Lyndsay, Reid Derek, Rayner Ronald. *Mushrooms and other fungi of Great Britain and Europe*. Mushrooms : and other fungi of Great Britain and Europe. London: Pan Books; 1981.

170. Jordan Peter. *Field guide to edible mushrooms of Britain and Europe*. Field guide to edible mushrooms of Britain and Europe. London: New Holland; 2006.

171. Singh M, Kamal S, Sharma VP. Species and region-wise mushroom production in leading mushroom producing countries - China, Japan, USA, Canada and India. *Mushroom Research*. 2022;30(2): 99. https://doi.org/10.36036/mr.30.2.2021.119394.

172. Royse DJ, Baars J, Tan Q. Current overview of mushroom production in the world. In: Cunha Zied D, Pardo-Giménez A (eds.) *Edible and medicinal mushrooms: technology and applications*. John Wiley & Sons; 2017.

173. Sima P, Vannucci L, Vetvicka V. β-glucans and cholesterol (Review). *International Journal of Molecular Medicine*. 2018;41(4): 1799–1808. https://doi.org/10.3892/ijmm.2018.3411.

174. Shin HJ, Ro HS, Kawauchi M, Honda Y. Review on mushroom mycelium-based products and their production process: from upstream to downstream. *Bioresources and Bioprocessing*. 2025;12(1). https://doi.org/10.1186/s40643-024-00836-7.

175. Islam MR, Tudryn G, Bucinell R, Schadler L, Picu RC. Morphology and mechanics of fungal mycelium. *Scientific Reports*. 2017;7(1). https://doi.org/10.1038/s41598-017-13295-2.

176. Ko WC, Liu WC, Tsang YT, Hsieh CW. Kinetics of winter mushrooms (Flammulina velutipes) microstructure and quality changes during thermal processing. *Journal of Food Engineering*. 2007;81(3): 587–598. https://doi.org/10.1016/j.jfoodeng.2006.12.009.

177. Van De Velde F, De Hoog EHA, Oosterveld A, Tromp RH. Protein-polysaccharide interactions to alter texture. *Annual Review of Food Science and Technology*. 2015;6: 371–388. https://doi.org/10.1146/annurev-food-022814-015558.

178. Yang X, Li A, Li X, Sun L, Guo Y. An overview of classifications, properties of food polysaccharides and their links to applications in improving food textures. *Trends in Food Science and Technology*. 2020;102: 1–15. https://doi.org/10.1016/j.tifs.2020.05.020.

179. Wang Z, Wang L, Yu X, Wang X, Zheng Y, Hu X, et al. Effect of polysaccharide addition on food physical properties: A review. *Food Chemistry*. 2024;431(137099). https://doi.org/10.1016/j.foodchem.2023.137099.

180. Funami T. In vivo and rheological approaches for characterizing food oral processing and usefulness of polysaccharides as texture modifiers- A review. *Food Hydrocolloids*. 2017;68: 2–14. https://doi.org/10.1016/j.foodhyd.2017.01.020.

181. Kripp R, Seibert A, Fries D, Fessenbecker A, Ruehle T. *Lubricant compositions containing beta-glucans*. World Intellectual Property Organisation; EP2015060995, 2015.

182. Vlassopoulou M, Yannakoulia M, Pletsa V, Zervakis GI, Kyriacou A. Effects of fungal beta-glucans on health-a systematic review of randomized controlled trials. *Food and Function*. 2021;12: 3366–3380. https://doi.org/10.1039/d1fo00122a.

183. Ahmad I, Arif M, Xu M, Zhang J, Ding Y, Lyu F. Therapeutic values and nutraceutical properties of shiitake mushroom (Lentinula edodes): A review. *Trends in Food Science and Technology*. 2023;134: 123–135. https://doi.org/10.1016/j.tifs.2023.03.007.

184. Rezaeian S, Pourianfar HR, Dowom SA. Comparative assessment of β-glucan composition and structural characterization in wild and commercial Enoki mushrooms, Flammulina velutipes. *Journal of Food Composition and Analysis*. 2023;120. https://doi.org/10.1016/j.jfca.2023.105286.

185. Gupta K, Tejaswini M, Umekar MJ. Medicinal Value of Mushroom: A Deeper Insight. *Current Indian Science*. 2024;02. https://doi.org/10.2174/012210299x285895240521042601.

186. Kumar A, Paliwal R, Gulbake A. Lentinan: An unexplored novel biomaterial in drug and gene delivery applications. *Journal of Controlled Release*. 2023;356: 316–336. https://doi.org/10.1016/j.jconrel.2023.02.034.

187. Xu M, Qu Y, Li H, Tang S, Chen C, Wang Y, et al. Improved Extraction Yield, Water Solubility, and Antioxidant Activity of Lentinan from Lentinula edodes via Bacillus subtilis natto Fermentation. *Fermentation*. 2023;9(4). https://doi.org/10.3390/fermentation9040333.

188. Song W, Li M, Yue X, Zheng Y. Effect of extraction and purification on the structure and activity of Flammulina velutipes polysaccharides: a review. *International Journal of Food Science and Technology*. 2024; https://doi.org/10.1111/ijfs.17393.

189. Zhou S, Song J, Xu P, He M, Xu M, You F. A review on tribology, characterization and lubricants for water-based drilling fluids. *Geoenergy Science and Engineering*. 2023;229. https://doi.org/10.1016/j.geoen.2023.212074.

190. Lee SJ, Sohn YC, Kim CL. Tribological Effects of Water-Based Graphene Lubricants on Graphene Coatings. *Materials*. 2023;16(1). https://doi.org/10.3390/ma16010197.

191. Ding M, Lin B, Sui T, Wang A, Yan S, Yang Q. The excellent anti-wear and friction reduction properties of silica nanoparticles as ceramic water lubrication additives. *Ceramics International*. 2018;44(12): 14901–14906. https://doi.org/10.1016/j.ceramint.2018.04.206.

192. Li X, He Y, Zeng P, Liu Y, Zhang M, Hao C, et al. Molecular basis for Poria cocos mushroom polysaccharide used as an antitumour drug in China. *Journal of Cellular and Molecular Medicine*. 2019;23(1): 4–20. https://doi.org/10.1111/jcmm.13564.

193. Puliga F, Zuffi V, Zambonelli A, Francioso O, Sanchez-Cortes S. Spectroscopic analysis of mushrooms by surface-enhanced Raman scattering (SERS). *Chemical*

and Biological Technologies in Agriculture. 2022;9(1). https://doi.org/10.1186/s40538-022-00367-3.

194. Kour H, Kour D, Kour S, Singh S, Jawad Hashmi SA, Yadav AN, et al. Bioactive compounds from mushrooms: Emerging bioresources of food and nutraceuticals. *Food Bioscience*. 2022;50. https://doi.org/10.1016/j.fbio.2022.102124.

195. *Lentinan, C42H72O36, CID 37339-90-5 – PubChem n.d. https://pubchem.ncbi.nlm.nih.gov/compound/37723 (accessed April 1, 2025)*.

196. Dakhil H, Wierschem A. Measuring low viscosities and high shear rates with a rotational rheometer in a thin-gap parallel-disk configuration. *Applied Rheology*. 2014;24(6). https://doi.org/10.3933/APPLRHEOL-24-63795.

197. Hunter RJ. *Foundations of colloid science*.. 2nd ed. Foundations of colloid science. Oxford: Oxford University Press; 2001.

198. Dwyer-Joyce RS, Sayles RS, Ioannides E. An investigation into the mechanisms of closed three-body abrasive wear. *Wear*. 1994;175(1–2): 133–142. https://doi.org/10.1016/0043-1648(94)90176-7.

199. Ramakrishnan V. *An Investigation into 'Squeezing' or Three-Body Wear caused by Abrasive Particles*. KTH Royal Institute of Technology.; https://urn.kb.se/resolve?urn=urn:nbn:se:kth:diva-283552 [Accessed 22nd June 2025].

200. Cann PM. The 'leaves on the line' problem - A study of leaf residue film formation and lubricity under laboratory test conditions. *Tribology Letters*. 2006;24(2): 151–158. https://doi.org/10.1007/s11249-006-9152-2.

201. Zhang L, Zhu Z, Zhao D, Gao X, Wang B. Tribological Performance of ZrO2 Nanoparticles as Friction and Wear Reduction Additives in Aviation Lubricant. *Materials Research Express*. 2024; https://doi.org/10.1088/2053-1591/ad78b3.

202. Chen YY, Horng JH. Investigation of lubricant viscosity and third-particle contribution to contact behavior in dry and lubricated three-body contact conditions. *Frontiers in Mechanical Engineering*. 2024;10. https://doi.org/10.3389/fmech.2024.1390335.

203. Chojnicka A, De Jong S, De Kruif CG, Visschers RW. Lubrication properties of protein aggregate dispersions in a soft contact. *Journal of Agricultural and Food Chemistry*. 2008;56(4): 1274–1282. https://doi.org/10.1021/jf0720988.

204. Shipway PH, Wirojanupatump S. The role of lubrication and corrosion in abrasion of materials in aqueous environments. *Tribology International*. 2002;35: 661–667.

205. Chern SY, Chen YY, Liu WL, Horng JH. Contact Characteristics at Interface in Three-Body Contact Conditions with Rough Surfaces and Foreign Particles. *Lubricants*. 2022;10(7). https://doi.org/10.3390/lubricants10070164.

206. Funami T. Next target for food hydrocolloid studies: Texture design of foods using hydrocolloid technology. *Food Hydrocolloids*. 2011;25(8): 1904–1914. https://doi.org/10.1016/j.foodhyd.2011.03.010.

207. Garg S, Garg A. Hydrogel: Classification, Properties, Preparation and Technical Features. *Asian Journal of Biomedical Research*. 2016;(2(6)): 163–170.

208. Akhtar MF, Hanif M, Ranjha NM. Methods of synthesis of hydrogels… A review. *Saudi Pharmaceutical Journal*. 2016;24(5): 554–559. https://doi.org/10.1016/j.jsps.2015.03.022.

209. Alavarse AC, Frachini ECG, da Silva RLCG, Lima VH, Shavandi A, Petri DFS. Crosslinkers for polysaccharides and proteins: Synthesis conditions, mechanisms, and crosslinking efficiency, a review. *International Journal of Biological Macromolecules*. 2022;202: 558–596. https://doi.org/10.1016/j.ijbiomac.2022.01.029.

210. Duque-Ossa LC, Ruiz-Pulido G, Medina DI. Triborheological study under physiological conditions of PVA hydrogel/Ha lubricant as synthetic system for soft tissue replacement. *Polymers*. 2021;13(5): 1–15. https://doi.org/10.3390/polym13050746.

211. El Sayed MM. Production of Polymer Hydrogel Composites and Their Applications. *Journal of Polymers and the Environment*. 2023;31: 2855–2879. https://doi.org/10.1007/s10924-023-02796-z.

212. Giavasis I, Harvey LM, McNeil B. Gellan gum. *Critical Reviews in Biotechnology*. 2000;20(3): 177–211. https://doi.org/10.1080/07388550008984169.

213. Cebrián-Lloret V, Martínez-Abad A, López-Rubio A, Martínez-Sanz M. Exploring alternative red seaweed species for the production of agar-based hydrogels for food applications. *Food Hydrocolloids*. 2024;146. https://doi.org/10.1016/j.foodhyd.2023.109177.

214. Udo T, Mummaleti G, Mohan A, Singh RK, Kong F. Current and emerging applications of carrageenan in the food industry. *Food Research International*. 2023;173(113369). https://doi.org/10.1016/j.foodres.2023.113369.

215. Cao Y, Cong H, Yu B, Shen Y. A review on the synthesis and development of alginate hydrogels for wound therapy. *Journal of Materials Chemistry B*. 2023;11(13): 2801–2829. https://doi.org/10.1039/d2tb02808e.

216. Said NS, Olawuyi IF, Lee WY. Pectin Hydrogels: Gel-Forming Behaviors, Mechanisms, and Food Applications. *Gels*. 2023;9(9). https://doi.org/10.3390/gels9090732.

217. Necas J, Bartosikova L. Carrageenan: a review. *Veterinarni Medicina*. 2013;58(4): 187–205.

218. Cunha L, Grenha A. Sulfated seaweed polysaccharides as multifunctional materials in drug delivery applications. *Marine Drugs*. 2016;14(3). https://doi.org/10.3390/md14030042.

219. Bertasa M, Dodero A, Alloisio M, Vicini S, Riedo C, Sansonetti A, et al. Agar gel strength: A correlation study between chemical composition and rheological properties. *European Polymer Journal*. 2020;123(109442). https://doi.org/10.1016/j.eurpolymj.2019.109442.

220. Rhein-Knudsen N, Meyer AS. Chemistry, gelation, and enzymatic modification of seaweed food hydrocolloids. *Trends in Food Science and Technology*. 2021;109: 608–621. https://doi.org/10.1016/j.tifs.2021.01.052.

221. Hotta M, Kennedy J, Higginbotham C, Morris N. Durum Wheat Seed Germination Response to Hydrogel Coatings and Moisture under Drought Stress. *American Journal of Agricultural and Biological Sciences*. 2016;11: 67–75. https://doi.org/10.3844/ajabssp.2016.67.75.

222. Imeson A, Imeson A. Agar. In: *Food Stabilisers, Thickeners and Gelling Agents*. United Kingdom: Wiley; 2011. p. 31–49.

223. Coutinho DF, Sant S V., Shin H, Oliveira JT, Gomes ME, Neves NM, et al. Modified Gellan Gum hydrogels with tunable physical and mechanical properties. *Biomaterials*. 2010;31(29): 7494–7502. https://doi.org/10.1016/j.biomaterials.2010.06.035.

224. Bradbeer JF, Hancocks R, Spyropoulos F, Norton IT. Low acyl gellan gum fluid gel formation and their subsequent response with acid to impact on satiety. *Food Hydrocolloids*. 2015;43: 501–509. https://doi.org/10.1016/j.foodhyd.2014.07.006.

225. Chen Y, Li L, Chen L, Shao W, Chen X, Fan X, et al. Gellan gum-gelatin scaffolds with Ca2+ crosslinking for constructing a structured cell cultured meat model. *Biomaterials*. 2023;299. https://doi.org/10.1016/j.biomaterials.2023.122176.

226. Usman A, Khalid S, Usman A, Hussain Z, Wang Y. Algal Polysaccharides, Novel Application, and Outlook. In: *Algae Based Polymers, Blends, and Composites: Chemistry, Biotechnology and Materials Science*. Elsevier; 2017. p. 115–153. https://doi.org/10.1016/B978-0-12-812360-7.00005-7.

227. Helgerud T, Gåserød O, Fjæreide T, Andersen PO, Larsen CK, Imeson A. Alginates. In: *Food Stabilisers, Thickeners and Gelling Agents*. United Kingdom: Wiley; 2011. p. 50–72.

228. Thakur BR, Singh RK, Handa AK. Chemistry and Uses of Pectin - A Review. *Critical Reviews in Food Science and Nutrition*. 1997;37(1): 47–73. https://doi.org/10.1080/10408399709527767.

229. Su Y, Cockerill I, Wang Y, Qin YX, Chang L, Zheng Y, et al. Zinc-Based Biomaterials for Regeneration and Therapy. *Trends in Biotechnology*. 2019;37(4): 428–441. https://doi.org/10.1016/j.tibtech.2018.10.009.

230. Wang Y, Wen T, Mao F, Yang S, Zhang Q, Fu X, et al. Engineering copper and copper-based materials for a post-antibiotic era. *Frontiers in Bioengineering and Biotechnology*. 2025;13. https://doi.org/10.3389/fbioe.2025.1644362.

231. Sibiya NP, Mahlangu TP, Tetteh EK, Rathilal S. Review on advancing heavy metals removal: The use of iron oxide nanoparticles and microalgae-based adsorbents. *Cleaner Chemical Engineering*. 2025;11: 100137. https://doi.org/10.1016/j.clce.2024.100137.

232. Baruah MJ, Dutta R, Zaki MEA, Bania KK. Heterogeneous Iron-Based Catalysts for Organic Transformation Reactions: A Brief Overview. *Molecules*. 2024;29(13). https://doi.org/10.3390/molecules29133177.

233. Xu Y, Wang Y, An K, Ni C, Zhang H, Ren Y, et al. Advances on Hydrogel Lubrication Modification Under Diverse Design Strategies. *Lubricants*. 2025;13(9): 373. https://doi.org/10.3390/lubricants13090373.

234. Liu W, Ma M, Lei Z, Xiong Z, Tao T, Lei P, et al. Intra-articular injectable hydroxypropyl chitin/hyaluronic acid hydrogel as bio-lubricant to attenuate osteoarthritis progression. *Materials and Design*. 2022;217. https://doi.org/10.1016/j.matdes.2022.110579.

235. Blum MM, Ovaert TC. Low friction hydrogel for articular cartilage repair: Evaluation of mechanical and tribological properties in comparison with natural cartilage tissue. *Materials Science and Engineering C*. 2013;33(7): 4377–4383. https://doi.org/10.1016/j.msec.2013.06.035.

236. Milcovich G, Antunes FE, Farra R, Grassi G, Grassi M, Asaro F. Modulating carbohydrate-based hydrogels as viscoelastic lubricant substitute for articular cartilages. *International Journal of Biological Macromolecules*. 2017;102: 796–804. https://doi.org/10.1016/j.ijbiomac.2017.04.079.

237. Hu J, Andablo-Reyes E, Soltanahmadi S, Sarkar A. Synergistic Microgel-Reinforced Hydrogels as High-Performance Lubricants. *ACS Macro Letters*. 2020;9(12): 1726–1731. https://doi.org/10.1021/acsmacrolett.0c00689.

238. Zhou S, Bismarck A, Steinke JHG. Ion-responsive alginate based macroporous injectable hydrogel scaffolds prepared by emulsion templating. *Journal of Materials Chemistry B*. 2013;1(37): 4736–4745. https://doi.org/10.1039/c3tb20888e.

239. Adams MJ, Briscoe BJ, Johnson SA. Friction and lubrication of human skin. *Tribology Letters*. 2007;26(3): 239–253. https://doi.org/10.1007/s11249-007-9206-0.

240. Schulze KD. *The Contact Mechanics of Soft Surfaces: Cells, Gels and Elastomers*. University of Florida; 2017.

241. Moraes ICF, Hilliou L. Viscoelastic Reversibility of Carrageenan Hydrogels under Large Amplitude Oscillatory Shear: Hybrid Carrageenans versus Blends. *Gels*. 2024;10(8). https://doi.org/10.3390/gels10080524.

242. Schroyen B, Vlassopoulos D, Van Puyvelde P, Vermant J. Bulk rheometry at high frequencies: a review of experimental approaches. *Rheologica Acta*. 2020;59: 1–22. https://doi.org/10.1007/s00397-019-01172-w.

243. Tran Vo TM, Kobayashi T, Potiyaraj P. Viscoelastic Analysis of Pectin Hydrogels Regenerated from Citrus Pomelo Waste by Gelling Effects of Calcium Ion Crosslinking at Different pHs. *Gels*. 2022;8(12). https://doi.org/10.3390/gels8120814.

244. Hashemnejad SM, Kundu S. Rheological properties and failure of alginate hydrogels with ionic and covalent crosslinks. *Soft Matter*. 2019;15(39): 7852–7862. https://doi.org/10.1039/c9sm01039d.

245. BeMiller JN. 13 - Carrageenans. In: BeMiller JN (ed.) *Carbohydrate Chemistry for Food Scientists (Third Edition)*. Third Edition. AACC International Press; 2019. p. 279–291. https://doi.org/https://doi.org/10.1016/B978-0-12-812069-9.00013-3.

246. Sacco P, Piazza F, Marsich E, Abrami M, Grassi M, Donati I. Ionic Strength Impacts the Physical Properties of Agarose Hydrogels. *Gels*. 2024;10(2). https://doi.org/10.3390/gels10020094.

247. Stephen A, Phillips G, Williams P, [eds.]. *Food Polysaccharides and Their Applications*.. 2nd ed. CRC Press, Taylor & Francis; 2006.

248. Saha D, Bhattacharya S. Hydrocolloids as thickening and gelling agents in food: A critical review. *Journal of Food Science and Technology*. 2010;47(6): 587–597. https://doi.org/10.1007/s13197-010-0162-6.

249. Moritaka H, Naito S, Nishinari K, Ishihara M, Fukuba H. Effects of gellan gum, citric acid and sweetener on the texture of lemon jelly. *Journal of Texture Studies*. 1999;30(1): 29–41. https://doi.org/10.1111/j.1745-4603.1999.tb00200.x.

250. Zhou Y, Yan J, Xu BY, Wang BC. The study on mechanical properties of Phytagel medium. *IOP Conference Series: Earth and Environmental Science*. 2019;346(1). https://doi.org/10.1088/1755-1315/346/1/012089.

251. Vancauwenberghe V, Katalagarianakis L, Wang Z, Meerts M, Hertog M, Verboven P, et al. Pectin based food-ink formulations for 3-D printing of customizable porous food simulants. *Innovative Food Science and Emerging Technologies*. 2017;42: 138–150. https://doi.org/10.1016/j.ifset.2017.06.011.

252. Karvinen J, Ihalainen T, Calejo MT, Jönkkäri I, Kellomäki M. Characterization of the microstructure of hydrazone crosslinked polysaccharide-based hydrogels through rheological and diffusion studies. *Materials Science & Engineering C*. 2019;(94): 1056–1066.

253. Annabi N, Nichol JW, Zhong X, Ji C, Koshy S, Khademhosseini A, et al. Controlling the Porosity and Microarchitecture of Hydrogels for Tissue Engineering. *Tissue Engineering: Part B*. 2010;16(4): 371–383.

254. Shoaib T, Espinosa-Marzal RM. Advances in understanding hydrogel lubrication. *Colloids and Interfaces*. 2020;4(4). https://doi.org/10.3390/colloids4040054.

255. Tsuji Y, Li X, Shibayama M. Evaluation of mesh size in model polymer networks consisting of tetra-arm and linear poly(Ethylene glycol)s. *Gels*. 2018;4(2). https://doi.org/10.3390/gels4020050.

256. Sievers-Liebschner J, Dockhorn R, Friedrichs J, Kurth T, Fratzl P, Sommer JU, et al. Unravelling the molecular network structure of biohybrid hydrogels. *Materials Today Bio*. 2025;34. https://doi.org/10.1016/j.mtbio.2025.102249.

257. Nicolella P, Koziol MF, Löser L, Saalwächter K, Ahmadi M, Seiffert S. Defect-controlled softness, diffusive permeability, and mesh-topology of metallo-supramolecular hydrogels. *Soft Matter*. 2022;18(5): 1071–1081. https://doi.org/10.1039/d1sm01456k.

258. Qiu F, Fan X, Chen W, Xu C, Li Y, Xie R. Recent Progress in Hydrogel-Based Synthetic Cartilage: Focus on Lubrication and Load-Bearing Capacities. *Gels*. 2023;9(144). https://doi.org/10.3390/gels9020144.

259. Zhao X, Xia Y, Zhang X, Lin X, Wang L. Design of mechanically strong and tough alginate hydrogels based on a soft-brittle transition. *International Journal of Biological Macromolecules*. 2019;139: 850–857. https://doi.org/10.1016/j.ijbiomac.2019.08.057.

260. Dintwa E, Tijskens E, Ramon H. On the accuracy of the Hertz model to describe the normal contact of soft elastic spheres. *Granular Matter*. 2008;10(3): 209–221. https://doi.org/10.1007/s10035-007-0078-7.

261. Hertz H. *Miscellaneous Papers*. London: Macmillan and Co. Ltd.; 1896.

262. Putignano C, Carbone G, Dini D. Mechanics of rough contacts in elastic and viscoelastic thin layers. *International Journal of Solids and Structures*. 2015;69–70: 507–517. https://doi.org/10.1016/j.ijsolstr.2015.04.034.

263. Putignano C, Campanale A. Squeeze lubrication between soft solids: A numerical study. *Tribology International*. 2022;176. https://doi.org/10.1016/j.triboint.2022.107824.

264. Menga N, Putignano C, Afferrante L, Carbone G. The Contact Mechanics of Coated Elastic Solids: Effect of Coating Thickness and Stiffness. *Tribology Letters*. 2019;67(1). https://doi.org/10.1007/s11249-019-1137-z.

265. Putignano C, Carbone G. A review of boundary elements methodologies for elastic and viscoelastic rough contact mechanics. *Physical Mesomechanics*. 2014;17(4): 321–333. https://doi.org/10.1134/S1029959914040092.

266. Putignano C, Carbone G. Indenting viscoelastic thin layers: A numerical assessment. *Mechanics Research Communications*. 2022;126. https://doi.org/10.1016/j.mechrescom.2022.104011.

267. Johnson KL. *Contact mechanics* . Contact mechanics. Cambridge: Cambridge University Press; 1985.

268. Liu Y, Guo X, Wang B, Gong PX, Liu Y, Li HJ, et al. Lentinan as an eco-friendly corrosion inhibitor for Q235 steel in acid medium: Experimental and theoretical studies. *Journal of Molecular Liquids*. 2022;360. https://doi.org/10.1016/j.molliq.2022.119513.

Appendix A – Static Scenario

Definitions

Magnitude of indentation at Contact radius: $\delta_a = \delta - R + \sqrt{R^2 - a^2}$

Gradient at Contact radius: $\frac{d\delta_a}{dr} = \frac{a}{\sqrt{R^2 - a^2}}$

Ratio of Limit radius over Contact radius: $K = \frac{L_0}{a}$

Strain in Z-direction: $\varepsilon_z = \frac{u_z}{t}$

Strain in R-direction: $\varepsilon_r = \frac{du_r}{dr}$

Strain in θ-direction: $\varepsilon_\theta = \frac{u_r}{r}$

Stress in Z-direction: $\sigma_z = \begin{cases} -\frac{3F_z}{2\pi a^3}(a^2 - r^2)^{\frac{1}{2}} & for\ 0 \le r \le a \\ 0 & for\ r \ge a \end{cases}$

Displacement in Z-direction: $u_z = \begin{cases} -\left(\delta - R + \sqrt{R^2 - r^2}\right) & for\ 0 \le r \le a \\ Case - defined & for\ a \le r \le L_0 \\ 0 & for\ r \ge L_0 \end{cases}$

Indentation force: $-F_z = \int_0^a 2\pi r \sigma_z dr$

Radial force: $F_r = \int_0^a \pi r \sigma_r dr$

Derivation

Starting with linear elasticity correlations between strains and stresses in cylindrical coordinates:

$$\begin{cases} E\varepsilon_z = \sigma_z - v(\sigma_r + \sigma_\theta) \\ E\varepsilon_r = \sigma_r - v(\sigma_z + \sigma_\theta) \\ E\varepsilon_\theta = \sigma_\theta - v(\sigma_z + \sigma_r) \end{cases}$$

Summing up the last two equations:

$$E(\varepsilon_r + \varepsilon_\theta) = (1 - v)(\sigma_r + \sigma_\theta) - 2v\sigma_z$$

Substituting the first linear elasticity equation:

$$E(\varepsilon_r + \varepsilon_\theta) = (1-v)\frac{\sigma_z - E\varepsilon_z}{v} - 2v\sigma_z$$

$$E(\varepsilon_r + \varepsilon_\theta) = \frac{(1+v)(1-2v)}{v}\sigma_z - \frac{1-v}{v}E\varepsilon_z$$

$$\varepsilon_r + \varepsilon_\theta = \frac{(1+v)(1-2v)}{vE}\sigma_z - \frac{1-v}{v}\varepsilon_z$$

Applying strain definitions:

$$\frac{du_r}{dr} + \frac{u_r}{r} = \frac{(1+v)(1-2v)}{vE}\sigma_z - \frac{1-v}{v}\frac{u_z}{t}$$

$$r\frac{du_r}{dr} + u_r = \frac{(1+v)(1-2v)}{vE}r\sigma_z - \frac{1-v}{v}\frac{ru_z}{t}$$

Integrating with respect to r from $r = 0$ to a general radius r:

$$\int_0^r \left(r\frac{du_r}{dr} + u_r\right) dr = \int_0^r \left(\frac{(1+v)(1-2v)}{vE}r\sigma_z - \frac{1-v}{vt}ru_z\right) dr$$

$$[ru_r]_0^r = \frac{(1+v)(1-2v)}{vE}\int_0^r r\sigma_z\, dr - \frac{1-v}{vt}\int_0^r ru_z\, dr$$

Using the definition of Limit radius: $r = L_0$, $u_r(r = L_0) = 0$:

$$0 = \frac{(1+v)(1-2v)}{vE}\int_0^{L_0} r\sigma_z\, dr - \frac{1-v}{vt}\int_0^{L_0} ru_z\, dr$$

Using definitions of Stress in Z-direction and Indentation Force:

$$0 = \frac{(1+v)(1-2v)}{vE}\left(\frac{-F_z}{2\pi}\right) - \frac{1-v}{vt}\int_0^{L_0} ru_z\, dr$$

Rearranging for the z-displacement integral:

$$\int_0^{L_0} ru_z\, dr = -\frac{(1+v)(1-2v)}{(1-v)}\frac{F_z t}{2\pi E}$$

Further solving the known part of z-displacement integral:

$$\int_a^{L_0} ru_z\, dr = -\frac{(1+v)(1-2v)}{(1-v)}\frac{F_z t}{2\pi E} + (\delta - R)\frac{a^2}{2} + \frac{R^3}{3} - \frac{(R^2-a^2)^{\frac{3}{2}}}{3}$$

Solving for the radial displacement:

a) For $0 \leq r \leq a$:

$$ru_r = \frac{(1+v)(1-2v)}{vE}\int_0^r -r\frac{3F_z}{2\pi a^3}(a^2-r^2)^{\frac{1}{2}}\,dr + \frac{1-v}{vt}\int_0^r r\left(\delta - R + (R^2-r^2)^{\frac{1}{2}}\right)dr$$

$$ru_r = \frac{(1+v)(1-2v)}{vE}\left(-\frac{3F_z}{2\pi a^3}\right)\int_0^r r(a^2-r^2)^{\frac{1}{2}}\,dr + \frac{1-v}{vt}\int_0^r r(\delta - R) + r(R^2-r^2)^{\frac{1}{2}}\,dr$$

$$ru_r = \frac{(1+v)(1-2v)}{vE}\left(-\frac{3F_z}{2\pi a^3}\right)\left[-\frac{1}{3}(a^2-r^2)^{\frac{3}{2}}\right]_0^r + \frac{1-v}{vt}\left[\frac{\delta - R}{2}r^2 - \frac{1}{3}(R^2-r^2)^{\frac{3}{2}}\right]_0^r$$

$$u_r = \frac{(1+v)(1-2v)}{rvE}\left(\frac{F_z}{2\pi a^3}\right)\left((a^2-r^2)^{\frac{3}{2}} - a^3\right) + \frac{1-v}{rvt}\left(\frac{\delta - R}{2}r^2 - \frac{1}{3}(R^2-r^2)^{\frac{3}{2}} + \frac{R^3}{3}\right)$$

b) For $a \leq r \leq L_0$:

$$ru_r = \frac{(1+v)(1-2v)}{vE}\int_0^a -r\frac{3F_z}{2\pi a^3}(a^2-r^2)^{\frac{1}{2}}\,dr + \frac{1-v}{vt}\int_0^a r\left(\delta - R + (R^2-r^2)^{\frac{1}{2}}\right)dr - \frac{1-v}{vt}\int_a^r ru_z\,dr$$

$$u_r = -\frac{(1+v)(1-2v)}{rvE}\frac{F_z}{2\pi} + \frac{1-v}{rvt}\left(\frac{\delta - R}{2}a^2 - \frac{1}{3}(R^2-a^2)^{\frac{3}{2}} + \frac{R^3}{3}\right) - \frac{1-v}{rvt}\int_a^r ru_z\,dr$$

As σ_z, u_z and u_r are now known, it is possible to define all the remaining stresses and strains:

$$\varepsilon_z = \frac{u_z}{t}$$

$$\varepsilon_\theta = \frac{u_r}{r}$$

$$\varepsilon_r = -\varepsilon_\theta + \frac{(1+v)(1-2v)}{vE}\sigma_z - \frac{1-v}{vt}\varepsilon_z$$

$$\sigma_r = v(\sigma_z + \sigma_\theta) + E\varepsilon_r$$

$$\sigma_\theta = \frac{E}{1-v^2}(\varepsilon_\theta + v\varepsilon_r) + \frac{v}{1-v}\sigma_z$$

Appendix B – Case A Deformation

Definitions of Case A:

$$u_z = Ar^n + Br^{n-1} + Cr^{n-2}$$

$$\frac{du_z}{dr} = nAr^{n-1} + (n-1)Br^{n-2} + (n-2)Cr^{n-3}$$

From Criterion 3, where $u_z(r = L_0) = 0$:

$$0 = AL_0^n + BL_0^{n-1} + CL_0^{n-2}$$

$$\boxed{C = -AL_0^2 - BL_0}$$

Updated definitions:

$$u_z = Ar^n + Br^{n-1} - AL_0^2 r^{n-2} - BL_0 r^{n-2}$$

$$u_z = Ar^n\left(1 - \frac{L_0^2}{r^2}\right) + Br^{n-1}\left(1 - \frac{L_0}{r}\right)$$

$$u_z = r^{n-1}\left(1 - \frac{L_0}{r}\right)\left(Ar\left(1 + \frac{L_0}{r}\right) + B\right)$$

$$\frac{du_z}{dr} = nAr^{n-1} + B(n-1)r^{n-2} - AL_0(n-2)r^{n-3} - BL_0(n-2)r^{n-3}$$

$$\frac{du_z}{dr} = Ar^{n-1}\left(n - (n-2)\frac{L_0^2}{r^2}\right) + Br^{n-2}\left(n - 1 - (n-2)\frac{L_0}{r}\right)$$

From Criterion 4, where $\frac{du_z}{dr}(r = L_0) = 0$:

$$0 = AL_0^{n-1}\left(n - (n-2)\frac{L_0^2}{L_0^2}\right) + BL_0^{n-2}\left(n - 1 - (n-2)\frac{L_0}{L_0}\right)$$

$$0 = 2AL_0^{n-1} + BL_0^{n-2}$$

$$\boxed{B = -2AL_0}$$

Updated definitions:

$$u_z = r^{n-1}\left(1 - \frac{L_0}{r}\right)\left(Ar\left(1 + \frac{L_0}{r}\right) - 2AL_0\right)$$

$$u_z = r^{n-1}\left(1 - \frac{L_0}{r}\right)(Ar - AL_0)$$

$$u_z = Ar^n\left(1 - \frac{L_0}{r}\right)^2$$

$$\frac{du_z}{dr} = Ar^{n-1}\left(n-(n-2)\frac{L_0^2}{r^2}\right) - 2AL_0r^{n-2}\left(n-1-(n-2)\frac{L_0}{r}\right)$$

$$\frac{du_z}{dr} = Ar^{n-1}\left(n-(n-2)\frac{L_0^2}{r^2} - 2\frac{L_0}{r}\left(n-1-(n-2)\frac{L_0}{r}\right)\right)$$

$$\frac{du_z}{dr} = Ar^{n-1}\left(n-(n-2)\frac{L_0^2}{r^2} - 2(n-1)\frac{L_0}{r} + 2(n-2)\frac{L_0^2}{r^2}\right)$$

$$\frac{du_z}{dr} = Ar^{n-1}\left((n-2)\frac{L_0^2}{r^2} - 2(n-1)\frac{L_0}{r} + n\right)$$

From Criterion 1, where $u_z(r=a) = -\delta_a$:

$$-\delta_a = Aa^n\left(1-\frac{L_0}{a}\right)^2$$

$$A = -\frac{\delta_a}{a^n(1-K)^2}$$

Updating the definitions to their closed forms:

$$u_z = -\delta_a\left(\frac{r}{a}\right)^n\frac{\left(1-\frac{L_0}{r}\right)^2}{(1-K)^2}$$

$$\frac{du_z}{dr} = -\delta_a\frac{r^{n-1}}{a^n}\frac{\left((n-2)\frac{L_0^2}{r^2} - 2(n-1)\frac{L_0}{r} + n\right)}{(1-K)^2}$$

By applying Criterion 2, where $\frac{du_z}{dr}(r=a) = \frac{d\delta_a}{dr}$, definition of K can be derived:

$$\frac{d\delta_a}{dr} = -\delta_a\frac{a^{n-1}}{a^n}\frac{\left((n-2)\frac{L_0^2}{a^2} - 2(n-1)\frac{L_0}{a} + n\right)}{(1-K)^2}$$

$$\frac{a}{\delta_a}\frac{d\delta_a}{dr}(1-K)^2 = -(n-2)K^2 + 2(n-1)K - n$$

$$\frac{a}{\delta_a}\frac{d\delta_a}{dr}(1-K)^2 = -(n-2)K^2 + (n-2)K + nK - n$$

$$\frac{a}{\delta_a}\frac{d\delta_a}{dr}(1-K)^2 = -(n-2)K(K-1) + n(K-1)$$

$$\frac{a}{\delta_a}\frac{d\delta_a}{dr}(1-K) = (n-2)K - n$$

$$\frac{a}{\delta_a}\frac{d\delta_a}{dr} + n = K\left(n - 2 + \frac{a}{\delta_a}\frac{d\delta_a}{dr}\right)$$

$$K = \frac{a\frac{d\delta_a}{dr} + n\delta_a}{a\frac{d\delta_a}{dr} + (n-2)\delta_a}$$

By definition, $K \geq 1$, thus imposing the limits on the values of n:

$$\frac{a\frac{d\delta_a}{dr} + n\delta_a}{a\frac{d\delta_a}{dr} + (n-2)\delta_a} \geq 1$$

If $a\frac{d\delta_a}{dr} + (n-2)\delta_a \geq 0$, thus $n \geq 2 - \frac{a}{\delta_a}\frac{d\delta_a}{dr}$:

$$a\frac{d\delta_a}{dr} + n\delta_a \geq a\frac{d\delta_a}{dr} + (n-2)\delta_a$$

$0 \geq -2\delta_a$ always valid, if $n \geq 2 - \frac{a}{\delta_a}\frac{d\delta_a}{dr}$

If $a\frac{d\delta_a}{dr} + (n-2)\delta_a \leq 0$, thus $n \leq 2 - \frac{a}{\delta_a}\frac{d\delta_a}{dr}$:

$$a\frac{d\delta_a}{dr} + n\delta_a \leq a\frac{d\delta_a}{dr} + (n-2)\delta_a$$

$0 \leq -2\delta_a$ impossible

Hence, $K \geq 1$ for $\boxed{n \geq 2 - \frac{a}{\delta_a}\frac{d\delta_a}{dr}}$.

Deriving the equation for Criterion 5:

$$\int_a^{L_0} r u_z \, dr = -\frac{(1+v)(1-2v)}{(1-v)}\frac{F_z t}{2\pi E} + (\delta - R)\frac{a^2}{2} + \frac{R^3}{3} - \frac{(R^2-a^2)^{\frac{3}{2}}}{3}$$

$$-\frac{(1+v)(1-2v)}{(1-v)}\frac{F_z t}{2\pi E} + (\delta - R)\frac{a^2}{2} + \frac{R^3}{3} - \frac{(R^2-a^2)^{\frac{3}{2}}}{3} = \int_a^{L_0} r\left(-\delta_a\left(\frac{r}{a}\right)^n \frac{\left(1-\frac{L_0}{r}\right)^2}{(1-K)^2}\right) dr$$

$$-\frac{(1+v)(1-2v)}{(1-v)}\frac{F_z t}{2\pi E}+(\delta-R)\frac{a^2}{2}+\frac{R^3}{3}-\frac{(R^2-a^2)^{\frac{3}{2}}}{3}$$
$$=\frac{-\delta_a}{a^n(1-K)^2}\int_a^{L_0} r^{n+1}\left(1-\frac{2L_0}{r}+\frac{L_0^2}{r^2}\right)dr$$

$$\frac{(1+v)(1-2v)}{(1-v)}\frac{F_z t}{2\pi E}-(\delta-R)\frac{a^2}{2}-\frac{R^3}{3}+\frac{(R^2-a^2)^{\frac{3}{2}}}{3}$$
$$=\frac{\delta_a}{a^n(1-K)^2}\int_a^{L_0} r^{n+1}-2L_0 r^n+L_0^2 r^{n-1}\,dr$$

$$\frac{(1+v)(1-2v)}{(1-v)}\frac{F_z t}{2\pi E}-(\delta-R)\frac{a^2}{2}-\frac{R^3}{3}+\frac{(R^2-a^2)^{\frac{3}{2}}}{3}$$
$$=\frac{\delta_a}{a^n(1-K)^2}\left[\frac{r^{n+2}}{n+2}-2L_0\frac{r^{n+1}}{n+1}+L_0^2\frac{r^n}{n}\right]_a^{L_0}$$

$$\frac{(1+v)(1-2v)}{(1-v)}\frac{F_z t}{2\pi E}-(\delta-R)\frac{a^2}{2}-\frac{R^3}{3}+\frac{(R^2-a^2)^{\frac{3}{2}}}{3}$$
$$=\frac{\delta_a}{a^n(1-K)^2}\left(\frac{L_0^{n+2}-a^{n+2}}{n+2}-2L_0\frac{L_0^{n+1}-a^{n+1}}{n+1}+L_0^2\frac{L_0^n-a^n}{n}\right)$$

$$\frac{(1+v)(1-2v)}{(1-v)}\frac{F_z t}{2\pi E}-(\delta-R)\frac{a^2}{2}-\frac{R^3}{3}+\frac{(R^2-a^2)^{\frac{3}{2}}}{3}$$
$$=\frac{\delta_a a^{n+2}}{a^n(1-K)^2}\left(\frac{K^{n+2}-1}{n+2}-\frac{2K(K^{n+1}-1)}{n+1}+\frac{K^2(K^n-1)}{n}\right)$$

$$\frac{(1+v)(1-2v)}{(1-v)}\frac{F_z t}{2\pi E}-(\delta-R)\frac{a^2}{2}-\frac{R^3}{3}+\frac{(R^2-a^2)^{\frac{3}{2}}}{3}$$
$$=\frac{\delta_a a^{n+2}}{a^n(1-K)^2}\left(\frac{2K^{n+2}}{n(n+1)(n+2)}-\frac{K^2}{n}+\frac{2K}{n+1}-\frac{1}{n+2}\right)$$

From Criterion 6, where $\frac{du_z}{dr}\geq 0$ for $a\leq r\leq L_0$, the following limit on n is imposed:

$$-\delta_a\frac{r^{n-1}}{a^n}\frac{\left((n-2)\frac{L_0^2}{r^2}-2(n-1)\frac{L_0}{r}+n\right)}{(1-K)^2}\geq 0$$

$$(n-2)\frac{L_0^2}{r^2}-2(n-1)\frac{L_0}{r}+n\leq 0$$

To simplify, a definition of $T = \frac{L_0}{r}$, where $1 \leq T \leq K$, is used and roots of the equation are found:

$$(n-2)T^2 - 2(n-1)T + n \leq 0$$

$$T = \frac{2(n-1) \pm \sqrt{4(n-1)^2 - 4n(n-2)}}{2(n-2)} = \frac{(n-1) \pm \sqrt{n^2 - 2n + 1 - n^2 + 2n}}{n-2}$$

$$T = \frac{(n-1) \pm 1}{n-2} = \begin{cases} \frac{n}{n-2} \\ 1 \end{cases}$$

Rewriting the inequality:

$$(T-1)\left(T - \frac{n}{n-2}\right) \leq 0$$

$$T \leq \frac{n}{n-2}$$

If $n - 2 > 0$, thus $n > 2$:

$$T(n-2) \leq n \quad \rightarrow \quad n(T-1) \leq 2T \quad \rightarrow \; n \leq 2\frac{T}{T-1} \quad \rightarrow \quad \boxed{2 < n \leq 2\frac{T}{T-1}}$$

If $n - 2 < 0$, hence $n < 2$:

$$T(n-2) \geq n \; \rightarrow \; n(T-1) \geq 2T \; \rightarrow \; n \geq 2\frac{T}{T-1} \; \rightarrow \; 2\frac{T}{T-1} \leq n < 2 \quad \rightarrow \quad \text{impossible}$$

Hence the limits of n for fulfilling the Criterion 6 are $\boxed{2 < n \leq 2\frac{T}{T-1}}$

Appendix C – Case B Deformation

Definitions of Case B:

$$u_z = \frac{A}{r^n} + B$$

$$\frac{du_z}{dr} = -n\frac{A}{r^{n+1}}$$

For this Case, Criterion 4 could not be fulfilled, thus is ignored.

From Criterion 3, where $u_z(r = L_0) = 0$:

$$0 = \frac{A}{L_0^n} + B$$

$$B = -\frac{A}{L_0^n}$$

Updating the definition:

$$u_z = \frac{A}{r^n} - \frac{A}{L_0^n} = \frac{A}{L_0^n}\left(\frac{L_0^n}{r^n} - 1\right)$$

From Criterion 1, where $u_z(r = a) = -\delta_a$:

$$-\delta_a = \frac{A}{L_0^n}\left(\frac{L_0^n}{a^n} - 1\right)$$

$$A = -\frac{\delta_a L_0^n}{K^n - 1}$$

Updating definitions to their closed forms:

$$u_z = -\delta_a \frac{\left(\frac{L_0}{r}\right)^n - 1}{K^n - 1}$$

$$\frac{du_z}{dr} = n\delta_a \frac{L_0^n}{r^{n+1}} \frac{1}{K^n - 1} = n\delta_a \frac{a^n}{r^{n+1}} \frac{K^n}{K^n - 1}$$

By applying Criterion 2, where $\frac{du_z}{dr}(r = a) = \frac{d\delta_a}{dr}$, definition of K can be derived:

$$\frac{d\delta_a}{dr} = n\delta_a \frac{a^n}{a^{n+1}} \frac{K^n}{K^n - 1}$$

$$a\frac{d\delta_a}{dr}(K^n - 1) = n\delta_a K^n$$

$$K^n\left(a\frac{d\delta_a}{dr} - n\delta_a\right) = a\frac{d\delta_a}{dr}$$

$$K = \left(\frac{a\frac{d\delta_a}{dr}}{a\frac{d\delta_a}{dr} - n\delta_a}\right)^{\frac{1}{n}}$$

By definition, $K \geq 1$, thus imposing the limits on n:

$$\left(\frac{a\frac{d\delta_a}{dr}}{a\frac{d\delta_a}{dr} - n\delta_a}\right)^{\frac{1}{n}} \geq 1$$

If $n > 0$:

$$\frac{a\frac{d\delta_a}{dr}}{a\frac{d\delta_a}{dr} - n\delta_a} \geq 1$$

If $a\frac{d\delta_a}{dr} - n\delta_a > 0$, thus $n < \frac{a}{\delta_a}\frac{d\delta_a}{dr}$:

$$a\frac{d\delta_a}{dr} \geq a\frac{d\delta_a}{dr} - n\delta_a$$

$0 \geq -n\delta_a$ valid for $0 < n < \frac{a}{\delta_a}\frac{d\delta_a}{dr}$

If $a\frac{d\delta_a}{dr} - n\delta_a < 0$, thus $n > \frac{a}{\delta_a}\frac{d\delta_a}{dr}$:

$$a\frac{d\delta_a}{dr} \leq a\frac{d\delta_a}{dr} - n\delta_a$$

$0 \leq -n\delta_a$ valid for $n < 0$, thus impossible

If $n < 0$:

$$\frac{a\frac{d\delta_a}{dr} - n\delta_a}{a\frac{d\delta_a}{dr}} \geq 1$$

$$a\frac{d\delta_a}{dr} - n\delta_a \geq a\frac{d\delta_a}{dr}$$

$0 \geq n\delta_a$ valid for $n < 0$

Hence, $K \geq 1$ for $n < 0$ and $0 < n < \frac{a}{\delta_a}\frac{d\delta_a}{dr}$.

Deriving the equation for Criterion 5:

$$\int_a^{L_0} ru_z\, dr = -\frac{(1+v)(1-2v)}{(1-v)}\frac{F_z t}{2\pi E} + (\delta - R)\frac{a^2}{2} + \frac{R^3}{3} - \frac{(R^2-a^2)^{\frac{3}{2}}}{3}$$

$$-\frac{(1+v)(1-2v)}{(1-v)}\frac{F_z t}{2\pi E} + (\delta - R)\frac{a^2}{2} + \frac{R^3}{3} - \frac{(R^2-a^2)^{\frac{3}{2}}}{3} = \int_a^{L_0} r\left(-\delta_a \frac{\left(\frac{L_0}{r}\right)^n - 1}{K^n - 1}\right) dr$$

$$\frac{(1+v)(1-2v)}{(1-v)}\frac{F_z t}{2\pi E} - (\delta - R)\frac{a^2}{2} - \frac{R^3}{3} + \frac{(R^2-a^2)^{\frac{3}{2}}}{3} = \frac{\delta_a}{K^n - 1}\int_a^{L_0} L_0^n r^{1-n} - r\, dr$$

$$\frac{(1+v)(1-2v)}{(1-v)}\frac{F_z t}{2\pi E} - (\delta - R)\frac{a^2}{2} - \frac{R^3}{3} + \frac{(R^2-a^2)^{\frac{3}{2}}}{3} = \frac{\delta_a}{K^n - 1}\left[\frac{L_0^n r^{2-n}}{2-n} - \frac{r^2}{2}\right]_a^{L_0}$$

$$\frac{(1+v)(1-2v)}{(1-v)}\frac{F_z t}{2\pi E} - (\delta - R)\frac{a^2}{2} - \frac{R^3}{3} + \frac{(R^2-a^2)^{\frac{3}{2}}}{3} = \frac{\delta_a}{K^n - 1}\left(\frac{L_0^n L_0^{2-n} - L_0^n a^{2-n}}{2-n} - \frac{L_0^2 - a^2}{2}\right)$$

$$\frac{(1+v)(1-2v)}{(1-v)}\frac{F_z t}{2\pi E} - (\delta - R)\frac{a^2}{2} - \frac{R^3}{3} + \frac{(R^2-a^2)^{\frac{3}{2}}}{3} = \frac{\delta_a a^2}{K^n - 1}\left(\frac{K^2 - K^n}{2-n} - \frac{K^2 - 1}{2}\right)$$

$$\frac{(1+v)(1-2v)}{(1-v)}\frac{F_z t}{2\pi E} - (\delta - R)\frac{a^2}{2} - \frac{R^3}{3} + \frac{(R^2-a^2)^{\frac{3}{2}}}{3} = \frac{\delta_a a^2}{K^n - 1}\left(\frac{nK^n}{2(2-n)} - \frac{K^n}{2-n} + \frac{1}{2}\right)$$

$$\frac{(1+v)(1-2v)}{(1-v)}\frac{F_z t}{2\pi E} - (\delta - R)\frac{a^2}{2} - \frac{R^3}{3} + \frac{(R^2-a^2)^{\frac{3}{2}}}{3} = \frac{\delta_a a^2}{K^n - 1}\left(\frac{1}{2} - \frac{nK^n}{2(n-2)} + \frac{K^n}{n-2}\right)$$

$$\frac{(1+v)(1-2v)}{(1-v)}\frac{F_z t}{2\pi E} - (\delta - R)\frac{a^2}{2} - \frac{R^3}{3} + \frac{(R^2-a^2)^{\frac{3}{2}}}{3} = \frac{\delta_a a^2}{K^n - 1}\left(\frac{2(K^n - 1) - n(K^2 - 1)}{2(n-2)}\right)$$

$$\frac{(1+v)(1-2v)}{(1-v)}\frac{F_z t}{2\pi E} - (\delta - R)\frac{a^2}{2} - \frac{R^3}{3} + \frac{(R^2-a^2)^{\frac{3}{2}}}{3} = \frac{\delta_a a^2}{(\mathrm{n}-2)}\left(1 - \frac{n}{2}\frac{K^2 - 1}{K^n - 1}\right)$$

The Criterion 6, where $\frac{du_z}{dr} \geq 0$ for $a \leq r \leq L_0$, the following limit on n is imposed:

$$n\delta_a \frac{a^n}{r^{n+1}} \frac{K^n}{K^n - 1} \geq 0$$

$$\frac{n}{K^n - 1} \geq 0$$

If $n > 0$:

$$\frac{n}{K^n - 1} = \frac{positive}{positive} > 0$$

If $n < 0$:

$$\frac{n}{K^n - 1} = \frac{negative}{negative} > 0$$

Hence, Criterion 6 is fulfilled for all values of n, except $n = 0$.